AD-A225 813

# FINAL REPORT
# FOR
# QUANTUM DEVICE DEVELOPMENT

## CONTRACT NO. N00014-87-C-0363

| | |
|---|---|
| ARPA Order Number: | DE14Y01070 |
| Program Code Number: | 4145176-01/26 |
| Name of Contractor: | Texas Instruments Incorporated<br>13500 N. Central Expressway<br>P.O. Box 655936, M.S. 105<br>Dallas, Texas 75265 |
| Contract Period Covered by Report: | 4 September 1987–30 June 1990 |
| Amount of Contract: | $2,324,459 |
| Contract Number: | N00014-87-C-0363 |
| Effective Date of Contract: | 4 September 1987 |
| Contract Expiration Date: | 3 June 1990 |
| Short Title of Work: | Quantum Device Development |
| Program Manager: | R.T. Bate<br>(214) 995-3036 |
| Principal Investigators: | W.R. Frensley, J.H. Luscombe,<br>J.N. Randall, M.A. Reed,<br>A. Seabaugh, C.H. Yang,<br>S.K. Diamond (Stanford University)<br>D.M. Bloom (Stanford University) |

DTIC
ELECTE
AUG 28 1990
S D

Best Available Copy

20 July 1990

Approved for public release; distribution unlimited

The views and conclusions contained in this document are those of the authors and should not be interpreted as necessarily representing the official policies, either expressed or implied, of the Defense Advanced Research Projects Agency or the United States Government.

90 08 27 002

| REPORT DOCUMENTATION PAGE | 1. REPORT NO. | 2. | 3. Recipient's Accession No. DE14Y01070 |
|---|---|---|---|

| | |
|---|---|
| 4. Title and Subtitle<br>Quantum Device Development | 5. Report Date<br>July 1990<br>6. |
| 7. Author(s)<br>W.R. Frensley, J.N. Randall, R.T. Bate, A. Seabaugh, S.K. Diamond, and D.M. Bloom | 8. Performing Organization Rept. No.<br>08-90-36 |
| 9. Performing Organization Name and Address<br>Texas Instruments Incorporated<br>135336 N. Central Expressway, M/S 105<br>Dallas, Texas | 10. Project/Task/Work Unit No.<br>11. Contract (C) or Grant (G) No.<br>(C) N00014-87-C-0363<br>(G) |
| 12. Sponsoring Organization Name and Address<br>Office of Naval Research<br>800 N. Quincy Street<br>Arlington, VA 22214-5000 | 13. Type of Report and Period Covered<br>Final Technical Report<br>4 Sept. 1987-30 June 1990<br>14. |

15. Supplementary Notes

16. Abstract (Limit 200 Words)

A research and development program on quantum transistors is described. Bipolar and unipolar resonant tunneling transistors were designed, fabricated, and characterized. These devices exhibit negative transconductance, and dc and microwave gain at room temperature. Recommendations are made for further work.

17. Document Analysis a. Descriptors

Gallium Arsenide, Resonant Tunneling, Quantum Effect Transistors

b. Identifiers and Open-Ended Terms

c. COSATI Field/Group

| 18. Distribution Statement | 19. Security Class (This Report)<br>Unclassified | 21. No. of Pages<br>94 |
|---|---|---|
| | 20. Security Class (This Page)<br>Unclassified | 22. Price |

# TABLE OF CONENTS


| Section | Title | Page |
|---|---|---|
| | EXECUTIVE SUMMARY | 1 |
| I | INTRODUCTION | 3 |
| | A. NEED FOR QUANTUM DEVICES/CIRCUITS | 3 |
| | B. RESONANT TUNNELING | 4 |
| | C. RESONANT-TUNNELING TRANSISTORS | 4 |
| | 1. Quantum-Classical Hybrid Devices | 4 |
| | 2. True Resonant Tunneling Transistors (RTTs) | 6 |
| II | DEVICE SIMULATION AND MODELING | 11 |
| | A. TRANSISTOR DESIGN TOOLS | 11 |
| | 1. First-Generation Modeling Programs | 12 |
| | 2. Second-Generation Modeling Codes | 15 |
| | 3. Interactive Modeling Codes | 15 |
| | B. Physical Device Models | 19 |
| | 1. Schroedinger Equation Models | 19 |
| | 2. Quantum Kinetic Models | 25 |
| III | QUANTUM TRANSISTOR DEVELOPMENT | 27 |
| | A. GaAs RTT DEVELOPMENT | 27 |
| | B. QUANTUM-WELL RTT PERFORMANCE CONSIDERATIONS | 29 |
| | C. InP-BASED RTT | 33 |
| | 1. Materials Development | 33 |
| | 2. Device Development | 40 |
| | D. Process Development for RTTs | 55 |
| | 1. Fabricating GaAs/AlGaAs/InGaAs RTTs | 57 |
| | 2. Fabricating InGaAs/AlAs/InAlGaAs RTTs | 63 |
| | 3. Electron-Beam Processing of RTTs | 64 |
| IV | MANUFACTURING ISSUES | 68 |
| V | HIGH SPEED RESONANT TUNNELING DIODE CIRCUITS (STANFORD UNIVERSITY) | 81 |
| | A. INTRODUCTION | 81 |
| | B. PULSE FORMING WITH RESONANT TUNNELING DEVICES | 81 |
| | C. RTD TRIGGER CIRCUITS | 82 |
| VI | SUMMARY OF ACCOMPLISHMENTS | 89 |
| VII | CONCLUSIONS AND RECOMMENDATIONS | 90 |
| | REFERENCES | 91 |



Accesion For
NTIS CRA&I ☑
DTIC TAB ☐
Unannounced ☐
Justification
By
Distribution /
Availability Codes
Dist | Avail and/or Special
A-1

## APPENDIXES


A HBAND: An Interactive Heterostructure Device Modeling Program
B Determination of the Fermi Level in Semiconductor Superlattices
C Quantum Kinetic Theory of Nanoelectronic Devices
D Effect of Inelastic Processes on the Self-Consistent Potential in the Resonant-Tunneling Diode
E Improved $Al_xGa_{1-x}As/Ga_{1-y}In_yAs/GaAs$ Strained-Layer Double Barrier Resonant Tunneling Structure
F Observation of Negative Differential Resistance in $Al_{0.2}Ga_{0.6}As/Al_{0.4}Ga_{0.6}As/GaAs$ Double Barrier Resonant Tunneling Structure
G Dependence of Peak Current Density on Impurity Doping in Double Barrier Resonant Tunneling Structures
H Quantitative Resonant Tunneling Spectroscopy: Current-Voltage Characteristics of Precisely Characterized Resonant Tunneling Diodes
I Pseudomorphic Bipolar Quantum Resonant-Tunneling Transistor
J Quantum-Well Resonant-Tunneling Transistors
K Implant and Annealed Ohmic Contact to a Thin Quantum Well
L A New Field-Effect Resonant Tunneling Transistor: Observation of Oscillatory Transconductance
M Improved MBE Growth Structures for High-Performance Device Applications1
N Realization of a Three-Terminal Resonant Tunneling Device: The Bipolar Quantum Resonant Tunneling Transistor


## LIST OF FIGURES


| *Figure* | *Title* | *Page* |
|---|---|---|
| 1 | Characteristics and conduction band profile of resonant tunneling diode | 5 |
| 2 | I(V) characteristics of a series combination of RTD and MOSFET | 6 |
| 3 | (a) Hot-electron tunneling transistor. (b) Band diagram through AA′ shows tunneling behavior, but (c) that through BB′ shows parasitic base current | 7 |
| 4 | (a) Quantum excited-state tunneling transistor. (b) Shows collector current derived from tunneling through excited (upper) quantum-well state. (c) Control carriers supplied to ground state by base contact and confined by medium-gap collector | 9 |
| 5 | (a) Bipolar tunneling transistor. Energy-band diagram through Section AA′ shown in (b) illustrates problem of forward bias required for this device to operate | 9 |
| 6 | (a) Bipolar resonant tunneling transistor. Energy-band diagram through Section AA′ shown in (b) illustrates reduced forward-bias voltage caused by narrow-bandgap quantum well | 10 |
| 7 | Results of typical run of BiQuaRTT modeling program BIQMODEL | 13 |
| 8 | Output of QUESTTMOD. Left plot shows conduction-band energy as function of position through structure | 13 |
| 9 | Scattering-theory I(V) curves for laterally confined structures | 14 |
| 10 | Output of HETEROSTAT, modeling BiQuaRTT structure | 16 |

# LIST OF FIGURES
## (Continued)


| *Figure* | *Title* | *Page* |
|---|---|---|
| 11 | Output of TRANSBAND, showing transmission and reflecting resonances | 16 |
| 12 | Sun workstation CRT display for HBAND modeling program | 18 |
| 13 | Time evolution of electron wave packet escaping from quantum well by tunneling | 20 |
| 14 | Results of simulation of escape of wave packet from quantum well | 21 |
| 15 | Results of simulation of transmission of wave packet through quantum well | 23 |
| 16 | Pseudomorphic BiQuaRTT energy-band profile computed by simulation tool BIQMODEL | 28 |
| 17 | Computed energy-band diagrams for In(GaAl)As/AlAs/InGaAs (a) BiQuaRTT and (b) same structure with AlAs tunnel barriers removed, i.e., HBT with 12-nm base. Dashed lines indicate quasi-Fermi levels with $V_{be}$=1.05 V and $V_{cb}$=0.5 V | 31 |
| 18 | Performance projections of $f_T$ and $f_{MAX}$ for AlGaAs/GaAs BiQuaRTT and their dependence on base thickness and doping using parameters in Table 3 | 31 |
| 19 | Performance projections of $f_T$ and $f_{MAX}$ for In(GaAl)As/InGaAs BiQuaRTT and their dependence on base thickness and doping using parameters in Table 4 | 32 |
| 20 | Calculated room-temperature energy-band profile and RTD characteristics for pseudomorphic barrier AlAs/InGaAs/AlAs RTD | 35 |
| 21 | Calculated room-temperature energy-band profile and RTD characteristics for pseudomorphic barrier AlAs/InGaAs/InAs/InGaAs/AlAs RTD | 35 |
| 22 | Temperature dependence of RTD structure described in Figure 21 | 36 |
| 23 | Room-temperature I-V characteristics for material of Figure 20 with emitter area of 9 $\mu m^2$ | 36 |
| 24 | Calculated room-temperature energy-band profile and RTD characteristics for raised emitter and collector RTD, InAlAs/AlAs/InGaAs/AlAs/InAlAs | 37 |
| 25 | Calculated room-temperature energy-band profile and RTD characteristics for a raised emitter and collector RTD, $In_{0.5}(Ga_{0.5}Al_{0.5})_{0.5}As$/AlAs/InGaAs/AlAs/$In_{0.5}(Ga_{0.5}Al_{0.5})_{0.5}As$ | 38 |
| 26 | Transmission electron micrograph of device structure of Figure 25 showing rotation-induced ordering of InGaAs collector layer adjacent to the $n^+$ InP substrate | 38 |
| 27 | Transmission electron micrograph of double-barrier RTD of Figure 25 showing quantum well and rotation-induced ordering of $In_{0.5}(Ga_{0.5}Al_{0.5})_{0.5}As$ quaternary emitter and collector layers | 39 |
| 28 | RTD characteristics for same structure described in Figure 21, here grown on Fe-doped InP substrate. Diode area is $3 \times 22$ $\mu m^2$ | 40 |
| 29 | Measured S-parameters (S11) for AlAs/InGaAs/InAs RTD with $4 \times 10$ $\mu m^2$ emitter at room temperature | 41 |
| 30 | Lumped equivalent circuit for RTD determined from measured S-parameters | 42 |
| 31 | Measured electrical properties of $In_{0.53}Ga_{0.47}As$ showing dependence of electron and hole Hall mobility on doping density | 42 |
| 32 | Calculated energy-band diagram for InGaAlAs/InGaAs/InAs pseudomorphic HBT with 4-nm $p^+$ base used as process test structure | 43 |
| 33 | Room-temperature common-emitter transistor characteristics for 4-nm base InGaAlAs/InGaAs/InAs HBT | 44 |

# LIST OF FIGURES
## (Continued)


| *Figure* | *Title* | *Page* |
|---|---|---|
| 34 | (a) Calculated energy-band diagram in vicinity of quantum-well region of BiQuaRTT under bias. Dashed lines indicate quasi-Fermi level energies in (left to right) emitter, base, and collector. Computed transmission coefficient for energies exceeding conduction-band energies in emitter are plotted in (b). For energies less than emitter conduction band edge, resonances are plotted by computing change in wave-function phase with energy [see lower axis in (b)] | 45 |
| 35 | Calculated energy-band and carrier density profiles for AlAs/InGaAs/AlAs RTD of dimensions 2/40/2 nm with 2D quantum-well states indicated with dotted lines and quasi-Fermi energies indicated by dashed lines | 45 |
| 36 | Room-temperature current and conductance (dI/dV) voltage characteristics for AlAs/InGaAs RTD with 40-nm quantum well | 47 |
| 37 | Calculated dependence of quantum-well energy state dependence on applied voltage for AlAs/InGaAs RTD of Figure 36 | 47 |
| 38 | Room-temperature (a) common-emitter transistor characteristics, (b) common-emitter characteristics showing dependence of $I_c$ on $V_{be}$, and (c) base/emitter junction I-V characteristics with collector open for RBT | 48 |
| 39 | Room-temperature (a) common-emitter BiQuaRTT characteristics, (b) common-emitter characteristics showing dependence of $I_c$ on $V_{be}$, and (c) base/emitter junction I-V characteristics with collector open | 49 |
| 40 | Room-temperature (a) common-emitter RBT characteristics, (b) common-emitter characteristics showing dependence of $I_c$ on $V_{be}$. Same transistor as measured in Figure 38 | 51 |
| 41 | Common-emitter transistor characteristics for 40-nm QuESTT at 4.2 K. Emitter is 2 μm in diameter | 52 |
| 42 | (a) Calculated energy-band diagram for 40-nm base QuESTT. Dashed lines indicate quasi-Fermi level energies in (left to right) emitter, base, and collector. (b) Computed transmission coefficient for energies exceeding conduction-band energies in emitter. For energies less than emitter conduction-band edge, resonances are plotted by computing change in wave-function phase with energy [see lower axis in (b)] | 52 |
| 43 | Room-temperature characteristics of (a) common-emitter 40-nm base QuESTT, (b) common-emitter characteristics showing dependence of $I_c$ on $V_{be}$. Emitter area is $2 \times 10\ \mu m^2$ | 54 |
| 44 | Dependence of collector current $I_C$ and input conductance $dI_e/dV_{be}$ at 4.2 K on base/emitter voltage $V_{be}$ and collector base voltage for same device shown in Figure 41 | 55 |
| 45 | Scanning electron microscope photograph of air-bridge interconnect to RTT | 56 |
| 46 | Vector network measurement of current gain $h_{212}$ and maximum available gain as function of frequency with $V_{be} = 0.8$ V and $V_{ce} = 1.22$ V. Emitter area is $3 \times 10\ \mu m^2$ | 56 |
| 47 | Depth profile of triple implant used to contact well in BiQuaRTT devices | 58 |
| 48 | SIMS profile of pseudomorphic BiQuaRTT transistor with 5-nm AlAs tunnel barriers and 25-nm Be-doped InGaAs quantum-well base | 59 |
| 49 | Cross-section TEM of selectively etched (RIE) and regrown QuESTT structure | 60 |
| 50 | Cross-section TEM of selectively etched (thermal MBE) and regrown QuESTT structure | 61 |

# LIST OF FIGURES
## (Continued)


| *Figure* | *Title* | *Page* |
|---|---|---|
| 51 | Mask set for fabricating RTTs on InGaAs/AlAs/InAlGaAs | 65 |
| 52 | Coplanar transmission-line transistor layout | 66 |
| 53 | Self-aligned process for InGaAs/AlAs/InAlGaAs-based RTTs | 67 |
| 54 | Resonant peak voltage as function of spacer and contact doping density for InP/InGaAs RTDs, at 300 K | 69 |
| 55 | I-V and G-V characteristics at 300K for (a) 3196, (b) 3205, and (c) 3208 | 70 |
| 56 | Band structure calculations for samples (a) 3196, (b) 3205, and (c) 3208 | 72 |
| 57 | I-V and G-V characteristics at 77 K for samples (a) 3196, (b) 3205, and (c) 3208 | 73 |
| 58 | Slice map of (a) positive resonant tunneling voltages, (b) positive peak current, (c) positive valley current, (d) negative resonant tunneling voltages, (e) negative peak current, and (f) negative valley current for sample 3208 | 75 |
| 59 | Contour plot fit to Figure 58(a) | 78 |
| 60 | Origin of large fluctuations in RTD resonant voltage | 80 |
| 61 | Device cross section of proton-implanted, microwave-compatible RTD process | 83 |
| 62 | S11 measurements and calculations | 83 |
| 63 | Electro-optically sampled output of pulse-forming structure | 85 |
| 64 | Experimental setup to demonstrate trigger action at 60 GHz using RTD circuit | 85 |
| 65 | Four different switching waveforms | 86 |
| 66 | Experimental setup for using RTD trigger circuit output as trigger input to digital scope | 86 |
| 67 | Scope plot of 60-GHz signal triggered by output of RTD trigger circuit | 87 |
| 68 | Network analyzer receiver (a) and random sampling oscilloscope, (b) using an RTD triggering circuit | 88 |


# LIST OF TABLES


| *Table* | *Title* | *Page* |
|---|---|---|
| 1 | Device Modeling Codes on VAX Computer | 17 |
| 2 | Comparison of Selected Materials Properties for the Lattice-Matched Compound Semiconductors Grown on GaAs and InP Substrates | 30 |
| 3 | Input parameters for the AlGaAs/GaAs BiQuaRTT projections of Figure 18 | 32 |
| 4 | Input parameters for the In(GaAl)As/InGaAs BiQuaRTT projections of Figure 19 for the same transistor geometry as described in Table 3 caption | 33 |
| 5 | Comparison of Extracted Equivalent Circuit RTD Parameters With Estimates Based on DC Device Characteristics and Geometry | 42 |
| 6 | Samples Used in Study of Spacer Layer/Doping Effects on IV Characteristics of InGaAs/AlAs RTDs on InP substrates | 68 |
| 7 | Samples Used in Study of Spacer Layer/Doping Efffects on IV Characteristics of InGaAs/AlAs RTDs | 69 |
| 8 | Fit to Spatial Maps, Resonant Voltage $V_r$ | 79 |
| 9 | Fit to Spatial Maps, Peak Current $I_p$ and Valley Current $I_v$ | 79 |

# QUANTUM DEVICE DEVELOPMENT

# FINAL TECHNICAL REPORT

# FOR CONTRACT NO. N00014-87-C-0363

## EXECUTIVE SUMMARY

The historical trend of exponential improvement in cost and performance of integrated circuits can be traced primarily to downscaling of minimum geometries resulting from progress in design, lithography, and processing. However, because of the onset of fundamental limits, downscaling will cease to be an option for noncryogenic operation in the mid-1990s, unless revolutionary devices and chip architectures are developed. Unipolar tunneling devices based on heterojunction technology appear to circumvent the scaling limits of conventional devices, and are, therefore, of interest as a potential solution to the device portion of this problem. A particular type of heterojunction device called a resonant tunneling transistor was selected for this effort.

In this report, results of a program of research and development of resonant tunneling transistors are described. Unlike some devices that have been called "resonant tunneling transistors" but are really conventional devices incorporating resonant tunneling diode structures, these are "true" resonant tunneling transistors. A true resonant tunneling transistor consists of a single-well, double-barrier resonant tunneling diode structure to which a third terminal, directly contacting the quantum well, has been added. Two types of resonant tunneling transistor (RTT) were included within the scope of the contract: a unipolar version called the quantum excited-state tunneling transistor (QuESTT), and a pseudomorphic bipolar version called the bipolar quantum resonant tunneling transistor (BiQuaRTT). A lattice-matched version of the BiQuaRTT was developed by the contractor under an earlier Air Force contract. Although the bipolar devices do not meet the downscaling requirements, they require less difficult processing and can serv as a valuable proof of principle and guide to design of unipolar devices.

The report describes the development of a theory of resonant tunneling structures and its use to derive device models that have been used in the design of device structures. It also describes the extensive process development that has been required to permit contacting the very thin (5-nanometer) quantum-well base layers, and also to isolate the emitter, base, and collector layers. The processes developed have been used to fabricate transistors, and these devices have been characterized electrically.

Unipolar and bipolar RTTs in both GaAs- and InP-based heterojunction material systems were fabricated and characterized. Initial demonstration of the pseudomorphic InGaAs base BiQuaRTT was achieved in the GaAs/AlGaAs/InGaAs system. Resonant tunneling was observed in the pseudomorphic AlGaAs/InGaAs/GaAs system and the $Al_xGa_{1-x}As/Al_yGa_{1-y}As/GaAs$ system. High current density, important for high-speed applications, of $10^5$ A/cm$^2$ with a peak-to-valley current ratio of 2:1 at 77 K was achieved in an AlGaAs/GaAs RTD. The heterojunction device models developed under this contract were used to interpret the I(V) characteristics of a set of precisely characterized RTDs. This work established the predictive ability of the heterojunction models and provided a simple

explanation for I(V) asymmetry in RTDs in terms of monolayer thickness fluctuations. An implantation process for contacting an n-type quantum well was developed and used to contact the quantum well of a unipolar GaAs RTT. This device is the first Stark-effect Transistor (SET) to exhibit oscillatory negative transconductance at 77 K and was an important test vehicle for understanding transport into and out of n-type quantum wells.

A state-of-the-art MBE growth capability for In(AlGa)As compounds lattice-matched in InP was demonstrated. Methods for growth of resonant tunneling heterostructures and for heavily doping InGaAs with Be and Si were developed. A microwave resonant tunneling transistor process was also developed and microwave characterization of RTDs and RTTs was performed. In the final weeks of the contract, both unipolar and bipolar InP RTTs were demonstrated and characterized. We achieved for the first time room-temperature dc and microwave gain from the unipolar InP-based RTTs. These unipolar hot-electron transistors are the first ever to show room-temperature dc and microwave gain.

Recommendations for further work include engineering of the transistor heterostructure to optimize the device at room temperature. Development of selective wet- and dry-etch processes are needed to realize the full potential of these advanced device structures and provide for a manufacturable process. As quantum transistors are moved into a manufacturing environment, device design rules will be required to allow the realization of circuits. These must evolve from a strong theoretical understanding of the basic device transport that must be built concurrently and in close collaboration with the experimental effort. No insurmountable technical impediments to the realization of quantum transistor devices and circuits were found, and continued development of resonant tunneling transistors and circuits is recommended.

# SECTION I

# INTRODUCTION

## A. NEED FOR QUANTUM DEVICES/CIRCUITS

The downscaling of minimum geometries of transistor-based integrated circuits (ICs) will eventually be brought to an end by a combination of problems related to devices, interconnections, noise, and reliability. The resulting saturation of circuit densities almost certainly implies a saturation of the historical exponentially downward trend in cost and volume per bit or function, which has been a primary driving force for the increasing pervasiveness of electronics in Department of Defense (DoD) systems. Scaling has also provided exponential improvements in device speed and power dissipation, which have led to substantial enhancement of system performance. Because the introduction of sophisticated electronics into these systems has significantly improved their capabilities, it is appropriate to inquire whether an alternative scenario that significantly prolongs exponential trends in cost and performance exists.

Estimates based on abstract physical switching device models that are independent of specific device technologies indicate that several orders of magnitude in downscaling of device power in devices with minimum geometries of a few nanometers would be theoretically permitted, if an appropriate nontransistor device technology could be found. The key to this search is to employ electronic phenomena that are characterized by dimensions much smaller than the depletion layer widths and diffusion lengths that provide the basis for conventional transistor function.

A step can be taken in this direction by using heterojunctions rather than p-n junctions to introduce potential barriers for purposes of carrier confinement. This approach is currently limited to GaAs, however, because of the absence of an adequate heterojunction technology for silicon. Nevertheless, as we shall see, this approach can be carried to the limit of completely unipolar devices employing only heterojunctions for confinement, totally eliminating all p-n junctions, and their associated space-consuming depletion layers, from the device.

The advent of molecular-beam epitaxy (MBE) and similar technologies permits the fabrication of semiconductor heterostructures with features on the scale of nanometers. These capabilities have been applied to the development of semiconductor devices with significantly improved performance. Three distinct thrusts may be identified within this worldwide development effort. The first is to apply heterostructure technology to improve what are essentially classical semiconductor devices. The selectively doped heterostructure transistor (SDHT), which is also known as the high electron mobility transistor (HEMT), and the heterojunction bipolar transistor (HBT) are examples of this thrust. The second thrust is to employ heterostructures in optoelectronic devices, to exploit their ability to confine carriers and optical fields and to modify quantum states of electrons. The third thrust, which has had by far the smallest total effort of the three, is to find novel physical phenomena enabled by nano-scale heterostructures that can lead to truly revolutionary device mechanisms. Because semiconductor structures having dimensions comparable to the Bloch wavelength of electrons can be fabricated, the obvious place to look for such phenomena is in quantum-mechanical effects.

Quantum-mechanical tunneling is an electron transport mechanism that becomes important when the thickness of potential barriers to carrier transport becomes very small, about 0.01 μm (10 nm). The mechanism is of interest because it potentially permits carrier transport control by electrical means in structures far too small to operate as conventional transistors. Three-terminal devices based on tunneling may thus provide a means of continuing the historical exponentially downward trend in minimum device geometries, and in switching power and delay, beyond the limits of transistors.[1]

The progress of AlGaAs/GaAs heterojunction technology has rejuvenated interest in tunneling devices, and particularly in the use of quantum wells to modify the density of states available to tunneling carriers. The most popular structure for study has been the single quantum well, double-barrier resonant tunneling diode (RTD).[2,3] Before the inception of this contract, the contractor and others had demonstrated RTDs with superior low-temperature negative differential resistance (NDR) characteristics,[4] and the contractor had shown that NDR persists at high temperatures in these devices.[5] NDR, perhaps because of incoherent resonant tunneling, has also been shown to persist at frequencies as high as 2.5 THz.[3]

Early experience with Esaki diodes has shown, however, that, although diodes exhibiting NDR can be used for switching, large-scale ICs based on such threshold logic devices are not realizable.[6] Three-terminal devices that provide sufficient current gain for fanout are required, and the fabrication process must be suitable for integration

## B. RESONANT TUNNELING

Resonant tunneling structures are the simplest case of devices exhibiting quantum confinement and coupling. The confinement in this type of structure is achieved in one dimension by using quantum-well heterostructures. The first investigation of these structures was done by Chang, Esaki and Tsu[2] who observed weak structure in the current-voltage characteristics of resonant tunneling diodes at low temperatures. Interest in these structures was revived by the work of Sollner et al.[3] A number of groups are now actively studying resonant-tunneling diodes and attempting to incorporate resonant-tunneling structures into three-terminal devices (transistors).

A typical RTD structure is shown in Figure 1. The most often used material is the lattice-matched GaAs/AlGaAs system, where the highly doped contacts and central quantum well are GaAs and the barriers are $Al_xGa_{1-x}As$. The two $Al_xGa_{1-x}As$ layers that define the central GaAs quantum well serve as partially transparent barriers to electron transport through the device. Resonant tunneling occurs when the bias voltage across the outer electrodes is such that one of the quantum-well bound states is at the same energy as some occupied states in the cathode and some unoccupied states in the anode. Peaks in the electron transmission as a function of incident electron energy thus lead to peaks in the current-versus-voltage characteristic of the diode. The structure is an electrical analog of a Fabry-Perot resonator.

## C. RESONANT-TUNNELING TRANSISTORS

### 1. Quantum-Classical Hybrid Devices

If one seeks to exploit resonant tunneling in a three-terminal (transistor) device, there are, broadly, two different ways to approach this task. The simpler and presently more popular approach is to insert a resonant-tunneling quantum-well structure into one electrode

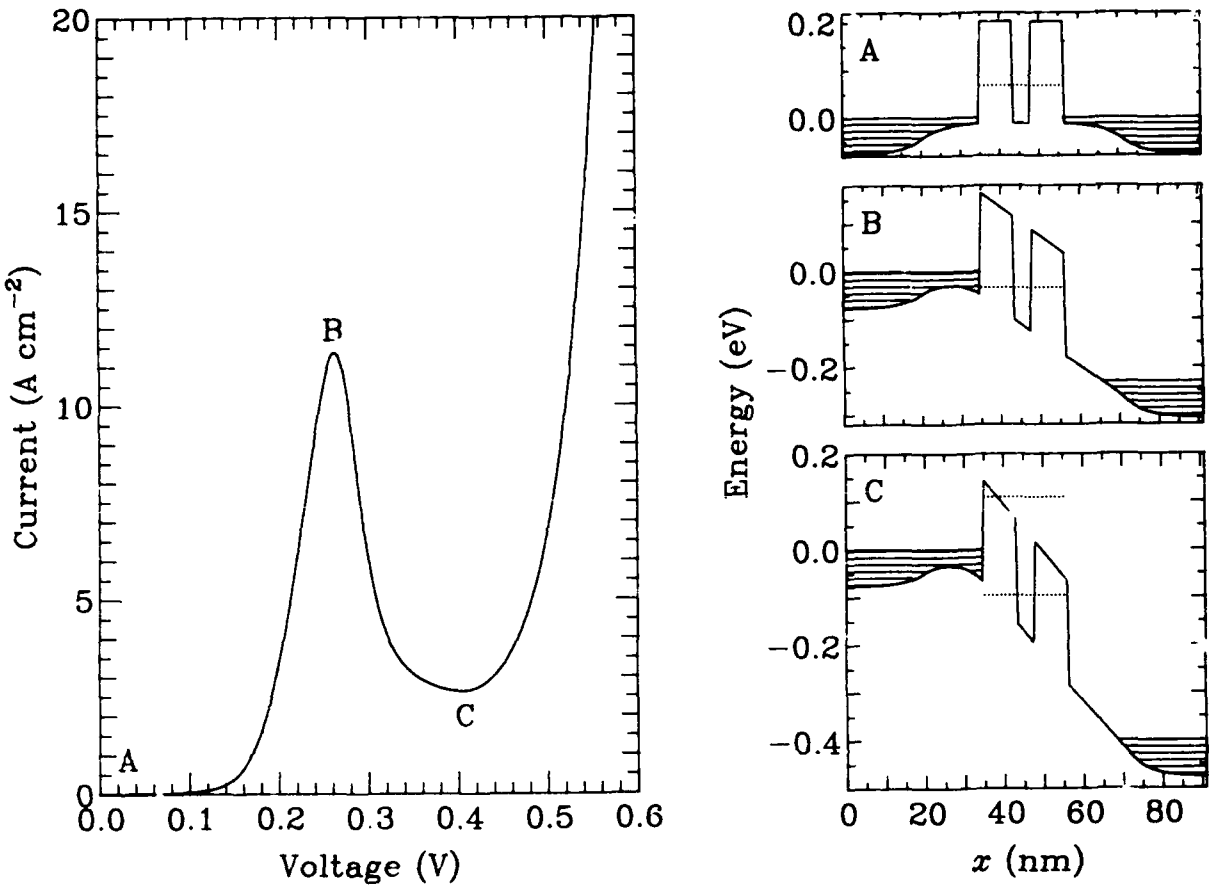


**Figure 1**
**Characteristics and conduction band profile of resonant tunneling diode. I (V) characteristic is plotted on right. Points labeled A, B, and C correspond to conduction-band profiles plotted on right. Shaded areas of band-profile plots show occupied electron states and dotted lines show resonant energy levels. No current flow in equilibrium (A). As bias voltage is applied, resonant level is pulled down to permit resonant tunneling (B), which appears as peak in I(V) curve. Tunneling current then declines (C) as resonant level is pulled below conduction-band edge on upstream side.**

of an otherwise conventional device. Examples of this approach employ bipolar[7], hot-electron[8], and various field-effect[9] transistors. The perceived advantages of such structures lie in their novel I(V) characteristics, typically including a negative resistance region and leading to multistable states in simple circuits. The problem with this approach is that the same characteristics would be more easily obtained by simply connecting a negative-resistance RTD in series with the conventional device. To illustrate this, we have fabricated such a device in the simplest possible way: by wiring together a resonant-tunneling diode with an off-the-shelf transistor. The I(V) characteristic of such a hybrid is shown in Figure 2. The hybrid device consists of a series combination of a normal MOSFET and a double-barrier resonant-tunneling structure and exhibits the characteristics that most series combinations do: negative differential resistance, negative transconductance, etc.

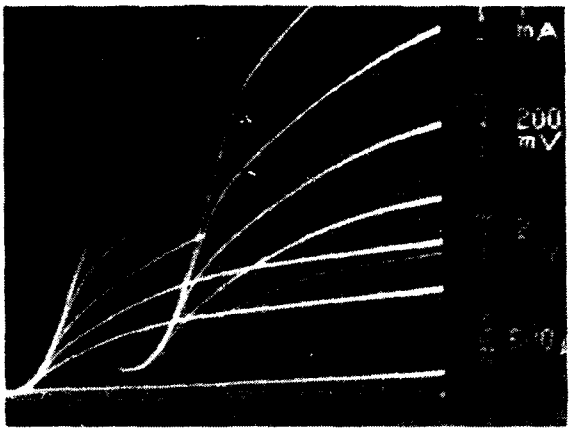


**Figure 2**
**I(V) characteristics of a series combination of RTD and MOSFET. MOSFET is at room temperature; RTD at 77 K.**

Therefore, there is no persuasive reason for intimately integrating the transistor and the RTD; they could just as well be fabricated side-by-side on the same chip. The more promising approach is to build what we describe as a "true" tunneling transistor, in which the structure is designed so that the quantum well is independently contacted and its potential may be adjusted independently of the adjacent electrodes. This will permit a full exploitation of the tunneling transport mechanism, and is the approach of the present program.

## 2. True Resonant Tunneling Transistors (RTTs)

The goal of the present program is to demonstrate three-terminal-quantum semiconductor devices of each of two designs, described in the following paragraphs. They are referred to by the acronyms QuESTT (for quantum excited-state tunneling transistor) and BiQuaRTT (for bipolar quantum resonant-tunneling transistor). These devices were conceived within the constraint that nanometer resolution should only be required in the vertical direction, which is readily achieved using epitaxial growth techniques. Because quantum-mechanical effects are permitted in only one spatial dimension, the present devices are closely analogous to the purely classical bipolar and hot-electron transistors. However, the obvious approach of simply scaling down a classical device to quantum dimensions[10] leads to fundamental problems that require a modification of the device design. The analysis of these problems and the rationale behind the QuESTT and BiQuaRTT designs are discussed in the following paragraphs.

To make a three-terminal quantum device requires a way to control the current through the device with a voltage or current supplied to the control electrode. The current through the device may be presumed to be conducted by resonant tunneling of electrons. The obvious approach should be to try to manipulate the potential of the quantum well. If this is to be done through the electrostatic potential, then mobile charges must be added to or removed from the structure by the control electrode, to act as sources of the perturbation in the potential. The fundamental problems that lie in the nature and behavior of these charges.

In semiconductors, the available charge carriers are electrons and holes. In view of the recent successes of ballistic hot-electron devices,[11,12] consider first what happens when trying to use electrons to control the tunneling current. The problem with such schemes is that the "cold" electrons in the base are still quantum-mechanical particles, and they have to occupy allowed quantum states in the quantum well. The lowest state is typically the state through which the current-carrying electrons are supposed to tunnel. Thus, it is difficult to maintain the distinction between the controlling and current-carrying electrons in this structure. Another way to view this problem, as illustrated in Figure 3, is that the base-collector barrier is not sufficient to confine the electrons in the base, if it is thin enough to permit resonant tunneling. This leads to an excessive base-collector leakage current, of sufficient magnitude to completely short out the base and make transistor action impossible. Devices of this structure have been built and show precisely this behavior.[13]

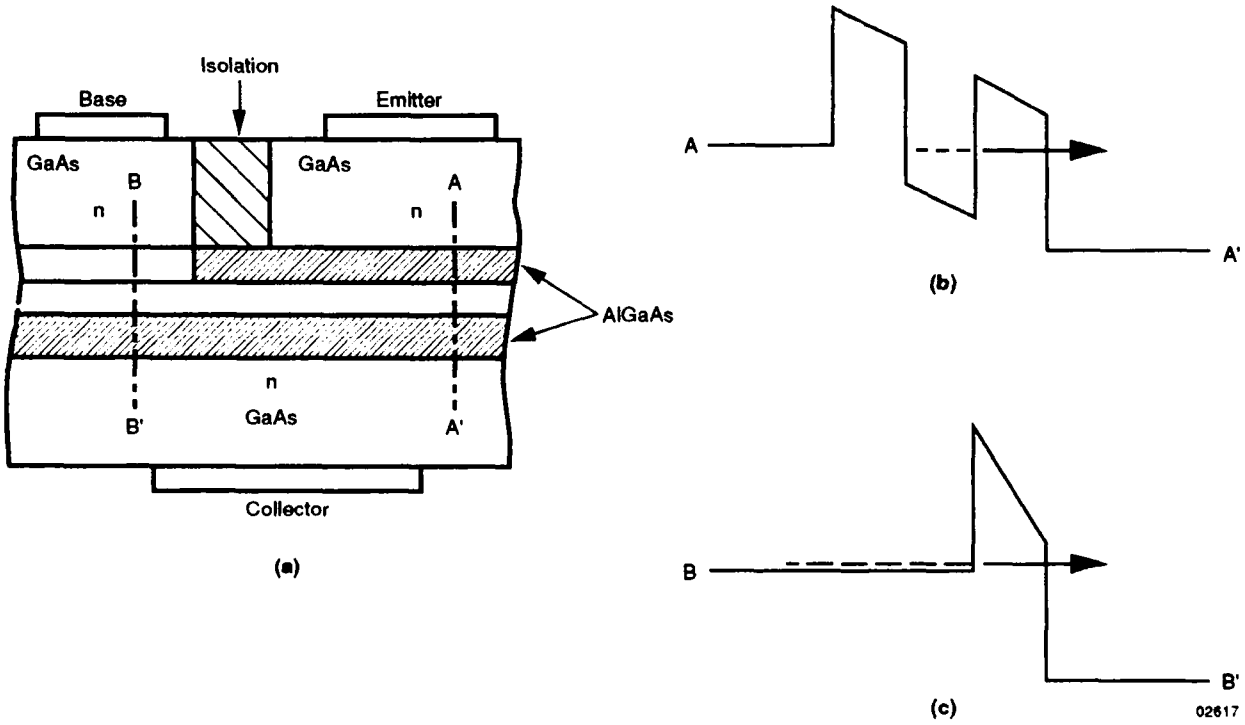


**Figure 3**
**(a) Hot-electron tunneling transistor. (b) Band diagram through AA′ shows tunneling behavior, but (c) that through BB′ shows parasitic base current.**

To overcome this problem, a device called the QuESTT was invented by the contractor. This structure uses a narrower-bandgap quantum-well layer to "hide" the lowest-lying electron state from the tunneling electrons, thus making it available to the control electrons (Figure 4). The control electrons are injected into and removed from the base by a tunneling contact to a thick layer of the narrow-bandgap material. This device thus requires a selective epitaxial regrowth process to make the base contact.

As with the unipolar device described, the most obvious bipolar quantum transistor structure will not work. The problem becomes apparent when considering the energy-band diagram of the resonant-tunneling structure. Such a band diagram is shown in Figure 5. To achieve resonant tunneling, the potential of the bottom of the quantum well must be biased below the bottom of the conduction band in the source electrode. Notice what this implies about the emitter-base bias: it must be greater than the narrower bandgap, and in the forward direction for current flow. To have some way to make contact to the holes in the quantum well implies a bulk region that is doped p-type. If this p region is in contact with the n-type emitter, a catastrophic current will result.

The solution to this problem is the same as that which led to the QuESTT. The quantum well can be made of a narrower-bandgap material, which will reduce the bias voltage required to turn on the device to a manageable level. This device is the BiQuaRTT. The band diagram of the resulting structure is shown in Figure 6. The contact to the base of this device can be achieved with conventional fabrication technology, using either ion implantation or diffusion of acceptors. The compositional disorder resulting from either of these processes is actually of benefit, because it helps to reduce the energy barrier between the contact and the base layer.

In view of the known band alignments at GaAs-based heterojunctions, a practical BiQuaRTT design will usually involve tunneling through the second state in the well, leaving the ground state vacant for control carriers. However, catastrophic leakage currents still exist. Since the ground state is not actively involved in the tunneling, it can be "hidden" below the conduction band.[14]

A number of options exist for the creation of wider-bandgap regions in the emitter and collector (with respect to the quantum well). One option is to use an $Al_xGa_{1-x}As$ emitter/ $Al_yGa_{1-y}As$ tunnel barrier/$Al_zGa_{1-z}As$ quantum-well structure ($y > x > z \quad 0$). Another is to use multimaterial systems, such as a GaAs emitter/$Al_xGa_{1-x}As$ tunnel barrier/$In_yGa_{1-y}As$ quantum-well structure, as previously mentioned. A third option is to create a wider-bandgap material in the emitter/collector by using superlattices; i.e., a (GaAs/$Al_xGa_{1-x}As$) superlattice emitter/ $Al_yGa_{1-y}As$ tunnel barrier/GaAs quantum-well structure.

However, the structure cannot be designed indiscriminately since the screening of the quantum well by the $n^+$ cladding layers can deplete the well. This implies that (a) the well may have to be doped to unrealistically high levels, or (b) the doping in the collector/emitter regions must be physically moved farther away. One quickly realizes that the structure need not be symmetric, since the current density through the structure is determined by the emitter source contact. Progress on this variation is outlined in Section III.

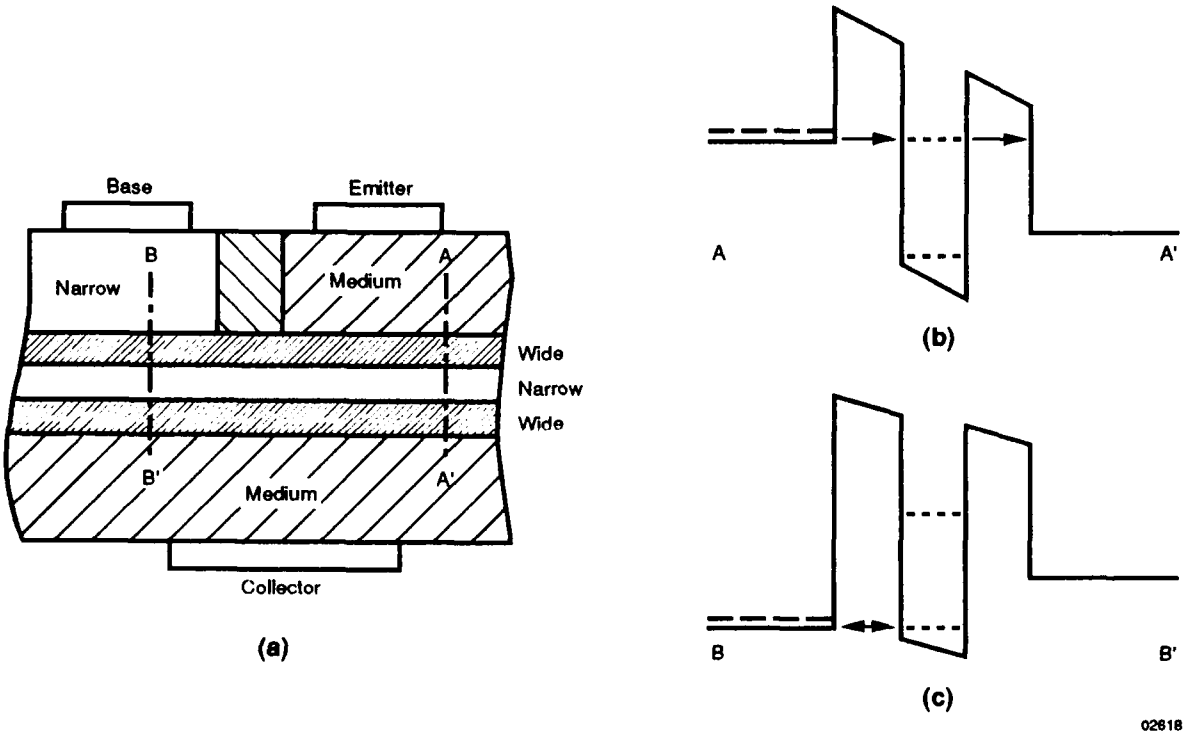


**Figure 4**
**(a) Quantum excited-state tunneling transistor. (b) Shows collector current derived from tunneling through excited (upper) quantum-well state. (c) Control carriers supplied to ground state by base contact and confined by medium-gap collector.**

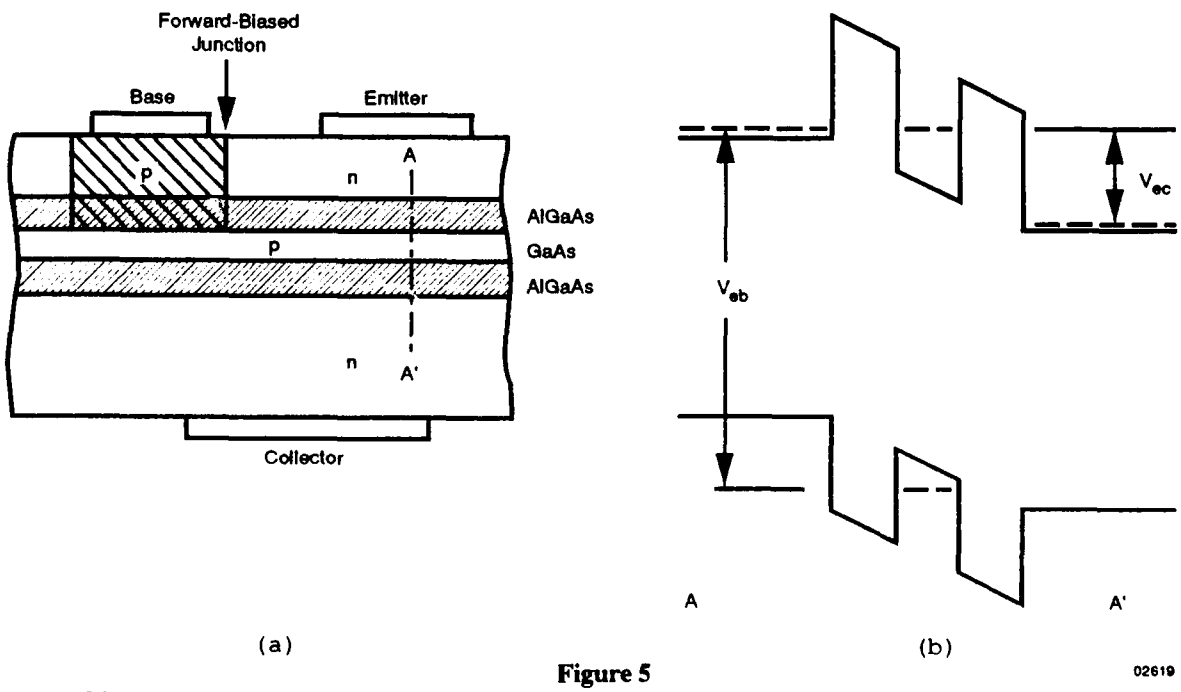


**Figure 5**
**(a) Bipolar tunneling transistor. Energy-band diagram through Section AA′ shown in (b) illustrates problem of forward bias required for this device to operate.**

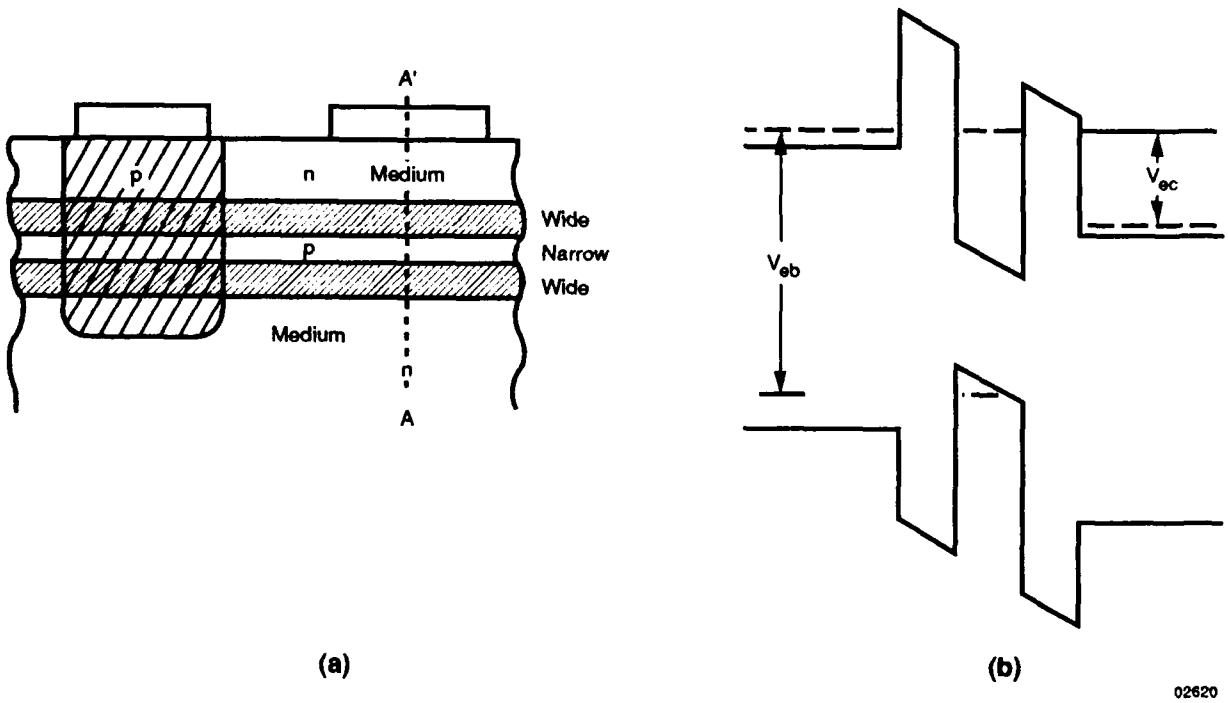


**Figure 6**
**(a) Bipolar resonant tunneling transistor. Energy-band diagram through Section AA′ shown in (b) illustrates reduced forward-bias voltage caused by narrow-bandgap quantum well.**

# SECTION II

# DEVICE SIMULATION AND MODELING

The theoretical tasks within the present program were directed toward two different objectives. The first was to support the experimental development of the BiQuaRTT and QuESTT by providing usable models that relate the structural design of the device to its electrical properties. The second was to advance the fundamental understanding of the physics of tunneling in semiconductor heterostructures to provide the scientific basis for further progress on nanoelectronic devices. The primary approach to both these objectives was to use numerical techniques to simulate, at a number of different levels of sophistication, the behavior of the device structures.

## A. TRANSISTOR DESIGN TOOLS

The key to understanding and designing any heterostructure device is the energy-band profile of that device (that is, the energy of the band edges as a function of position). When considering how such a device might operate, or how it might fail to operate, it is necessary to consider the band profile. Designing a device requires specification of the epitaxial layer thicknesses and doping levels. This should produce the desired band profile under the applied voltage bias. To ensure that this is the case, one must have a way to compute the band profile given the layer sequence and the applied voltages. The programs that fall under the heading of "transistor design tools" perform this function.

In the course of this program and related ones conducted in the contractor's Advanced Concepts branch, it was found that an additional element is required if device modeling is to have a significant impact on the progress of experimental device development: the device modeling programs must be usable by, and delivered to, those who are responsible for developing specific devices. The more common situation wherein a specialist in device modeling both develops and runs modeling programs, delivering only the modeling results, is much less satisfactory. The device engineer is the person who most thoroughly understands the details of the design, the constraints imposed by the fabrication process, and the existing experimental data; consequently, the device engineer is the person who knows which questions need to be addressed by modeling. If the model is directly available to the device engineer in the form of a usable computer program, those questions will be most effectively answered. For example, we have observed that device engineers typically run a much larger number of cases than do device modelers.

The idea of delivering usable modeling tools requires a redirection of the usual approach of the device modeling specialist. The emphasis must now be on physically simpler, more quickly executing models (primarily one-dimensional), rather than on more comprehensive models requiring large computer resources. In addition, much more attention must be directed toward the input and output functions of the program code, to provide a means of interpreting an input description of the device structure and displaying the results in a meaningful way. The evolution of our expertise in these areas is observable in the report of activities pursued under the present program.

## 1. First-Generation Modeling Programs

A computer code that models the BiQuaRTT structure was developed before the start of the present program. During the program, it was modified to model the QuESTT. Both these codes were released to staff members who are concerned with device design and fabrication.

These program codes solve the self-consistent Fermi screening problem. That is, they assume that, in the contact layers of the device (meaning everything outside the quantum well), the electron density is given by the Fermi distribution function. (This is also known as the zero current approximation.) The quantized states in the quantum well are found by solving Schroedinger's equation, and the occupation of these states is derived from the assumption that those carriers are in equilibrium with the base electrode. The resulting charge distribution is evaluated self-consistently with Poisson's equation for the electrostatic potential by a conventional Newton iterative algorithm. The program, which models the BiQuaRTT is named BIQMODEL, and the output from a typical run of this code are shown in Figure 7. The energies of the resonant states are found by evaluating the quantum-mechanical transmission coefficient from a finite-difference approximation to the Schroedinger equation and searching for peaks in the transmission.

A new computer code, QUESTTMOD, was developed during the course of the program to implement a Fermi-screening model of the QuESTT. It is similar in function and use to BIQMODEL. An example of the output of QUESTTMOD is shown in Figure 8.

The numerical techniques used in all contractor modeling codes are fundamentally finite-difference techniques. That is to say, the carrier density, electrostatic potential, and quantum-mechanical wavefunctions are approximated by a finite set of values associated with a discrete mesh of points in space. The differential equations that describe these quantities (Poisson's and Schroedinger's equations) then become sets of simultaneous algebraic equations that may be solved by standard techniques. In the first-generation modeling programs, the electrostatic potential and carrier densities were regarded as independent variables, the potential satisfying Poisson's equation and the electron density satisfying the Joyce-Dixon approximation for the Fermi level. This scheme, together with the coupling to the confined states in the quantum well, produced sets of equations that were represented by banded, but not tridiagonal, matrices. The resulting Newton iteration steps were implemented with a general-purpose sparse-matrix solver that we had developed earlier. The required scalar coefficients in the Newton algorithm were determined by a somewhat empirical method: An iteration was never permitted to drive the density negative and, if a sustained oscillation was detected, the coefficient was reduced to damp out the oscillation. The resulting codes required a few minutes to 2 hours of CPU time on a VAX 785 computer.

In the early development of nanoelectronic device modeling, the contractor generally created new modeling capabilities by a "copy and modify" approach, building on the existing capabilities. This led to a number of programs with large segments of nearly identical code. During the development of QUESTTMOD, the contractor realized that a severe source-code management problem had been created, and that better software engineering practices should be applied to the family of programs that includes QUESTTMOD, BIQMODEL, and some other programs for modeling resonant-tunneling diode structures. These practices consisted primarily of consolidating code that performs identical functions in different programs into a

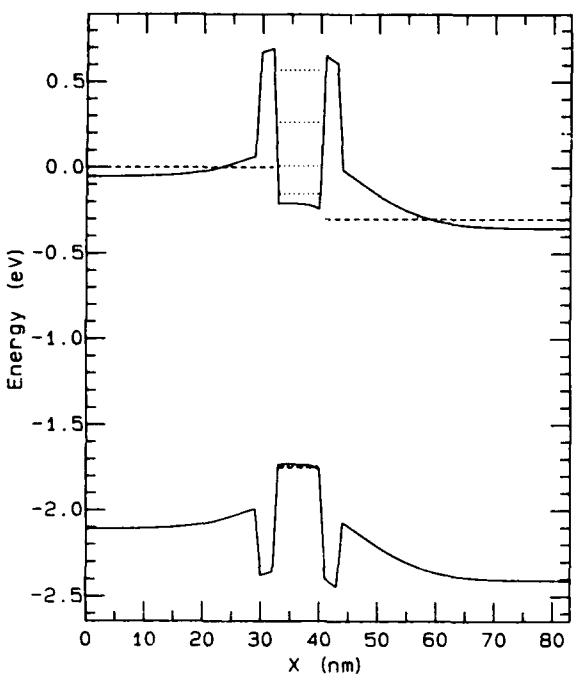


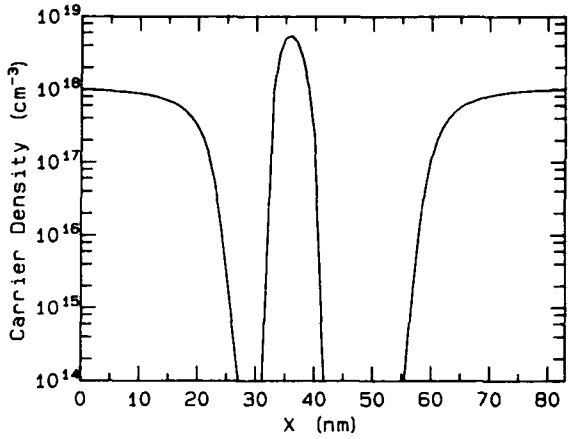


T = 77 K 10 DEC 1987 10:25

| Thickness | Composition | Doping |
|---|---|---|
| 25 nm | $Al_{0.35}Ga_{0.65}As$ | N $1.0\times10^{18}cm^{-3}$ |
| 5 nm | $Al_{0.35}Ga_{0.65}As$ | Intrinsic |
| 3 nm | AlAs | Intrinsic |
| 8 nm | GaAs | P $6.0\times10^{18}cm^{-3}$ |
| 3 nm | AlAs | Intrinsic |
| 5 nm | $Al_{0.35}Ga_{0.65}As$ | Intrinsic |
| 35 nm | $Al_{0.35}Ga_{0.65}As$ | N $1.0\times10^{18}cm^{-3}$ |

**Figure 7**
**Results of typical run of BiQuaRTT modeling program BIQMODEL.**

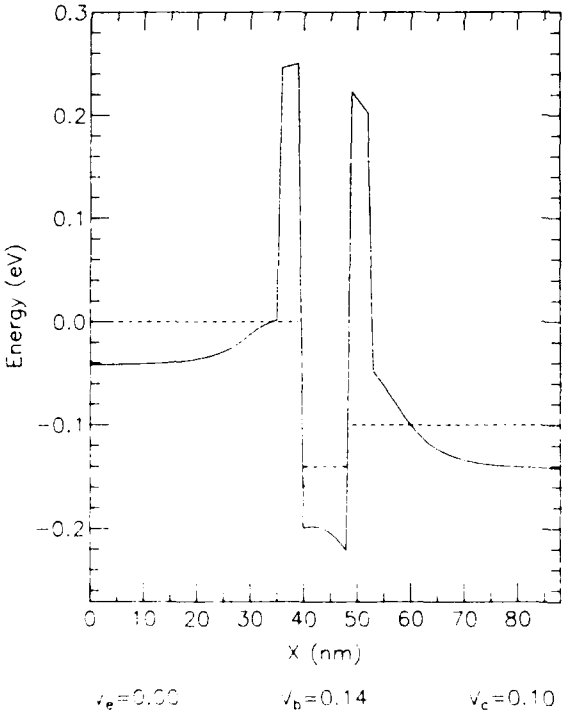


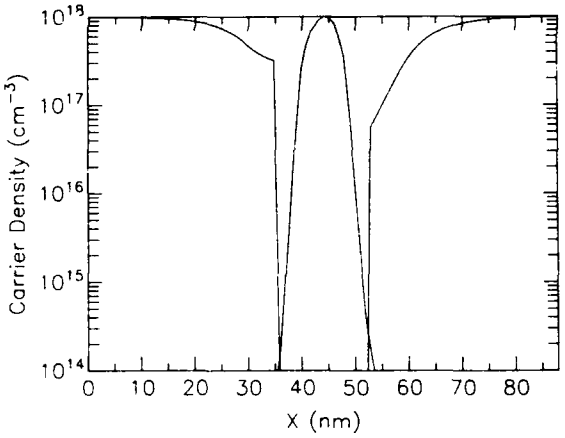


T = 300 K 9 JUN 1988 09:42
Number of bound states = 1

| Thickness | Composition | Doping |
|---|---|---|
| 30 nm | GaAs | N $1.0\times10^{18}cm^{-3}$ |
| 6 nm | GaAs | N $1.0\times10^{14}cm^{-3}$ |
| 4 nm | $Al_{0.30}Ga_{0.70}As$ | N $1.0\times10^{14}cm^{-3}$ |
| 9 nm | $In_{0.30}Ga_{0.70}As$ | N $1.0\times10^{14}cm^{-3}$ |
| 4 nm | $Al_{0.30}Ga_{0.70}As$ | N $1.0\times10^{14}cm^{-3}$ |
| 6 nm | GaAs | N $1.0\times10^{14}cm^{-3}$ |
| 30 nm | GaAs | N $1.0\times10^{18}cm^{-3}$ |

**Figure 8**
**Output of QUESTTMOD. Left plot shows conduction-band energy as function of position through structure. Fermi levels of three terminals are shown as dashed lines, and quantum-well state energies are shown as dotted lines. Right plot shows carrier densities as functions of position. Table below right plot documents structure and parameters of this run.**

common file, which was included into each of the separate programs by a compiler directive. This made corrected or upgraded code immediately available to all the programs using that common code file. The implementation of this practice required some effort to resolve differences in the approaches or semantics of the different programs. The process of code consolidation was completed by the end of the first year of the program.

As a part of this code consolidation process, the contractor systematically incorporated improved algorithms into these programs. Some subtle modifications were made to the way that the effective-mass discontinuity is modeled in the finite-difference solution of Schroedinger's equation. This improved the agreement between resonant energies calculated with this method and those evaluated analytically, so that the difference is now less than 1 millielectron volt (meV) for a typical structure. The contractor also implemented a better algorithm for integrating over the transmission coefficients to obtain the total current. A rather "brute force" numerical integration algorithm with a fixed step size had been used previously. The new code recursively refines the step size and chooses an appropriate approximating form for the transmission coefficient curve (Lorentzian near a resonance, polynomial elsewhere). This code runs in a much shorter time than the previous routine. We have also configured the code so that different distribution functions for the electron sources, representing structures of different dimensionality, may be employed in evaluating the current. This was done to investigate the effects of lateral confinement on the I(V) curve of a resonant-tunneling structure, and the results are shown in Figure 9.

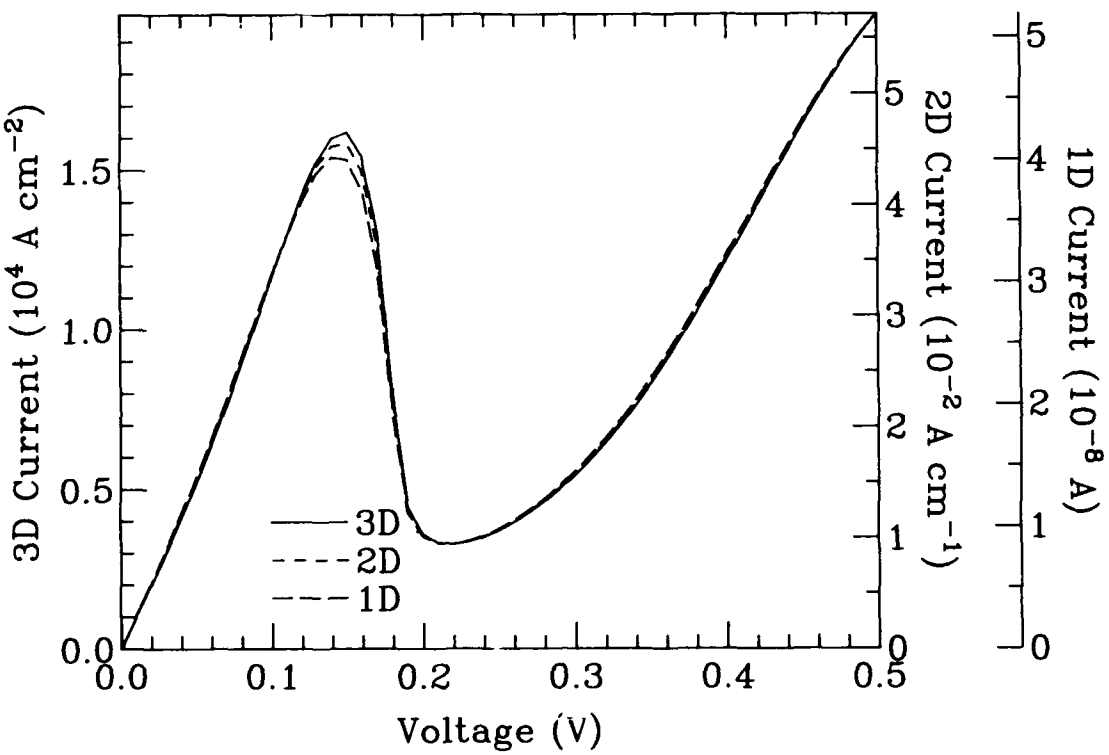


**Figure 9**

**Scattering-theory I(V) curves for laterally confined structures. Curves are shown for large-area resonant-tunneling diode (labeled "3D"), diode in which electrons are confined in one lateral dimension (labeled "2D"), and diode in which electrons are confined in both lateral dimensions (labeled "1D"). Lateral confinement apparently will not significantly affect peak-to-valley current ratio.**

## 2. Second-Generation Modeling Codes

A second generation of modeling codes was built on a different approach to solving the coupled nonlinear equations derived from the self-consistent Fermi screening model. This technique simplifies the Newton iteration scheme for solving the coupled nonlinear equations derived from this model, and employs the Bank-Rose damping scheme to stabilize and optimize each step of the Newton iteration. The Bank-Rose scheme works for problems that can be derived from a variational principle, and it chooses the scalar coefficient of each Newton step to minimize that function that appears in the variational formulation. The Bank-Rose scheme requires that the potential be regarded as the only independent variable, with the carrier density entering only implicitly into Poisson's equation. This has an additional benefit that the equations to be solved are now represented by a tridiagonal matrix, for which very efficient solution algorithms exist. Because of the combined effects of tridiagonal solution and optimized coefficient selection, the second-generation codes execute about one order of magnitude faster than the first-generation codes.

The primary embodiment of the second-generation approach is a program named HETEROSTAT. It includes the semi-classical models for both electrons and holes, so it is useful for modeling classical heterostructure bipolar devices. Other versions of the program also include deep impurity levels. One of the innovations in this program is the provision for user-specified boundary conditions. In previous program codes, the boundary conditions were "hard coded" to represent various types of physical interfaces such as ohmic or Schottky-barrier contacts. HETEROSTAT permits the user to specify which type of boundary condition will be applied and adds a third possibility: the bulk boundary condition. This models a semi-infinite piece of semiconductor material with fixed composition and doping level. Mathematically, the bulk boundary is implemented by matching the potential to an analytic solution of the Fermi screening equation. At present, HETEROSTAT does not evaluate size-quantized states. However, it can still produce qualitatively useful results for quantum devices, as in the BiQuaRTT simulation shown in Figure 10.

Another very useful second-generation program is TRANSBAND, which solves the Fermi-screening problem for a two-terminal structure and then plots the band profile and the resulting transmission probabilities versus energy. Also plotted, for energies below the minimum for propagation, is the derivative of the argument of the reflection coefficient. It is in this quantity that the resonant states appear if the energy is such that the electrons are totally reflected. An example of the output of TRANSBAND is shown in Figure 11.

Table 1 provides a summary of the previously described programs. They are routinely used by the device engineers working on heterostructure devices. They are implemented on a DEC VAX computer, producing graphical output on a Hewlett-Packard (HP) plotter. All the code is written in VAX Pascal. Because the VAX is shared by the contractor's entire Central Research Laboratories, the turnaround time for running a device model has ranged from a few minutes to a few hours.

## 3. Interactive Modeling Codes

To increase the effectiveness of the modeling programs by improving access to them, we are moving toward the use of a single-user scientific workstation environment. A Sun Microsystems 3/260 workstation was installed in late December 1988 for use in modeling nanoelectronic devices. This provides not only a hardware platform to support interactive

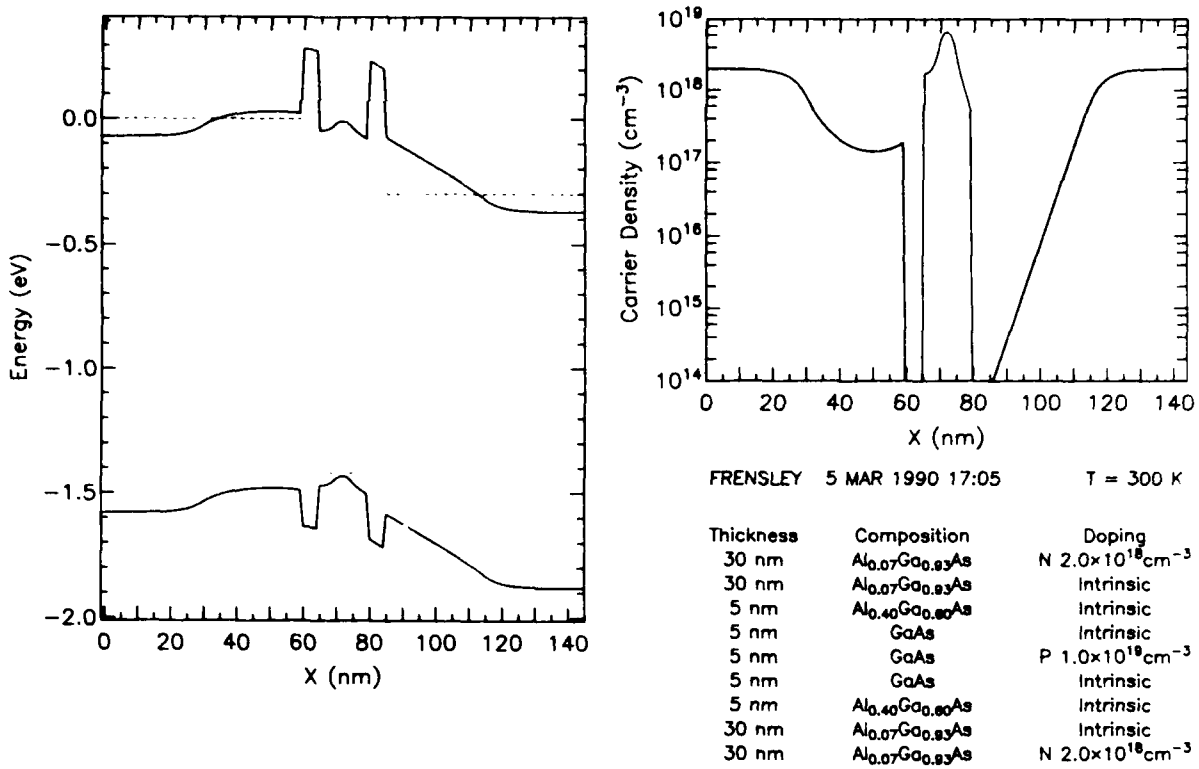


**Figure 10**
**Output of HETEROSTAT, modeling BiQuaRTT structure.**

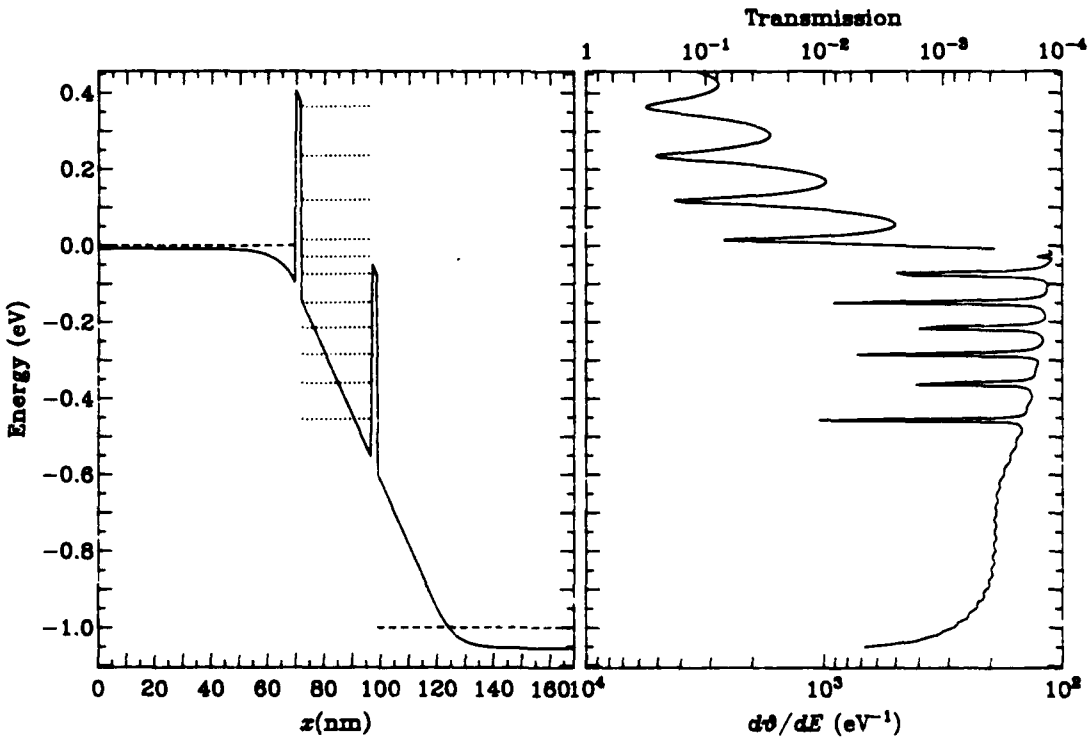


**Figure 11**
**Output of TRANSBAND, showing transmission and reflecting resonances.**

**Table 1. Device Modeling Codes on VAX Computer**

| Piecewise-Linear Potential | Self-Consistent Fermi Screening | |
|---|---|---|
| | Old Numerical Technology | New Numerical Technology |
| RTD-IV<br>Evaluates I (V) curve | HEMT MODEL<br>BC:Schottky | RTD SCREEN<br>BC:bulk<br>Double barrier structure<br>Resonant-level finder |
| PSICAD<br>Interactive program<br>Runs on Tektronix terminal<br>Evaluates: STS2 (V), STS2 (E), Y (x) | BIQMODEL<br>BC:bulk<br>Double-barrier structure<br>Quantized holes in base<br>Resonant-level finder | TRANSBAND<br>RTDSCREEN with STS2 (E) plot<br>HETEROSTAT<br>Bipolar capability<br>User specified BC |
| | QUESTTMOD<br>BC:bulk<br>Double-barrier structure<br>Quantized electrons in base<br>Resonant-level finder | SIGAAS<br>BC:Schottky, bulk<br>Deep levels<br>Implanted profiles |

BC = Boundary Conditions

graphic programs but also allows us to exploit the features of the Unix operating system for software development.

The process of transporting all our modeling programs to the Sun workstation involved a significant effort, translating the code from Pascal to C and redesigning the code to take full advantage of the Unix environment. The following code modules have been translated and tested:

- Two-dimensional graphics
- Data plotting
- Complex arithmetic
- Matrix and vector operations
- Eigensystem solution
- Semiconductor statistics
- III-V materials properties
- Heterostructure setup (takes heterostructure described as a list of layers and generates finite-difference data structures)
- Nonlinear equation solution
- Fermi screening
- Band profile and density plotting.

These modules, together with the main program code of HBAND (described next), total about 11,000 lines of C code.

We have completed initial development of an interactive heterostructure device modeling program running on the Sun workstation. This program, HBAND, is derived from HETEROSTAT and, thus, it evaluates a bipolar zero-current model and displays the energy-band profile of the device given the heterostructure design and the applied terminal voltages. The user interface to HBAND is illustrated in Figure 12. The interface is made up of four large subwindows and two smaller control-panel windows.

To the upper left is the band-profile window which displays the energy-band profile and the associated chemical potentials (Fermi levels). Positioning the cursor within this window, the user can use the mouse to "grasp" a Fermi level and move it up or down in energy, changing the applied bias voltage. When the mouse button is released, a recomputation of the self-consistent potential is triggered and the resulting band profile displayed. This is the primary mode of operation of HBAND.

The subwindow at the lower left of Figure 12 is the density-profile window. It displays a graph of the composition, doping, and carrier density as functions of position. By positioning the cursor within this window, the user can select a segment of the device over which the carrier density may be integrated (such as the 2DEG region in a MODFET to find the sheet carrier density, or the base of a bipolar transistor to find the Gummel number).

**Figure 12**
**Sun workstation CRT display for HBAND modeling program.**

To the upper right is the design-file window and its associated control panel. The file containing the text description of the heterostructure design is displayed in this window. This is a fully functional text edit window, so the design can be edited interactively. Each line of the design description specifies a layer of the heterostructure in terms of its thickness, composition, doping level, and the terminal to which it is presumed to be connected. The first and last lines specify the boundary conditions to be applied to the simulation in terms of the physical structure to be modeled: SCHOTTKY and OHMIC represent metallic contacts, and BULK implements a model in which the adjacent semiconductor material is assumed to continue on indefinitely.

To the lower right is the log window. Diagnostic information on the progress of the iterative solution and various other "archival" data are displayed in this window. Immediately above the log window is the display control panel. It provides functions that let the user change the format of the band-profile display.

HBAND has been installed on the nanoelectronics Sun workstation, and also on another workstation used by the GaAs Microwave branch. The HBAND user's manual is included as Appendix A.

## B. PHYSICAL DEVICE MODELS

An adequate exploration of the physics of tunneling in semiconductors requires a broad array of theoretical techniques. We have employed three general techniques to investigate issues of particular importance to the overall understanding of quantum transistor physics. These include two approaches based on the Schroedinger equation: wave packet calculations and scattering-state calculations. A quantum transport theory based on the evaluation of an open-system Wigner distribution function has been employed to investigate time-irreversible phenomena.

### 1. Schroedinger Equation Models

#### *a. Wavepacket Calculations*

We performed calculations in which the time-dependent Schroedinger equation was integrated to observe the evolution of a wavefunction in a resonant-tunneling structure and to test the more abstract estimates of the characteristic tunneling time. Most of these estimates invoke the width (in energy) of the resonance peak in the transmission coefficient. To obtain the detailed time-dependent wavefunction, we developed a computer code that calculates directly from the time-dependent Schrodinger equation the time evolution of an initially specified electron wavefunction. A key aspect of this algorithm is that it preserves the fundamental unitary requirement (preservation of normalization) on the time-dependent wavefunction to extremely high precision. This is implemented through a Cayley or Crank-Nicholson finite difference scheme. We used this program to address several questions pertaining to the lifetime of an electron in a double-barrier resonant tunneling structure. In particular, we compared the results of our direct microscopic calculation to the more ad hoc estimates of resonant state lifetimes obtained from standard transmission coefficient calculations.

Figure 13 shows the time-dependent probability (absolute magnitude squared of the wavefunction) of finding an electron in a double-barrier quantum well, as obtained from our

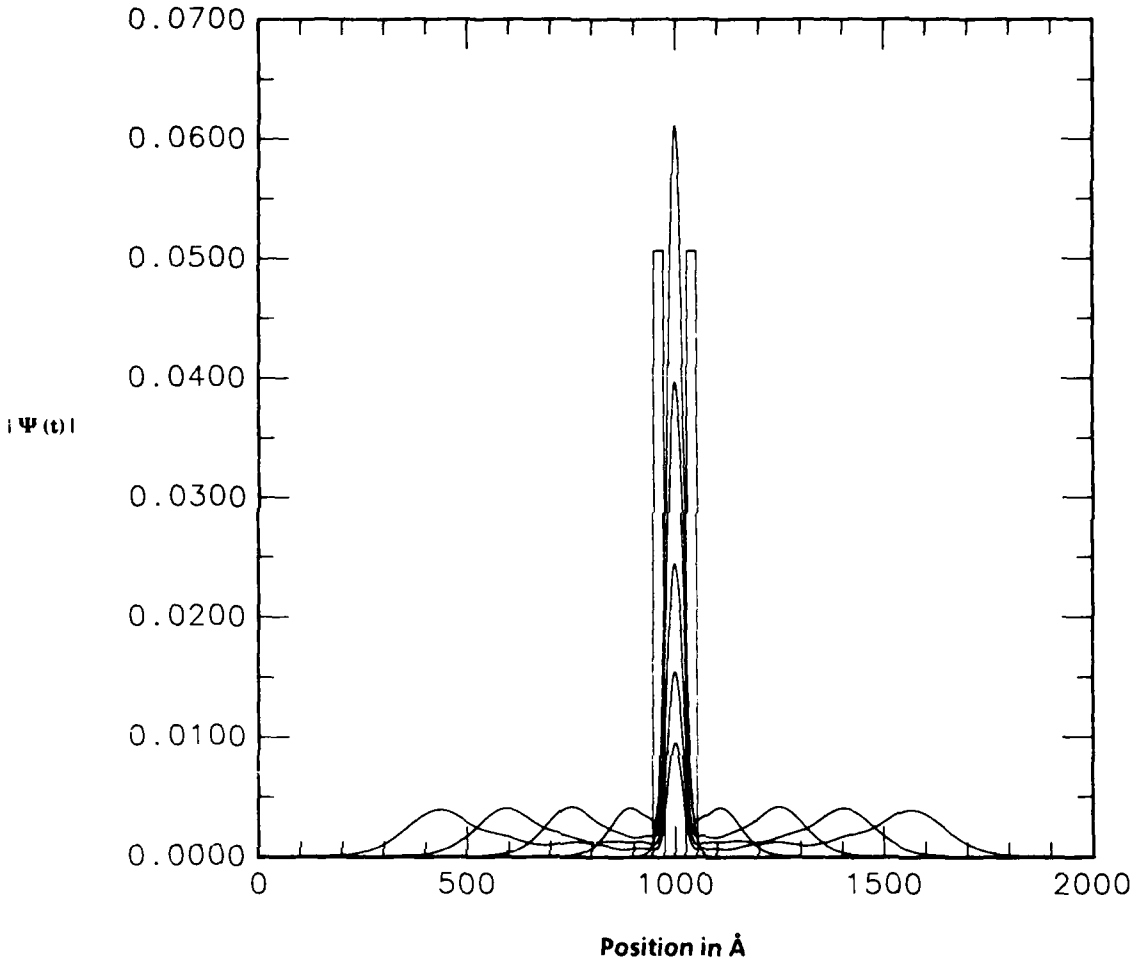


**Figure 13**
**Time evolution of electron wave packet escaping from quantum well by tunneling.**

program. The location of the double-barrier structure is also shown for reference and is plotted in arbitrary units. The system here is of 200 nm total length, and consists of two 225-meV barriers of 2.4-nm width with the quantum well being 5 nm wide. An effective electron mass appropriate to GaAs was used throughout. The initial state is for an electron localized to the quantum well, and has an energy of 71 meV. The subsequent drop in probability in the center of the well is clearly seen as the electron leaks out of the well via tunneling. Once outside the well, there is a clear front to the wavefunction, which indicates a freely propagating particle. Note that there is also diffusive broadening in the width of the wavefunction as time proceeds. A snapshot of the wavefunction has been given at every 36 fs.

Figure 14(a) illustrates the decay in time of the probability of finding an electron in the quantum well of an idealized (flat-band) symmetric double-barrier structure, given that the electron was placed there initially with an energy close to the tunneling resonance. The results of Figure 14(a) have been obtained from a direct numerical integration of Schrodinger's equation, starting from a suitably chosen wavefunction localized in the quan-

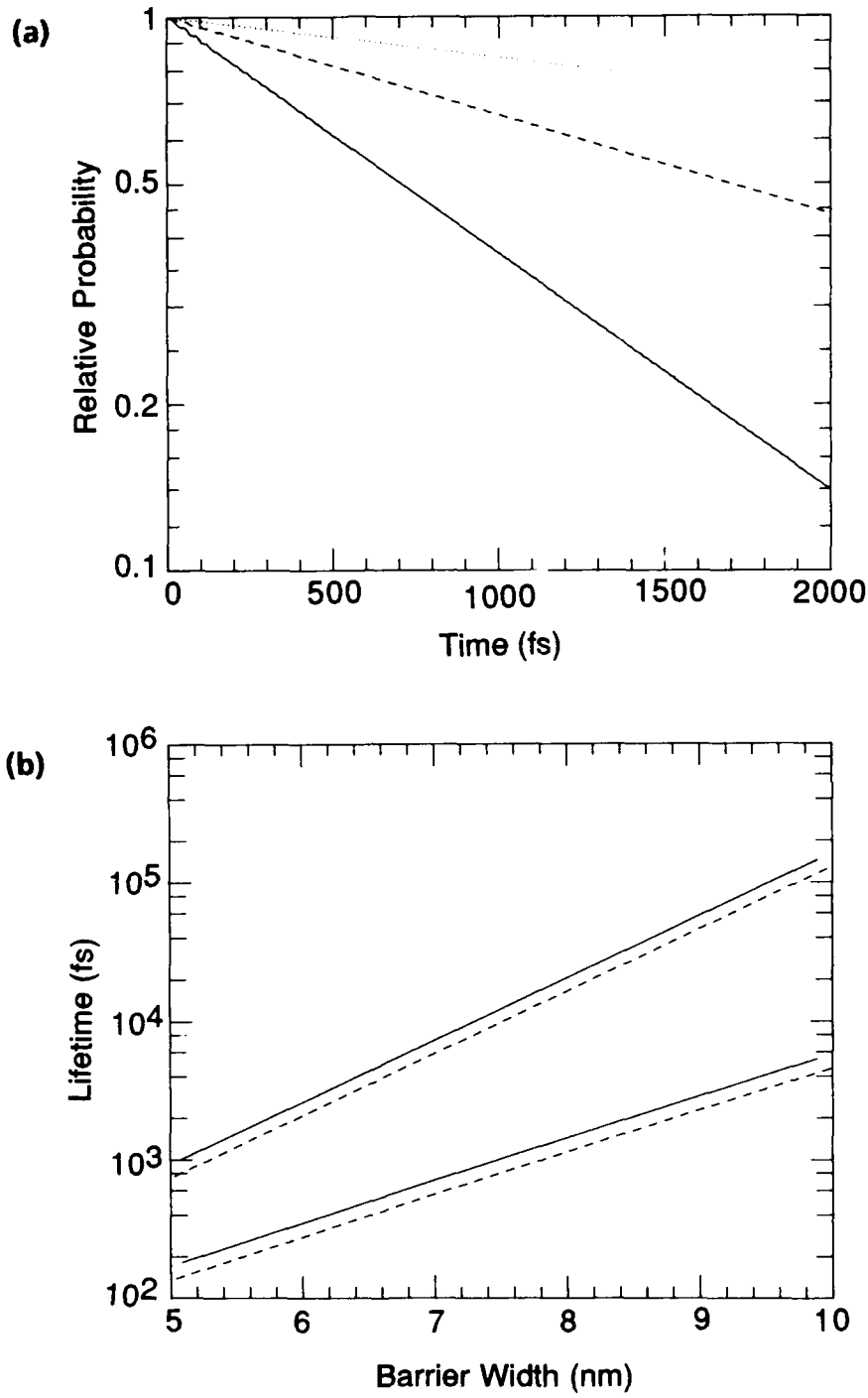


**Figure 14**

**Results of simulation of escape of wave packet from quantum well. (a) Time-dependent decay of an electron's probability of being found in quantum well of double-barrier structure, given that it was there at time zero. Results for several barrier thicknesses are shown, with well width and electron energy held fixed. (b) Lifetime for escape versus barrier thickness. Upper curves are for electron placed in ground state; lower curves are for electron placed in first excited state. Solid lines are from time-dependent Schrodinger equation. Dashed lines show scattering theory time delay.**

tum well. Data are shown for three barrier widths of 5.1, 5.9, and 6.8 nm, corresponding to the solid, dashed, and dotted lines, respectively, with the well width held fixed at 5.4 nm in all three cases. Parameters representative of GaAs-AlGaAs systems have been employed. Note that the electron escapes fastest for the thinnest barrier, as would be expected. The dependence of the tunneling rate on barrier width is discussed next. The initial wavefunction has been selected as an eigenstate of an isolated quantum well with the same width and depth as the well in the double-barrier structure. The bound-state eigenvalues of the single well form a good approximation to the resonant tunneling levels of the corresponding double-barrier system, for energies not too near the top of the well. From Figure 14(a), the electron probability decays with an overall exponential time dependence, with some small oscillations superimposed. These oscillations are believed to be the result of the small admixture of some higher-lying state into the initial condition.

The inverse of the decay rate defined by the slope of the line in Figure 14(a) forms a simple characterization of an electron's lifetime in a double-barrier quantum well. Figure 14(b) shows (solid lines) the lifetime results obtained from a least-squares analysis of time-dependent probability data, such as in Figure 14(a), for 18 barrier widths between 5 and 10 nm with the well width held fixed. (A discussion of the dashed lines follows.) The two solid lines correspond to quantum-well widths of 8.2 nm (lower) and 5.4 nm (upper), respectively. The lower solid line was obtained from the tunneling escape of an electron placed in an excited level of the quantum-well as the initial state, while the upper was derived from a ground state. The excited state has a higher tunneling probability, and, thus, it yields a generally smaller lifetime (for fixed barrier width), in agreement with the results in Figure 14(b). It is readily seen that the lifetime increases exponentially with barrier width. The difference in slope between the two solid lines in Figure 14(b) is attributable to the difference in the resonant tunneling energy levels between the lowest and first excited tunneling levels for the two wells considered.

The dashed lines in Figure 14(b) are from a widely used estimate of the lifetime of a resonant tunneling state, which we can compare with the results of our calculation for the escape lifetime. If one assumes the transmission coefficient to have a Lorentzian shape near a tunneling resonance, then the time delay of steady-state scattering of incident plane waves is given by the width of the transmission coefficient at resonance divided by the reduced Planck constant. We have taken this width to be the full width at half-maximum (FWHM). This is also the lifetime estimate one would obtain by invoking the uncertainty principle. It is commonly asserted in the literature that the scattering time delay is equal to the quantum mechanical tunneling time through double-barrier structures. We find from our calculation that the lifetime for escape of an electron suddenly created in a quantum well is approximately 25 percent longer than the scattering time delay. The latter, of course, refers to the delay across the scattering region of plane waves, which are infinite in extent. The disparity between these two measures of the lifetime in a double-barrier resonant tunneling system, although not significant for the purposes of order-of-magnitude estimates, points out the importance of initial conditions in defining a relevant time. One must specify the process one is interested in to obtain meaningful times. Simply put, there is not a single time scale to characterize the response of a double-barrier structure. To further explore the role of initial conditions, and recognizing that electrons come in wave packets of finite extent, we have used our time-dependent Schroedinger equation code to study the transmission times of wave packets at the resonant energy incident on a double-barrier structure.

Figure 15 shows the time development of the probability of finding an electron in the quantum well, given that a Gaussian wave packet with a mean wave vector corresponding to the resonant energy tunnels through the system. The system chosen has a well width of 8.2 nm, barrier widths of 5.1 nm, and a barrier height of 225 meV, as do all the systems reported here. The parameters considered for Figure 15 correspond to the system with the smallest lifetime shown in Figure 14(b). The mean energy is such that the wave packet tunnels through an excited state of the double barrier system at 158 meV. The effective mass of GaAs was used uniformly throughout the system. There are three curves shown in Figure 15. The solid line is for a wave packet with a momentum spread in the Fourier components comprising itself, which corresponds to the energy width (FWHM) of the transmission coefficient at the tunneling resonance.

The dashed line is for a momentum uncertainty corresponding to twice the FWHM in the transmission coefficient, while the dotted line is for a momentum spread half the FWHM. Thus, from the dashed to the solid to the dotted lines in Figure 15, progressively more wave vector components in the wave packet are near the tunneling resonance. In real space, the wave packet becomes progressively broader as the momentum uncertainty becomes smaller. Figure 15 shows that, as we get more nearly "on" the resonance, it takes longer to build up the resonant state amplitude in the well. Note that the time involved for the buildup process is of the order of thousands of femtoseconds. This measure of the lifetime of the electron in the

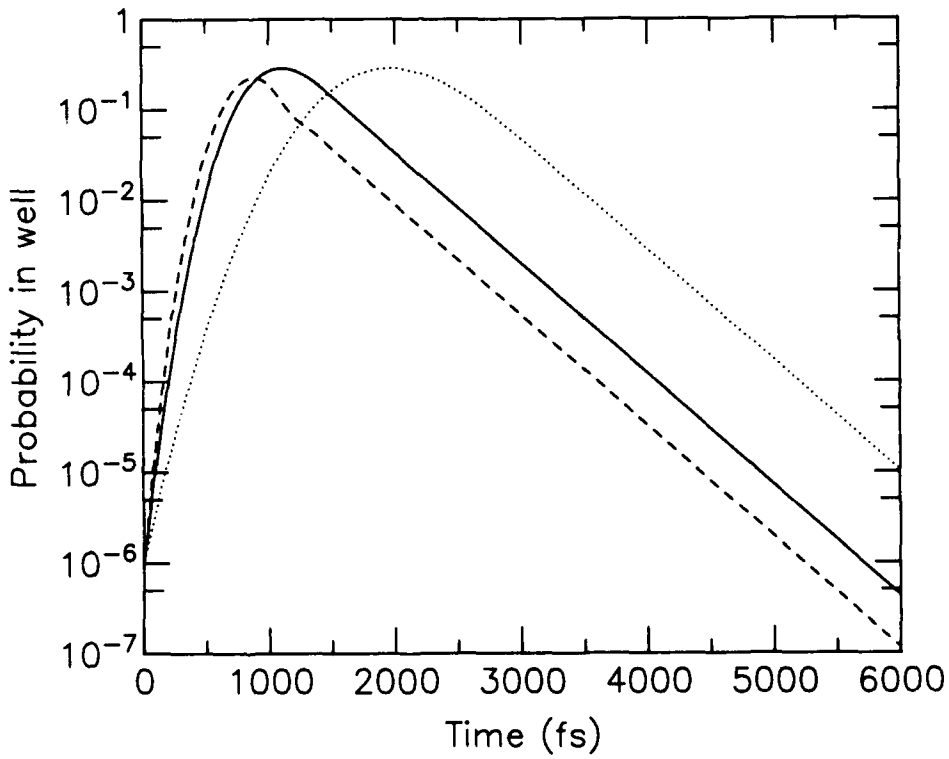


**Figure 15**

**Results of simulation of transmission of wave packet through quantum well. Curves plot total probability for electron to be in quantum well as functions of time. Different curves correspond to incident wave packets with different widths. Rate of initial buildup of probability increases as spatial width of packet decreases. Rate of decay of probability is independent of initial condition.**

well is clearly an order of magnitude larger than the times indicated in Figure 14(b) (for the same system parameters). It is interesting to note that, while the "rise time" characteristics of the buildup of probability in the well are determined by the initial condition, the decay of probability is universal as indicated by the curves in Figure 15 being parallel for later times. This decay time differs from those in Figure 14(b). Figure 14(b) indicates a decay time of approximately 150 fs for the system considered in Figure 15, while the universal decay time in Figure 15 is about 350 fs. It is not surprising that the decay time from Figure 15 does not agree with the time delay shown in Figure 14(b), since the latter is tied to the behavior of a plane wave of a single Fourier component exactly on the resonance. The momentum uncertainty is zero here, which corresponds to a electron wave infinite in spatial extent. Such a wave continuously populates the quantum well at the resonant amplitude and, thus, the decay time of Figure 15 is not obtained in this type of steady-state theory.

### *b. Scattering-State and Superlattice Calculations*

The calculation of stationary scattering states is the most popular approach to the theory of tunneling phenomena, and has largely shaped the conventional intuition concerning such phenomena. Stationary scattering states are solutions to the time-independent Schroedinger equation that are asymptotically free states and are, thus, unnormalizable. (Note that, in this context, "scattering" refers to the coherent scattering of the wave function from the device structure, not to random scattering from phonons or impurities.) Such calculations are usually implemented as evaluations of the transmission matrix. We have preferred to use a purely numerical finite-difference approach to the solution of Schroedinger's equation. This has the advantage that it can handle arbitrarily shaped potentials, and incorporate such realistic details as discontinuities in the effective mass and nonparabolicity of the energy-band structure. We have used the computer codes that implement these calculations for a variety of purposes, including evaluating the current density through QuESTT and BiQuaRTT structures and as a standard of comparision for the Wigner-function calculations.

We have also developed a capability for calculating the Fermi level in doped semiconductor superlattice (SL) systems, based on the thermal occupation of the allowed conduction states. Superlattices are of interest in that the artificial periodicity of the SL further quantizes the conduction bands of the host materials into a series of smaller "minibands." The minibands can then be selectively used for desired applications. We have employed SL injectors in some of our resonant tunneling transistor designs, and this investigation arose from the need to better understand the transport properties of superlattices. While there has been much interest, both theoretical and experimental, in elucidating the allowed electronic states of superlattices, little attention has been paid to the occupation of such states. It is common practice to adopt bulk Fermi-level values as applying to superlattices. We have found, however, that the SL Fermi level can differ significantly from bulk approximations, depending on the relative spacings and widths of the minibands. This is related to the fact that the density of states for an SL is a hybrid between a two- and a three-dimensional density of states, and the theoretical treatment must reflect this difference. Included as Appendix B is a preprint of an article describing these calculations, which has been submitted for publication. We mention here only the conclusions.

For a given density of carriers, the SL Fermi level is higher than that for bulk systems, and the difference is approximately given by the energy gap between the lowest mini-

band and the bulk conduction band minimum of the smallest bandgap material in the SL. In general, to populate an SL with the same carrier density as for a bulk system, the Fermi level must be correspondingly larger, to overcome the energy gaps ("minigaps") between the minibands. We also find a novel dependence of the Fermi level on the doping scheme, whereby selective doping of the quantum wells leads to results different from a uniform doping of the SL. These results will be incorporated into future versions of the Fermi-screening device models.

## 2. Quantum Kinetic Models

As a part of the present program, we continued to elaborate the quantum transport theory of tunneling devices, based on evaluation of the Wigner distribution function, which was originally developed by the contractor under contract N00014-84-C-0125, "Research on GaAs Quantum-Coupled Structures That Can Be Used as Electron Devices." Because this approach is based on quantum statistical mechanics, rather than pure-state quantum mechanics, it is able to handle irreversible phenomena such as phonon scattering in a much more complete fashion than the more widely practiced approaches. This allowed us to identify and investigate a critical issue: how do inelastic scattering processes affect the self-consistent electrostatic potential in a resonant-tunneling diode, and, in particular, how accurate is the screening picture employed in the device models described previously.

The simple screening picture assumes that there is a high rate of inelastic processes in the contacting layers. This is required to enforce the local equilibrium condition and, in particular, to create the electron accumulation layer on the upstream side of the tunneling structure. If such processes are not operative, the qualitative features of the band profile are not immediately apparent.

Investigation of this question required development of a program code that would implement self-consistency of the electrostatic potential. Whereas the nonself-consistent model is cast as a set of linear equations that are easily solved by direct calculation, the coupling to Poisson's equation introduces a nonlinearity into the model. This means that an iterative algorithm must be used to solve the equations. We implemented a multidimensional Newton iteration scheme, of the sort employed in the Fermi-screening models. In this scheme, the nonlinear equations are rewritten as a (large) vector of functions so that the equations are satisfied when the functions are all equal to zero. The zero of the vector of functions is found by repeated moves in a downward direction, as determined by the solution of a Jacobian equation. One of the tricky issues in such a calculation is determination of the optimum distance to move in a given step. The Bank-Rose damping scheme described previously gives a good answer to this question for equations that may be derived from a variational principle (such as equilibrium or quasi-equilibrium problems). However, transport equations are necessarily time-irreversible (not self-adjoint) and are not obtainable from a simple variational principle; thus, the Bank-Rose scheme does not apply to the steady-state problem for the self-consistent Wigner function. Therefore, we developed an empirical (numerical) damping scheme that works well for all the cases we have tested. It leads to convergence in about 30 iterations in most cases. The Jacobian of the nonlinear problem has about twice as many nonzero elements as the Liouville super-operator of the linear problem, which means that it takes four times as much CPU time to perform one iteration of the self-consistent calculation as it takes to solve a linear case. Thus, a 4-minute solution of the nonself-consistent case requires 8 hours when self-consistency is implemented.

The results of the self-consistent Wigner function calculations demonstrate the issue identified previously: the nature and strength of the inelastic scattering processes in a resonant-tunneling device have a profound effect on the shape of the self-consistent potential. These results are discussed in detail in Appendixes C and D.

Another activity, which was supported in part by the present program, was the development of a long tutorial article on this approach to quantum kinetic transport theory. The article, "Boundary Conditions for Open Quantum Systems Driven Far From Equilibrium," by W.R. Frensley, has been accepted for publication in *Reviews of Modern Physics*, and is tentatively scheduled for publication in the July 1990 issue. (Because of its length, it is not reproduced in this report.) In the course of writing this article, we performed a comparative analysis of the various published approaches to Wigner-function calculations. We found that these approaches differ significantly in the order to which they satisfy such fundamental relations as continuity, momentum balance, stability, and detailed balance (in equilibrium). No single approach is optimum with respect to all of these criteria.

# SECTION III

# QUANTUM TRANSISTOR DEVELOPMENT

Unipolar and bipolar resonant tunneling transistors (RTTs) in both GaAs- and InP-based heterojunction material systems were fabricated and characterized. Initial demonstrations of the devices were achieved in the GaAs/AlGaAs/InGaAs materials system. As the work progressed, the materials limitations of the GaAs-based system became apparent, and development of the In(GaAl)As compounds lattice-matched to InP began. A state-of-the-art capability for growth of resonant tunneling heterostructures was developed, and techniques for the heavy-doping of Be and Si in InGaAs were demonstrated. A microwave RTT process was also developed and microwave characterization of RTDs and RTTs was performed. In the final weeks of the contract, both unipolar and bipolar InP RTTs were demonstrated and characterized. We have achieved, for the first time, room-temperature dc and microwave gain from unipolar InP-based RTTs. These hot-electron transistors are the first to show room-temperature dc and microwave gain.

The work is presented in chronological order. Most of the effort on both GaAs unipolar and bipolar RTTs has already been published in the archival literature. This work is summarized, and the published papers are included as appendixes. Most of the InP transistor development has not yet been published, so this will be elaborated in some detail, including the motivations for transferring the effort to this material system. Finally, we summarize the essential aspects of the device processes that were developed.

## A. GaAs RTT DEVELOPMENT

To fabricate the quantum-well transistors, three-bandgap resonant tunneling double-barrier (RTD) structures were initially investigated. Resonant tunneling was observed in the pseudomorphic AlGaAs/InGaAs/GaAs system[15] (Appendix E), and the $Al_xGa_{1-x}As/Al_yGa_{1-y}As/GaAs$[16] (Appendix F). High current density is important for high-speed applications, and current density as high as $10^5$ A/cm$^2$ with a peak-to-valley current ratio of 2:1 at 77 K was achieved in an AlGaAs/GaAs RTD[17] (Appendix G). The heterojunction device models developed under this contract were used to interpret the I(V) characteristics of a set of precisely characterized RTDs[18] (Appendix H). This work established the predictive ability of the heterojunction models and provided a simple explanation for I(V) asymmetry in RTDs in terms of monolayer thickness fluctuations. This is described in greater detail in Section IV, Manufacturing Issues.

Initial demonstration of transistor action in the BiQuaRTT was achieved in an AlGaAs/ GaAs quantum-well structure using superlattice AlGaAs/GaAs emitter and collector.[19] Under this contract, a similar transistor with a pseudomorphic InGaAs base was fabricated and characterized[20,21] (Appendixes I and J). Evidence for resonant tunneling through the two-dimensional electron gas states in the base was observed at 77 K; however, these transistors did not exhibit dc gain at resonant bias.

Extensive characterization of BiQuaRTTs fabricated using our initial dc device layout has revealed several important factors necessary for achieving gain at resonance. For the base/emitter voltages necessary to bring the device into resonance, the holes in the base must remain bound by the quantum-well base/emitter heterojunction. The modeling program

BIQMODEL has been used to elucidate this problem in the original BiQuaRTT device designs. Shown in Figure 16 are computed conduction-band profiles for a pseudomorphic GaAs/AlAs/ InGaAs BiQuaRTT in thermodynamic equilibrium, and biased into resonance. It can be seen that, for the base/emitter biases required to place the device into resonance, ~$E_{gap}$/ q V, that there is no longer an internal potential barrier to prevent hole injection into the emitter. Consequently, without minority carrier confinement, gain will be degraded by hole injection into the emitter.

The obvious remedy is to use a narrower bandgap material in the well. Unfortunately, because of lattice mismatch, we are near the critical layer thickness for this indium concentration in the well, 23 percent. We have found experimentally that a BiQuaRTT structure containing a 25-nm $In_{0.23}Ga_{0.77}As$ quantum well is heavily dislocated, whereas a structure containing a 15-nm well shows good surface morphology. Another way to improve minority carrier confinement is to use an AlGaAs emitter. AlGaAs-emitter BiQuaRTTs were also fabricated, but in these structures, no evidence of resonant tunneling was observed. These results suggest a limitation, problematic to the GaAs/AlGaAs/InGaAs material system. When the bandgap of the emitter is raised, the energy at which the electrons in the base are injected becomes comparable to the intervalley transfer energy. If a significant fraction of injected electrons scatters into the X- or L-bands in the InGaAs base, the resonant tunneling transport path is obscured. This explanation is qualitatively consistent with our experimental findings.

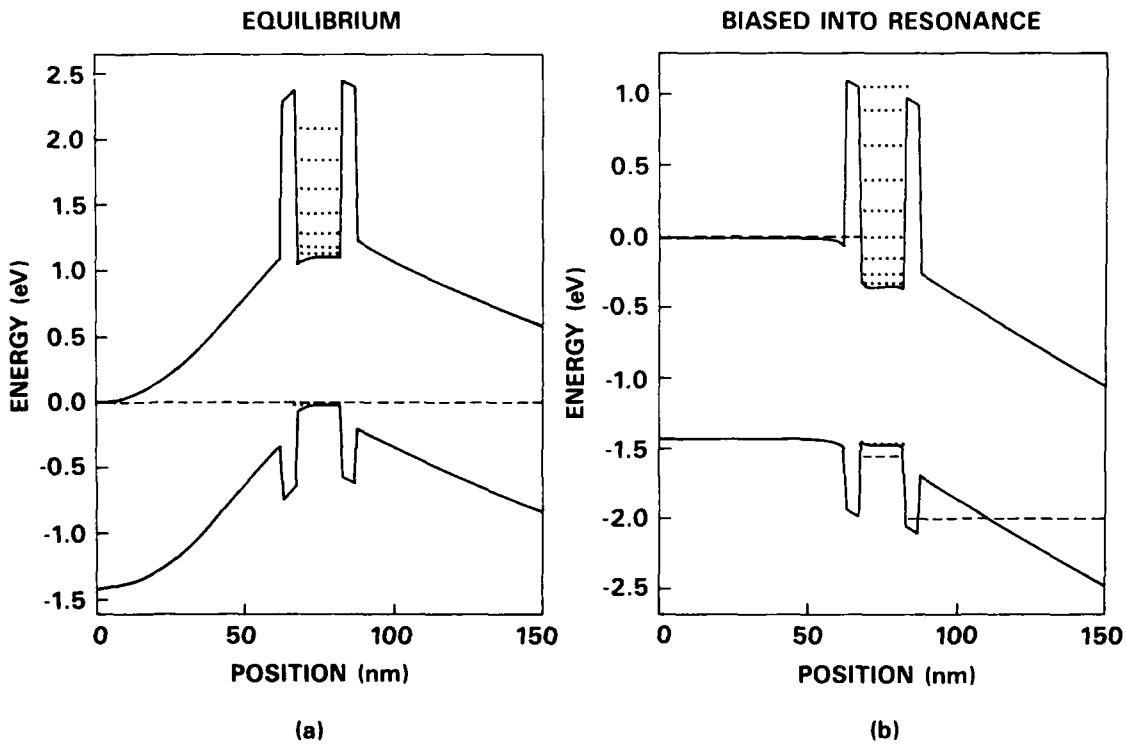


**Figure 16**
**Pseudomorphic BiQuaRTT energy-band profile computed by simulation tool BIQMODEL. Structure is shown in (a) equilibrium and (b) under bias to bring n = 4 quantum-well base state into resonance with emitter electron distribution, $V_{be}$=1.5 V, $V_{ce}$=2.5 V, 300 K. Dashed lines designate quasi-Fermi level position; dotted lines designate electron and hole states in quantum well.**

It is also recognized that recombination in the quantum-well base can severely degrade the device gain and resonant tunneling characteristics. Increased recombination can result from ionic scattering from the quantum-well base dopants or from strong quantum-mechanical reflection at the base/collector junction. The effect of ionic scattering centers in the quantum well has been experimentally investigated in RTDs[22] for both n- and p-type dopants. These results indicate that n- and p-type dopant densities of $10^{18}$ $cm^{-3}$ can be introduced into the quantum well with less than 25 percent reduction in peak-to-valley ratio in comparison with undoped quantum wells. Thus, no experimental evidence exists to suggest that ionic scattering is a fundamental limitation.

Scattering from the base/collector tunnel barrier can also cause increased recombination in the base and low gain. This scattering can be reduced by (1) eliminating the wide-bandgap collector altogether and/or (2) eliminating or reducing the thickness of the base/collector tunnel barrier. For the case of no base/collector tunnel barrier, resonant tunneling occurs though virtual states that occur in energy above the quantum-well base/ collector heterojunction barrier.

Unipolar RTTs were also investigated using the GaAs-based material system. Both an epitaxial regrowth technique using a $CCl_2F_2$:He selective reactive ion etch[23] and an implantation approach were applied to the problem of contacting the n-type quantum-well base. Subsection III.D includes a discussion of the regrowth experiments; the implantation experiments were published[24] (Appendix K). The implantation process was used to contact the quantum-well of a Stark effect transistor.[25] This unipolar GaAs RTT[26] (Appendix L) marked the first observation of oscillatory negative transconductance in the SET device and was an important test vehicle for understanding transport into and out of the n-type quantum well.

## B. QUANTUM-WELL RTT PERFORMANCE CONSIDERATIONS

The GaAs-based material system has several important materials limitations that significantly reduce the effectiveness of hot-electron heterojunction device designs in comparison to the In(GaAl)As compounds grown on InP. A comparison of several of the key material properties is shown in Table 2. The lower effective mass of the electron in $In_{0.53}Ga_{0.47}As$ means that quantum size effects occur at larger physical dimensions in $In_{0.53}Ga_{0.47}As$ compared to GaAs. This allows the fabrication of slightly wider bases and a relaxed base contact requirement. Broader transmission resonances are also expected, with lower carrier effective masses, which lead to higher peak current densities.

Intervalley scattering is reduced in InGaAs in comparison to GaAs because of the increased $\Gamma$ to L- and X-band separations. The InAlAs/InGaAs heterojunction combination presents a larger heterojunction band discontinuity than AlGaAs/GaAs, giving rise to decreased off-resonance valley current and more flexibility in heterojunction design.

The best reported room-temperature peak-to-valley ratio in GaAs/AlAs RTDs is just less than 4:1,[27] while in the lattice-matched InAlAs/InGaAs double barrier, nearly 12:1 has been obtained.[28] Peak-to-valley current ratios as high as 30:1 at room temperature have been obtained with pseudomorphic AlAs barriers and an InAs quantum well notch.[29] This translates into larger room-temperature negative transconductance in the InP-based RTTs.

Surface-state density is typically an order of magnitude less on InGaAs than on GaAs. In addition, ohmic contacts to InGaAs are obtained without thermal annealing, offering the possibility of nonalloyed quantum-well contact in the QuESTT and BiQuaRTT.

**Table 2. Comparison of Selected Materials Properties for the Lattice-Matched Compound Semiconductors Grown on GaAs and InP Substrates**

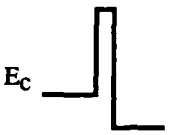


| | GaAs/AlAs/InGaAs on GaAs | InAlAs/AlAs/InGaAs on InP |
|---|---|---|
| Effective mass | 0.067 GaAs | 0.041 ($In_{0.53}Ga_{0.47}As$) |
| Γ- L-band separation | 0.3 | 0.55 |
| Conduction-band offset range | 0.3 (unstrained) | 0.49 (unstrained) |
| RTD 300K PVR | 4:1 | 14:1 |
| Surface-state density | $10^{12}$ to $10^{13}$ | $10^{10}$ to $10^{11}$ |
| | Strained | Lattice-matched |
| | Alloyed ohmic | Nonalloyed ohmic |

There are a few disadvantages. A comparable implantation isolation technology does not exist for the InGaAs materials because of the large intrinsic carrier density. This can be circumvented by mesa etching. Second, selective etching techniques for the InAlAs/InGaAs heterojunctions are not well established. Controlled chemical etch processes must be used in the interim.

We have attempted to estimate the extrinsic performance of the BiQuaRTT to project how it will compare with conventional heterojunction transistors for high-speed applications. This is a difficult task, as the framework of a quantum transport theory is only now being established.[30] To allow an estimate, we note that the BiQuaRTT with its tunnel barriers excluded is a heterojunction bipolar transistor with a quantum-well base (Figure 17). Since the transport through these tunnel barriers is a subpicosecond process, an estimate based on HBT models should be a reasonable starting point.

We have used the physical device model of Sunderland and Dapkus[31] to project the figures-of-merit $f_T$ and $f_{MAX}$. This model includes published materials parameters such as effective masses, conduction band offsets, mobilities as a function of dopant densities, and dielectric constants. Other input parameters are layer thicknesses, doping level, collector current density, contact resistances, and contact geometry; thus the model accounts for the effects of layout and external parasitics.

Figures 18 and 19 show results of the calculations of $f_T$ and $f_{MAX}$ for the AlGaAs/GaAs BiQuaRTT, and the In(GaAl)As/InGaAs BiQuaRTT, respectively. The input parameters for these calculations are listed in Tables 3 and 4. In the absence of experimental data on the dependence of doping on mobility in In(GaAl)As, we use values obtained for InP, which are slightly lower than AlGaAs.

The small-signal current-gain cutoff frequency, Equation (1), is inversely related to the emitter-to-collector transit time, Equation (2), which is the sum of transit delays in the base $\tau_b$ and collector, $\tau_c$ and the charging times in the emitter and collector $r_e (C_e + C_c)$. Referring to the AlGaAs/GaAs case of Figure 18, note that $f_T$ increases monotonically as the base

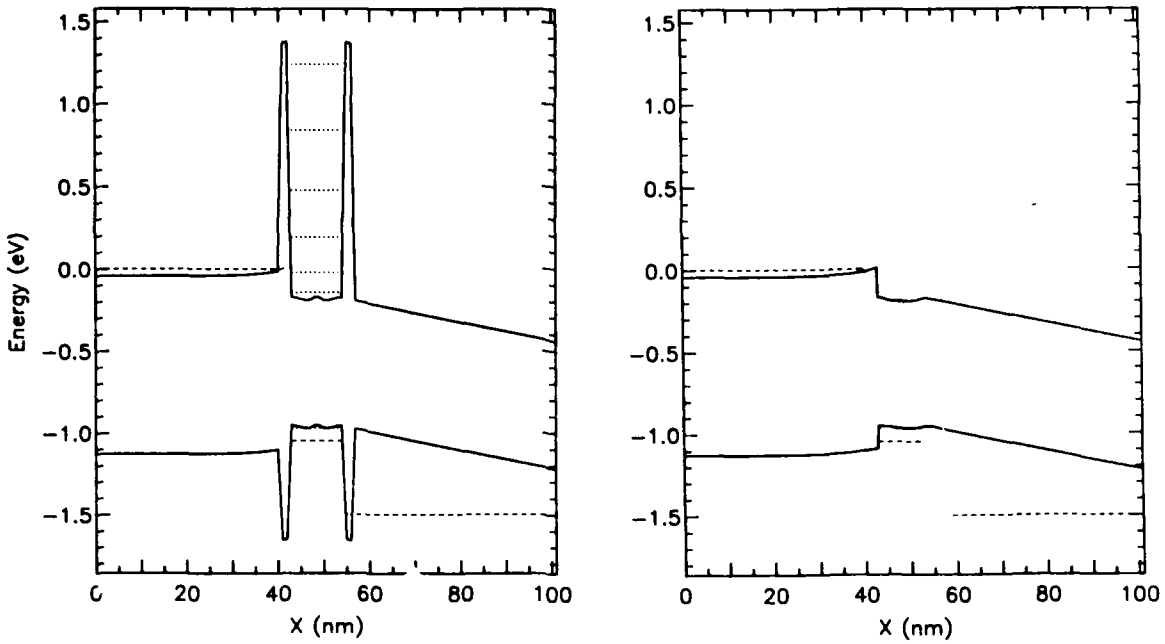


**Figure 17**
**Computed energy-band diagrams for In(GaAl)As/AlAs/InGaAs (a) BiQuaRTT and (b) same structure with AlAs tunnel barriers removed, i.e., HBT with 12-nm base. Dashed lines indicate quasi-Fermi levels with $V_{be}$=1.05 V and $V_{cb}$=0.5 V.**

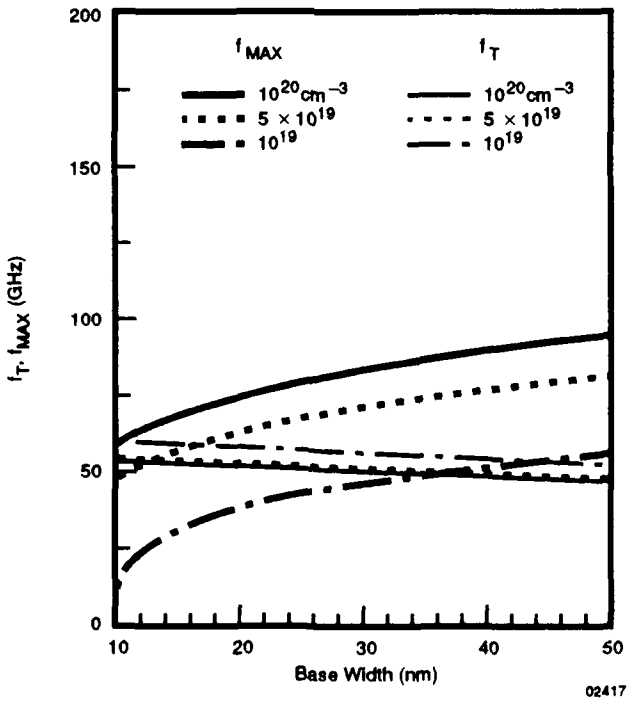


**Figure 18**
**Performance projections of $f_T$ and $f_{MAX}$ for AlGaAs/GaAs BiQuaRTT and their dependence on base thickness and doping using parameters in Table 3.**

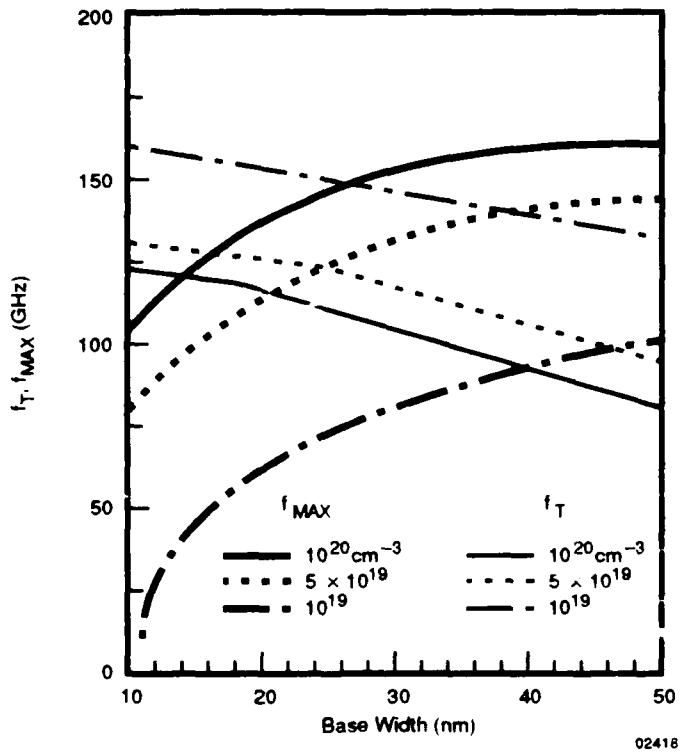


**Figure 19**
**Performance projections of $f_T$ and $f_{MAX}$ for In(GaAl)As/InGaAs BiQuaRTT and their dependence on base thickness and doping using parameters in Table 4.**

**Table 3. Input parameters for the AlGaAs/GaAs BiQuaRTT projections of Figure 18. The transistor geometry consists of $2 \times 10$ µm² emitter, base, and collector metallizations with base/emitter spacing of 0.1 µm and base/collector spacing of 0.5 µm. Contact resistances for these metallizations are assumed to be $1 \times 10^{-6}$ ohm-cm².**

| | | | |
|---|---|---|---|
| Emitter cap | 200 nm | $1 \times 10^{19}$ cm$^{-3}$ | $n^+$ GaAs |
| Emitter | 50 nm | $1 \times 10^{19}$ cm$^{-3}$ | $n^+$ AlGaAs Base Variable Variable $p^+$ GaAs |
| Collector | 150 nm | $2 \times 10^{16}$ cm$^{-3}$ | $n^-$ GaAs |
| Subcollector | 250 nm | $3 \times 10^{19}$cm$^{-3}$ | $n^+$ GaAs |
| InP:Fe substrate | | | |

**Table 4. Input parameters for the In(GaAs)As/InGaAs BiQuaRTT projections of Figure 19 for the same transistor geometry as described in Table 3 caption. The contact resistances for the metallizations to InGaAs are assumed to be $1 \times 10^{-7}$ ohm-cm$^2$.**

| | | | |
|---|---|---|---|
| Emitter cap | 200 nm | $7 \times 10^{19}$ cm$^{-3}$ | $n^+$ InGaAs |
| Emitter | 50 nm | $7 \times 10^{19}$ cm$^{-3}$ | $n^+$ In(GaAl)As |
| Base | Variable | Variable | $p^+$ InGaAs |
| Collector | 150 nm | $2 \times 10^{16}$ cm$^{-3}$ | $n^-$ InGaAs |
| Subcollector | 250 nm | $3 \times 10^{19}$ cm$^{-3}$ | $n^+$ InGaAs |
| InP:Fe substrate | | | |

thickness is reduced from 50 nm to a quantum-well base dimension of 10 nm. As doping increases, $f_T$ decreases because of the corresponding increase in emitter-to-base capacitance $C_e$ and base transit time across the wider neutral base.

$$f_T = \frac{1}{2\,\pi\,\tau_{ec}} \tag{1}$$

$$\tau_{ec} = r_e\,(C_e + C_c) + \tau_b + \tau_c \tag{2}$$

The frequency at which the unilateral power gain becomes zero, $f_{MAX}$, is given by:

$$f_{MAX} = \frac{1}{4\,\pi\,\sqrt{\tau_{ec}\,R_b\,C_c}} \tag{3}$$

and is maximized when the base resistance $R_b$, the effective collector capacitance $C_c$, and the emitter-to-collector delay time are minimized. From the calculation of Figure 18, $f_{MAX}$ is reduced as the base dimension is reduced, because the base resistance becomes larger. Increasing the base doping ameliorates this situation. The same trends are observed in Figure 19 for the In(GaAl)As/InGaAs BiQuaRTT; however, because of the higher bulk n-type doping densities in InGaAs and the lower contact resistance, the In(GaAl)As/InGaAs BiQuaRTT will yield a much higher $f_T$ and $f_{MAX}$ than the AlGaAs/GaAs device. We also see that $f_T$ and $f_{MAX}$ greater than 50 GHz are expected for a 10-nm quantum-well base, indicating that high-speed BiQuaRTTs are feasible using In(GaAl)As materials grown on InP. For these reasons, as well as the materials and technology issues described earlier, the transistor development effort was transferred to InP-based heterostructures in 1989.

## C. InP-BASED RTT

### 1. Materials Development

This effort began with the development of device-quality lattice-matched materials on InP[32] (Appendix M). Next, we began to optimize the RTD structure by investigating the effect of incorporating $In_xAl_{1-x}As$ and $Al_xGa_{1-x}As$ pseudomorphic tunnel barriers. The best result, a peak-to-valley ratio (PVR) of 12:1 at a peak current density of $2.1 \times 10^4$ A/cm$^2$ was

obtained in the pseudomorphic AlAs/InGaAs/AlAs resonant tunneling diode, as shown in Figure 20. An unexpected result is that, for GaAs tunnel barriers, we observe no NDR at room temperature or 77 K. In the structure with AlGaAs barriers (x = 0.25), there is no 300 K NDR, with a very small NDR appearing at 77 K. This is especially puzzling since the morphological appearance of the AlGaAs barrier sample was markedly superior to AlAs barrier samples, which yield our best results.

Our best PVR was obtained with a quantum-well state-lowering scheme reported by Broekaert, et al.[29] In this pseudomorphic structure (Figure 21), an InAs layer is placed in the center of the quantum well to depress the ground state so that the device goes into resonance at a lower voltage. This leads to a lower valley current since the structure goes out of resonance at a lower voltage. A typical room-temperature PVR of 23:1 is observed at a peak current density of $1.3 \times 10^4$ A/cm$^2$. From this same material, we have also obtained diodes with 29:1 peak-to-valley ratio, increasing to 52:1 at 4.2 K.

Since this resonant-tunneling diode exhibits a PVR comparable to the best ever achieved in any material system, we have measured the electric and magnetic field dependence of the current-voltage characteristics to better understand the transport properties. Figure 22 shows the I-V temperature dependence on logarithmic axes for both polarities of electron flow. For electrons directed toward the top surface of the wafer (dashed lines), a lower peak current is observed at all temperatures. This suggests that the tunnel barrier nearest the surface is thinner than the tunnel barrier closest to the substrate.[18] Beyond this effect, the characteristics are largely symmetric. The dark current is observed to decrease monotonically with temperature.

One of the most intriguing characteristics is the preresonance inflection in the I-V characteristics, seen at about 300 mV in Figures 21 and 22. The inflection is not as apparent for the bias polarity shown in Figure 20, but is obvious at room temperature for the opposite bias polarity, (Figure 23). On the right side of Figure 23 is plotted the temperature dependence of the device conductance as a function of bias. At approximately –0.3 V and +0.3 V, a shoulder is apparent in the current-voltage characteristic. If we look at the differential conductance of this device (Figure 23, right), we can see a clear decrease in the conductance occurring at ±0.4 V. The effect becomes more pronounced as temperature is lowered. (This phenonomenon has been observed in InGaAs RTDs by at least one other laboratory.[33])

Before ending our discussion of the devices shown in Figures 20 and 21, note that the calculated electrostatic band profiles are in good agreement with the measured results. The biases we have selected to show correspond to the bias where we predict the valley current to appear. These voltages agree remarkably well with the valley current observed in our measurements of the current-voltage characteristic. This is important since it indicates that our modeling is useful in guiding the material designs of the alloy resonant tunneling structures on InP.

The next step in forming the BiQuaRTT or QuESTT structure with InP-based materials is to develop a heterostructure with increased bandgap energy emitter and collector layers. The obvious choice for this wider bandgap layer is InAlAs so that the transistor structure looks like InAlAs/AlAs/InGaAs/AlAs/InAlAs. This structure was fabricated and tested. The band diagram and room-temperature I-V characteristic of this structure are shown in Figure 24. The peak-to-valley ratio in this RTD is seen to be very weak. A second structure was grown and repeated these results.

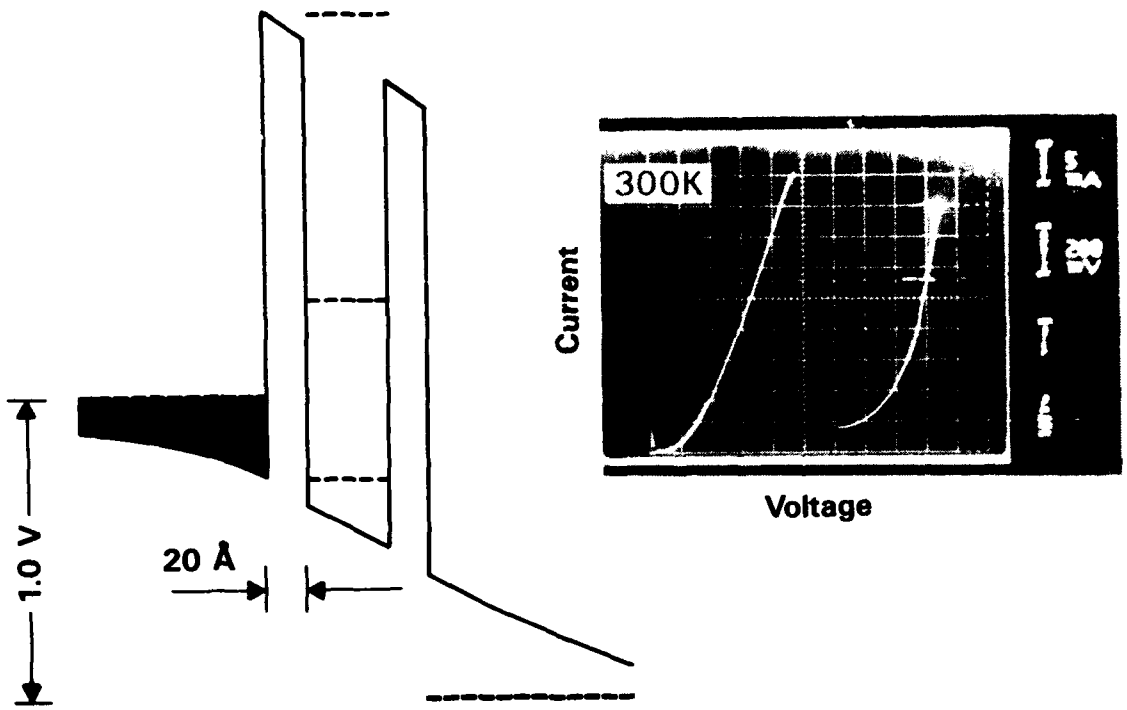


**Figure 20**
**Calculated room-temperature energy-band profile and RTD characteristics for pseudomorphic barrier AlAs/InGaAs/AlAs RTD. Diode area is 14 × 14 μm².**

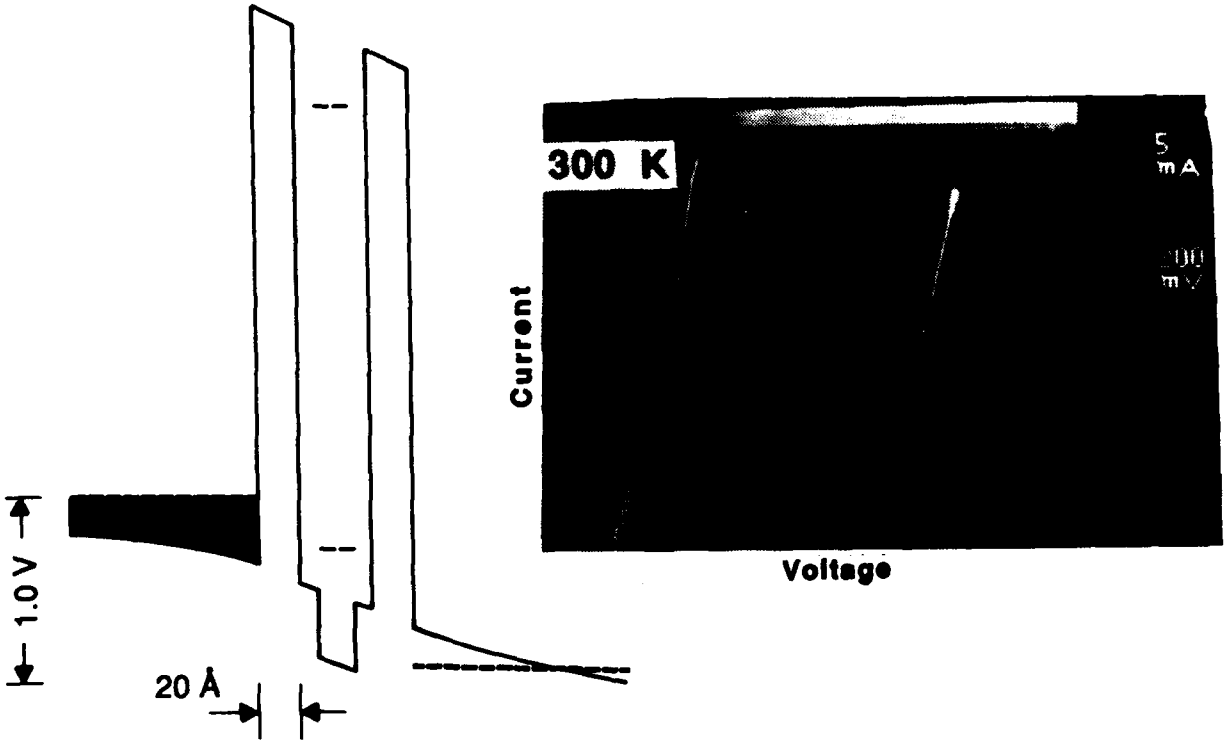


**Figure 21**
**Calculated room-temperature energy-band profile and RTD characteristics for pseudomorphic barrier AlAs/InGaAs/InAs/InGaAs/AlAs RTD. Diode area is 19 × 19 μm².**

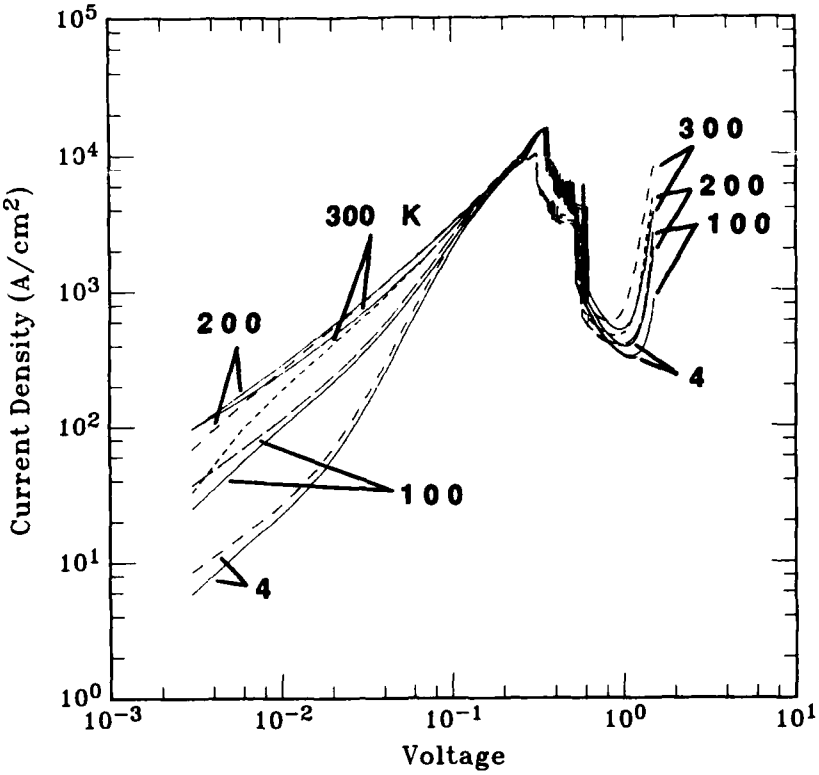


**Figure 22**
**Temperature dependence of RTD structure described in Figure 21.**

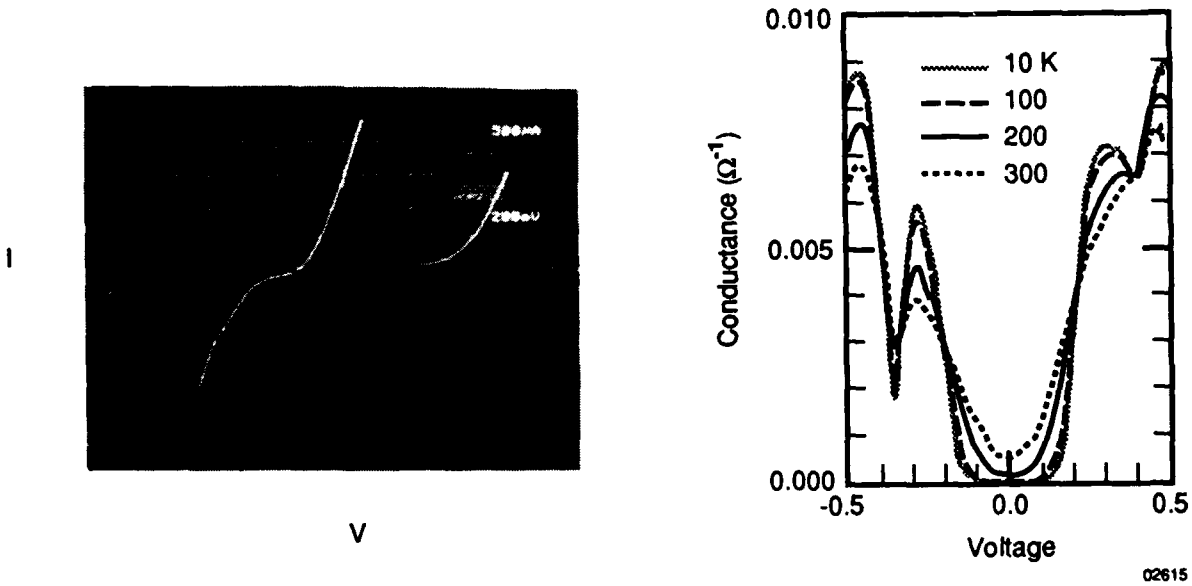


**Figure 23**
**Room-temperature I-V characteristics for material of Figure 20 with emitter area of 9 μm². At right, measured temperature dependence of conductance is plotted. Peak observed in conductivity (±0.3 V) before onset of fundamental resonance.**

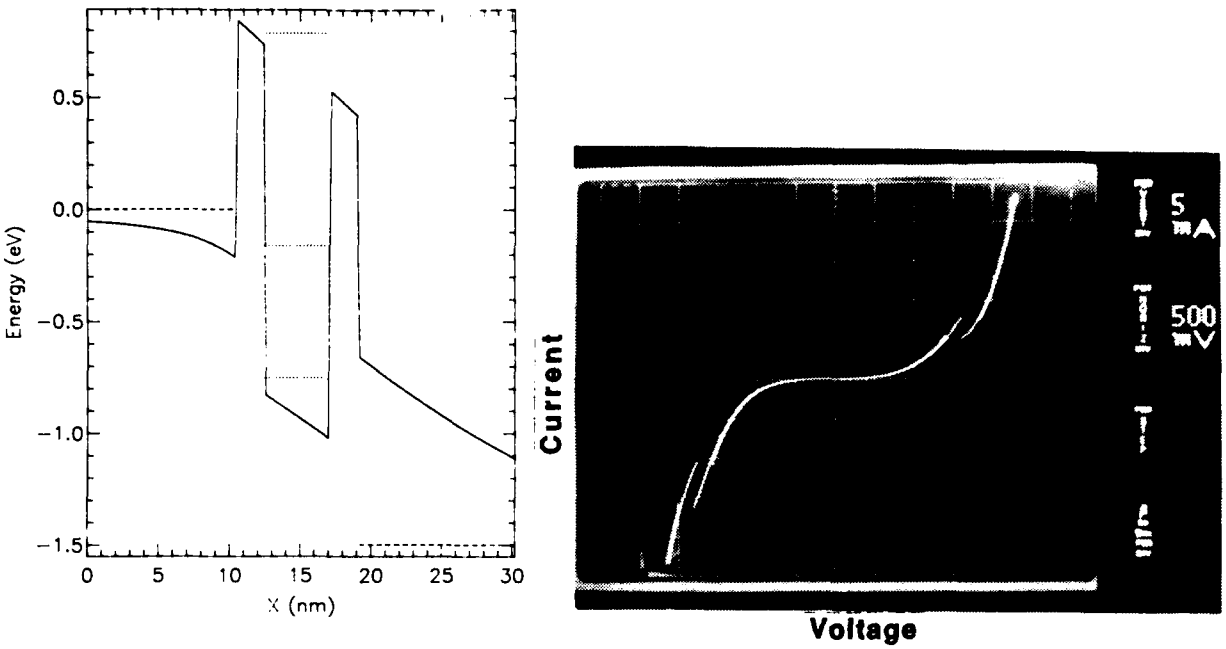


**Figure 24**
**Calculated room-temperature energy-band profile and RTD characteristics for raised emitter and collector RTD, InAlAs/AlAs/InGaAs/AlAs/InAlAs. Diode area is 14 × 14 μm².**

Much improvement is obtained when the lattice-matched quaternary In(GaAl)As is used as the tunnel barrier. The characteristics of this device are shown in Figure 25. We offer a possible explanation for this improvement. With the InAlAs emitter, electrons are injected into the quantum well at an energy that corresponds approximately to the energy of the L satellite valley of the InGaAs base. Transfer into this higher electron mass minimum degrades the resonant tunneling. When we inject into the base at a lower energy, that is, using an $In_{0.5}(Ga_{0.5}Al_{0.5})_{0.5}As$ injector, intervalley transfer is reduced, and the valley current is significantly reduced.

Also seen in the RTD of Figure 25 is a full NDR in the preresonance inflection, which we described earlier. In further materials studies to understand this characteristic, we discovered an unexpected property of these materials. Physical characterization of these structures by x-ray rocking curve measurements and transmission electron microscopy (TEM) has shown that the InGaAs emitter and collector layers are ordered. TEM micrographs of the superlattice ordering are shown in Figures 26 and 27. This unintentional superlattice ordering occurs during growth because of the natural inhomogeneity of beam fluxes in molecular-beam epitaxy. The superlattice period and composition are found to correlate with the substrate rotation rate. For the device cross sections shown, a period of 5.4 nm is present, which is close to the measured period of 5.9 ±0.15 nm deduced from x-ray rocking curve measurements.

It is possible that these rotation-induced superlattices contribute to the I(V) inflections described. Future experimental and theoretical effort will be required to understand the effect

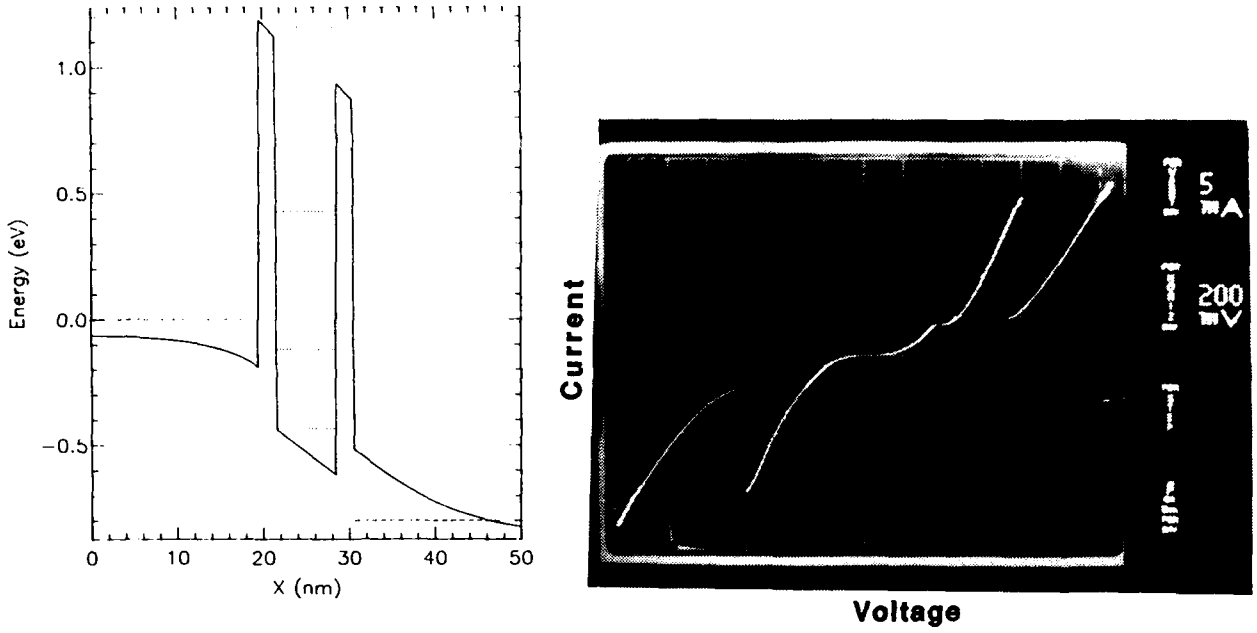


**Figure 25**
**Calculated room-temperature energy-band profile and RTD characteristics for a raised emitter and collector RTD, $In_{0.5}(Ga_{0.5}Al_{0.5})_{0.5}As$/AlAs/ InGaAs/AlAs/$In_{0.5}(Ga_{0.5}Al_{0.5})_{0.5}As$. Diode area is $10 \times 10$ μm².**

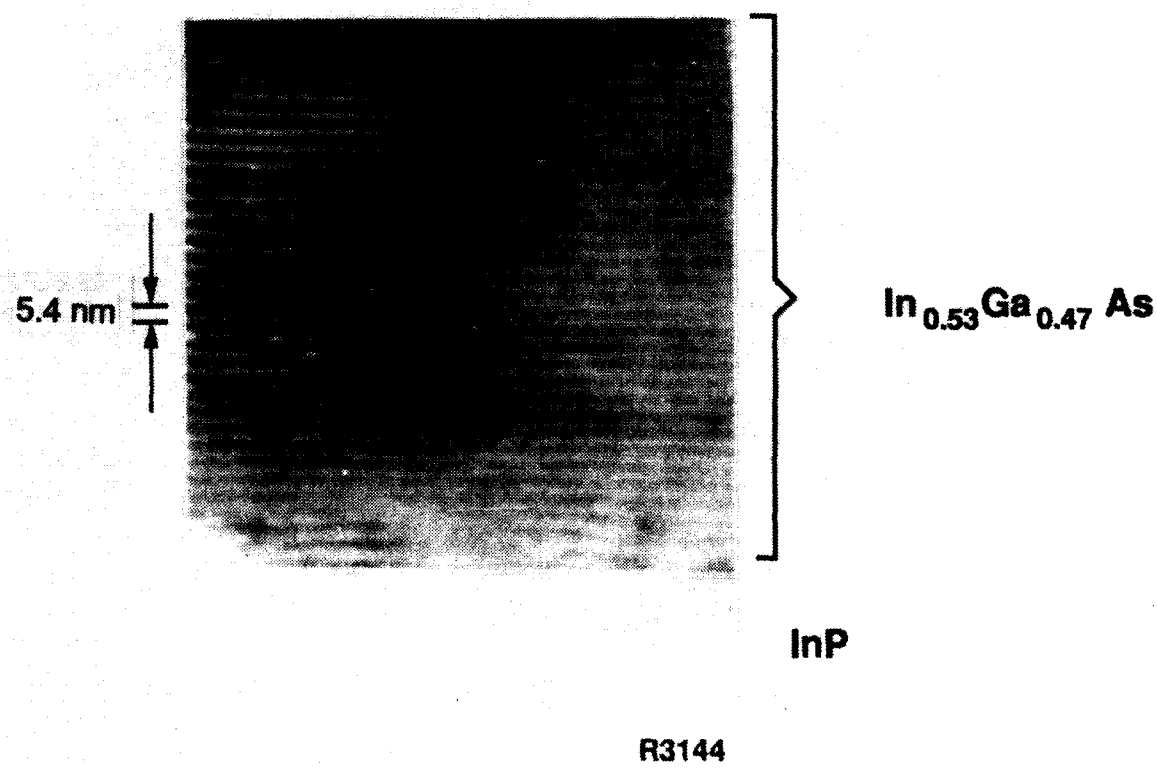


**Figure 26**
**Transmission electron micrograph of device structure of Figure 25 showing rotation-induced ordering of InGaAs collector layer adjacent to the $n^+$ InP substrate.**

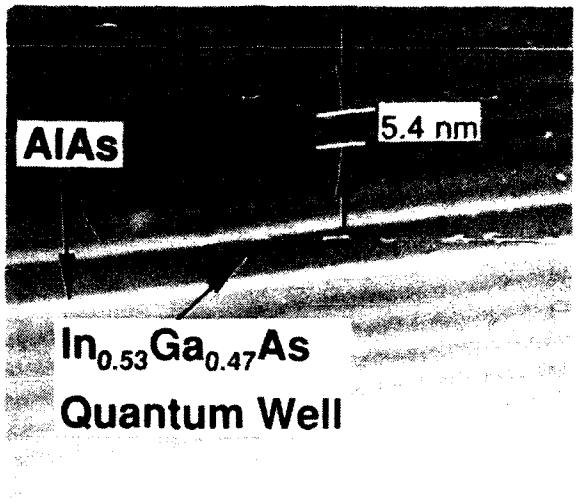


**Figure 27**
**Transmission electron micrograph of double-barrier RTD of Figure 25 showing quantum well and rotation-induced ordering of $In_{0.5}(Ga_{0.5}Al_{0.5})_{0.5}As$ quaternary emitter and collector layers.**

of the rotation-induced superlattice. Since the ordering is controllable by adjusting the sample rotation rate during growth, the effect of this ordering may be used to advantage in the quantum devices. Since reduced alloy scattering is predicted for ordered versus random ternary alloys, this method for ordering the alloys could prove useful for improving device performance. It can also be readily eliminated by increasing the rotation speed of the sample during growth.

All these initial InP-based materials results were obtained on sulfur-doped n-type substrates. For high-speed device tests, fabrication on semi-insulating substrates is required. Growth of RTD structures on semi-insulating substrates did not yield the exceedingly high PVR values that we reported for the $n^+$ substrates. This may be related to the higher dislocation densities that are present in the semi-insulating InP substrates compared to the doped substrates, or it could be related to the different growth temperatures necessary to achieve high-quality growth on semi-insulating substrates. Figure 28 shows our best result for an RTD grown on an Fe-doped semi-insulating substrate. We have examined three substrate suppliers with similar results. Methods for improving these characteristics will undoubtedly be found, but these characteristics are clearly acceptable for RTT fabrication.

Microwave RTDs were completed on semi-insulating substrates using mesa etch processing and air bridge interconnects. The s-parameters of the InGaAs/AlAs RTD shown in Figure 28 were measured to examine the high-frequency characteristics of the quantum transistor mask set. The devices were lapped to 4 mils in thickness and bonded into a test fixture designed for operation through the range 0 to 26 GHz. Because of the large negative resistance the devices had to be stabilized by shunting them with a 10-ohm chip resistor to prevent low-frequency oscillations.

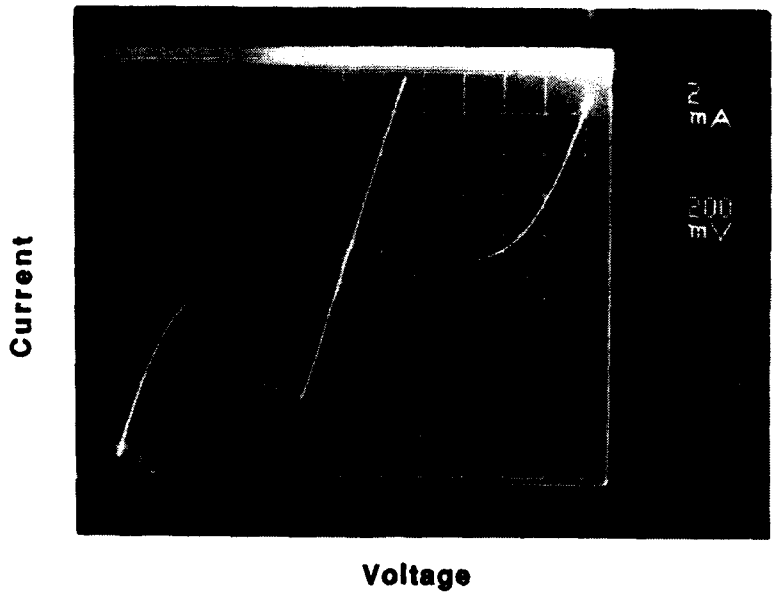


**Figure 28**
**RTD characteristics for same structure described in Figure 21, here grown on Fe-doped InP substrate. Diode area is 3 × 22 μm².**

In Figure 29, the measured values (solid line) of S11 are displayed on a Smith chart, starting from 100 MHz and following a clockwise path to 26 GHz. At low frequencies, the negative resistance is not observed because of the effect of the stabilizing network. The dashed line represents an equivalent circuit fit to the measured data. This circuit is shown in Figure 30. The circuit consists of the chip resistor at left, the bondpad impedance, and the RTD.

The values obtained from the fitting, using TOUCHSTONE, are about what would be expected from the dc characteristics, with the exception of the magnitude of the negative resistance and the bonding pad capacitance. A comparison of the measured and estimated values for the equivalent circuit are shown in Table 5, with comments on how we made the estimate.

The reason for the large negative resistance is not apparent, but it is smaller, by a factor of 3, than has been observed for GaAs RTDs.[34] The larger pad capacitance than expected suggests that the mesa isolation may not have been as deep as required, i.e., that the bond pads are placed on a thin layer of doped InGaAs. We can see from these measurements that the device speed is not limited by parasitics to frequencies less than 26 GHz.

To create a charge neutral base in the BiQuaRTT with heavily doped contact layers to minimize parasitic resistances, it was necessary to develop a capability for heavy n and p doping of $In_{0.53}Ga_{0.47}As$. Figure 31 gives the measured electrical properties of InGaAs, showing the dependence of Hall mobility on electron and hole density. Plots of the conductivity show that the mobility decreases sublinearly with doping for the conditions we have tested.

## 2. Device Development

The transistor process was demonstrated by fabrication of an HBT with a 4-nm $p^+$ base. The energy-band diagram for this transistor is shown in Figure 32. The layer structure,

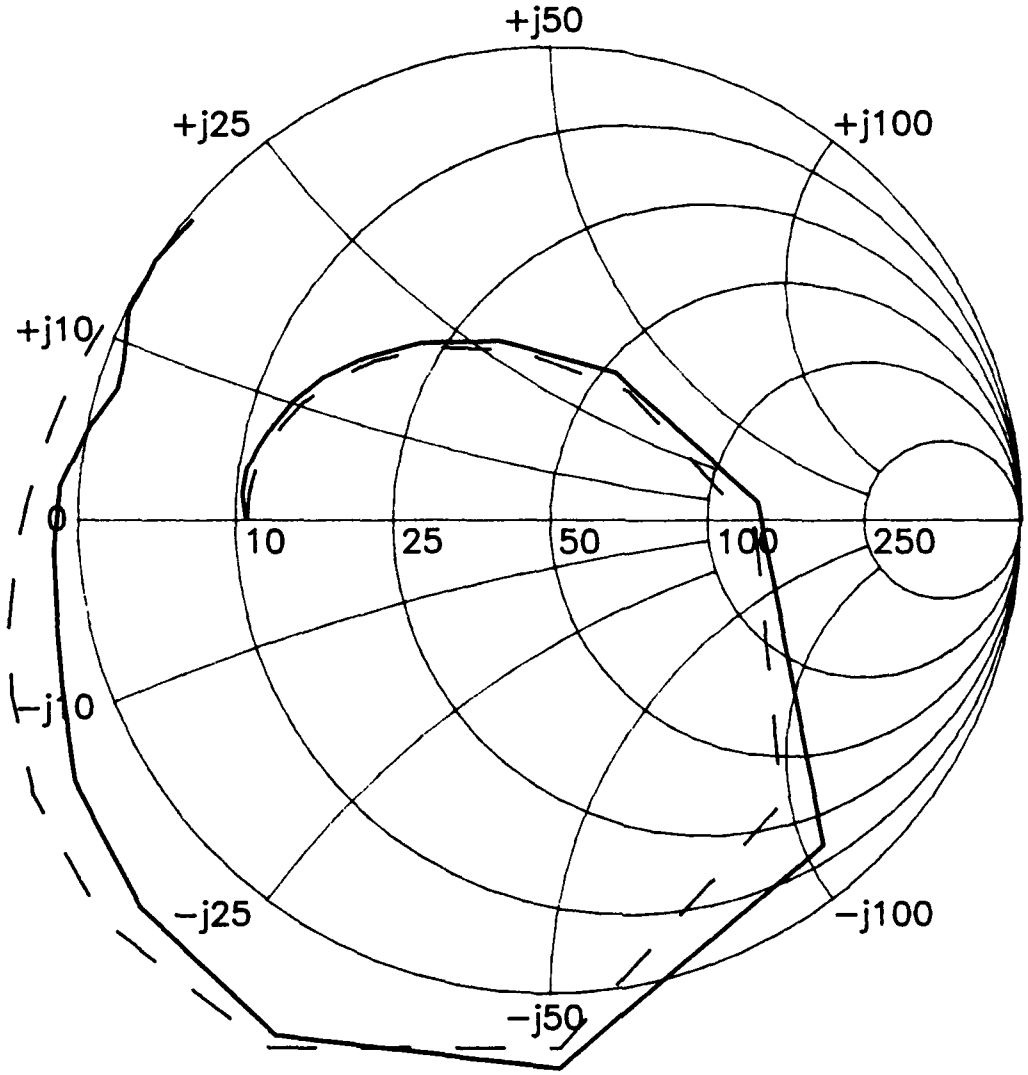


**Figure 29**
**Measured S-parameters (S11) for AlAs/InGaAs/InAs RTD with $4 \times 10\ \mu m^2$ emitter at room temperature. Solid line is measured data starting inside Smith chart at 100 MHz and ending at 26 GHz. Dashed line is equivalent circuit fit to measured results.**

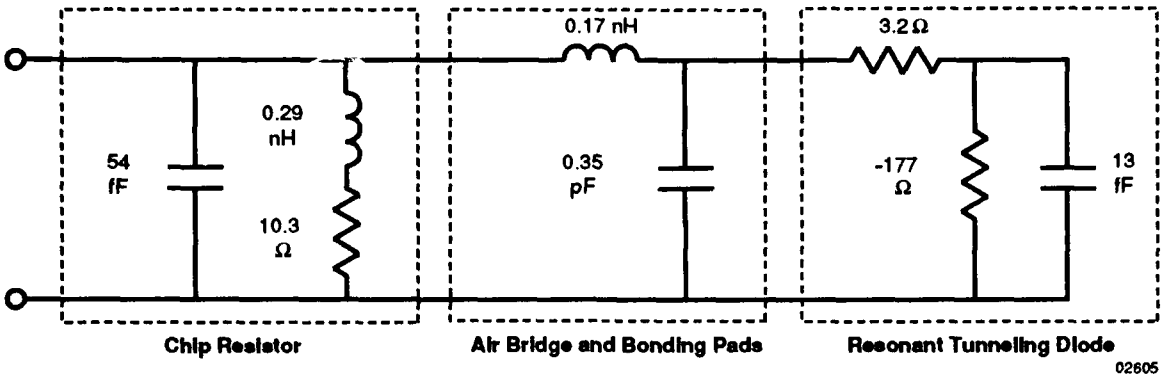


**Figure 30**
**Lumped equivalent circuit for RTD determined from measured S-parameters.**

**Table 5. Comparison of Extracted Equivalent Circuit RTD Parameters With Estimates Based on DC Device Characteristics and Geometry**

| Parameter | Equivalent Circuit | Estimate | Comments |
|---|---|---|---|
| $C_p$ | 0.35 pF | 0.011 pF | From geometry of bond pad |
| $R_c$ | 3.2 Ω | 3.2 | From contact resistance measurement |
| $R_n$ | −177 | ≤8 Ω | From I-V characteristic, depending on loading |
| $C_q$ | 13 fF | 87 fF | $C = \varepsilon A/d$ where d is thickness of RTD depletion layer |

$C_p$ is pad capacitance
$R_c$ is device contact resistance
$R_n$ is magnitude of negative resistance
$C_q$ is quantum-well capacitance

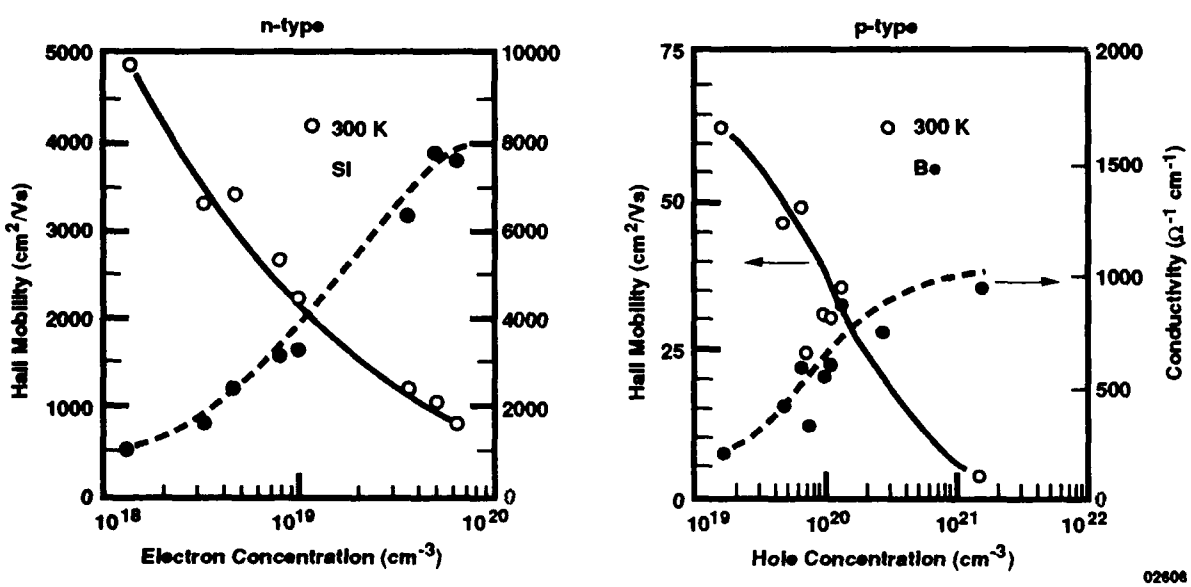


**Figure 31**
**Measured electrical properties of $In_{0.53}Ga_{0.47}As$ showing dependence of electron and hole Hall mobility on doping density.**

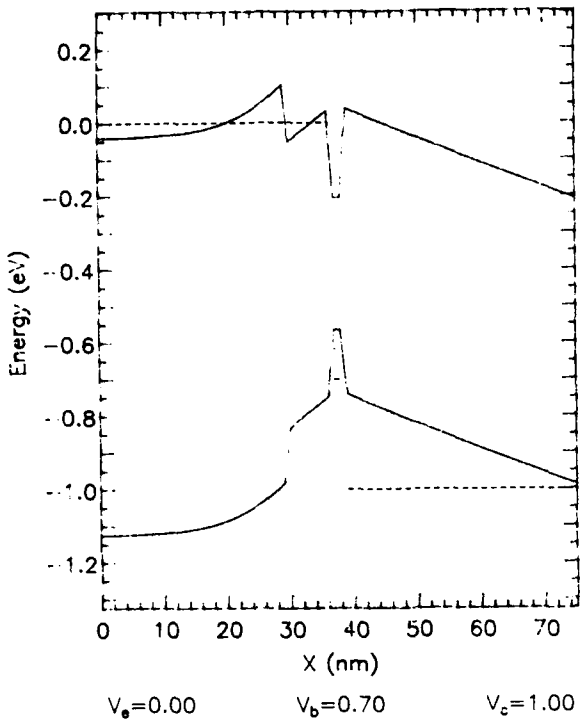


**Figure 32**
**Calculated energy-band diagram for InGaAlAs/InGaAs/InAs pseudomorphic HBT with 4-nm $p^+$ base used as process test structure.**

grown on an Fe-doped InP substrate, consists of 700 nm of lattice-matched InGaAs doped to $5 \times 10^{18}$ cm$^{-3}$, a 300-nm InGaAs collector doped to $2 \times 10^{16}$ cm$^{-3}$, 5.5 nm undoped InGaAs, a 4-nm $p^+$ InGaAs base doped to $5 \times 10^{19}$, 5.5 nm undoped InGaAs, an $In_{0.5}(Ga_{0.5}Al_{0.5})_{0.5}As$ quaternary emitter 100 nm thick doped to $1 \times 10^{18}$ cm$^{-3}$, and a 50-nm compositionally graded layer to a 250-nm emitter contact layer doped to $5 \times 10^{18}$ cm$^{-3}$. A 2-nm pseudomorphic InAs layer was grown in the center of the 4-nm $p^+$ base to lower the base sheet resistance.

The room-temperature common-emitter transistor characteristics of these devices are shown in Figure 33. Contact to the base was achieved by precise etching to the base and deposition of a nonalloyed Cr/Au contact. Two $75 \times 75$ µm$^2$ devices are shown. The device on the left side of the figure shows a current gain greater than ten with low output conductance, while another device with identical geometry (Figure 33 right) shows current gain of 30, but with significantly higher output conductance. Both devices are shown to point out that there is a degree of nonuniformity to the device characteristics that is probably related to the nonplanar etch front. Even so, this process demonstrates that control of the etch front can be obtained to achieve contact to a 4-nm base.

In the final weeks of the contract, this process was used to fabricate both InP-based bipolar and unipolar RTTs. The characterization of the best of these devices at dc, microwave frequencies, and low temperatures is summarized.

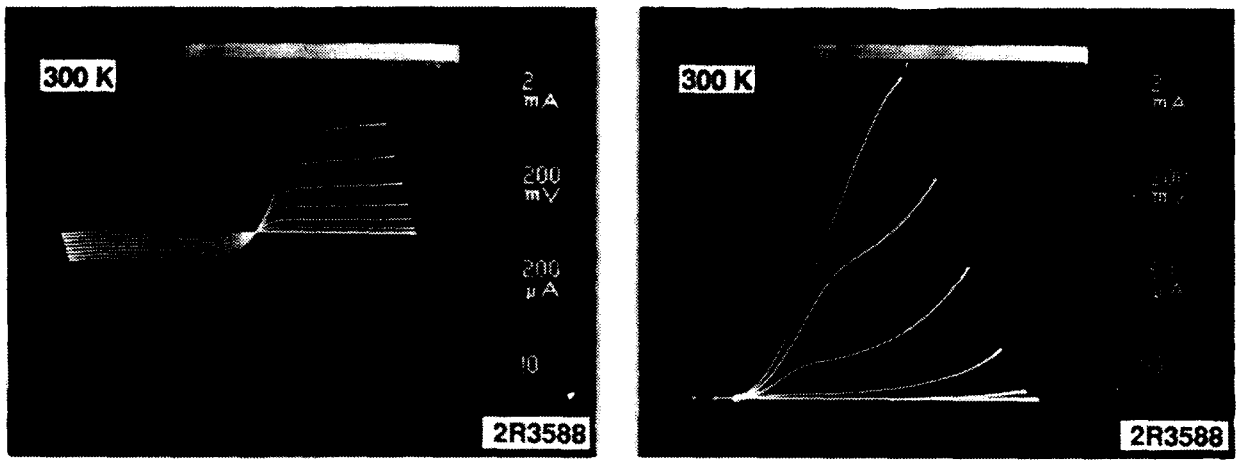


**Figure 33**
**Room-temperature common-emitter transistor characteristics for 4-nm base InGaAlAs/InGaAs/InAs HBT. Emitter dimension is 75 × 75 μm². Characteristics are shown for two geometrically identical devices on same wafer.**

### *a. BiQuaRTT*

Here we describe results of our final processing iteration on the bipolar RTTs using a 40-nm $p^+$ quantum well. While a 40-nm quantum well is roughly a factor of 3 wider than we anticipate will be used in an optimized BiQuaRTT, we chose this width to ease the quantum-well contacting requirements as we work to understand the effects of hot-electron transport across the base/collector junction in the presence of a heavy p-type base doping density.

The energy-band diagrams for this RTT iteration are shown in Figures 34 and 35. Figure 34 shows the energy-band diagram for the BiQuaRTT in the vicinity of the quantum well. The complete layer growth sequence on an Fe-doped InP substrate proceeded as follows: 700 nm InGaAs subcollector doped to $1 \times 10^{19}$ cm$^{-3}$, 300 nm undoped InGaAs collector, 2 nm AlAs tunnel barrier, 1.5 nm InGaAs spacer, 40 nm p-InGaAs base doped to $1 \times 10^{19}$, 1.5 nm InGaAs spacer, 2 nm AlAs tunnel barrier, 5 nm undoped injector quantum well (consisting of 1 nm InGaAs, 2 nm InAs, and 1 nm InGaAs), 2 nm AlAs tunnel barrier, 1.5 nm InGaAs spacer, 50 nm $In_{0.5}(Ga_{0.5}Al_{0.5})_{0.5}As$ emitter doped to $1 \times 10^{18}$ cm$^{-3}$, 50 nm graded layer to a 100-nm InAlAs minority-carrier confinement layer doped to $1 \times 10^{19}$ cm$^{-3}$, and a 50-nm graded layer to a 250-nm InGaAs emitter contact layer doped to $1 \times 10^{19}$ cm$^{-3}$.

The RTD injector monochromates for the incoming electron stream to the base and provides a test structure for determining when the etch to the base is complete. The InGaAlAs quaternary emitter injects electrons into the base at an energy below the intervalley transfer threshold of ~0.5 eV. The compositional grade to InAlAs in the emitter allows biasing the conduction bands in emitter and base to a pseudoflat-band condition while still providing minority carrier confinement. One BiQuaRTT structure as shown in Figure 34 was grown. A second MBE transistor structure was grown, which was nominally identical to Figure 34 except that the base/collector tunnel barrier was excluded. In this way, the effect of the base/collector tunnel barrier on base transport could be investigated. As it is described in

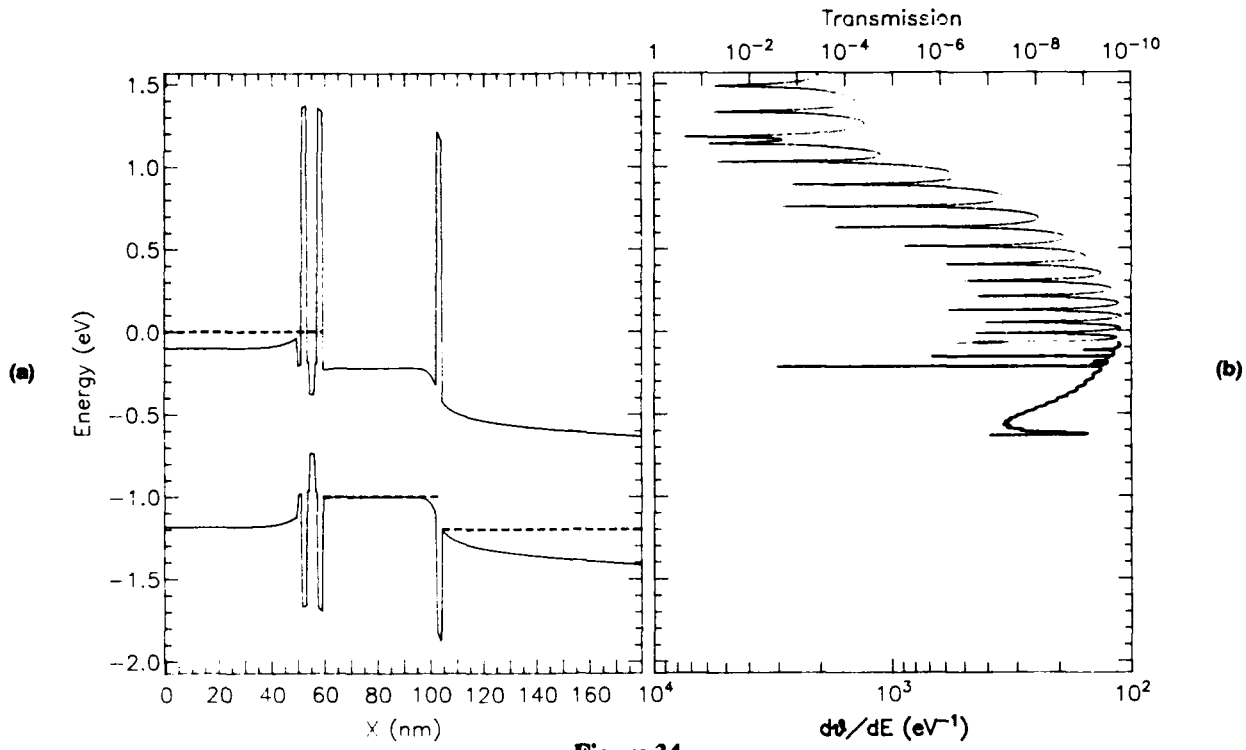


**Figure 34**

**(a) Calculated energy-band diagram in vicinity of quantum-well region of BiQuaRTT under bias. Dashed lines indicate quasi-Fermi level energies in (left to right) emitter, base, and collector. Computed transmission coefficient for energies exceeding conduction-band energies in emitter are plotted in (b). For energies less than emitter conduction band edge, resonances are plotted by computing change in wave-function phase with energy [see lower axis in (b)].**

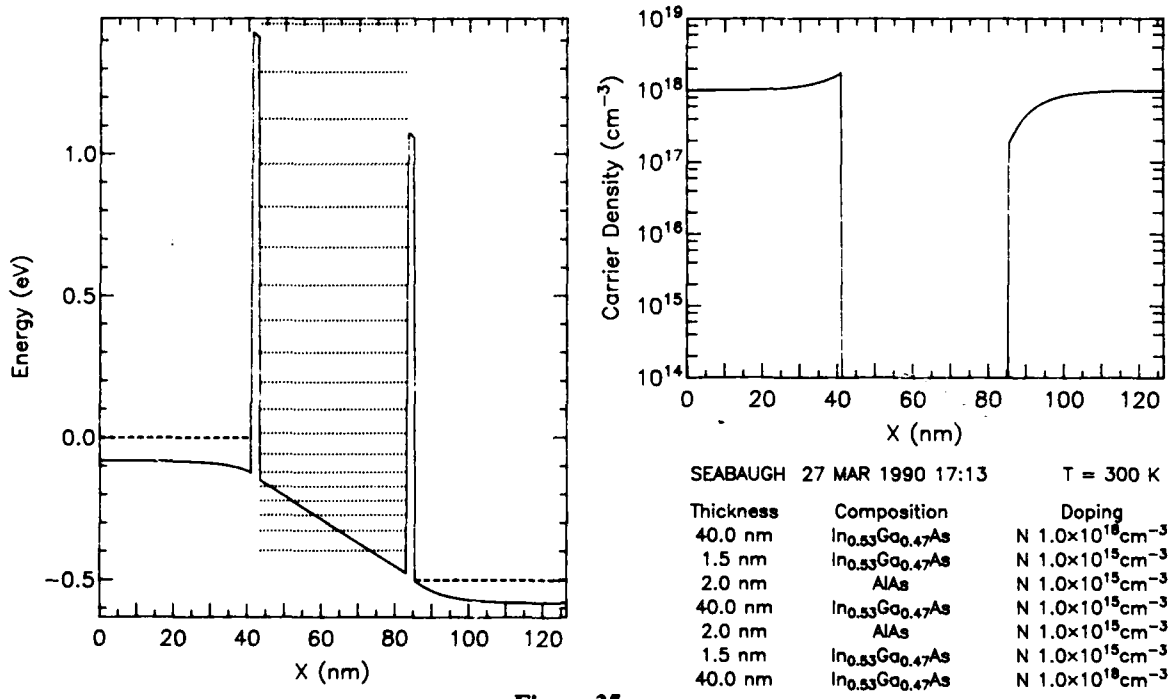


**Figure 35**

**Calculated energy-band and carrier density profiles for AlAs/InGaAs/AlAs RTD of dimensions 2/40/2 nm with 2D quantum-well states indicated with dotted lines and quasi-Fermi energies indicated by dashed lines.**

the literature,[35] this second RTT structure without the base quantizing tunnel-barrier is referred to as an RBT (resonant-tunneling bipolar transistor).

First, the characteristics of the RTD control structure are described. This RTD with 40-nm base is used to characterize the transport through a 40-nm quantum well in the absence of heavy p-doping. The band diagram and layer structure for the RTD in the region of the double barrier are shown in the Figure 35. The structure is symmetric with 60 nm more InGaAs doped to $1 \times 10^{18}$ cm$^{-3}$, and 400 nm InGaAs doped to $5 \times 10^{18}$ cm$^{-3}$ cladding the layer structure shown in Figure 35. An additional 400-nm InGaAs buffer layer doped to $5 \times 10^{18}$ cm$^{-3}$ separates the structure from the semi-insulating InP substrate and eases the precision with which the collector contact etching needs to be done.

The current-voltage and conductance (dI/dV) characteristics of a 40-μm$^2$ RTD are shown in Figure 36. Clear room-temperature conductance oscillations are apparent, corresponding to the tunneling of electrons through the 2-D quantum-well states. If the tunneling transport is resonant as opposed to sequential, the observed conductance oscillations imply that the electron is able to travel ballistically over distances exceeding twice the quantum-well width of 80 nm.

To account for the resonances, the quantum-well energy states were computed as a function of bias with respect to the Fermi energy in the emitter. When the bias voltage across the RTD is such as to lower a quantum-well state below the conduction band minimum in the emitter, a decrease in the conductance is expected. A plot summarizing the calculated movement of the quantum-well states with bias is shown in Figure 37. We expect from these calculations to observe 12 oscillations in the conductance, which is in agreement with the experimental data of Figure 36. Qualitatively identical 300 K conductance oscillations have been reported previously[36] in a 60-nm $In_{0.52}Al_{0.48}As$/ $In_{0.53}Ga_{0.47}As$ RTD.

We conclude from the RTD control structure results that it will be possible to use the 40-nm-wide BiQuaRTT base to optimize room-temperature operation of the transistor structure. Resonant tunneling through the base should be observable and the effects of base doping, collector/base heterostructure design, spacer layers, and base structuring (compositional and dopant grading and ordering) can be investigated. During this time, the base contact process can be further refined through the development of selective etching, while maintaining a good process yield. With optimized base transport at 40 nm, the final reduction in quantum-well base dimension can be employed as necessary to enhance the negative transconductance.

The room temperature common-emitter (CE) characteristics of the 40-nm RBT and BiQuaRTT are shown in Figures 38 and 39 for identical device geometries with measurements made over the same current-voltage range. The emitter area is $4 \times 20$ μm$^2$ with collector area of $20 \times 26$ μm$^2$. Figure 38(a) shows the CE characteristics, Figure 38(b) shows the measured base/emitter voltages used to maintain constant base current in the CE characteristics in Figure 38(a), and Figure 38(c) shows the base/emitter junction characteristics with collector junction open. Gain greater than 2 is observed in the RBT for $V_{be}$ exceeding the bandgap energy of InGaAs (0.78 eV) in agreement with what is expected from the band diagrams. Unlike a conventional HBT, inclusion of a tunnel barrier in the emitter decreases the current gain when $V_{be}$ is biased below emitter/base flatband.

Measurement of the base/emitter diode characteristics shows that the RTD injector goes into resonance at ~1.05 V, which is also in agreement with the band diagram of Figure

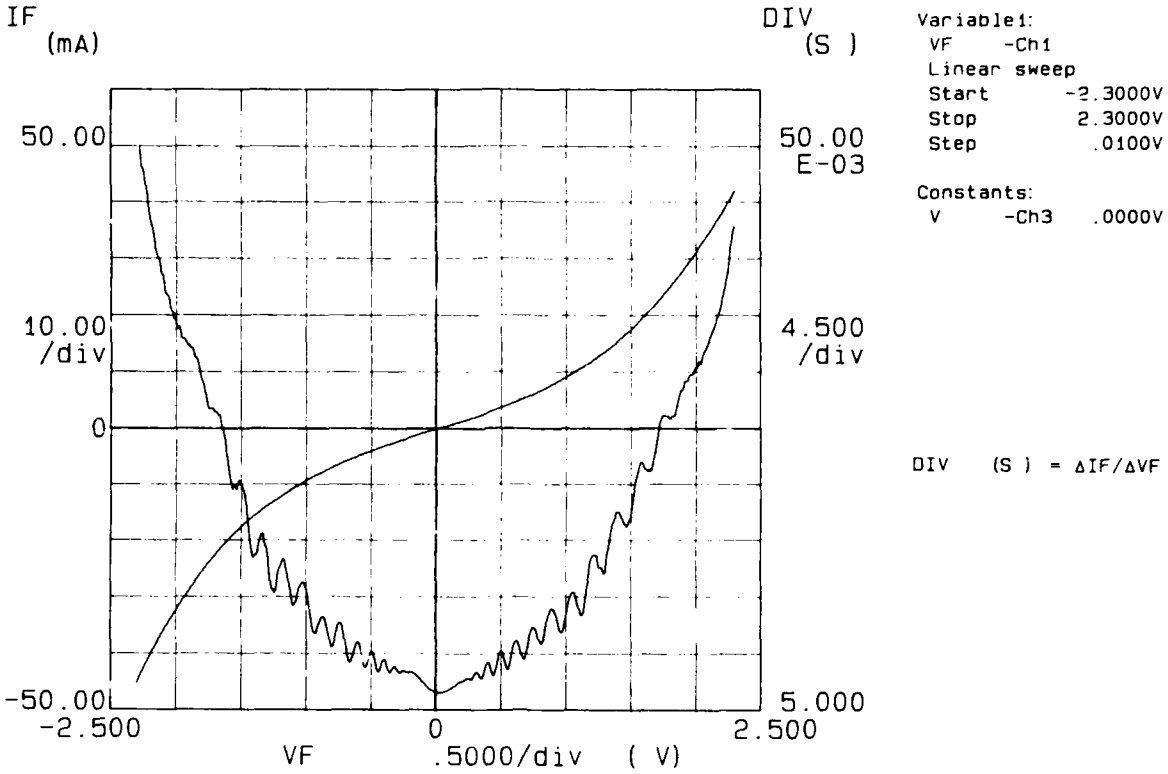


**Figure 36**

**Room-temperature current and conductance (dI/dV) voltage characteristics for AlAs/InGaAs RTD with 40-nm quantum well.**

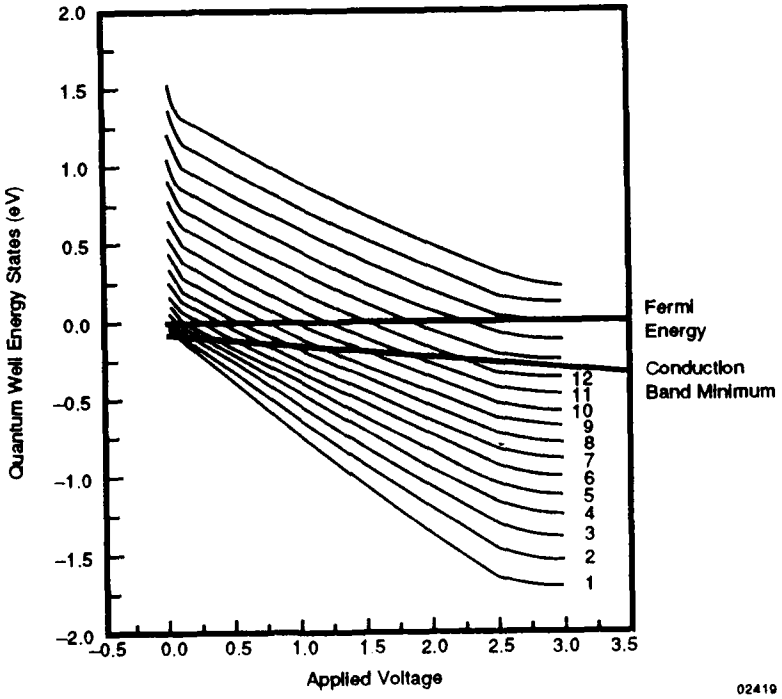


**Figure 37**

**Calculated dependence of quantum-well energy state dependence on applied voltage for AlAs/InGaAs RTD of Figure 36. Energies are plotted with respect to quasi-Fermi energy in electron-emitting side of structure.**

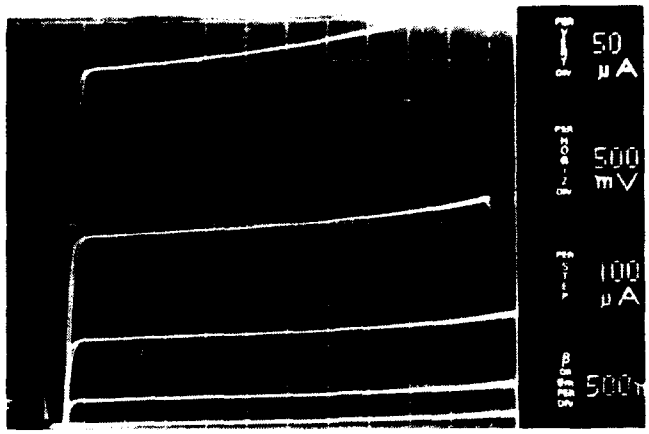


$I_c$ (a) $V_{ce}$

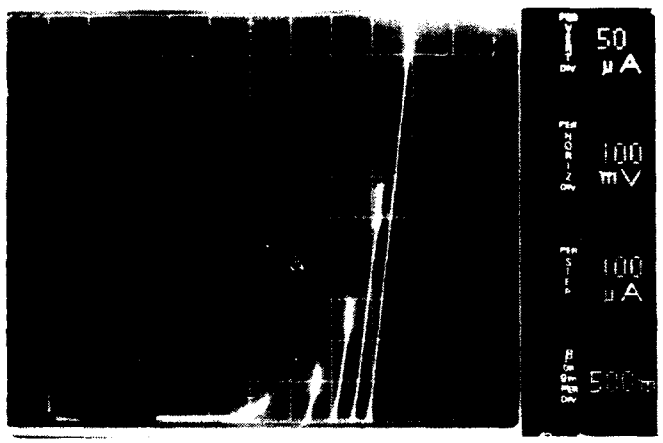


$I_c$ (b) $V_{be}$

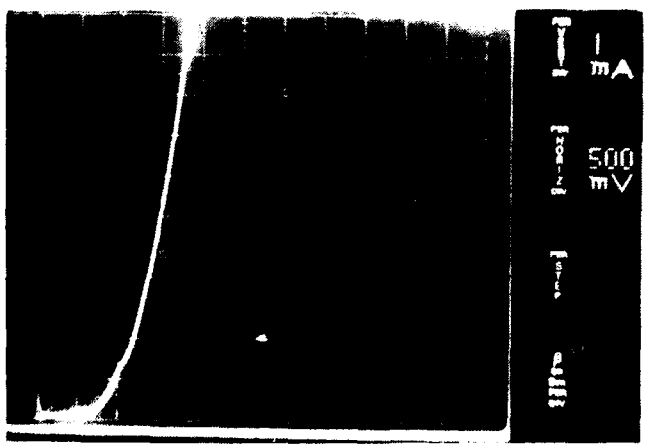


$I_b$ (c) $V_{beo}$

**Figure 38**
**Room-temperature (a) common-emitter transistor characteristics, (b) common-emitter characteristics showing dependence of $I_c$ on $V_{be}$, and (c) base/emitter junction I-V characteristics with collector open for RBT.**

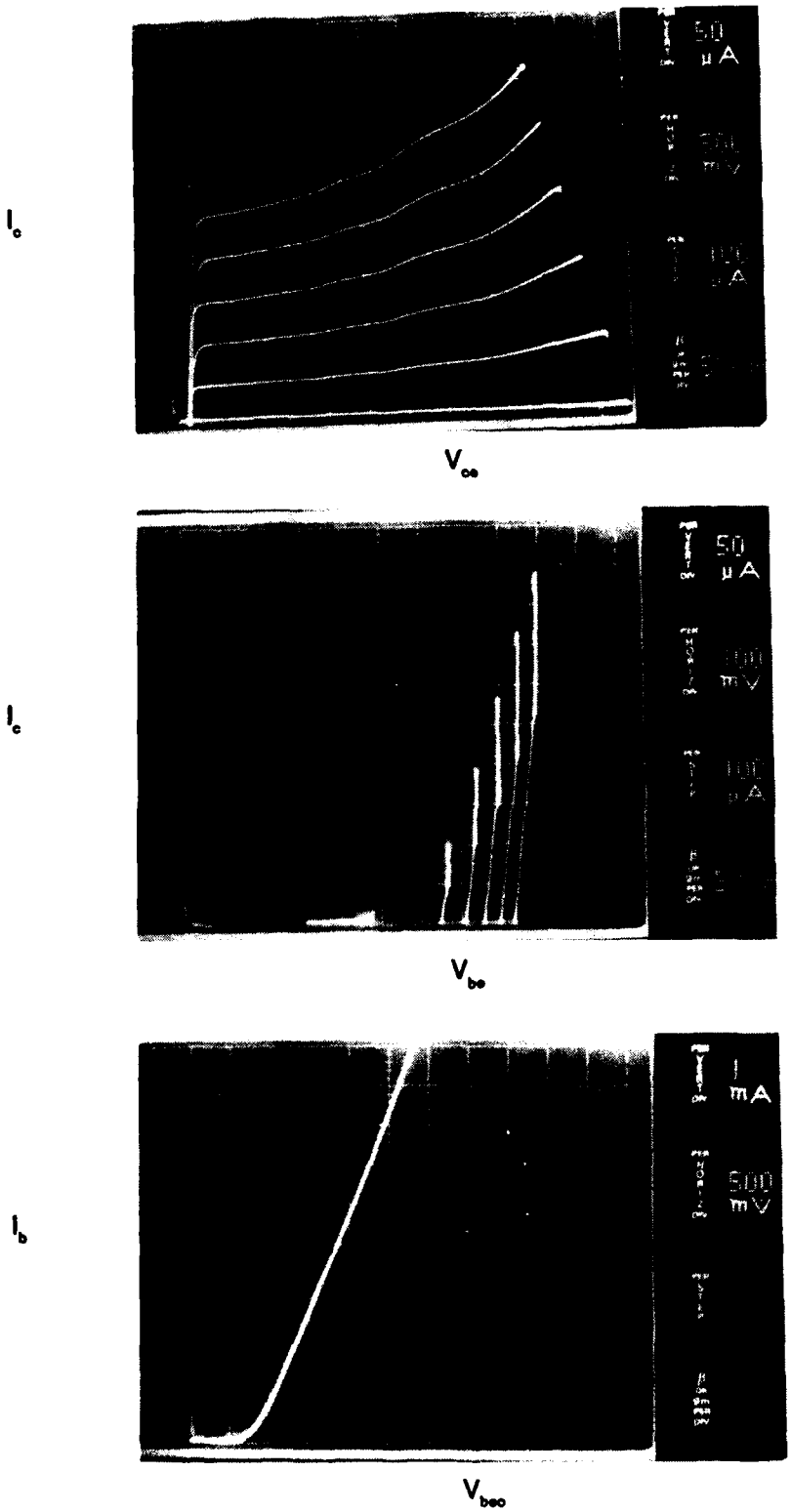


**Figure 39**
**Room-temperature (a) common-emitter BiQuaRTT characteristics, (b) common-emitter characteristics showing dependence of $I_c$ on $V_{be}$, and (c) base/emitter junction I-V characteristics with collector open.**

34. For the range of base currents supplied in the CE characteristics of Figure 38(a,b), the base voltage is less than 0.9 V, so no effects of the emitter injector RTD are observed. The characteristics biased into resonance are shown later. Noted also that, since there is no base/collector tunnel barrier, the base is three-dimensional and no effect of quantized base transport is observed.

In adding the base/collector tunnel barrier, we observe the base quantization in the current-voltage characteristics of the BiQuaRTT structure in Figure 39. Identical measurements are made to compare with the RBT of Figure 38. Apparent resonances are occurring at $V_{ce}$ = 1 V, 2.4 V, and 3.4 V as a result of adding the base/collector tunnel barrier at a base doping of $1 \times 10^{19}$ $cm^{-3}$. Also note that the current gain has been degraded to less than unity for collector/base biases of less than ~5 V in comparison to the RBT. Thus, it appears that the 2-nm AlAs tunnel-barrier in the base/collector junction quantizes the base and reduces the current gain. With collector/base bias sufficient to pull the tunnel-barrier maximum below the conduction band in the base, current gain is greater than unity. Impact ionization certainly also contributes to the current gain at large collector/base voltages since the breakdown voltage decreases with increasing collector current.

The effect of the RTD injector is not observed in the I-V characteristics of the base-emitter junction shown in Figure 39(c); neither are the apparent resonances that result with the addition of the base/collector tunnel barrier. These effects are the subject of a study that will be reported elsewhere and have been observed in BiQuaRTTs of both smaller and larger base width.

The conclusion from this final set is that quantum-mechanical reflections off the base/collector tunnel barrier can reduce the gain of the BiQuaRTT. To improve the gain, the transit time across the base should be minimized and the minority carrier lifetime increased. Reflections at the base/collector tunnel barrier increase the amount of time the electron spends in the base. Future designs will need to minimize these reflections by, for example, reducing the tunnel-barrier thickness. Increasing the minority carrier lifetime should also be possible by base structuring.[37]

As mentioned earlier, the RBT showed a resonance in $V_{be}$ at ~1.05 V [Figure 38(c)]. The CE transistor characteristics for this device when biased through this voltage range are shown in Figure 40. At resonance, the current gain is increased dramatically from a value of approximately 2 to a value exceeding 9. Beyond resonance, the current gain diminishes to approximately 4. This is qualitatively what we would expect given the measured characteristics of the base/emitter junction. It is not clear, however, why the RTD peak-to-valley ratio is so poor. Future experiments should determine whether the p-dopants in the base are affecting the emitter injector. Materials studies comparable to those done for Be in the GaAs pseudomorphic BiQuaRTT[20] will need to be done for the $In_{0.53}Ga_{0.47}As$ base to establish the Be diffusion length during growth.

### *b. QuESTT*

We report here the first unipolar resonant tunneling transistors to ever exhibit room-temperature dc and microwave gain. This achieves a significant milestone on the path toward realization of room-temperature quantum transistor circuits. Only one other hot-electron transistor has been previously reported to exhibit room-temperature gain, this being in the AlSb/InAs/GaSb system.[38]

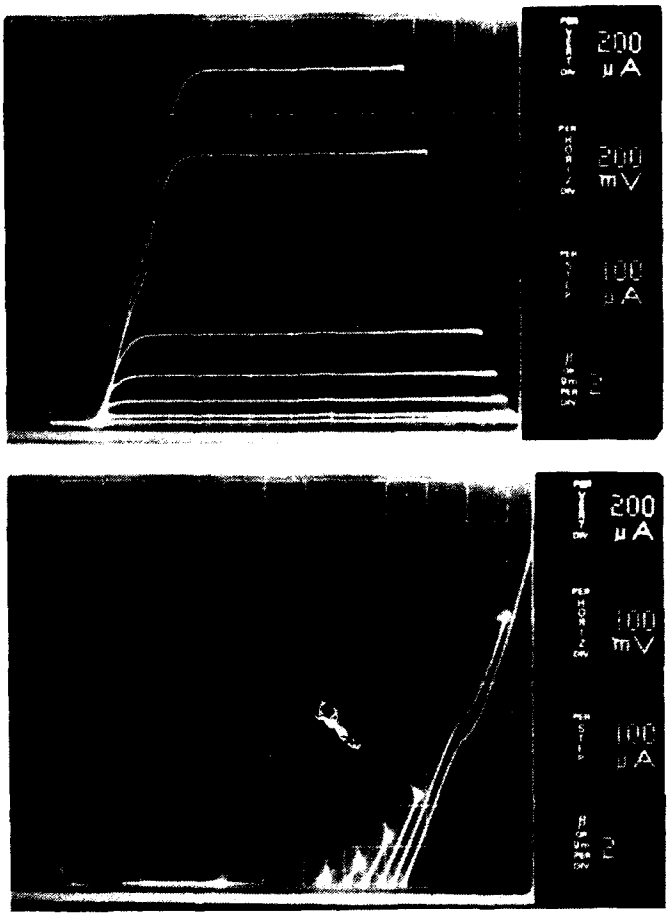


(a)

(b)

**Figure 40**
**Room-temperature (a) common-emitter RBT characteristics, (b) common-emitter characteristics showing dependence of $I_c$ on $V_{be}$. Same transistor as measured in Figure 38.**

The energy-band profile of these devices is shown in Figure 41. A set of three transistor structures was grown, differing only in the width of the quantum-well base which was by design 10 nm, 40 nm, and 60 nm. The layer growth sequence on Fe-doped InP substrates was as follows: 550-nm InGaAs collector contact layer doped to $1 \times 10^{19}$ cm$^{-3}$, 50-nm doping and compositional grade to undoped $In_{0.5}(Al_{0.5}Ga_{0.5})_{0.5}As$, 300-nm undoped In(AlGa)As collector, InGaAs quantum-well base doped to $1 \times 10^{18}$ cm$^{-3}$, emitter RTD injector consisting of a 2/1/2/1/2-nm AlAs/InGaAs/InAs/InGaAs/AlAs resonant tunneling structure clad by 1.5-nm undoped InGaAs spacer layers, 50-nm InGaAs emitter doped to $1 \times 10^{18}$ cm$^{-3}$, and finally a 300-nm InGaAs emitter contact layer doped to $1 \times 10^{19}$ cm$^{-3}$.

The transistor uses an RTD injector (Figure 42). This injector serves two purposes. One is to launch a monochromatic electron beam into the quantum-well base at an energy below the intervalley transfer energy. The quantum-well base is defined as the InGaAs region between the second AlAs tunnel barrier and the quaternary In(GaAl)As collector. Second, the RTD injector provides a test structure that can be used to make in-process measurements to indicate when the quantum-well base etching is completed.

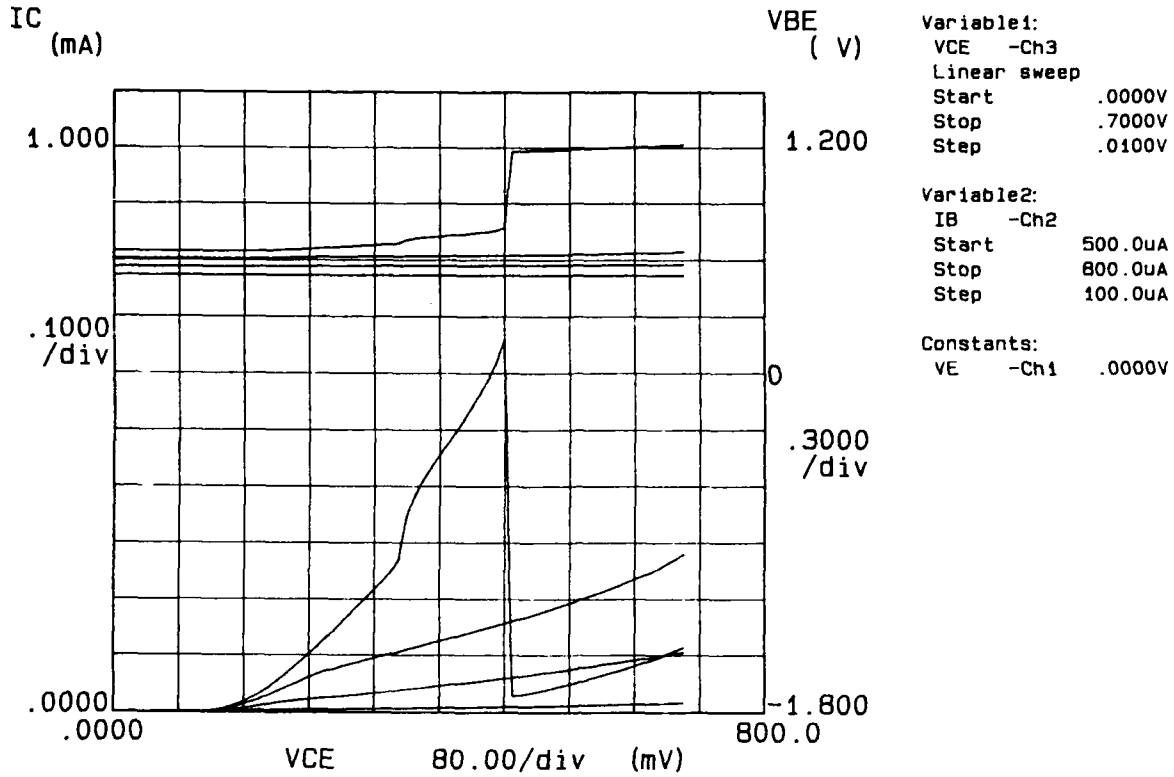


**Figure 41**
**Common-emitter transistor characteristics for 40-nm QuESTT at 4.2 K. Emitter is 2 μm in diameter.**

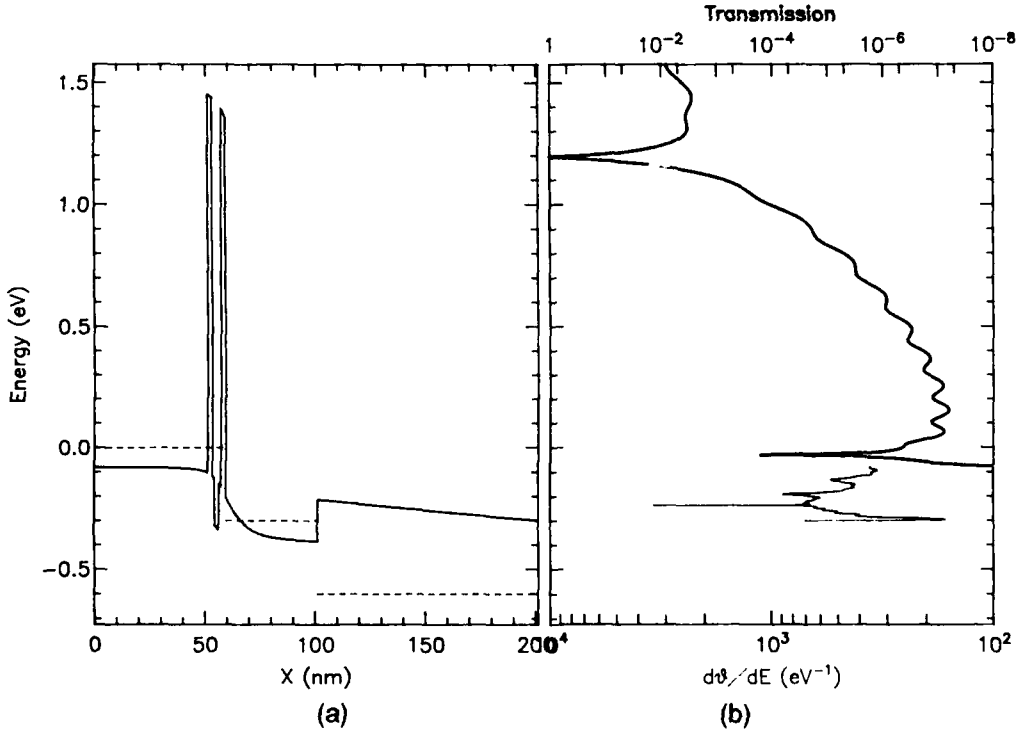


**Figure 42**
**(a) Calculated energy-band diagram for 40-nm base QuESTT. Dashed lines indicate quasi-Fermi level energies in (left to right) emitter, base, and collector. (b) Computed transmission coefficient for energies exceeding conduction-band energies in emitter. For energies less than emitter conduction-band edge, resonances are plotted by computing change in wave-function phase with energy [see lower axis in (b)].**

Evolution of the original QuESTT design may not be readily apparent from the energy-band diagram of Figure 42. In place of the wide-bandgap emitter injector, an RTD injector has been substituted to aid in the base contact process and to monochromate the injected electron stream. A wide-bandgap collector is used as originally proposed; however, the collector tunnel barrier is removed to increase the gain of the device. Base quantization is still achieved because of the wide-bandgap collector without the base/collector tunnel barrier. Resonant tunneling then occurs through the virtual states in the base.

In the device literature, this structure is referred to as the resonant-tunneling hot electron transistor (RHET).[39] There is a difference, however, between the device concepts for the RHET and theQuESTT. In the RHET, negative transconductance is obtained through bias control of the RTD injector, and injection takes place into a three-dimensional base. In the RHET, the base/collector junction is graded to minimize quantum mechanical reflections,[40] while in the QuESTT, negative transconductance is intended (not yet demonstrated) through control of the transport through the quantized 2-D base states; base quantization is required. We refer to the unipolar transistors described here as QuESTTs to emphasize the difference in motivation.

Room-temperature gain was achieved in all three of the QuESTTs: 10-nm, 40-nm, and 60-nm base. Shown in Figure 43(a) are the common emitter transistor characteristics for the 40-nm device and in Figure 43(b) the measured base voltage required to maintain the constant base current steps as a function of $V_{ce}$. A sketch of the device characteristic is made at the right of Figure 40(a) to make clear the order of the overlapping curves. The gain in the device exceeds 10 near resonance, which is comparable to the only other report of room-temperature gain in a hot-electron transistor.[38] Note that, at this current gain peak, the collector base voltage is near zero; therefore, the current gain is not caused by avalanche multiplication in the base/collector junction. It can be seen that, at $V_{be} = 1.3$ V, the injector RTD is switched out of resonance. When this occurs, the base/emitter voltage increases, causing the collector/base junction to switch to a slight forward bias. This manifests itself as a negative collector current in the off-resonance condition and is seen in both Figures 43(a) and 43(b).

Collector/base leakage gives rise to the nonzero collector current seen most readily for the zero base current step. Cooling the device to 77 K does not eliminate the leakage, although on cooling to 4.2 K, the leakage is significantly reduced. This suggests that the unintentional background doping density in the In(AlGa)As collector freezes out below 77 K. Shown in Figure 41 are the common-emitter transistor characteristics at 4.2 K, showing also the base/emitter voltage dependence on $V_{ce}$. A sharp increase in the conductance is observed at $V_{ce} = 340$ meV for $I_b = 800$ µA. This is explained by the line-up of a resonant state within the quantum well itself, which is the resonance we are seeking to optimize in the QuESTT.

It is possible to measure these transmission resonances through the quantum well by fixing the collector/base voltage and measuring $dI_c/dV_{be}$ as a function of $V_{be}$.[41] Enhanced conductance ($dI_c/dV_{be}$) occurs when the injected emitter electrons line up with quantum-well resonant states. This measurement is shown in Figure 44 where collector current and device input conductance, $dI_c/dV_{be}$, are plotted as a function of $V_{be}$ for four values of collector/base voltage. Clear peaks in the conductance are observed with approximately 100-mV spacings. These are consistent with the calculated energy separation between transmission resonances shown in Figure 42. The magnitude of the conductance oscillations increases with increasing collector/base bias, which is consistent with an increase in the base transport factor caused by more efficient collection of electrons at the base/collector junction.

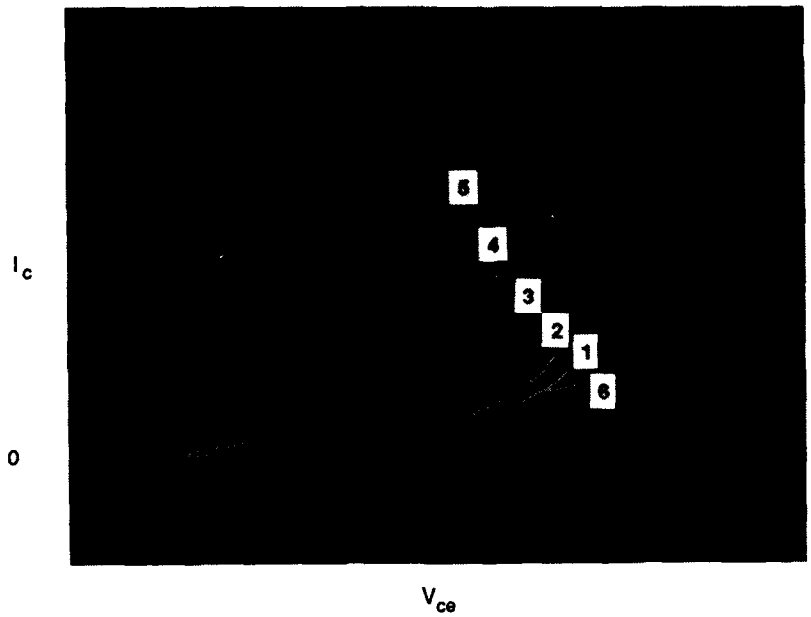


(a)

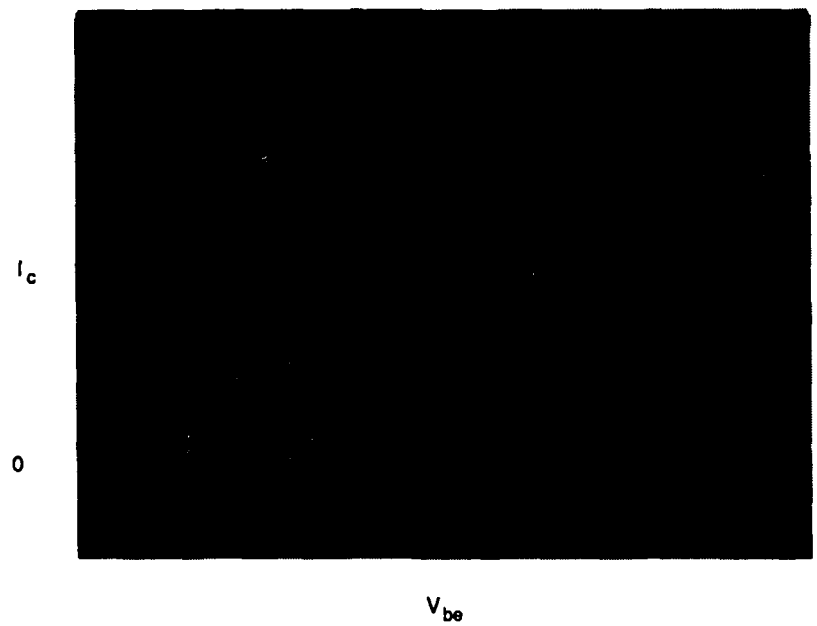


(b)

02422

**Figure 43**
**Room-temperature characteristics of (a) common-emitter 40-nm base QuESTT, (b) common-emitter characteristics showing dependence of $I_c$ on $V_{be}$. Emitter area is $2 \times 10\ \mu m^2$.**

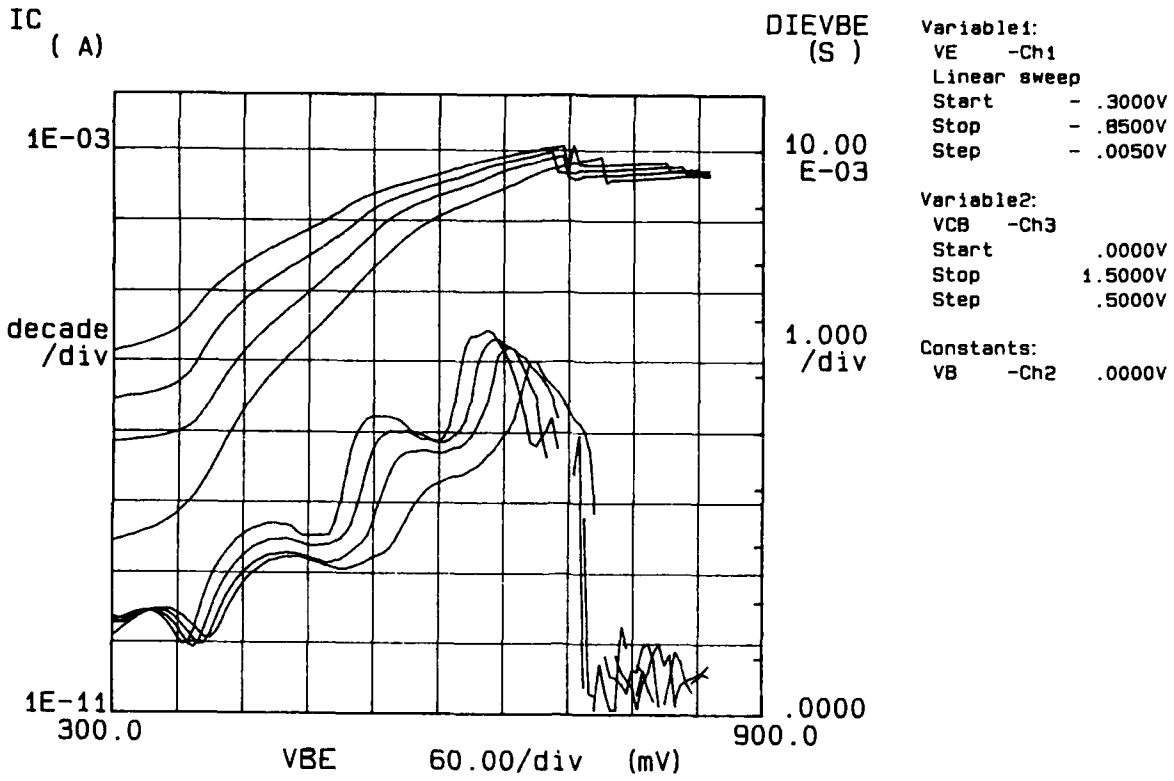


**Figure 44**

**Dependence of collector current $I_c$ and input conductance $dI_c/dV_{be}$ at 4.2 K on base/emitter voltage $V_{be}$ and collector base voltage for same device shown in Figure 41.**

The low-temperature measurements indicate that we have succeeded in forming resonant states in a 40-nm quantum well with base doping of $1 \times 10^{18}$ cm$^{-3}$. Negative transconductance through the quantum-well resonant states is not observed in the 10- or the 40-nm well device. Low-temperature measurements of the 60-nm well device have not yet been made.

Network analyzer S-parameter measurements were made to characterize the device speed. Using an air-bridge interconnect technology (Figure 45) and on-wafer Cascade-probeable coplanar transmission-line pads, the room temperature microwave performance was measured. Figure 46 shows the dependence of $|h_{21}|^2$ and the maximum available gain (MAG) on frequency. Extrapolating at –6 dB/octave, a value of $f_T$= 67 GHz and $f_{MAX}$ = 40 GHz are obtained. S-parameter measurements were also obtained on the 60-nm RTT. On this RTT, $f_t$ and $f_{MAX}$ values of 54 and 11, respectively, were measured. These are the first hot-electron transistors to exhibit dc and microwave gain at room temperature.

## D. PROCESS DEVELOPMENT FOR RTTs

The development of processing technology for RTTs was greatly facilitated by the wealth of in-house experience in compound semiconductor processing. Many of the fundamental processing requirements such as high-quality ohmic contacts, well-characterized etching techniques, dielectric deposition, and other techniques were already established.

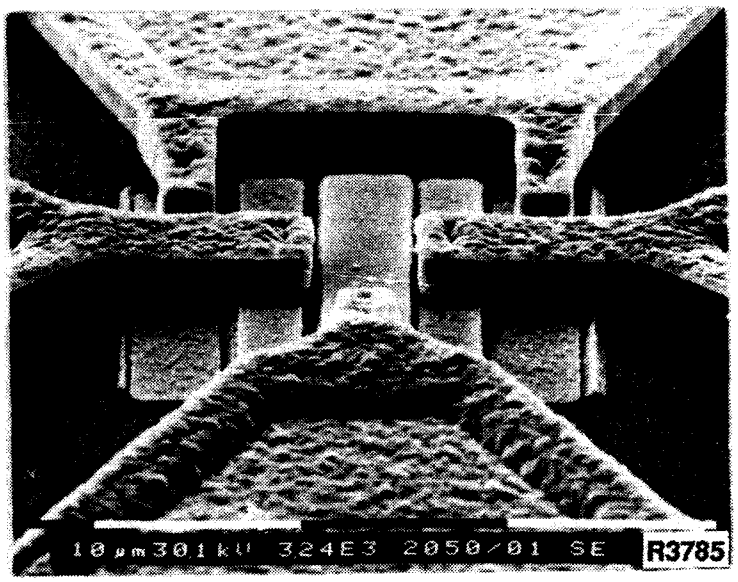


**Figure 45**
**Scanning electron microscope photograph of air-bridge interconnect to RTT. Center contact is emitter, on either side of emitter is base, and outside each base is collector. Separate air bridge to each base.**

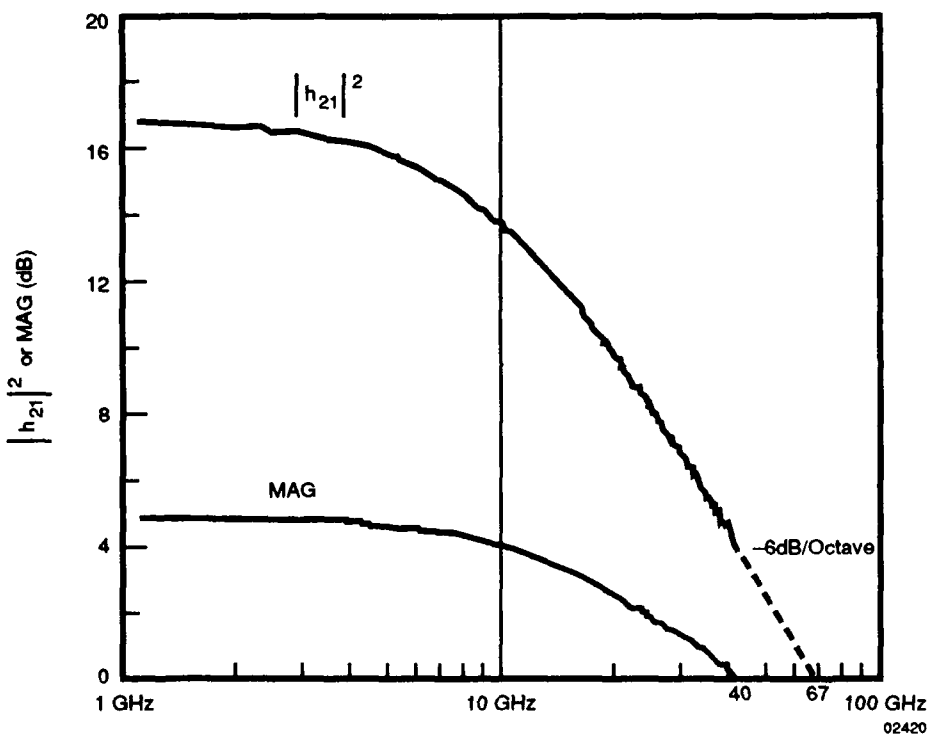


**Figure 46**
**Vector network measurement of current gain $h_{212}$ and maximum available gain as function of frequency with $V_{be}$ = 0.8 V and $V_{ce}$ =1.22 V. Emitter area is 3 × 10 µm².**

Special requirements for resonant tunneling transistors did require new processing techniques to be developed. In the earlier stages of the contract, we were working in the GaAs/AlGaAs/InGaAs system but later changed to the InGaAs/AlAs/InAlGaAs system on InP substrates. This change was justified from several points of view. As discussed in the transistor development section, the larger barrier heights and lower effective mass result in superior resonant tunneling devices. Additionally, as is discussed next, the ability to form nonalloyed ohmic contacts resulted in a significantly simplified approach to both bipolar and unipolar device fabrication.

We discuss in detail our approach (for both material systems) to two specific and interrelated processing goals that are particularly important to RTTs: contacting a quantum-well base and achieving good base-to-emitter isolation. We also describe the various mask sets used to fabricate RTTs and other process development issues.

## 1. Fabricating GaAs/AlGaAs/InGaAs RTTs

### *a. Base Contact and Isolation*

Resonant tunneling transistors of the type we are fabricating use a quantum well for the base. A prerequisite for the successful fabrication of these transistors is a good electrical contact to the very thin quantum well while maintaining reasonable isolation from the emitter and collector regions. Different solutions to these problems were developed for the bipolar BiQuaRTT and unipolar QuESTT.

In the case of the BiQuaRTT, we achieved contact to the p-type base by simply implanting a p-type dopant, Be, down to the quantum well. We developed an implant process that used three different energies to obtain a reasonably uniform doping level down to the quantum well, which was typically 500 nm below the surface. Figure 47 shows the distribution of Be in GaAs as predicted by LSS range tables when implanted at 30, 80, and 160 kV with a total fluence of $3 \times 10^{15}$ ions/cm$^2$. We optimized a rapid thermal annealing (RTA) process to minimize the bulk resistivity to the p-type implanted regions. A sacrificial GaAs wafer was placed over the implanted wafer during the RTA process to reduce As out-diffusion.

Be diffusion in our heterostructure was a serious concern, in part because anomalous redistribution of Be in MBE-grown GaAs had been reported.[42,43] We investigated Be concentrations in our structures by secondary ion mass spectroscopy (SIMS). We determined that Be is completely contained in the quantum-well structure as grown by MBE and that no diffusion out of the quantum well after RTA was evident. Figure 48 shows a SIMS depth profile of a 25-nm Be-doped quantum-well with AlAs barriers, where the Al and Be ion signals are plotted. The Be is clearly contained inside the well.

Electrical measurements of implanted contacts to the well have shown convincing evidence of electrical transport through the quantum well, and Hall bar measurements have confirmed that the charge carriers are holes. Hall measurements also determined a hole mobility of 780 cm$^2$/V s.

The p-type implant does form an undesired lateral pn junction with the emitter, and the tail of the implant penetrates the lower barrier layer and forms another pn junction with the collector. In principle, it should be possible to operate a BiQuaRTT so that neither of these junctions is strongly forward-biased. However, the devices we have been able to fabri-

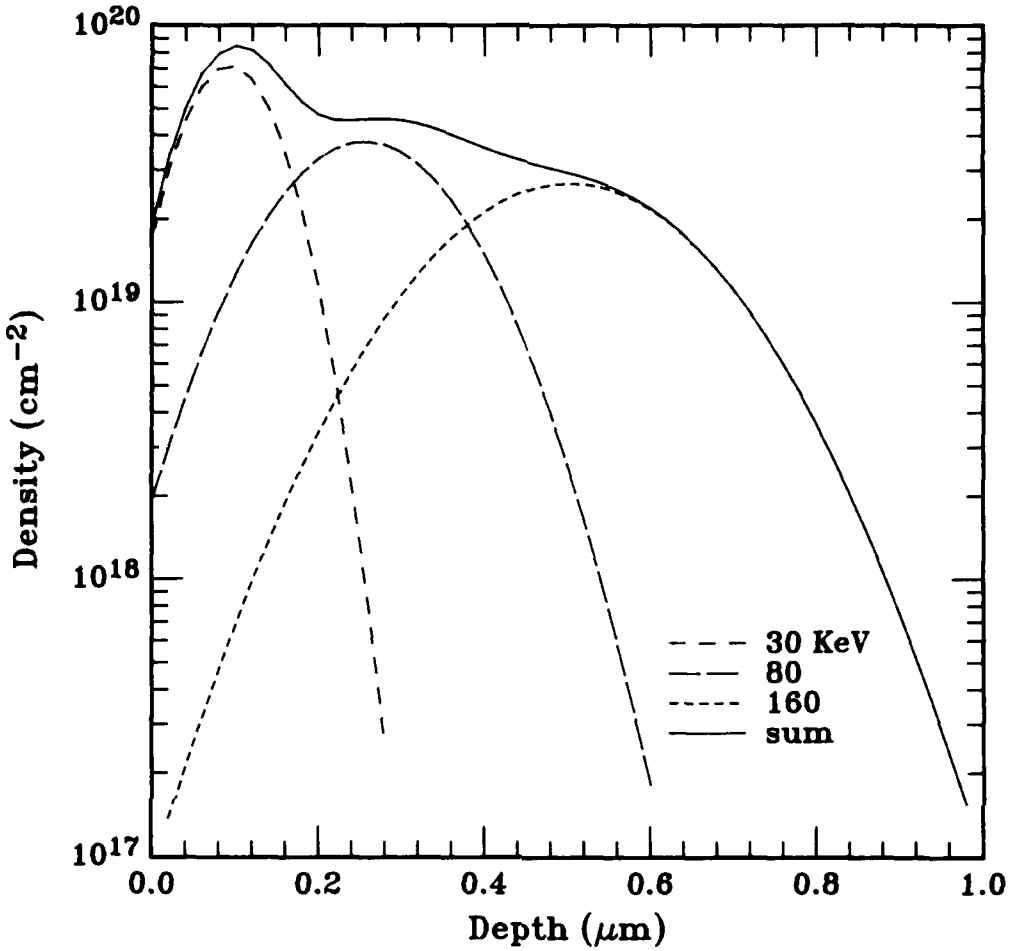


**Figure 47**
**Depth profile of triple implant used to contact well in BiQuaRTT devices.**

cate require for operation a base-emitter bias that significantly forward-biases the parasitic lateral pn junction.

Fortunately, it is possible to effectively remove this unwanted leakage path. A trench may be etched in the GaAs between the emitter and base contacts. If the bottom of the trench is positioned a few nanometers above the quantum well, the base-to-emitter leakage is eliminated. However, if the etch is too close to the well, surface depletion can effectively disconnect the base from its contact. Test structures were used to gauge the appropriate etch depth. A trench between two implanted contacts to the base was pre-etched a few nanometers. Then the trench in this test structure was etched along with the base-to-emitter isolation trench on devices. While etching in small increments, the resistivity of the base-to-base contact on the test structure can be monitored for any change. Once an increase in the resistivity of that measurement is detected, one can be sure that the etch-front is very near the quantum well and that the device isolation trenches are very near an optimum position. We have also monitored, as the etch progresses, the base-to-emitter forward-biased current on large, easily probed devices and have terminated etching once the current at a fixed bias drops below a prescribed value.

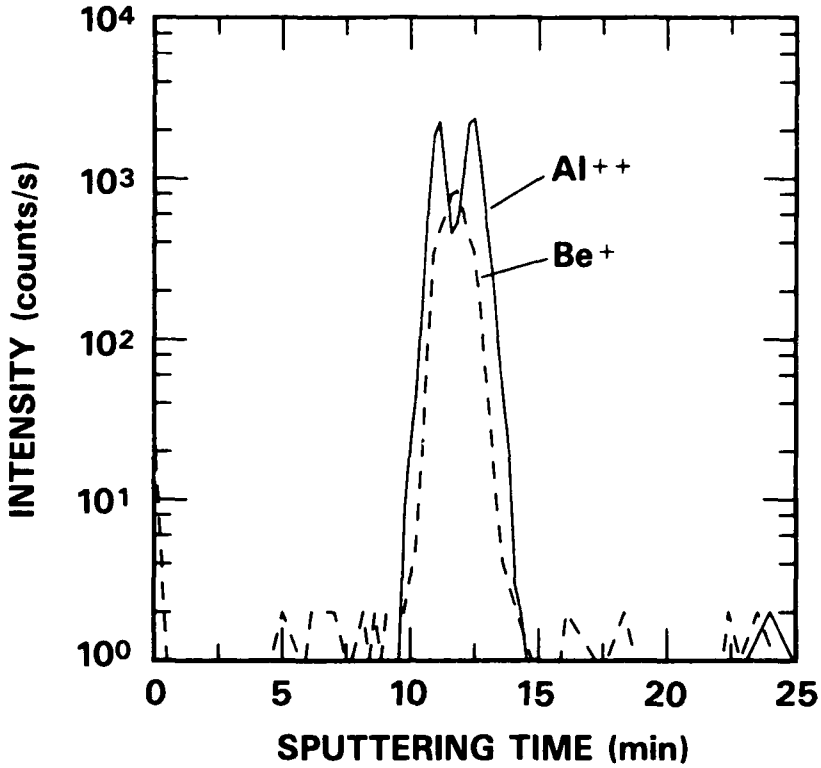


**Figure 48**
**SIMS profile of pseudomorphic BiQuaRTT transistor with 5-nm AlAs tunnel barriers and 25-nm Be-doped InGaAs quantum-well base.**

In an effort to improve this etch isolation process, we attempted to use selective dry etching. It is certainly possible to selectively stop on the AlGaAs barrier layers. However, this is too close to the quantum well and causes base depletion. A reactive ion etching process that will selectively stop on InGaAs has been reported in the literature[44] and was also developed here. We strategically placed a thin InGaAs layer slightly above the resonant tunneling structure and demonstrated the ability to use this layer as an etch stop. We had hoped that this low-bandgap layer spaced away from the resonant tunneling structure would have minimal impact on transport through the device. Unfortunately, there was serious degradation in the peak-to-valley ratios and current densities of resonant tunneling diodes that included the InGaAs layers. Further investigation of this approach is indicated.

We should also mention the parasitic base-collector junction resulting from the tail of the implant, which penetrates into the collector region. For the BiQuaRTT, this is not a serious problem since it is possible to operate the device with this junction reverse-biased.

The QuESTT device, however, does not lend itself to implanted contacts to the well. Although base-to-emitter isolation could be accomplished in the same manner as the BiQuaRTT, because the device is unipolar, there is no junction to provide isolation where the implant tail meets the collector.

In the proposal for this contract, we proposed a method for contacting the quantum well in the QuESTT involving etching and subsequent epitaxial regrowth on the well. This

was attempted using a highly selective reactive ion etching process to stop on the base layer and the regrowth of InGaAs to from the contact to the base. The selective etching was performed with a $CCl_2F_2$ and He reactive ion etch, which is found to effectively stop on buried layers of AlGaAs and InGaAs.[23]

Figure 49 is a transmission electron micrograph of the successful regrowth of InGaAs on the quantum well of the QuESTT. In the figure, the etch appears to consume or chemically alter the first 3.5-nm AlAs layer leaving an atomically smooth interface for regrowth of the thick InGaAs contact layer. The InGaAs well layer thickness is 8.5 nm.

Dislocations in the regrown InGaAs are apparent. These arise because the thickness of the regrown contact layer, 200 nm, exceeds the critical layer thickness for dislocation formation. In addition, we have observed microcontaminants that were left on the wafer surface after selective etching and cleanup. These amorphous particles are the source of the larger defects apparent in the regrown InGaAs.

Another feature of the etching is the undercut, which is obvious in the micrograph. Often the development of a highly selective etch leads to compromising the etch anisotropy. This undercut produces a shadowing effect during MBE growth and disconnects the regrowth of InGaAs between emitter and base. This is a desirable feature since no etch isolation step is then necessary to prevent parasitic emitter-base conduction. The free InGaAs surface between the regrown base layer and the emitter contact layer is, however, not desirable. Depletion of the quantum-well electrons from this surface results in an electrically open regrown

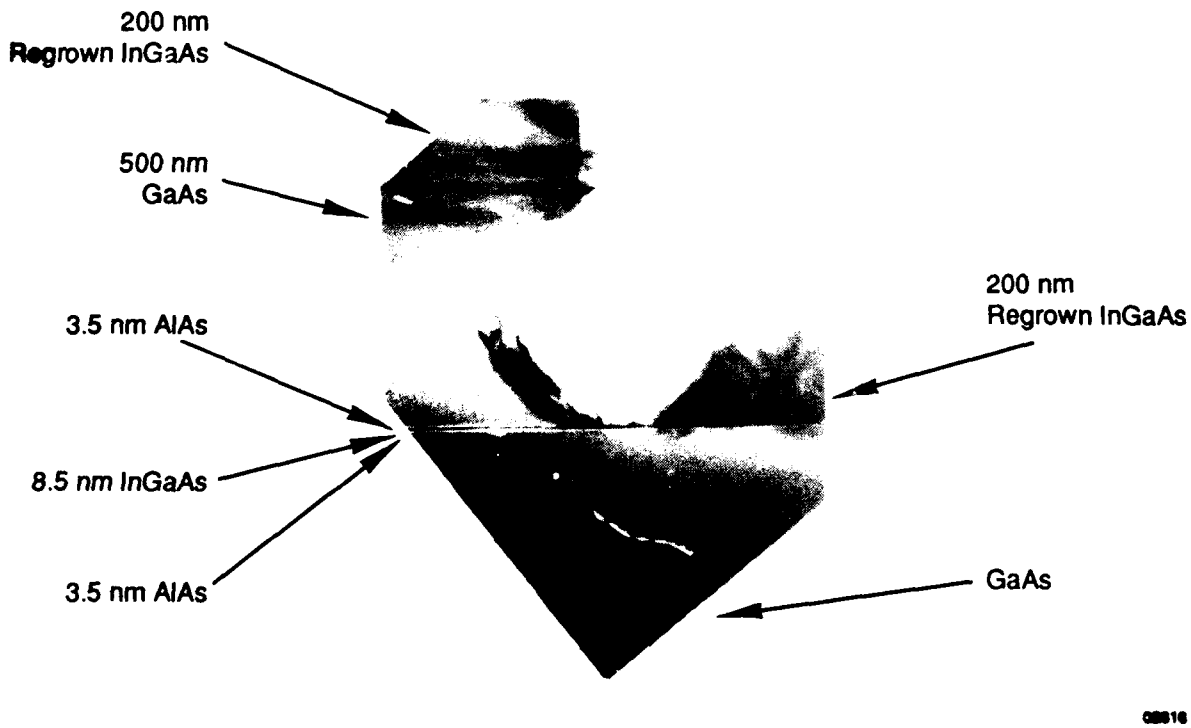


**Figure 49**
**Cross-section TEM of selectively etched (RIE) and regrown QuESTT structure.**

base contact. Although we were not able to fabricate successful QuESTTs in this way, we consider the approach to be a good one that could eventually succeed. We terminated this approach, however, in favor of developing RTTs in the InGaAs/AlAs/InAlGaAs system, which avoids regrowth processing.

Another approach to etching and regrowth was also attempted. The technique was first reported by workers at IBM.[45] The technique involved a thermal etch in an MBE chamber. A patterned wafer is placed in an MBE chamber. At 750°C with an As flux (similar to that used for growth), GaAs sublimes at approximately 1 μm/hr. For the same conditions, AlGaAs has a very low etch rate and, therefore, maybe used as an etch mask and/or etch stop. After etching (sublimation), the sample may be regrown without leaving the UHV chamber.

We determined in our own experiments that, at 750°C while maintaining an As flux similar to that used for GaAs growth, the GaAs/AlGaAs etch ratio is at least 100:1. We have demonstrated that we may stop on a layer of 40 percent AlGaAs as thin as 5 nm.

Figure 50 is a TEM cross-section of an etched and regrown sample. The original epitaxial structure consisted of a 100-nm AlGaAs cap layer, 500-nm GaAs layer, a 5-nm AlGaAs layer, 5-nm GaAs quantum well, and 200-nm AlGaAs layer on a GaAs substrate. A portion of the AlGaAs cap layer was patterned and chemically etched before reinserting in the MBE chamber. In the MBE chamber, 500 nm of GaAs was etched down to the 5-nm AlGaAs etch stop. Subsequently, 500-nm of GaAs was regrown.

Figure 50 shows that the material regrown in the etched portion of the sample (on the left) appears to be quite good with few defects despite the existence of a large number of inclusions at or near the regrowth interface. Furthermore, the sidewall coverage is excellent.

**Figure 50**
**Cross-section TEM of selectively etched (thermal MBE) and regrown QuESTT structure.**

On the other hand, higher magnification micrographs showed some penetration of the 5-nm AlGaAs layer, and a general roughness to the heterostructure interfaces that could be caused by diffusion resulting from the extended time at 750°C. This diffusion is a serious problem that could destroy the resonant tunneling behavior. We have just completed an experiment that has subjected RTDs to a wide range of thermal cycles. The data suggested that an extended time at 750°C should not seriously degrade tunneling performance.

While these results were encouraging and appeared to provide a possible path for QuESTT fabrication in the GaAs-based compounds, this approach was also abandoned when we switched over to the InP material system.

### *b. Other processing details*

The initial work on BiQuaRTTs and QuESTTs in the GaAs material system was accomplished with a mask set designed before the start of this contract. Based on experience with the older mask set, new mask designs were improved to minimize processing difficulties and add new test structures. Similar to the previous set, these masks were designed to produce discrete devices that have not been optimized for high-frequency operation. Eighteen different discrete devices were included on each die. The principal variations were in emitter size and base-to-emitter spacing. Three of the transistors employed circular rather than rectangular geometries. The first operational BiQuaRTT devices produced under this contract used this mask set.

In designing these devices, fairly conservative design rules were employed. No features smaller than 2 micrometers were included. The most demanding placement accuracy required is ±0.5 micrometer while most devices require no better than ±1.0 micrometer. While the contact alignment tools available in our laboratory are capable of considerably better performance than these figures, the practice of using a quarter or even smaller portion of a wafer (because of limited quantities of good epitaxial material) produces resist build-up on edges, particulates from cleaved edges, and mask bow during contact. All these factors make good contact and alignment considerably more difficult than on entire wafers. For these conditions, we believe our design rules were appropriate.

To provide the minimum distance from the low-resistance base contact to the tunneling areas of the device, the base contact was designed as an annulus that surrounds the emitter contact. This topology requires that a metal lead to the emitter contact cross over the base contact region. Although this arrangement has its problems, we believe that minimizing base resistance is a more significant issue. Different spacings between the emitter and base contacts have been used in different devices.

The emitter contact is an n-ohmic contact to a degeneratively doped n-type layer. We used a wide range of emitter sizes in our different devices. The emitters were square ranging from 3 micrometers on a side to 30 micrometers. Measurements on large test structures demonstrate good-quality ohmic contacts.

The collector layer is below the quantum-well. The emitter layer and quantum well structure must be etched away before the collector contact metal can be applied. With the previous mask set, the same layer was used for both etching and metal deposition. While this may be an acceptable process, it is possible for some of the metal to be deposited on the sidewalls of the etch trench, which would provide a short between the emitter and collector.

We have, therefore, employed separate mask levels for collector etching and collector contact where the contact metal layer fits easily inside the etched region, thereby avoiding the possibility of the aforementioned short.

The collector contact region is adjacent to three sides of the base annulus. One side is left open to permit metal runs to contact the base and emitter without crossing the collector trench and metal contact. The collector contacts are made to heavily n-doped GaAs and use the same type of metallization as in the emitter contacts. Again, we have measured good-quality ohmic contacts.

Three different base-to-emitter spacings are used in the mask set for different devices. If misalignment causes the etch pattern to expose emitter or base metal, the isolation etch is difficult to control. The largest spacing is 7 µm where a 3-µm-wide etch annulus has a 2-µm space between it and the emitter on one side and another 2 µm between the etch area and the base implant pattern. A 5.5-µm base-emitter spacing uses a 2.5-µm etch width and 1.5-µm spacing. The smallest base-emitter spacing is 4-µm where a 2-µm etch width has 1-µm spacing. This smallest spacing creates the most challenging alignment of our process, but also creates the lowest base resistances. The widest spacing ensures that some of the devices will be processed with no alignment problems.

After the metal contacts are formed and isolation etch is completed, deep trenches are etched down to the semi-insulating substrate to provide device-to-device isolation. A passivating silicon nitride layer is deposited over all devices. Contact vias are etched down to all devices, and a metal bond pad layer is patterned.

The mask set includes several test structures besides the isolation etch structure mentioned: seven different transmission line structures that measure the sheet resistivity of and contact resistance to different layers, several large transistors for checking devices before final metal deposition and bonding, a C-V measurement structure, a set of RTD structures, a Hall bar for measuring quantum-well conduction, a final metal step coverage test, and a test structure to measure contact via and nitride passivation quality.

## 2. Fabricating InGaAs/AlAs/InAlGaAs RTTs

### *a. Contact to Quantum Well and Isolation*

The ability to form nonalloyed ohmic contacts of both n- and p-type allows for a much simpler approach to fabricating RTTs. Both bipolar and unipolar RTTs were fabricated by simply etching down to the base layer and depositing metal directly on the base to make nonalloyed contacts. This approach is not possible in the GaAs material system because of the need to alloy the contacts, which would form alloy "spikes" and short the base to the collector.

The basic process for RTT fabrication is the InGaAs/AlAs/InAlGaAs system is as follows. The emitter contact is defined by metal lift-off. The entire surface is etched down to the base layer. Base contacts are lifted off. The sample is etched further to reveal the collector contact layer and metal contacts are lifted off. Note that this process provides a means of directly contacting the base and excellent base-to-emitter isolation.

A difficult part of this process is the requirement of etching down through several hundred nanometers and stopping on a base layer that is a few nanometers thick. Using a

scanning tunneling microscope, we have determined that our wet etch process (1:8:160 sulfuric acid:hydrogen peroxide:water) has an average surface roughness of 25 nm after etching down 500 nm. The termination to the etch was selected by monitoring a test structure with two emitter contacts. As long as the emitter layer provides the dominant current path, there will be a simple resistive measurement. However, once most or all of the emitter layer has been etched away, the current will flow through the resonant tunneling structure and an NDR region will be apparent in the IV measurement. The onset of this signature is used as an indication that the etch has reached the base.

### *b. Other Processing Details*

For processing RTTs in the InGaAs/AlAs/InAlGaAs material system, new mask sets were designed to make use of the new processing strategy and to improve high-frequency performance and testing capabilities. The new masks allowed us to use a self-aligned fabrication process for both the BiQuaRTT and the QuESTT. This was necessary to reduce parasitic base resistance and collector-base junction area. Cascade probeable devices were also provided to facilitate microwave testing to 40 GHz and electro-optic evaluation of the device switching speed at Stanford University.

Figure 51 shows the mask layout. The cell size is 2.1 × 2.1 mm and contains 16 discrete devices comprising most of the cell area. The upper row of devices was provided for dc transport studies and uses circular transistor geometries with emitter diameters of 1, 2, 4, and 8 μm. The remaining devices were designed to minimize device parasitics for high-speed testing. Emitter stripe widths of 0.5, 1, 2, and 4 μm were used. The second and third rows of devices differ only in their bonding scheme; the second row was for common-emitter connection while the third row was for common-base testing. The bottom row of devices was arranged in a 50-ohm coplanar transmission-line geometry for on-wafer evaluation of the transistor speed. Located about the edge of the cell are test structures for process development and material evaluation.

Figure 52 shows an enlarged view of one of the coplanar transmission-line devices. The center line is 50 μm wide; the emitter dimensions are $2 \times 22$ μm$^2$. The other three coplanar transistor structures have emitter sizes of $3 \times 22$, $3 \times 10$, and $2 \times 10$ μm$^2$. Connection to the mesa devices was accomplished with an existing air bridge technology.

The mask has been designed to accommodate aligned and self-aligned processes for both the BiQuaRTT and QuESTT devices. During this mask design phase, we also developed a self-aligned base and collector process on InP. Figure 53 is a scanning electron micrograph of the self-aligned transistor geometry showing successful realization of the self-aligned emitter-base and base-collector metallizations. The lower half of the figure is the device cross section.

## 3. Electron-Beam Processing of RTTs

We also made use of electron-beam (e-beam) lithography to process RTTs. The e-beam instrument used is a Philips EBPG-4HR. We did not pursue extremely small geometries. The smallest features were 0.5 μm. However, we did take advantage of the overlay alignment accuracy of this instrument, which is better than 80 nm three-sigma. This excellent alignment capability allowed us to use closely spaced geometries, which would have been impractical with our optical exposure tools.

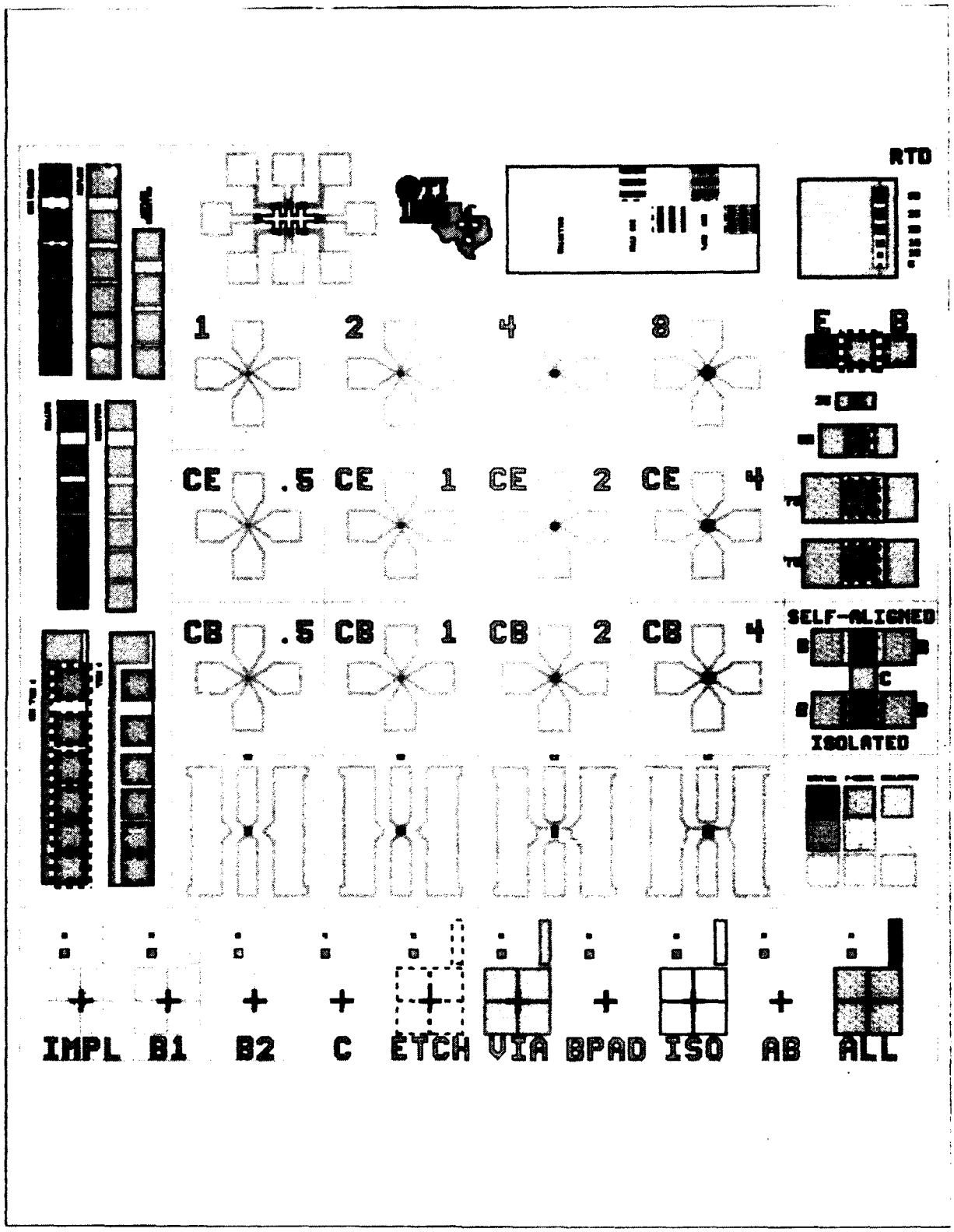


**Figure 51**
**Mask set for fabricating RTTs on InGaAs/AlAs/InAlGaAs.**

Exposures were typically done with a 50-keV electron beam using polymethylmethacrylate as a resist, with different resist thicknesses used depending on the particular process. A 0.25-μm spot size was used for large features and a 0.1-μm spot size was used for small features. Resist development was accomplished with a 1:1 mixture of MIBK and IPA.

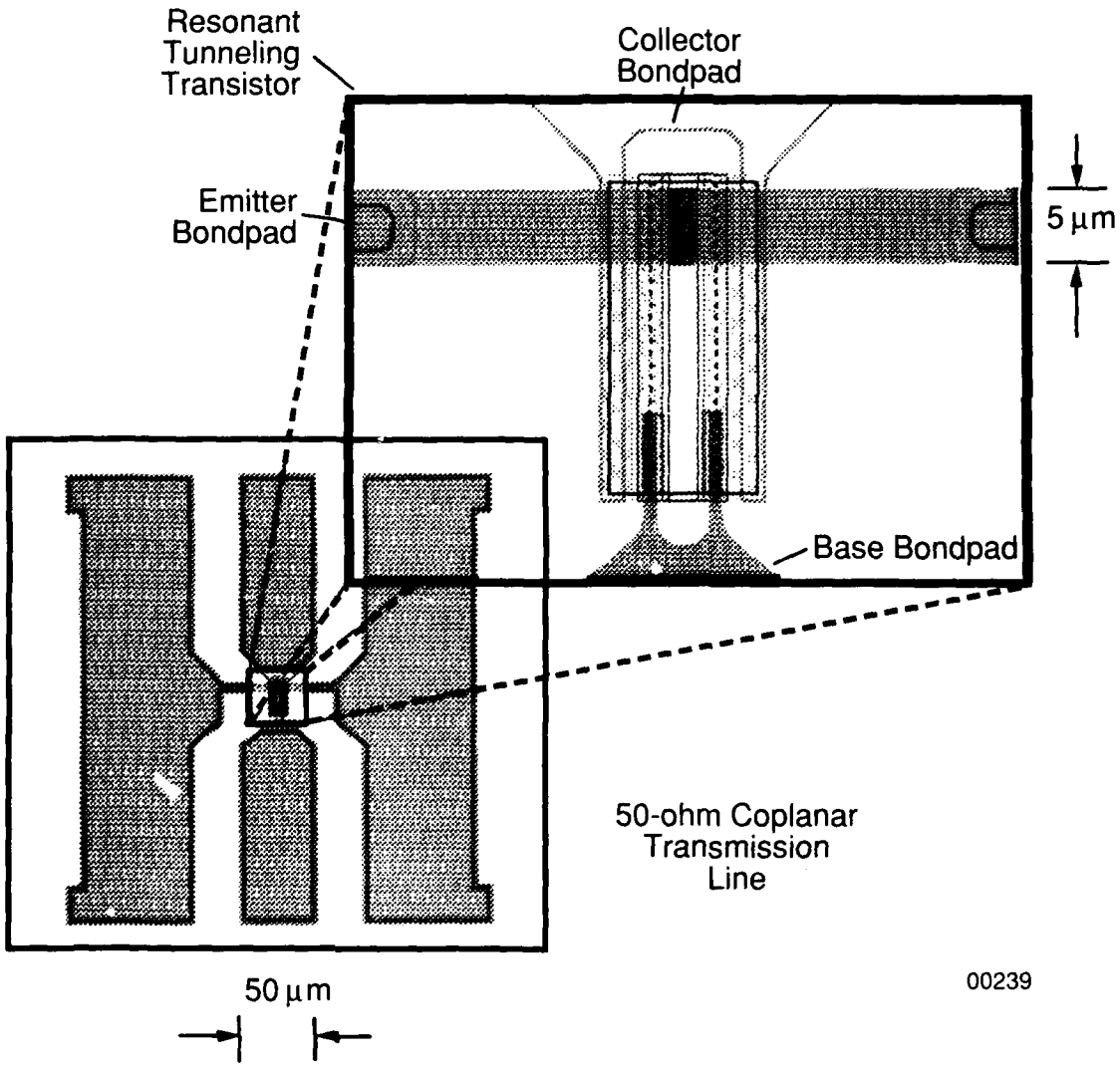


**Figure 52**
**Coplanar transmission-line transistor layout.**

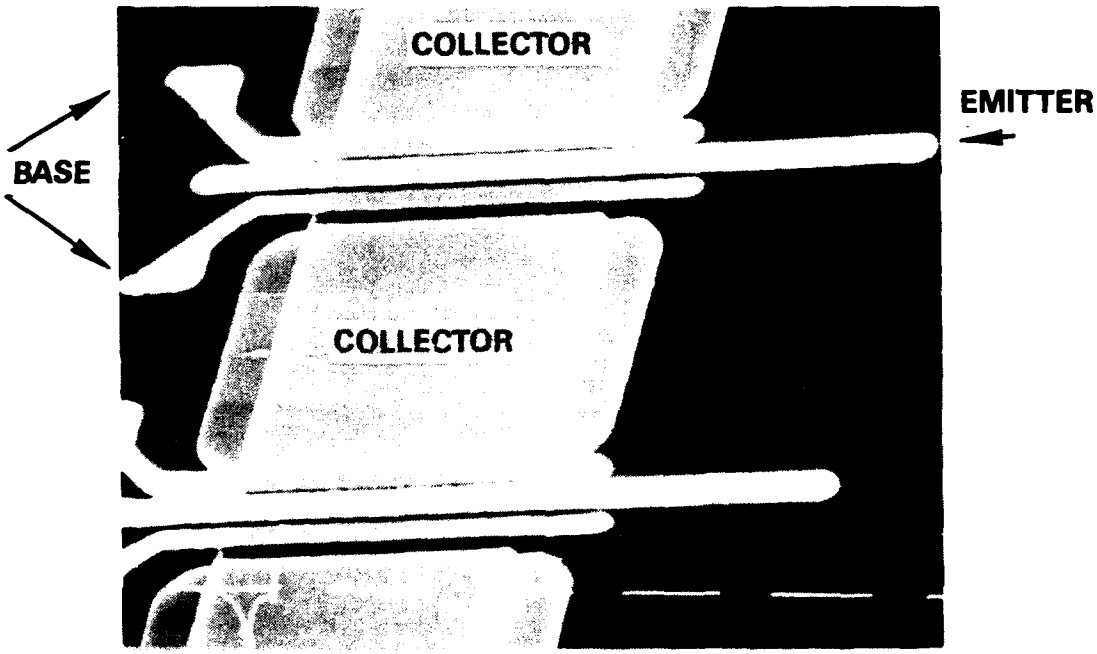


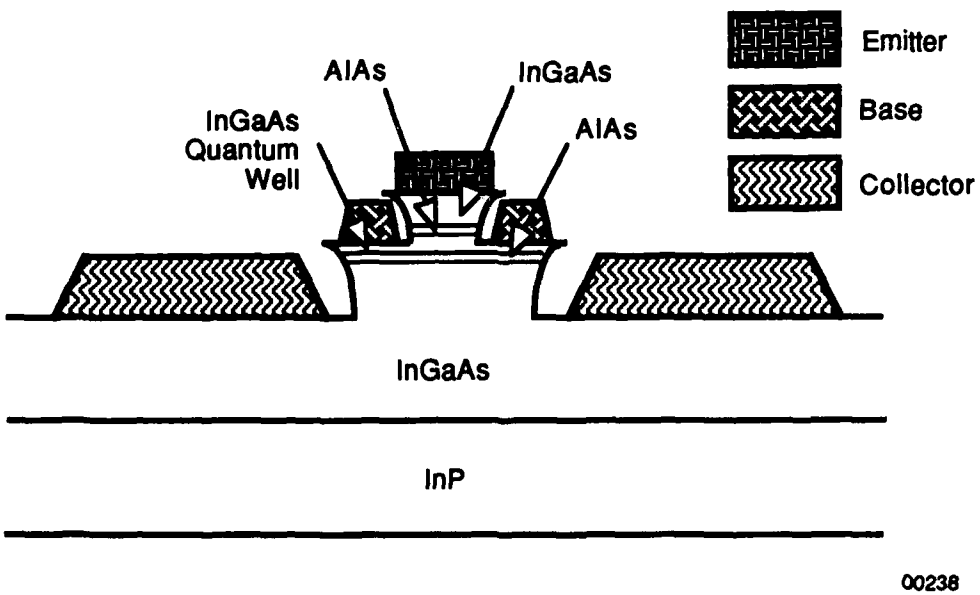


**Figure 53**
**Self-aligned process for InGaAs/AlAs/InAlGaAs-based RTTs.**

# SECTION IV

# MANUFACTURING ISSUES

We have not only developed an accurate BiQuaRTT/QuESTT modeling package to guide the development of transistor results, but have compared this type of model to straightforward resonant tunneling diode structures (under a separate ONR contract). The electrical characteristics of a series of highly characterized resonant tunneling diode structures were modeled, and the results were in excellent agreement with our self-consistent band-bending calculation. This work has been published[46] and is included as Appendix N.

We used these models to understand the details of InGaAs RTD structures, refine our device models, and explain the IV characteristics observed. As mentioned previously, we observe very pronounced inflections in the IV characteristics before resonance. To study this more, and to determine the structural parameters important for InGaAs/InP RTDs, we grew, fabricated, and measured a series of InGaAs (on InP)/AlAs RTDs, consecutively grown. Table 6 illustrates the parameter space explored.

X-ray four-circle diffractometry was used to determine the In percentage over the 3-day growth period, which varied from 54.7 (S2) to 56.0 (S14).

Figure 54 shows a result of the study, which is the resonant peak voltage as a function of the parameters. A trend to higher resonant voltages as the spacer layer increases and as the contact doping decreases is observed, as expected. The "preresonant inflection" is observed in many of these samples. One possible explanation is that this results from a resonance between electrons in a two-dimensional emitter accumulation layer and the quantum well; thus, low-temperature magnetotransport measurements were performed. To within experimental resolution (1 mV), the structure appeared not to shift with magnetic fields up to 9T, invalidating the accumulation layer hypothesis.

Second, there appears to be significant fluctuation from sample to sample. Determining the origin of the inflection from this database is difficult with these variations. Thus, we decided to do a baseline study of variations in a better understood system, a GaAs/AlAs RTD control sample set that spanned the same spacer/doping density parameter space. A study of these samples illustrated the problem that is responsible for the previously mentioned fluctuations.

Figure 55 shows a series of I-V and G-V characteristics for a series of the GaAs/AlAs control samples, with varying doping density, at 300 K. For easy reference, we will use the GaAs/AlAs sample designations, in a structure similar to Table 6. Table 7 shows the set under consideration. The symbol x implies no existing sample.

**Table 6. Samples Used in Study of Spacer Layer/Doping Effects on IV Characteristics of InGaAs/AlAs RTDs on InP substrates**

| Contact Doping ($cm^{-3}$) | Spacer Layer Thickness (nm) | | | | |
|---|---|---|---|---|---|
| | 0 | 2.5 | 5 | 10 | 20 |
| $1 \times 10^{17}$ | S1 | S2 | S3 | S4 | S5 |
| $3 \times 10^{17}$ | S6 | S7 | S8 | S9 | S10 |
| $1 \times 10^{18}$ | S11 | S12 | S13 | S14 | S15 |

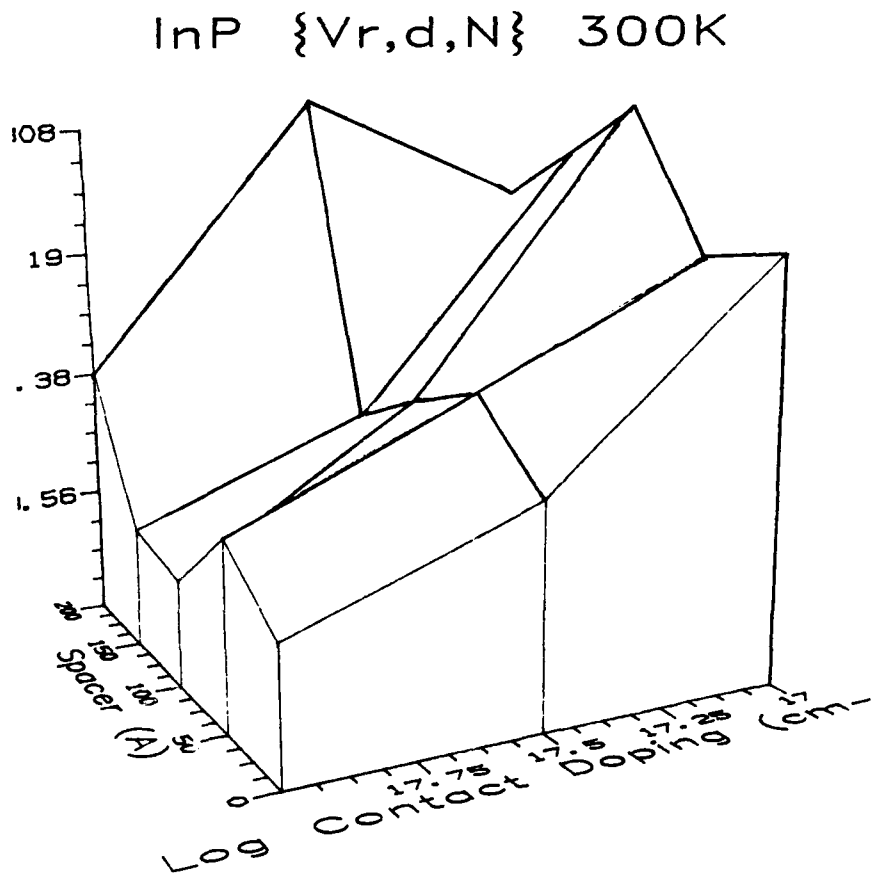


**Figure 54**
**Resonant peak voltage as function of spacer and contact doping density for InP/InGaAs RTDs, at 300 K.**

**Table 7. Samples Used in Study of Spacer Layer/Doping Efffects on IV Characteristics of InGaAs/AlAs RTDs**

| Contact Doping ($cm^{-3}$) | Spacer Layer Thickness (nm) | | | | |
|---|---|---|---|---|---|
| | 0 | 2.5 | 5 | 10 | 20 |
| $1 \times 10^{17}$ | 3197 | x | x | x | 3196 |
| $3 \times 10^{17}$ | 3206 | x | x | x | 3205 |
| $1 \times 10^{18}$ | 3215 | x | 3216 | 3209 | 3208 |

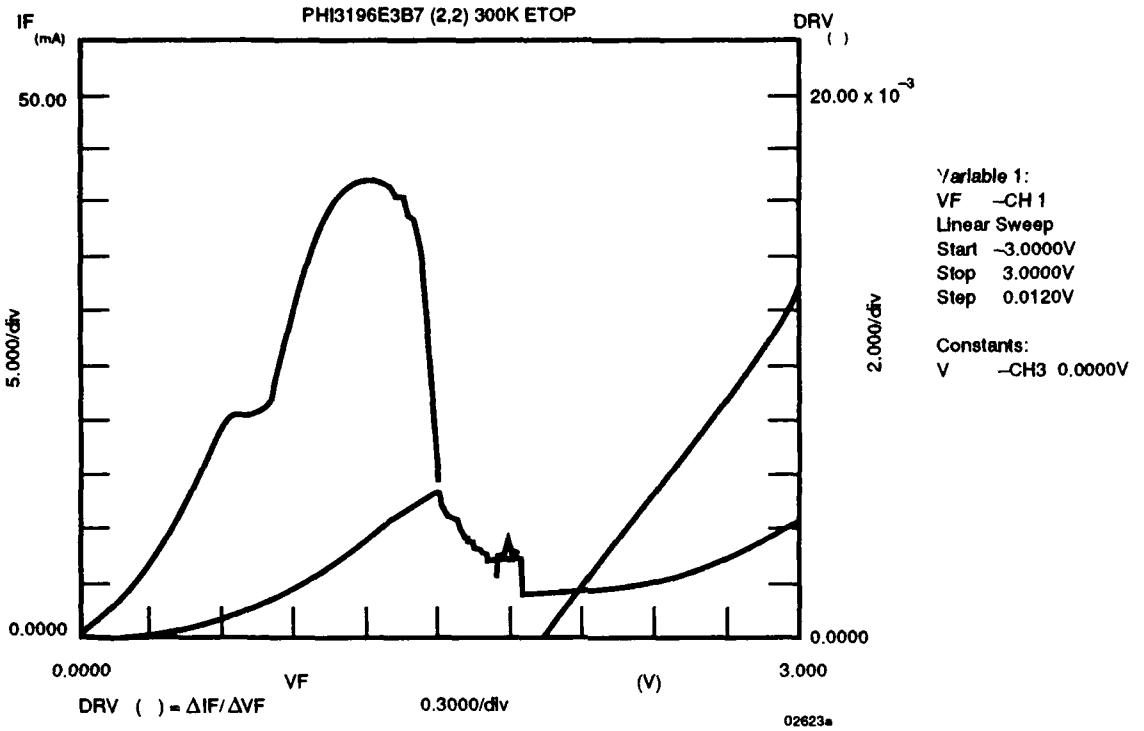


(a)

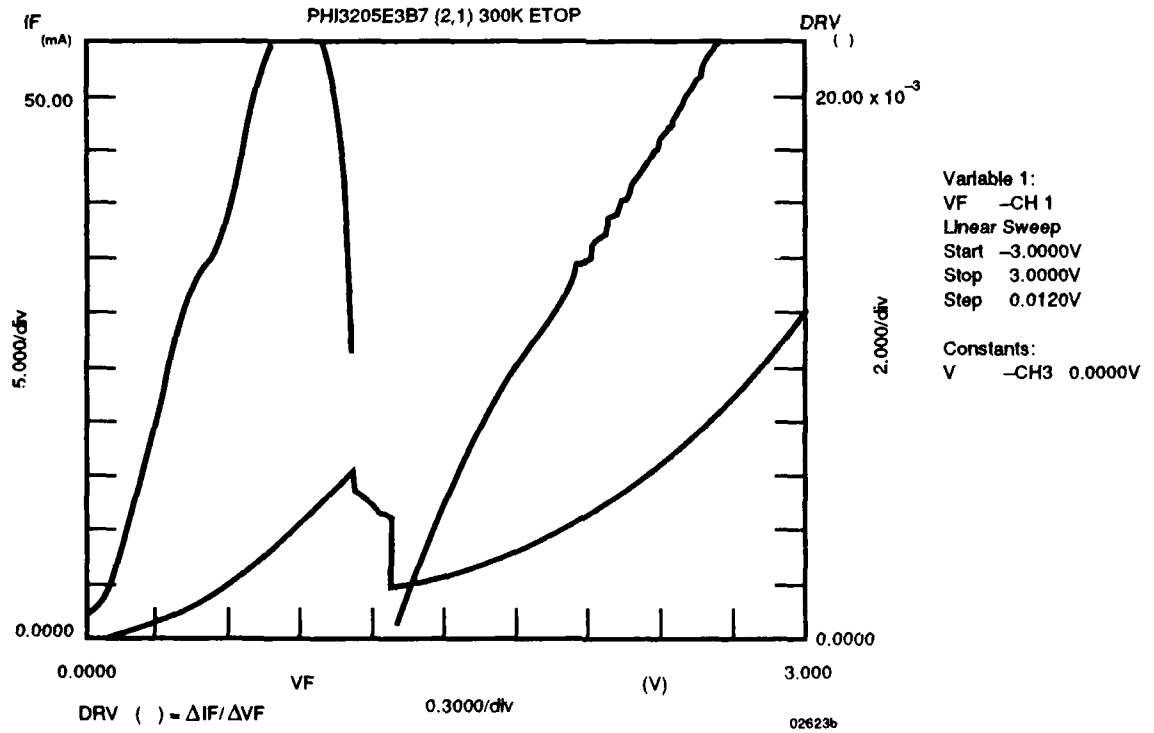


(b)

**Figure 55**
**I-V and G-V characteristics at 300K for (a) 3196, (b) 3205, and (c) 3208.**

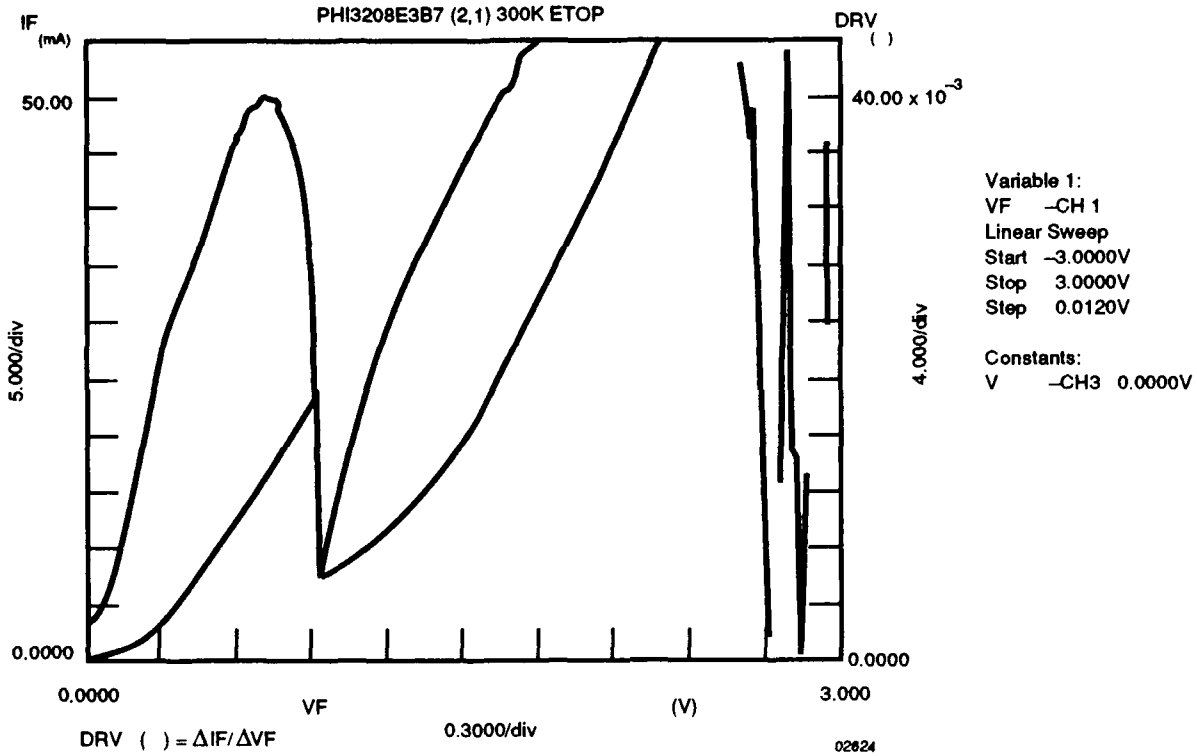


(c)

**Figure 55 (continued)**
**I-V and G-V characteristics at 300K for (a) 3196, (b) 3205, and (c) 3208.**

First, the variation of the peak voltage observed is expected: higher voltage for reduced doping. Second, the preresonant inflection is clearly present, strongest for the lowest doping density [Figure 55(a)]. Observation of this inflection in these samples implies the origin is not specific to the InGaAs system. The origin is as yet undetermined. A band structure modeling of these samples is shown in Figure 56. The accumulation notch is obviously largest in Figure 56(c), implying that the relative spacing of the inflection voltage to resonant voltage should increase from Figures 56(a) through 56(c). Actually, it appears to be constant, if not decreasing. In addition, the inflection decreases with decreasing temperature; e.g., see Figure 57 (77 K).

While collecting these data, the variation from sample to sample was carefully monitored to illuminate the origin of the fluctuations. Figure 58 shows a slice map of the resonant tunneling voltages (a), peak (b) and valley (c) currents, positive (a-c) and negative (d-f), for 1/4 of the 2-inch sample 3208. Figure 58(a) illustrates the problem—variation in the structural parameters shifts the resonant voltage by nearly a factor of 2. Likewise, the peak current [Figure 58(b)] varies by nearly the same amount. We have previously pointed out that such variations can be accounted for by quantum-well and tunnel-barrier thickness variations.[46] Studies of the lateral doping fluctuations show insignificant variations. Thus, sample-to-sample comparisons will always be suspect unless the variations can be quantified. Notice that both the quantum well and tunnel barriers appear to "thin" from the slice center (0,0) to the outside rim (a total of approximately 100 data points).

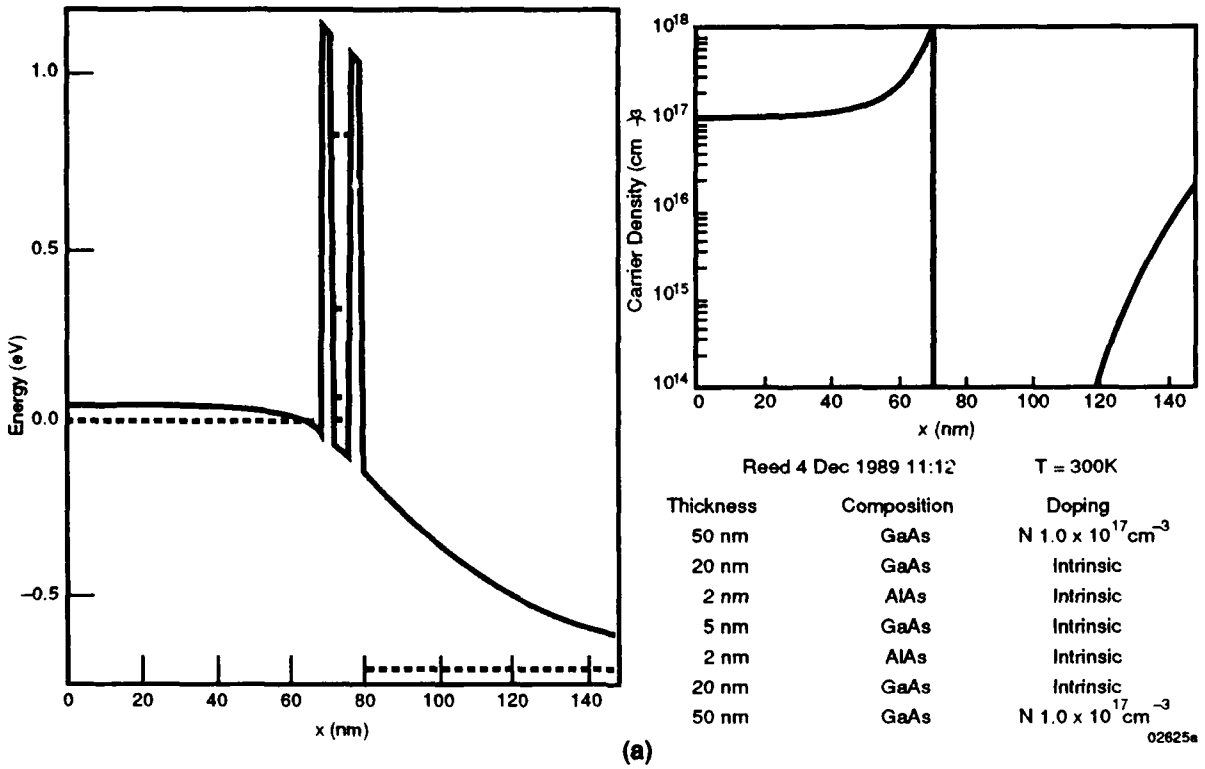


(a)

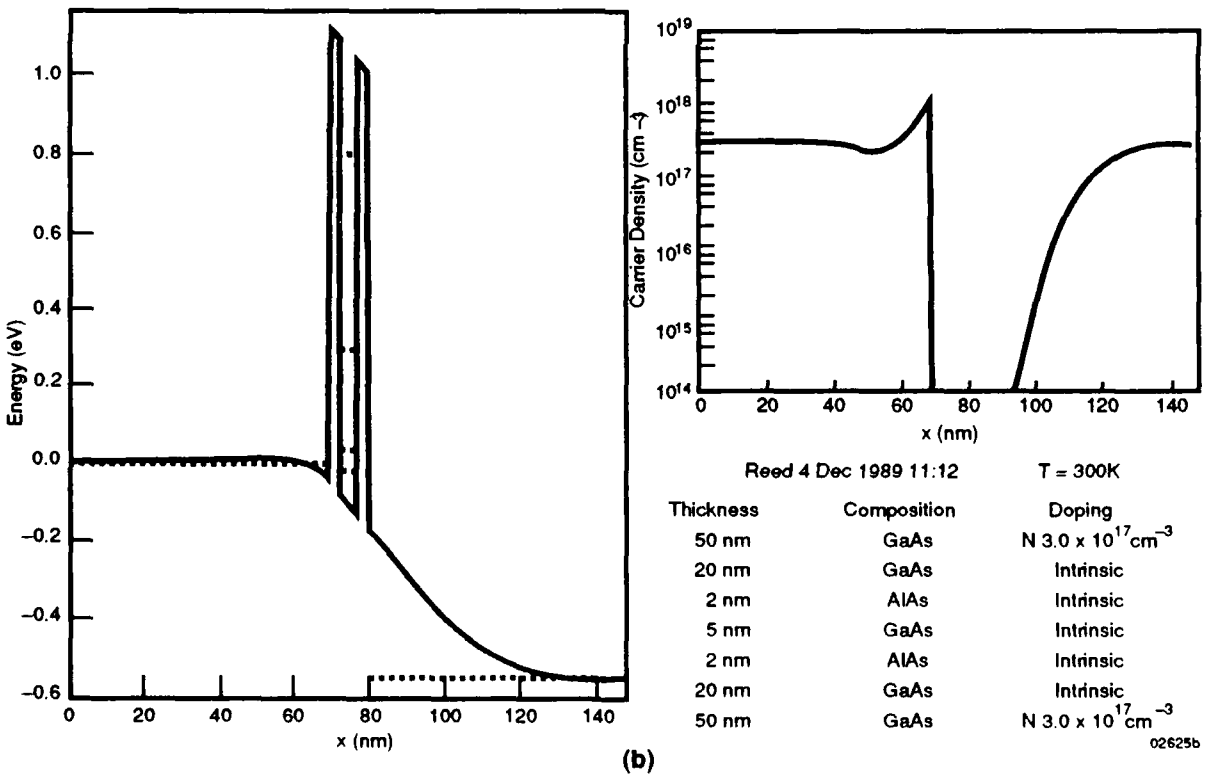


(b)

**Figure 56**
**Band structure calculations for samples (a) 3196, (b) 3205, and (c) 3208.**

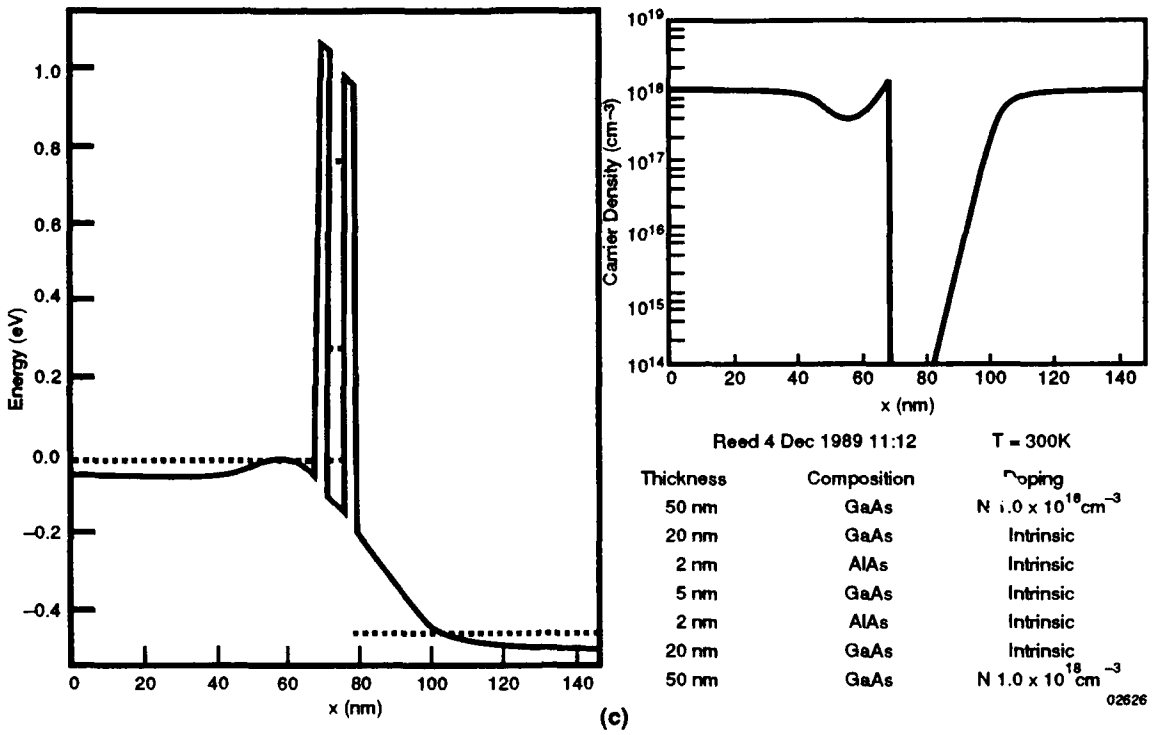


**Figure 56 (continued)**
**Band structure calculations for samples (a) 3196, (b) 3205, and (c) 3208.**

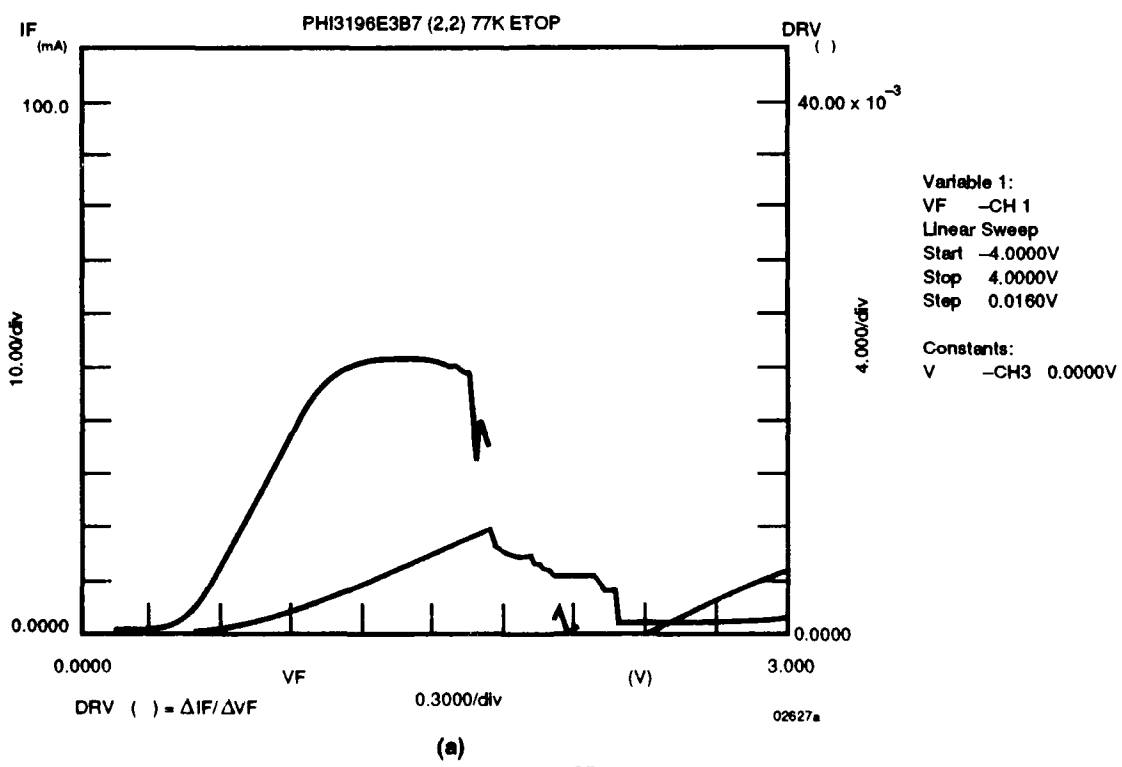


**Figure 57**
**I-V and G-V characteristics at 77 K for samples (a) 3196, (b) 3205, and (c) 3208.**

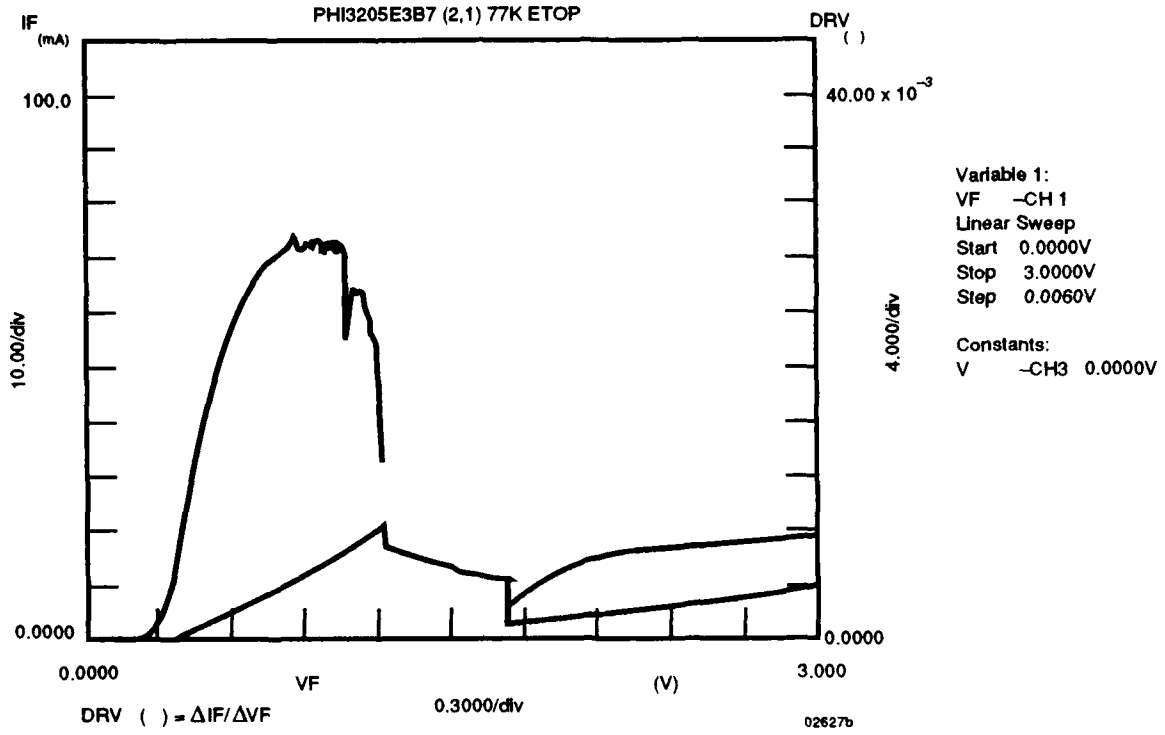


(b)

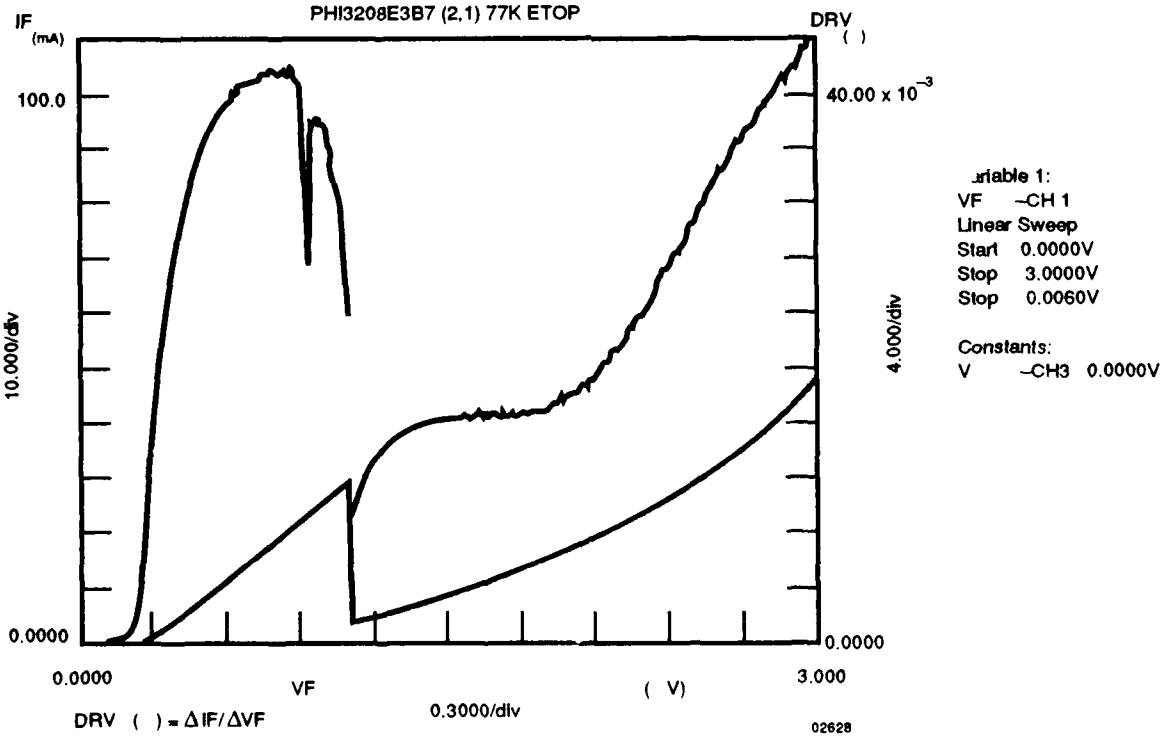


(c)

**Figure 57 (continued)**
**I-V and G-V characteristics at 77 K for samples (a) 3196, (b) 3205, and (c) 3208.**

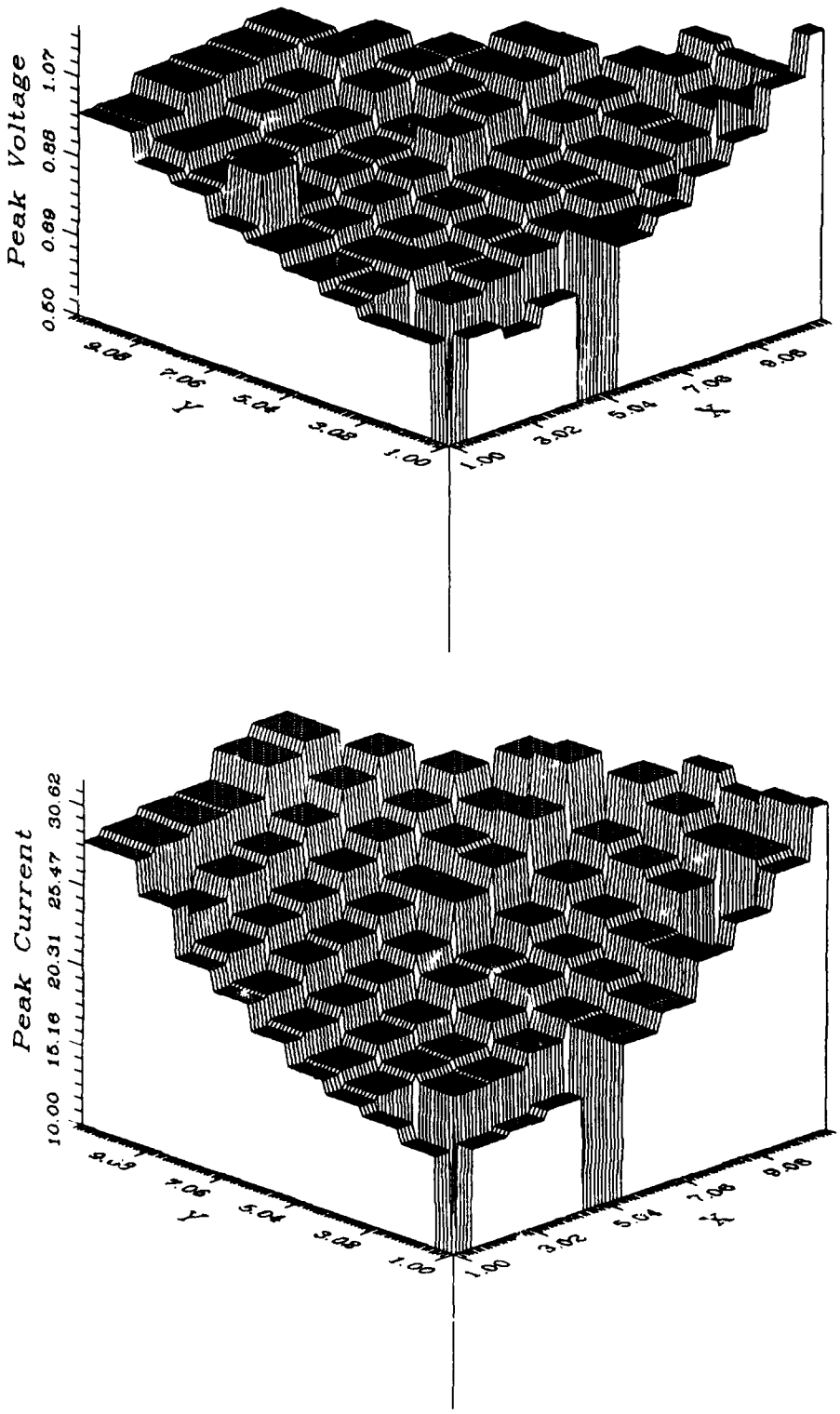


**Figure 58**
**Slice map of (a) positive resonant tunneling voltages, (b) positive peak current, (c) positive valley current, (d) negative resonant tunneling voltages, (e) negative peak current, and (f) negative valley current for sample 3208. The x and y axes are 0 to 1 inch along (100) directions (for 11 devices), with position (0,0) being slice center. T=300K.**

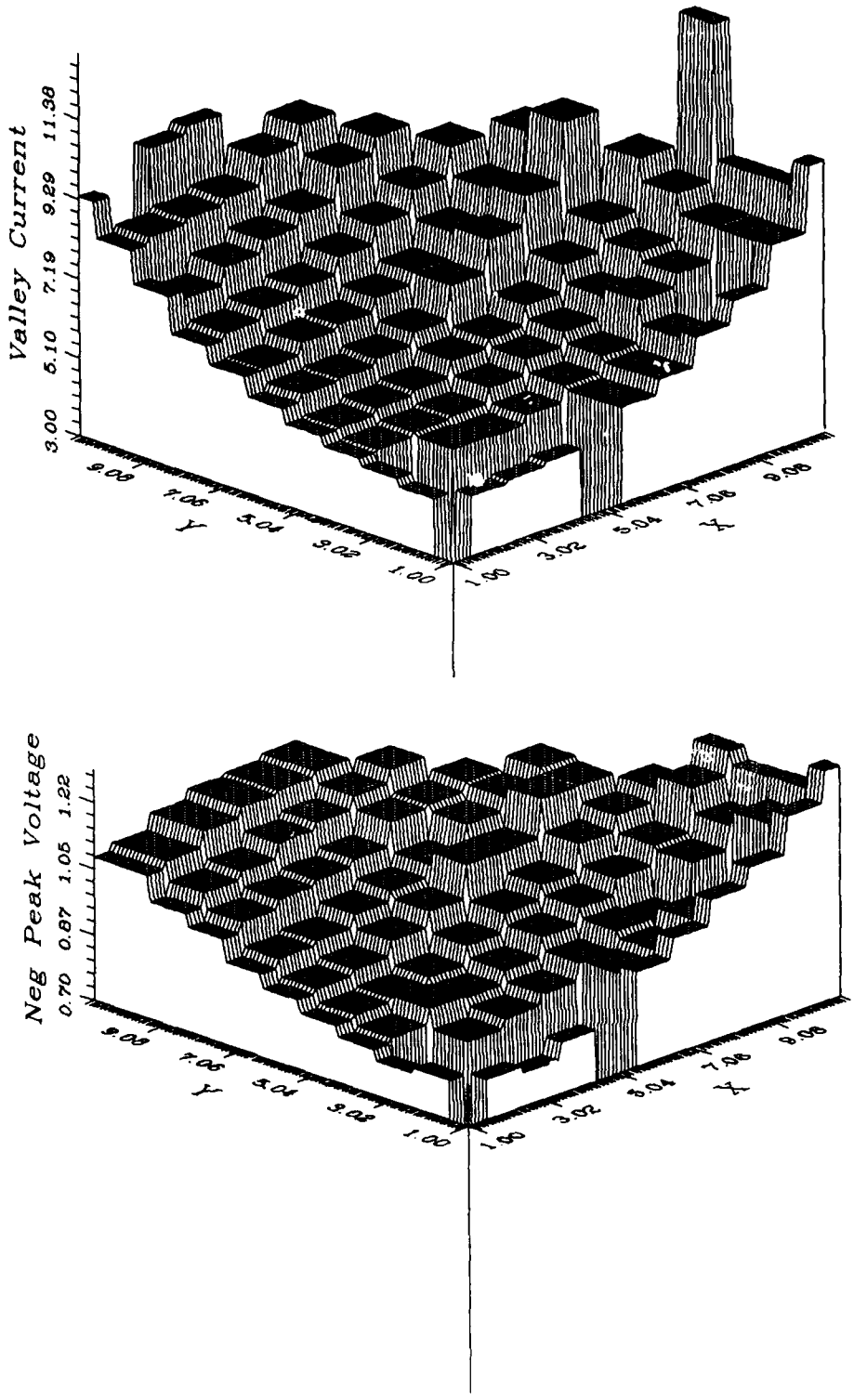


**Figure 58 (continued)**
**Slice map of (a) positive resonant tunneling voltages, (b) positive peak current, (c) positive valley current, (d) negative resonant tunneling voltages, (e) negative peak current, and (f) negative valley current for sample 3208. The x and y axes are 0 to 1 inch along (100) directions (for 11 devices), with position (0,0) being slice center. T=300K.**

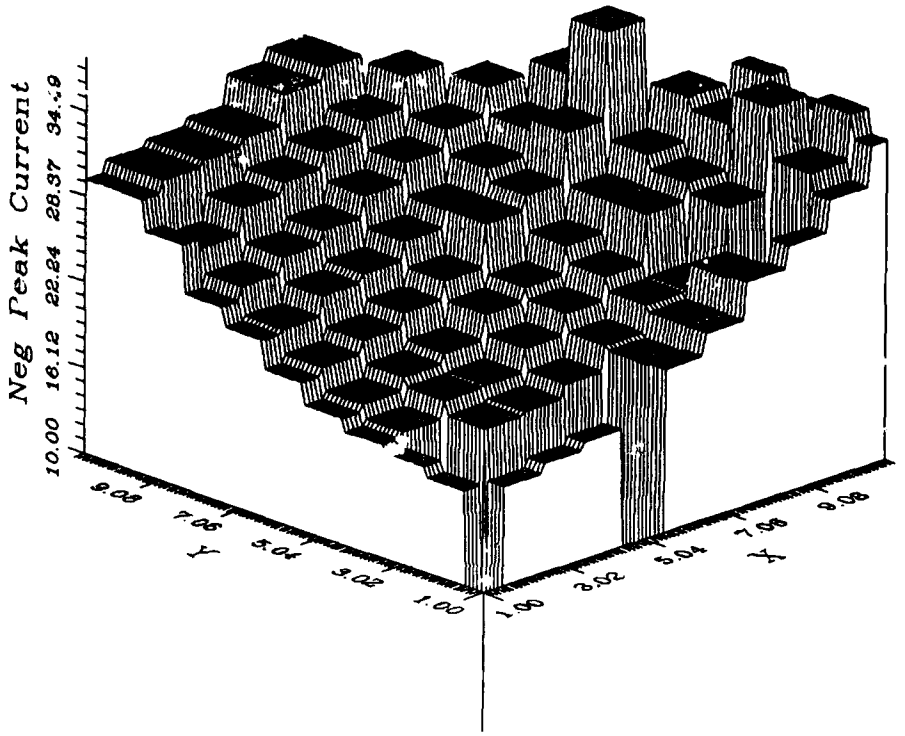


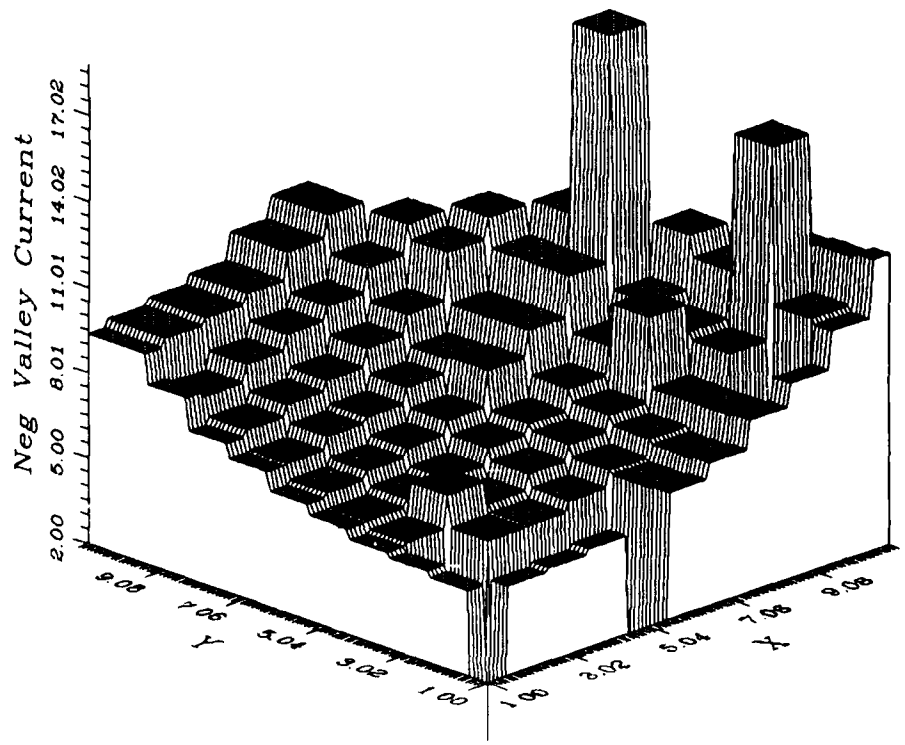


**Figure 58 (continued)**
**Slice map of (a) positive resonant tunneling voltages, (b) positive peak current, (c) positive valley current, (d) negative resonant tunneling voltages, (e) negative peak current, and (f) negative valley current for sample 3208. The x and y axes are 0 to 1 inch along (100) directions (for 11 devices), with position (0,0) being slice center. T=300K.**

To quantify this variation, we have found that a quadratic ($a + br^2$) provides reasonable fit data sets of each of the structures (as a function of r). Figure 59 shows such a fit to Figure 58(a). Tables 8 and 9 show the coefficients of these fits. The trends to lower $V_n$ with increased doping and decreased spacer (III) are evident, as well as the current density variations. The full data set can be found in Appendix O.

It is clear from this study that the inherent fluctuations in (at least, MBE-grown) RTDs give fluctuations of about a factor of 2 in resonant voltage. This is because of a "lever-arm" effect (Figure 60): the majority of the voltage is dropped across the downstream depletion layer. The impact this has on resonant tunneling device integration is severe—the resonant tunneling voltage "threshold" (i.e., NDR voltage) of a diode cannot be controlled up to a factor of $\sim x^2$.

At first glance, this study would seem to imply that RTT integration is not possible. On the contrary, it underscores the necessity for transistors where the quantum well is directly contacted and modulated independently (or nearly independently) of the contact regions. Device concepts such as the BiQuaRTT and QuESTT will work, since they do this; transistors that are essentially series combinations will suffer from this limitation.

Returning to the original motivation for this study, InP RTDs: the variations in the set {S(i)} are caused by the same problem. However, this set was grown on small pieces of InP substrates (because of the prohibitive cost of 15 InP substrates); thus, the respective orientations of the samples with respect to substrate and beam flux centers are not known.

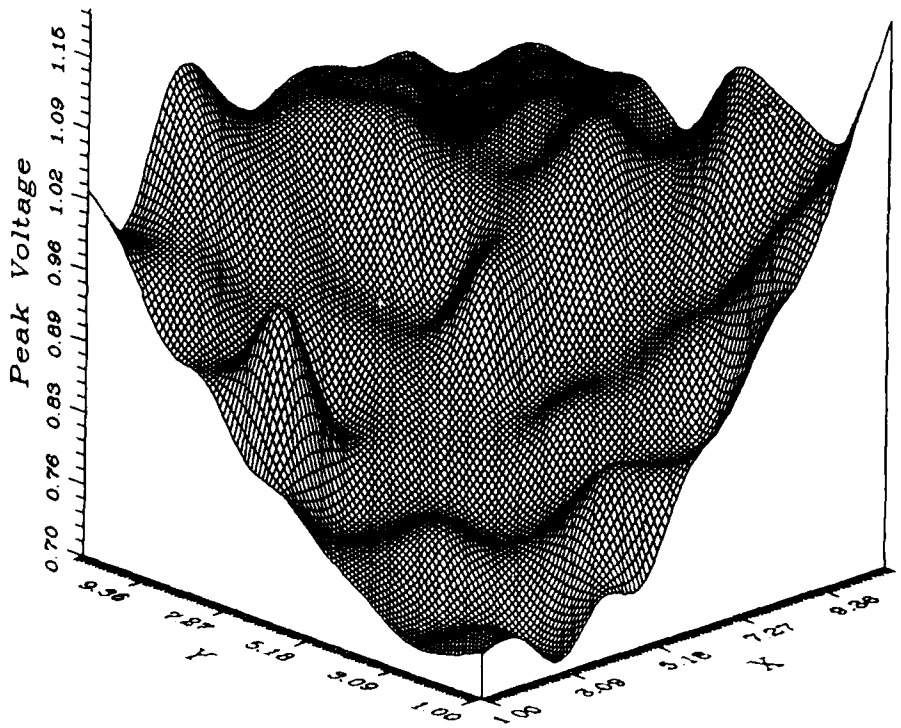


**Figure 59**
**Contour plot fit to Figure 58(a).**

**Table 8. Fit to Spatial Maps, Resonant Voltage $V_r$**

(Format: positive (negative), top number intercept (a), bottom number curvature (b).

| Contact Doping ($cm^{-3}$) | Spacer Layer Thickness (nm) | | | |
|---|---|---|---|---|
| | 0 | 50 | 100 | 200 |
| $1 \times 10^{17}$ | 1.04 (1.16)<br>0.007 (0.008) | x | x | 1.28 (1.55)<br>0.007 (0.007) |
| $3 \times 10^{17}$ | 0.855 (1.10)<br>0.012 (0.011) | x | x | 0.880 (970)<br>0.008 (0.012) |
| $1 \times 10^{18}$ | 0.625 (0.925)<br>0.006 (0.012) | 0.670 (0.750)<br>0.003 (0.004) | 0.490 (0.570)<br>0.003 (0.004) | 0.730 (0.800)<br>0.004 (0.005) |

**Table 9. Fit to Spatial Maps, Peak Current $I_p$ and Valley Current $I_v$.**

(Format: peak/valley, positive (negative); top set intercept (a), bottom set curvature (b).

| Contact Doping ($cm^{-3}$) | Spacer Layer Thickness (A) | | | |
|---|---|---|---|---|
| | 0 | 5 | 10 | 20 |
| $1 \times 10^{17}$ | 9.0/3.0<br>(9.6/3.2) | x | x | 9.4/2.95<br>(11/3.7) |
| | 0.090/0.038<br>(0.100/0.054) | | | 0.070/0.041<br>(0.100/0.054) |
| $3 \times 10^{17}$ | 8.15/3.55<br>(10.64/4.91) | x | x | 10.1/3.1<br>(10.4/3.32) |
| | 0.018/0.022<br>(0.045/0.040) | | | 0.075/0.034<br>(0.093/0.045) |
| $1 \times 10^{18}$ | 13.6/7.2<br>(20.9/12.0) | 24.8/9.7<br>(28.2/12.2) | 10.1/3.3<br>(11.1/3.85) | 15.9/4.6<br>(16.6/5.00) |
| | 0.78/0.075<br>(0.185/0.195) | 0.180/0.095<br>(0.195/0.135) | 0.105/0.045<br>(0.125/0.055) | 0.140/0.065<br>(0.148/0.070) |

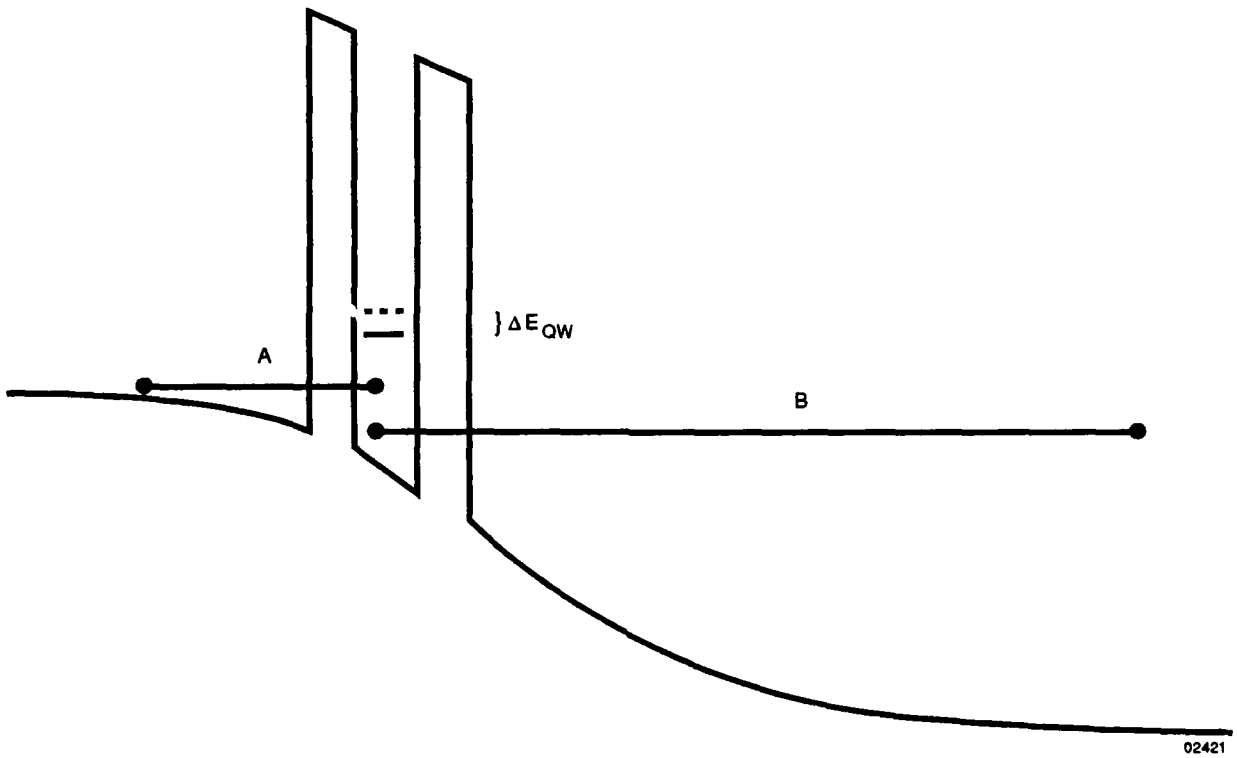


**Figure 60**
**Origin of large fluctuations in RTD resonant voltage. Structural variations causing quantum-well energy-level fluctuations ΔEqw cause voltage fluctuations β/α ΔEqw.**

# SECTION V

# HIGH SPEED RESONANT TUNNELING DIODE CIRCUITS (STANFORD UNIVERSITY)

## A. INTRODUCTION

Resonant Tunneling Diodes (RTDs) have superior high-frequency characteristics that are attractive for high-speed applications. As RTDs have terminal characteristics very similar to the Esaki tunnel diode, these new tunneling devices can also be used in the current high-speed applications of the Esaki tunnel diode.

RTDs have many advantages over Esaki tunnel diodes: their speed, for example. The RTD pulser-circuits we have recently fabricated and tested have switching times of 6 to 10 ps whereas Esaki tunnel diodes have switching times of only 20 ps.[47,48,49] In addition, Esaki tunnel diode circuits must be built from discrete parts, while we have developed a fabrication process for a monolithic RTD integrated circuit. By replacing Esaki tunnel diodes with RTDs, we can achieve both faster and simpler circuits.

In the 1960s, many ideas were proposed for using the Esaki tunnel diode. With the advent of the transistor, which has superior characteristics and IC capabilities, most of these ideas were never realized. A few of the remaining applications using the tunnel diode include high-frequency detection, oscillators, pulse formers, and trigger circuits. RTDs have already outperformed the tunnel diode in high-frequency oscillator applications. A group in MIT Lincoln Laboratories has recently reported oscillations up to 420 GHz using RTDs,[50] compared with a 40-GHz operation frequency for the best tunnel-diode oscillator.

We have focused our work on switching applications of RTDs. First, we built pulse-forming structures and demonstrated very fast switching transition times. Then, we used RTDs in trigger circuit applications up to 60 GHz. Our circuits outperformed both tunnel-diode trigger circuits and tunnel-diode pulse formers by a factor of 3.

## B. PULSE FORMING WITH RESONANT TUNNELING DEVICES

Under an ONR/SDI contract, RTD pulse-forming structures have been studied and fabricated.[47,48] A major achievement in this contract was the development of a proton implanted process for resonant tunneling diodes that provided device isolation and allowed fabrication of low-loss transmission lines (Figure 60). Pulse-forming structures were fabricated monolithically on chip. Based on the circuit parameters for these devices, minimum switching times on the order of 5 ps were expected. The structures were electro-optically sampled and a minimum switching time of 10 ps was measured. Larger-area devices were optimally matched to the switching load and should have achieved the predicted minimum switching time. However, these devices dissipated in excess of 3 mW/μm$^2$ and melted at the resonance voltage. The devices used a 70-nm space layer, which shifted the resonance voltage out to 2.5 volts and was responsible for the high power dissipation.

To avoid heating problems, new devices were grown with 35-nm spacer layers. The resonance voltage for the second generation of devices was 1.5 volts, and power dissipation was significantly reduced. With the first-generation devices, a maximum current of 33 mA

was achieved; with the second-generation devices, a maximum current of greater than 70 mA was achieved. Pulse-forming structures were again fabricated monolithically on chip.

Device circuit elements were determined by S-parameter measurements. Measured and predicted S-parameter results at three different bias points are shown in Figure 61. The theoretically predicted circuit elements were not varied for best fit to the data. Instead, each element was calculated independently. The device series resistance was estimated from on-wafer transmission-line structures and known resistivities of GaAs. The device capacitance was calculated from the buffer layer and the barrier specifications in the growth. The small-signal device resistance was estimated by the best linear fit to the I-V curve at each bias point. The close match between the predicted S-parameters and the measured results indicates that the simplest diode circuit model adequately describes the device.

From the S-parameter measurements and the switching models developed previously, these devices were estimated to have a minimum switching time of 4.5 ps. A 2-GHz sine-wave signal was applied to the input of a switching circuit, and a typical output switching waveform is shown in Figure 62. Switching times measured for these devices ranged from 6 to 10 ps.[51]

Calculations based on the device physics and circuit modeling for resonant tunneling diodes indicate that the minimum switching time achievable for any resonant tunneling diodes is on the order of 4 to 5 ps. The second generation of devices switches within 1.5 ps of the theoretical limit. The discrepancy between theory and measurement is probably the result of jitter in device switching. Further device generations will probably not significantly decrease switching time.

## C. RTD TRIGGER CIRCUITS

The principles of a trigger circuit are explained in a paper by Arpad Barna.[52] A device used as a threshold detector must have two threshold levels and hysteresis. The hysteresis differentiates this circuit from a limiter in which the output is continuous. It eliminates the output fluctuations caused by noise when the input reaches the threshold level. This type of circuit can be realized in two ways: as a Schmitt trigger using transistors, or as a trigger circuit using Esaki tunnel diodes. In terms of speed, Esaki tunnel diode trigger circuits are superior to Schmitt triggers. At present, 20-GHz Esaki tunnel diode trigger circuits have been introduced commercially, while Schmitt triggers are used in scopes with maximum bandwidths of 1 GHz.

Trigger performance is limited by the switching time and timing jitter or phase noise of the device. A paper by Donald E. Nelsen[53] discusses the study of the timing jitter of Esaki tunnel diodes. Application of his results to our RTDs gives an expected timing jitter less then 0.5 ps. Our microwave sources, however, have comparable timing jitter and, thus, not enough resolution to directly measure circuit phase noise. Using an indirect method, we plan to measure the jitter characteristics of our circuits. By increasing the total phase noise of the circuit by adding an additional noise source, we can increase our signal above the inherent noise floor and estimate the timing jitter of a single device.

The RTDs used in these experiments were monolithically connected to transmission lines. They were previously used as RTD pulsers by applying a bias and an RF signal through the transmission line. When the total voltage on the RTD reached a threshold volt-

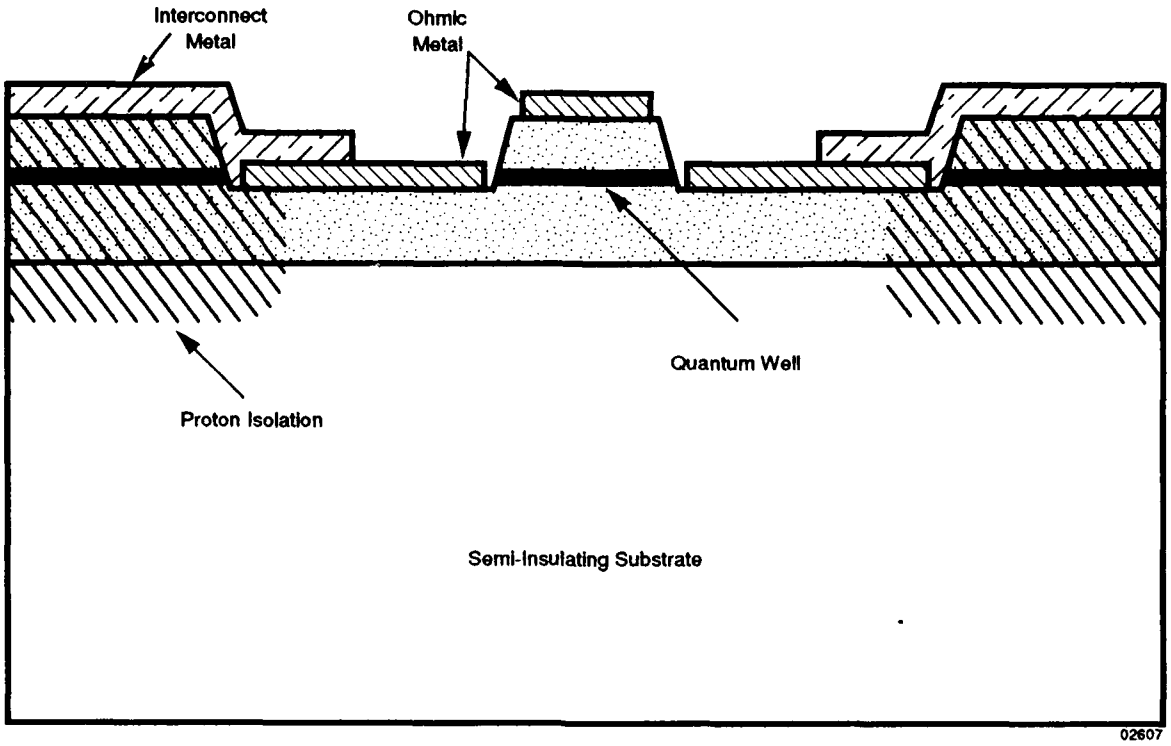


**Figure 61**
**Device cross section of proton-implanted, microwave-compatible RTD process.**

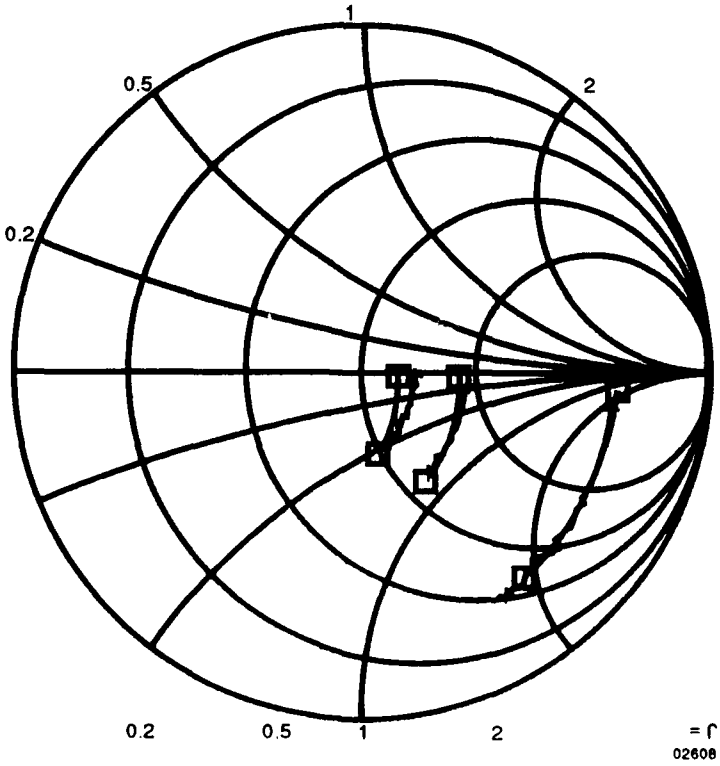


**Figure 62**
**S11 measurements and calculations.**

age, it switched from one state to another, and a fast voltage pulse formed on the transmission line. Previously, the output pulses were synchronous with the RF input; to achieve repetitive switching waveforms, the amplitude of the RF signal had to be large enough to reset the device.

The need for a large-amplitude RF signal was avoided by driving with the sum of two different signals. One signal was a very fast sinusoidal with a relatively small amplitude and the other was a slow sinusoidal with a larger amplitude. The resulting sum resembled an RF signal superimposed on a slowly rising ramp function (Figure 63). With the application of this signal to our device, switching occurs around the maximum of the fast RF signal. The voltage pulse train on the transmission line is now synchronous with the fast RF signal and is easily observed with a scope. To check that the pulse trains were synchronous with the fast RF signal, we changed the dc bias by small increments. If the pulses are synchronous, then at certain bias levels, the device should switch to the next peak of the RF signal. The time delay between the pulse obtained with the new bias and that obtained with the previous should then increase by one period of the fast signal.

The experimental setup for synchronization of the switching pulse with the RF signal can be found in Figure 64. A 60-GHz signal was obtained by feeding an amplified 20-GHz signal from a frequency synthesizer into a tripler. A large-amplitude, 500-MHz sinusoidal signal from another phase-locked synthesizer was summed with the output of the tripler. The dc bias was increased in 6-mV steps and each time, a different switching waveform was recorded. The resulting waveforms are shown in Figure 65. Each of the four switching waveforms is at a different bias point and corresponds to switching around consecutive maximums of the 60-GHz signal. The time delay between each consecutive waveform is around 16.6 ps, equal to one period of the 60-GHz signal. This shows that the switching pulse is synchronous with the fast 60-GHz RF signal.

To check that this switching step can be used as a real trigger pulse, we applied the output of the RTD circuit to the trigger input of a digital sampling scope (Figure 66). To ensure that the triggering is not caused by synchronization of the slow part of the input signal with the fast signal, we chose a 499-MHz signal. We then tried to observe a 60-GHz signal from another U-band tripler driven by the same frequency synthesizer. The result in Figure 67 shows that we were able to trigger a 60-GHz signal using our RTD trigger circuit.

Conventional Esaki tunnel diode trigger circuits operate up to 20 GHz. This was the best result before our research on RTD trigger circuits. Our first attempt extended this limit to 40 GHz.[34] The new setup has raised that record to 60 GHz, which we believe to be still limited by the experimental setup and not the device itself. Future planned work includes design and fabrication of a 100-GHz trigger circuit. This circuit will use two diodes and, in terms of high-frequency characteristics, the new circuit will be superior to the present RTD trigger circuit. Testing at 100 GHz will be made by using both electronic and electro-optic sampling techniques.

RTD trigger circuits have potential system applications. Currently, the largest commercial application of tunnel diodes is to trigger recognition in high-speed oscilloscopes. We expect that it is here that the RTD will also find its greatest utility. As has already been demonstrated, RTDs fabricated with the planar process developed in our laboratory can be used to trigger off signals up to 60 GHz, a factor of 3 faster than the Esaki tunnel diode. Furthermore, the speed of the RTD will allow it to serve an even broader role in high-speed instrumentation.

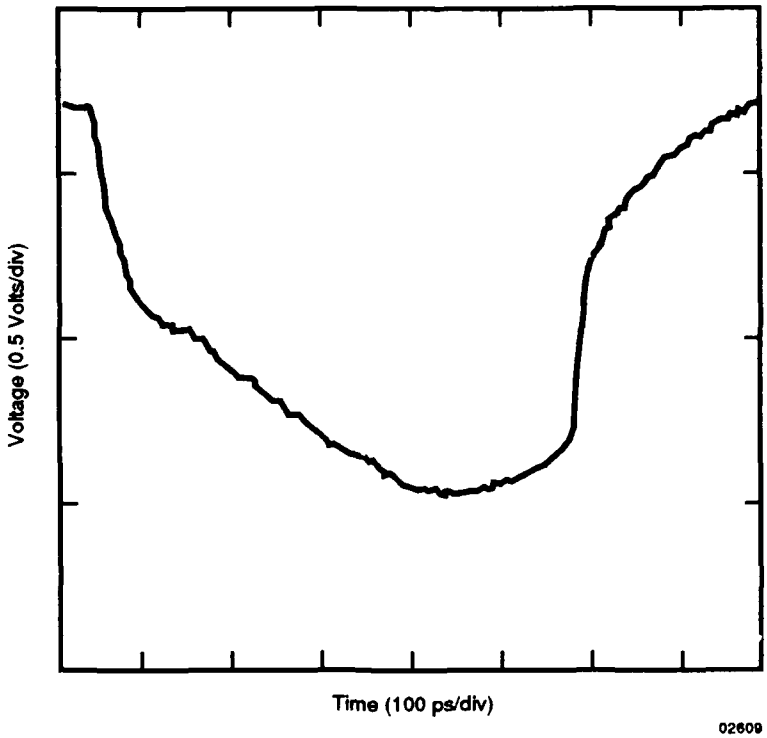


**Figure 63**
**Electro-optically sampled output of pulse-forming structure.**

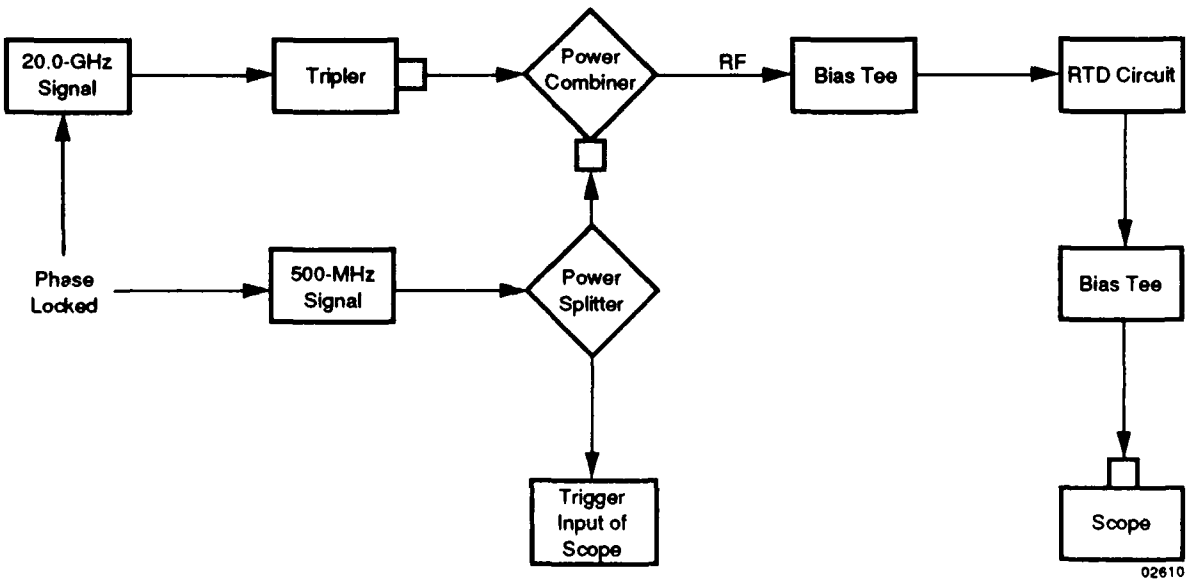


**Figure 64**
**Experimental setup to demonstrate trigger action at 60 GHz using RTD circuit.**

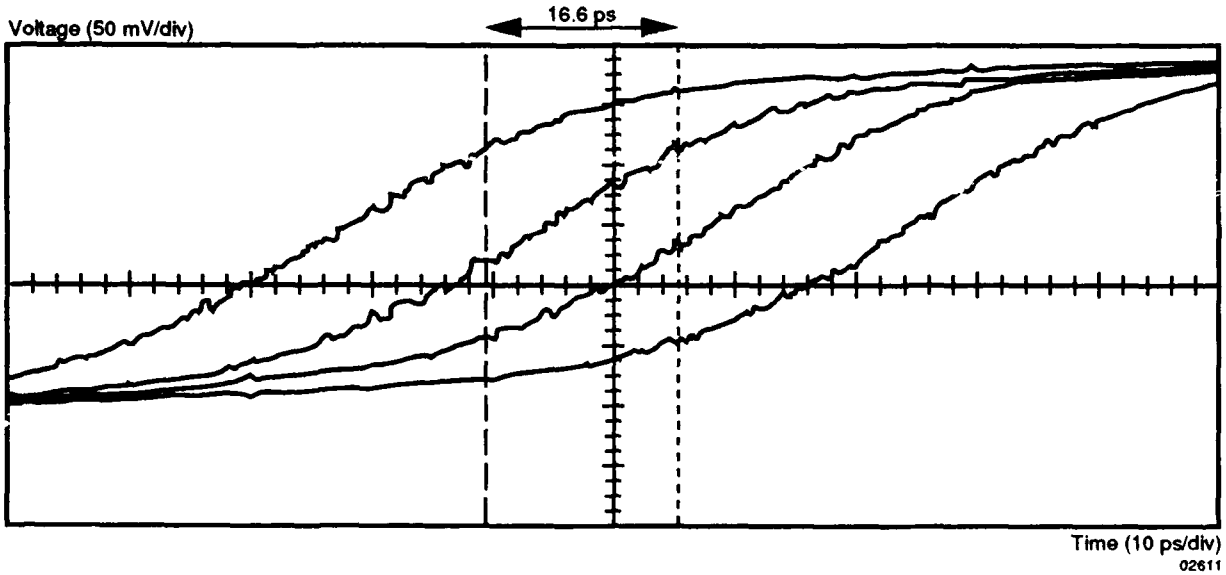


**Figure 65**
**Four different switching waveforms.**

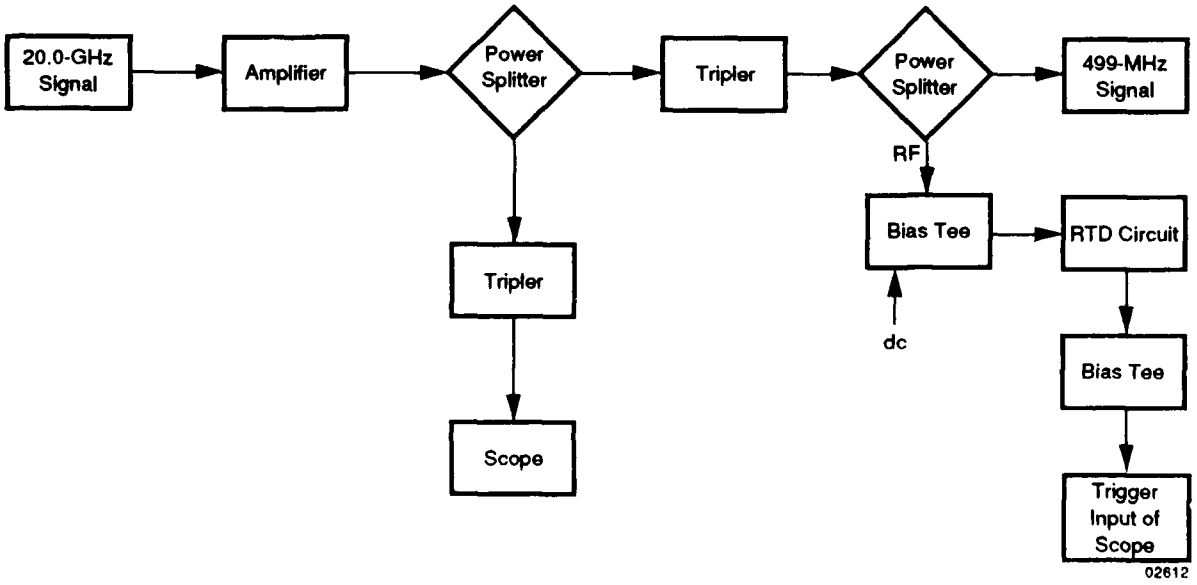


**Figure 66**
**Experimental setup for using RTD trigger circuit output as trigger input to digital scope.**

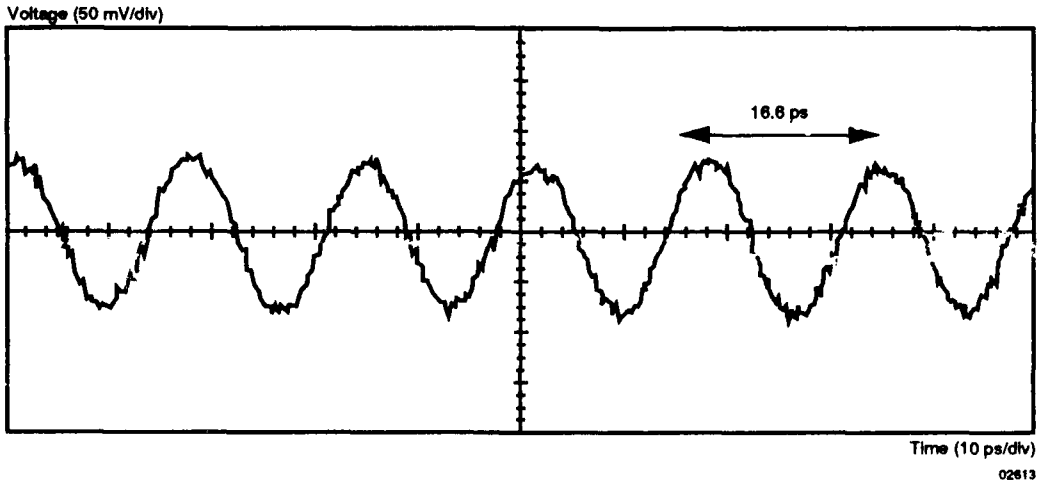


**Figure 67**
**Scope plot of 60-GHz signal triggered by output of RTD trigger circuit.**

Figure 68 shows two possible applications of the RTD. Figure 68(a) is a simplified description of a vector network analyzer. This system takes advantage of a high-speed RTD trigger circuit to avoid the necessity of frequency synthesis, making the system more flexible and possibly less costly. Here the trigger circuit, or "countdown," produces a lower-frequency output that is phase-synchronous with the RF input. This output can be passed through a digital phase shifter and a limiting amplifier to provide a local oscillator (LO) signal for the sampler. A microprocessor determines the rate of phase-shifting that is required to produce a mixer product at the desired intermediate frequency (IF). This information can also be used to determine the instantaneous frequency of the RF source. An equivalent-time sampling oscilloscope functions in much the same way.

Figure 68(b) illustrates how an RTD trigger would be used in a random sampling oscilloscope. In this case, the LO is run at a synthesized rate, so it is necessary to decide where the trigger event occurs relative to the sample. This is done by making a time interval measurement between the trigger event and the next sample pulse. The resulting time data are used to place the voltage sample at the correct point in time on the display.

Current commercial technology makes this time interval measurement with about 10-ps resolution. However, an integrated correlator circuit using the nonlinear transmission-line technology developed at Stanford University has the potential of relating the trigger event to the sample pulse with less than 1-ps resolution. This circuit consists of a nonlinear transmission line connected to a diode tapped delay line. The nonlinear transmission line produces a fast fall-time pulse, synchronous with the LO, which collides with an incoming trigger event pulse from the RTD on the tapped delay line. In the spatial region of the correlation between the two pulses, the tap diodes are forward-biased. The shape of the correlation is then captured by hold capacitors connected to the tap diodes, and the relative time of the incoming trigger event determined by the spatial position along the delay line of the correlation center.

The system examples presented here show that the RTD can extend the speed and flexibility of current high-speed instrumentation. In high-frequency network analysis, the RTD could possibly be used to eliminate the need of phase-locked sources. In sampling oscilloscopes, the RTD is a "drop-in" replacement for the old Esaki tunnel diode, but its speed demands that other system blocks such as the correlator be enhanced as well.

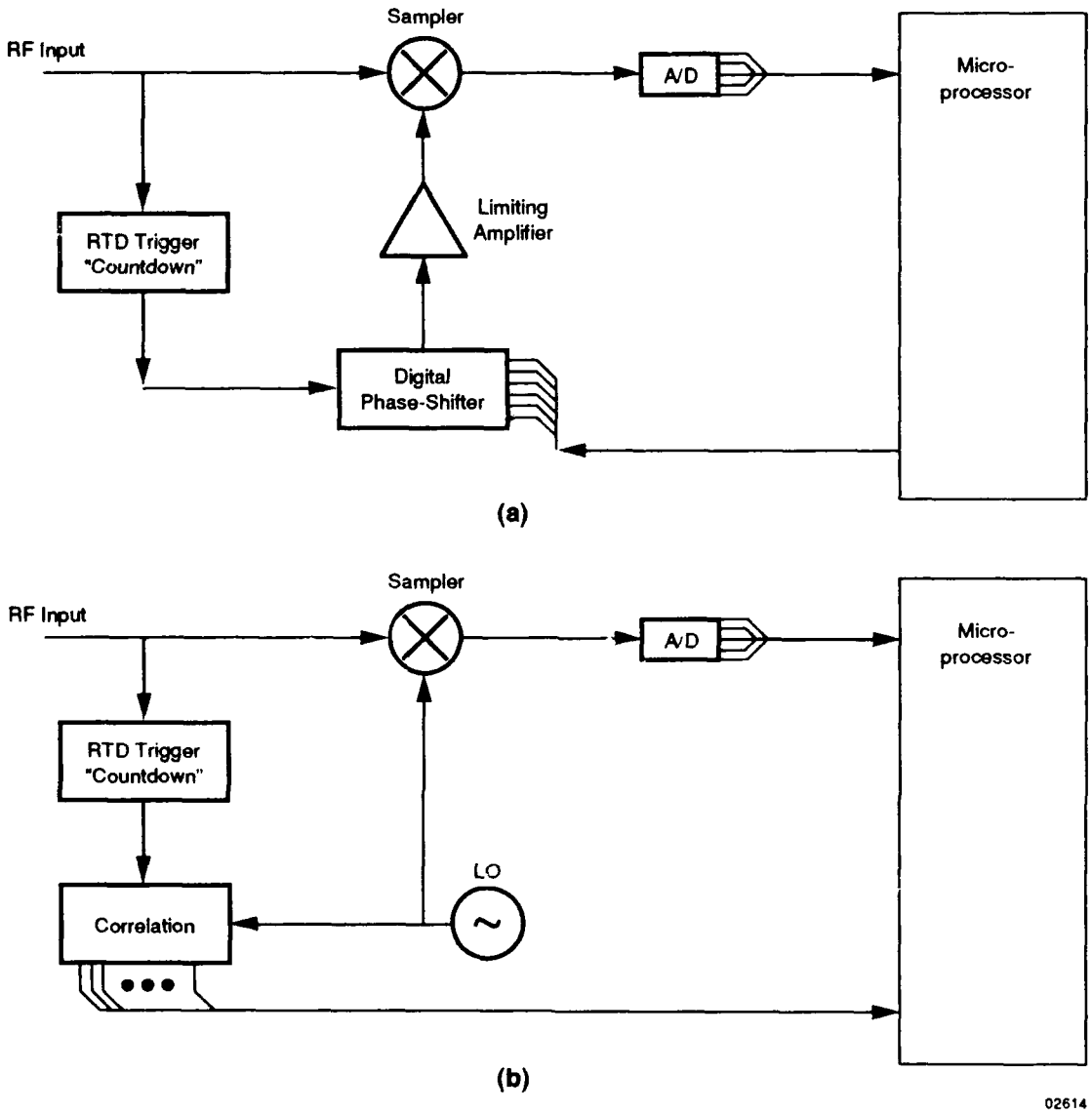


**Figure 68**
**Network analyzer receiver (a) and random sampling oscilloscope, (b) using an RTD triggering circuit.**

# SECTION VI

# SUMMARY OF ACCOMPLISHMENTS

Unipolar and bipolar resonant tunneling transistors (RTTs) in both GaAs- and InP-based heterojunction material systems were fabricated and characterized. Initial demonstration of the pseudomorphic InGaAs base BiQuaRTT was achieved in the GaAs/AlGaAs/InGaAs system[20,21] (Appendixes I and J). Resonant tunneling was observed in the pseudomorphic AlGaAs/InGaAs/GaAs system[15] (Appendix E), and the $Al_xGa_{1-x}As$/$Al_yGa_{1-y}As$/GaAs[16] (Appendix F). High current density, important for high-speed applications, of $10^5$ A/cm$^2$ with a peak-to-valley current ratio of 2:1 at 77 K was achieved in an AlGaAs/GaAs RTD[17] (Appendix G). The heterojunction device models developed under this contract were used to interpret the I(V) characteristics of a set of precisely characterized RTDs[18] (Appendix H). This work established the predictive ability of the heterojunction models and provided a simple explanation for I(V) asymmetry in RTDs in terms of monolayer thickness fluctuations. An implantation process for contacting an n-type quantum well was developed[24] (Appendix K) and used to contact the quantum well of a unipolar GaAs RTT[26] (Appendix L). This device is the first Stark-effect transistor (SET) to exhibit oscillatory negative transconductance at 77 K and was an important test vehicle for understanding transport into and out of n-type quantum wells.

A state-of-the-art MBE growth capability for In(AlGa)As compounds lattice-matched in InP was demonstrated[32] (Appendix M). Methods for growth of resonant-tunneling heterostructures and for heavily doping InGaAs with Be and Si were developed. A microwave resonant-tunneling transistor process was also developed, and microwave characterization of RTDs and RTTs was performed. In the final weeks of the contract, both unipolar and bipolar InP RTTs were demonstrated and characterized. We achieved for the first time room-temperature dc and microwave gain from the unipolar InP-based RTTs. These unipolar hot-electron transistors are the first ever to show room-temperature dc and microwave gain.

# SECTION VII

# CONCLUSIONS AND RECOMMENDATIONS

The resonant-tunneling transistors under development by the contractor represent the limiting cases in base thickness dimension of the double-heterojunction bipolar transistor (DHBT) and the hot-electron transistor. During the course of this contract, systematic progress was made toward the realization of practical quantum transistors, but much work remains. Further engineering of the transistor heterostructure is needed to optimize the device at room temperature as we have described. Development of selective wet and dry etch processes are needed to realize the full potential of these advanced device structures and provide for a manufacturable process. As quantum transistors are moved into a manufacturing environment, device design rules will be required to allow the realization of circuits. These must evolve from a strong theoretical understanding of the basic device transport, which must be built concurrently and in close collaboration with the experimental effort.

As we summarize and reflect on the findings of this effort, we find no insurmountable technical impediments to the realization of quantum transistor devices and circuits. We recommend that development of resonant-tunneling transistors and circuits be continued.

# REFERENCES


1. R.T. Bate, in *VLSI Handbook*, ed. by N.G. Einspruch (*Academic Press*, New York, 1985), Chapter 35, p. 615.
2. L.L. Chang, L.Esaki, and R.Tsu, *Appl. Phys. Lett.*, **24**:593 (1974).
3. T.C.L.G. Sollner et al., *Appl. Phys. Lett.*, **43**:588 (1983).
4. T.J. Shewchuk, P.C. Chapin, P.D. Coleman, W. Kopp, R. Fisher, and H. Morkoc, *Appl. Phys. Lett.*, **46**:508 (1985).
5. M.A. Reed, *Superlattices and Microstructures*, **2**:65 (1986).
6. R.W. Keyes, *Science*, **230**:138 (1985).
7. F. Capasso and R.A. Kiehl, *J. Appl. Phys.*, **58**:1366 (1985).
8. N. Yokoyama et al., *Jpn. J. Appl. Phys.*, **24**:853 (1985).
9. A.R. Bonnefoi, T.C. McGill, and R.D. Burnham, *IEEE Electron Device Lett.*, **EDL-6**:636 (1985).
10. T.C.L.G. Sollner et al., *Proceedings IEEE/Cornell Conference on Advanced Concepts in High Speed Devices and Circuits*, 252 (1985).
11. A.F.J. Levi J.R. Hayes, P.M. Platzman, and W. Wiegmann, *Phys. Rev. Lett.*, **55**:2071 (1985).
12. M. Heiblum, M.I. Nathan, D.C. Thomas, and C.M. Knodler, *Phys. Rev. Lett.*, **55**:2200 (1985).
13. H. Morkoc, unpublished presentation at Workshop on Compound Semiconductor Microwave Materials and Devices, San Francisco, CA (February 1986).
14. M.A. Reed and J.W. Lee, *Appl. Phys. Lett.*, **50**:845 (1987).
15. C.H. Yang and H.D. Shih, "Improved $Al_xGa_{1-x}As/Ga_{1-y}In_yAs/GaAs$ Strained-Layer Double Barrier Resonant Tunneling Structure," *Electronics Letters*, **24**:553 (1988).
16. C.H. Yang and H.D. Shih, "Observation of Negative Differential Resistance in $Al_{0.2}Ga_{0.6}As/Al_{0.4}Ga_{0.6}As/GaAs$ Double Barrier Resonant Tunneling Structure," *Electronics Letters*, **24**:1554 (1988).
17. C.H. Yang and R.J. Matyi, "Dependence of Peak Current Density on Impurity Doping in Double Barrier Resonant Tunneling Structures," *Inst. Phys. Conf.*, Ser. No. 96, 617 (1988).
18. M.A. Reed, W.R. Frensley, W.M. Duncan, R.J. Matyi, A.C. Seabaugh, and H.L. Tsai, "Quantitative Resonant Tunneling Spectroscopy: Current-Voltage Characteristics of Precisely Characterized Resonant Tunneling Diodes," *Appl. Phys. Lett.*, **54**:1256 (1989).
19. M.A. Reed, W.R. Frensley, R.J. Matyi, J.N. Randall, and A.C. Seabaugh, "Realization of a Three-Terminal Resonant Tunneling Device: The Bipolar Quantum Resonant Tunneling Transistor," *Appl. Phys. Lett.*, **54**:1034 (1989).

20. A.C. Seabaugh, W.R. Frensley, J.N. Randall, M.A. Reed, D.L. Farrington, and R.J. Matyi, "Pseudomorphic Bipolar Quantum Resonant-Tunneling Transistor," *IEEE Trans. Electron Dev.*, **36**:2329 (1989).

21. A.C. Seabaugh, W.R. Frensley, Y.-C. Kao, J.N. Randall, and M.A. Reed, "Quantum-Well Resonant-Tunneling Transistors" (invited), *Proceedings IEEE/Cornell Conference on Advanced Concepts in High Speed Semiconductor Devices and Circuits*, IEEE Cat. No. 89CH2790-4, 255 (1990).

22. E.L. Wolak, K.L. Lear, P.M. Pitner, E.S. Hellman, B.G. Park, T. Weil, J.S. Harris, Jr., and D. Thomas, "Elastic Scattering in Resonant Tunneling Diodes," *Appl. Phys. Lett.*, **53**:201 (1988). E.L. Wolak, "The Effects of Reduced Dimensionality and Elastic Scattering on the Current Voltage Characteristics of Resonant Tunneling Diodes," Ph.D. Thesis, Stanford University (1989).

23. A.C. Seabaugh, "Selective Reactive Ion Etching of GaAs on AlGaAs Using $CCl_2F_2$ and He," *J. Vac. Sci. Technol.*, **B6**:77 (1988).

24. C.H. Yang, D.L. Plumton, R. Lodenkamper, and H.D. Shih, "Implant and Annealed Ohmic Contact to a Thin Quantum Well," *Appl. Phys. Lett.*, **55**:1650 (1989).

25. A.R. Bonnefoi, D.H. Chow, and T.C. McGill, "Inverted Base-Collector Tunnel Transistors," *Appl. Phys. Lett.*, **47**:888 (1985).

26. C.H. Yang, Y.-C. Kao, and H.D. Shih, "A New Field-Effect Resonant Tunneling Transistor: Observation of Oscillatory Transconductance," *Appl. Phys. Lett.*, **55**:2742 (1989).

27. C.I. Huang, M.J. Paulus, C.A. Bozada, S.C. Dudley, K.R. Evans, C.E. Stutz, R.L. Jones, and M.E. Cheney, *Appl. Phys. Lett.*, **51**:121 (1987).

28. T. Inata, S. Muto, Y. Nakata, T. Fujii, H. Ohnishi, and S. Hiyamizu, *Jpn. J. Appl. Phys.*, **25**:L983 (1986).

29. T.P.E. Broekaert, W. Lee, and C.G. Fonstad, "Pseudomorphic $In_{0.53}Ga_{0.47}As$/AlAs/InAs Resonant Tunneling Diodes With Peak-to-Valley Current Ratios of 30 at Room Temperature," *Appl. Phys. Lett.*, **53**:1545 (1988).

30. W.R. Frensley, "Boundary Conditions for Open Quantum Systems Driven Far From Equilibrium," *Review of Modern Physics*, accepted for publication (1990).

31. D.A. Sunderland and D. Dapkus, "Optimizing n-p-n and p-n-p Heterojunction Bipolar Transistors for Speed," *IEEE Trans. Electron Dev.*, **ED-34**:367 (1987).

32. Y.-C. Kao, A.C. Seabaugh, H.Y. Liu, T.S. Kim, M.A. Reed, P. Saunier, B. Bayraktaroglu, and W.M. Duncan, "Improved MBE Growth Structures for High-Performance Device Applications," *SPIE 1144 Indium Phosphide and Related Materials for Advanced Electronic and Optical Devices*, 30 (1989).

33. E.R. Brown, APS Meeting (March 1989).

34. J.W. Owens, D.J. Halchin, K.L. Lear, W.S. Lee, and J.S. Harris, Jr., "Microwave Characteristics of MBE Grown Resonant Tunneling Devices," *1989 IEEE MTT-S Digest*, 471 (1989).

35. F. Capasso, S. Sen, A.C. Gossard, A.L. Hutchinson, and J.H. English, "Quantum-Well Resonant Tunneling Bipolar Transistor Operating at Room Temperature," *IEEE Electron Device Lett.*, **EDL-7**:573 (1986). Also T. Futatsugi, Y. Yamaguchi, K. Imamura, S. Muto, N. Yokoyama, and A. Shibatomi, "A Resonant-Tunneling Bipolar Transistor (RBT)—A New Functional Device With High Current Gain," *Jpn. J. Appl. Phys.*, **26**:L131 (1987).

36. R.C. Potter and A.A. Lakhani, "Observation of Electron Quantum Interference Effects Due to Virtual States in a Double-Barrier Heterostructure at Room Temperature," *Appl. Phys. Lett.*, **52**:1349 (1988).

37. D.C. Herbert, "Structure Base Hot-Electron Transistors," *Semicond. Sci. and Tech.*, **3**:1129 (1988).

38. A.F.J. Levi and T.H. Chiu, "Room-Temperature Operation of Hot-Electron Transistors," *Appl. Phys. Lett.*, **51**:985 (1987).

39. N. Yokoyama, K. Imamura, S. Muto, S. Hiyamizu, and H. Nishi, "A New Functional, Resonant-Tunneling Hot Electron Transistor (RHET)," *Jpn. J. Appl. Phys.*, **24**:L853 (1985).

40. T. Mori, H. Ohnishi, K. Imamura, S. Muto, and N. Yokoyama, "Resonant Tunneling Hot-Electron Transistor With Current Gain of 5," *Appl. Phys. Lett.*, **49**:1779 (1986).

41. M. Heiblum, M.V. Fischetti, W.P. Dumke, D.J. Frank, I.M. Anderson, C.M. Knoedler, and L. Osterling, "Electron Interference Effects in Quantum Wells: Observation of Bound and Resonant States," *Phys. Rev.*, **58**:816 (1987).

42. D.L. Miller and P.M. Asbeck, "Be Redistribution During Growth of GaAs and AlGaAs by Molecular Beam Epitaxy," *J. Appl. Phys.*, **57**:1816-1822 (1985).

43. P. Enquist, G.W. Wicks, L.F. Eastman, and C. Hitzman, "Anomalous Redistribution of Beryllium in GaAs Grown by Molecular Beam Epitaxy," *J. Appl. Phys.*, **58**:4130-4134 (1985).

44. C.B. Cooper III, S. Salimian, and H.F. MacMillan, "Use of Thin AlGaAs and InGaAs Stop-Etch Layers for Reactive Ion Etching of III-V Compound Semiconductor Devices," *Appl. Phys. Lett.*, **51**:2225 (1987).

45. A.C. Warren, J.M. Woodall, E.R. Fossum, G.D. Pettit, P.D. Kirchner, and D.T. McInturff, "Masked, Anisotropic Thermal Etching and Regrowth for *in situ* Patterning of Compound Semiconductors," *Appl. Phys. Lett.*, **51**:1818 (1987).

46. M.A. Reed, W.R. Frensley, W.M. Duncan, R.J. Matyi, A.C. Seabaugh, and H.L. Tsai, "Quantitative Resonant Tunneling Spectroscopy: Current-Voltage Characteristics of Precisely Characterized Resonant Tunneling Diodes," *Appl. Phys. Lett.*, **54**:1256 (1989).

47. S.K. Diamond et al., "Resonant Tunneling Diodes for Switching Applications," *Appl. Phys. Lett.*, **52**:2163-2165 ( 1989).

48. S.K. Diamond et al., "Fabrication of Resonant Tunneling Diodes for Switching Applications," *Electron Device Letters*, **EDL-10**:104-106 (1989).

49. Texas Instruments, Contract No. N00014-87-C-0363, Quarterly Report for December 1988-February 1989.

50. E.R. Brown et al., "Oscillations Up to 420 GHz in GaAs/AlAs Resonant Tunneling Diodes," *Appl. Phys. Lett.*, **55**:1777-1779 (1989).

51. E. Ozbay et al., "Pulse Forming and Triggering Using Resonant Tunneling Structures," submitted to *Applied Physics Letters.*

52. Arpad Barna, "Nanosecond Trigger Circuits," *IEEE Trans. on Nuclear Science*, pp. 17-21, (5 October 1973).

53. Donald E. Nelsen, "Statistics of Switching-Time Jitter for a Tunnel Diode Threshold-Crossing Detector," *IEEE Inter. Con. Rec. P7*, 288-294 (1966).

54. Texas Instruments, Contract No. N00014-87-C-0363, Quarterly Report for April-June 1989.

# APPENDIX A

# HBAND: AN INTERACTIVE HETEROSTRUCTURE DEVICE MODELING PROGRAM

# TEXAS INSTRUMENTS
## Incorporated
*POB 655936 • Dallas Texas 75265*
*Central Research Laboratories*


*HBAND: AN INTERACTIVE HETEROSTRUCTURE DEVICE MODELING PROGRAM*


*William R. Frensley*


**TECHNICAL REPORT**


TR 08-89-64 December 20, 1989


| | MS | | MS | | MS |
|---|---|---|---|---|---|
| R. J. Aggarwal | 154 | D. Hester | 369 | A. C. Seabaugh | 134 |
| R. T. Bate | 154 | D. D. Heston | 134 | D. J. Seymour | 134 |
| B. Bayraktaroglu | 134 | R. D. Hudgens | 134 | T. J. Shaffner | 147 |
| K. Bradshaw | 134 | P. Ikalainen | 134 | D. Shaw | 147 |
| C. Chang | 3926 | M. A. Khatibzadeh | 134 | H. Shichijo | 134 |
| P. Chatterjee | 944 | M. Kinch | 150 | R. Stratton | 136 |
| D.R. Collins | 134 | J. H. Luscombe | 154 | R. Tayrani | 134 |
| F.Doerbeck | 255 | D. McQuiddy | 245 | H.Q. Tserng | 134 |
| W. M. Duncan | 147 | F. Morris | 134 | D. Whitmire | 3926 |
| S. Evans | 404 | P. A. Penz | 154 | R. Williams | 404 |
| S.K. Fan | 134 | D. Plumton | 134 | W. R. Wisseman | 134 |
| G. Frazier | 154 | A. J. Purdes | 147 | L. C. Witkowski | 134 |
| M. T. Gately | 154 | J. N. Randall | 154 | J. Y. Yang | 134 |
| B. E. Gnade | 147 | M. A. Reed | 154 | P. H. Yang | 150 |
| G. H. Heilmeier | 400 | C. G. Roberts | 150 | H. T. Yuan | 134 |
| T. Henderson | 134 | J. B. Sampsell | 134 | TRS (2) | 8433 |
| | | P. Saunier | 134 | | |


TI Internal Data

hband

# HBAND: AN INTERACTIVE HETEROSTRUCTURE DEVICE MODELING PROGRAM

William R. Frensley
Central Research Laboratories
Texas Instruments Incorporated
Dallas, Texas 75265

## I. Summary

hband is an interactive program, implemented on the SUN 3/260 workstation, which solves for the self-consistent energy-band profile in heterostructure devices. It does so within a local quasi-equilibrium approximation (also known as the zero current model, and such programs are loosely termed "Poisson solvers"), for heterostructures in the AlGaAs and InGaAs material systems. It may be used to investigate such questions as the effects of grading in composition and doping in HBTs, optimum heterolayer design in heterostructure FETs, and the design of resonant-tunneling devices.

## II. Overview

The hband user-interface is a window in the SunView* environment. It consists of six subwindows which display particular types of information about the simulation. These are:

* The band-profile window in the upper left. The band-edge energies versus position (the primary result of the calculation) are displayed graphically.
* The density-profile window in the lower left. The composition, doping, and carrier densities versus position are displayed graphically.
* The design-file control panel at top left. This provides the functions required to manage the files of design data.
* The design-file text window at upper left. This displays the text of the design file and permits editing of the design.
* The display control panel at middle right. This provides functions to control the format of the displayed results and supplies feedback on some aspects of the calculation.
* The log window at lower right. Information on the status of the calculation which is generally of secondary interest is dumped into this window, where it may be examined should the need arise.

The layout of the interface is illustrated in Figure 1.

* SunView is a trademark of Sun Microsystems, Inc.

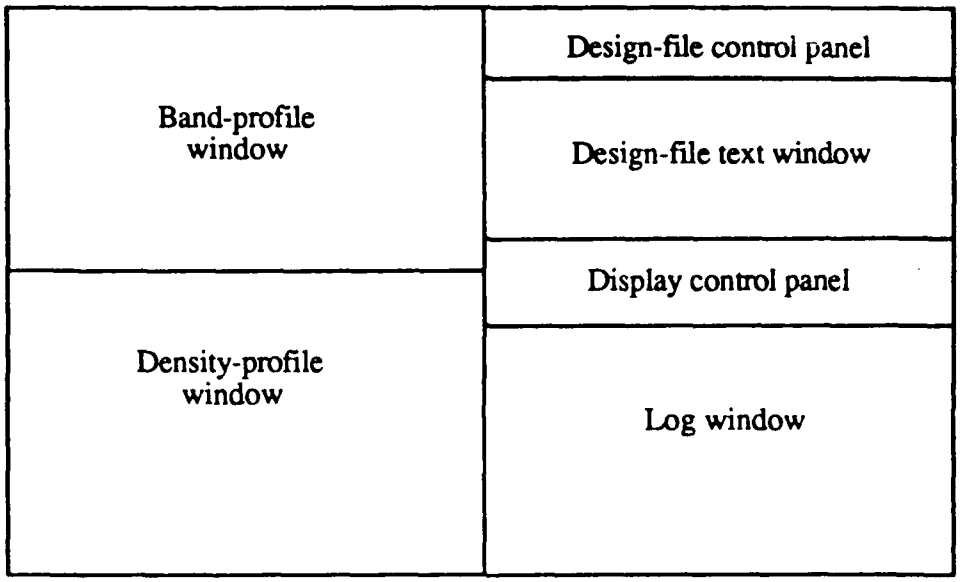


Figure 1. hband user interface

## III. Using hband

### A. Starting hband

hband must be run within the SunView environment. Normally, the user accounts of those primarily interested in device modeling will be set up so that SunView will automatically be entered upon login, and hband will be among the programs represented by an icon on entering SunView. To use hband, simply move the mouse so as to position the pointer over the hband icon and press the left mouse button.

hband relies heavily on the conventions and built-in functions of the SunView environment, and thus users should study the "SunView 1 Beginner's Guide" at some point in the process of learning to use hband. The important conventions to remember are the functions of the mouse buttons. The left button is used to make selections, as of text to edit, icons to open, or to push a control button. The middle mouse button is used to extend text selection s, and the right button brings up the pop-up menu. The "keyboard focus", the window to which keystrokes are sent, is the window in which the pointer is presently located. (Many of these details can be changed with the Defaults Editor, to more closely resemble the Macintosh interface, for example.)

If the hband icon is not displayed upon entering SunView it may be invoked from the SunView pop-up menu under Local. Otherwise it may be started from any shell by typing hband. (Technical detail: the executable file is located in /usr/local/bin, which should be in everyone's search path.)

## B. Editing the Device Structure

The heterostructure to be simulated is described to `hband` by a text file which is displayed and edited in the design-file text window. To introduce the format of such design files, the following example describes the original Fujitsu HEMT transistor:

```
v1  Schottky            1.1
v2  30.0      2.0E18    0.3   Al
v2  60.0     -1.0E14    0.0
v2  bulk
```

The file consists of a sequence of lines describing the layers of the heterostructure and the boundary conditions of the simulation. The first and last lines define the boundary conditions, and the intervening lines define the layers. The first item on any line is a two character sequence which for the moment we may think of as specifying the device terminal to which a given layer or boundary is connected. This sequence consists of the letter `V` followed by a digit in the range 1..8. (The `hband` input routine is not case-sensitive, so you can use either `V` or `v`.) We will refer to this below as a `V#` item. In the example above, the Schottky contact is connected to terminal 1, and all of the semiconductor layers are connected to terminal 2 (conceptually, the substrate). Now let us consider the rest of a layer definition line, such as:

```
v2  30.0  2.0E18  0.3  Al.
```

The number following the `v2` is the layer thickness in nanometers (30 in this case). Next is the doping level in atoms per cubic centimeter. Positive values imply N-type doping and negative values imply P-type doping. The rest of the line specifies the chemical composition, in this case $Al_{0.3}Ga_{0.7}As$. GaAs is specified by 0.0, 10% InGaAs would be specified by `0.1 In`. As presently configured `hband` models only the (Al,Ga)As and (In,Ga)As material systems.

There are three types of boundary conditions which may be specified: `OHMIC`, `SCHOTTKY`, and `BULK`. `OHMIC` and `SCHOTTKY` describe metallic contacts, with the `OHMIC` boundary condition fixing the band-edge energies so as to enforce charge neutrality at the boundaries. `SCHOTTKY` boundaries fix the conduction band energy to be the Schottky barrier height (which must be specified immediately after the keyword `SCHOTTKY`) above the Fermi level in the contact. The `BULK` boundary condition models a semi-infinite extent of semiconductor with the same composition and doping level as the adjacent layer. Note that each of these boundary conditions implicitly involves the concept of a Fermi level at the boundary, so a `V#` terminal specification is required to tell the program what Fermi level to apply at the boundary.

The design-file text window uses the standard SunView text-editor (`textedit`). For complete details on how to use this editor, see the "SunView 1 Beginner's Guide." To summarize the more important functions: To position the caret (insertion point), move the pointer to the desired location and press the left mouse button. If you start typing (with the pointer still within the text window) the characters will appear at the position of the caret. To select a region of text to delete or copy to another location, place the pointer over the first character in the region and press the left mouse button. Then move the pointer over the last character in the region and press the middle mouse button. The selected text will be displayed in inverse video. You can then use the "Cut" or "Copy" keys on the keyboard.

The selected text will be placed into the paste buffer and it can be inserted in another place by moving the caret as described above and then pressing the "Paste" key. The character to the right of the caret can be erased by pressing the "Delete" key.

The interactions with the file system are handled by the contents of the design-file control panel, located immediately above the design-file text window, and illustrated in Figure 2. The top row of this control panel contains five buttons, labeled `Load`, `Model`, `Store`, `List dir` and `Set dir`, which are largely self-explanatory. The current directory is displayed on the second line, and it can be changed by editing the directory name and then pushing the `Set dir` button. Pushing the `List dir` button causes a listing of the current directory to be displayed in the log window. A file name can then be selected and copied (as described above) from this window and placed after the `File:` prompt in the control panel, or the file name can be typed in after positioning the caret after the `File:` prompt. Pressing `Load` will load the contents of the named file into the text window, and pressing `Store` will store the contents of the window into the named file. The two remaining items in the control panel are the temperature and the mesh spacing. These values default to 300.0 K and 5.0 nm, respectively, when `hband` is started. The temperature can be set to any desired value greater than zero. The mesh spacing is best chosen so that the total number of mesh points (the total thickness of the modeled structure divided by the mesh spacing) is of the order of 100. Typical values are 5 nm for bipolar devices and 1 nm for FETs

```
[Load] [Model] [Store]                    [List dir] [Set dir]
Directory: /home/sclac1/frensley/modeling/hdemo
File: hbt_drift
Temperature =  300.0 K   Mesh spacing =  5.0 nm
```

Figure 2. Design-file Control Panel

C. Modeling a Device

Once a device structure has been defined in the design-file text window, the structure is interpreted and modeled by pressing `Model`. The contents of the design-file window are then read, interpreted into a finite-difference model whose elements are displayed in the density-profile window, and the self-consistent potential is evaluated by Newton iteration. Note that changes made in the design-file text window are made known to the rest of the program only by pushing `Model`.

D. The Band-Profile Window

The primary output of `hband` is the contents of the band-profile window, which is illustrated in Figure 3. It shows a graph of band-edge energy versus position, in white lines on a black background. Also shown are the Fermi levels, in red, of the various layers and boundaries. `hband` conceptually groups together all layers and boundaries (which need not be contiguous) with a given `V#` and manipulates the Fermi level of each of these groups as a unit. This is the true significance of the `V#` in the design file. The current value of each Fermi level is displayed digitally in the display control panel. Note that the

values presented on the graph and in the digital display differ in sign. The graph plots electron potential energy in eV and the digital display shows the terminal voltage.

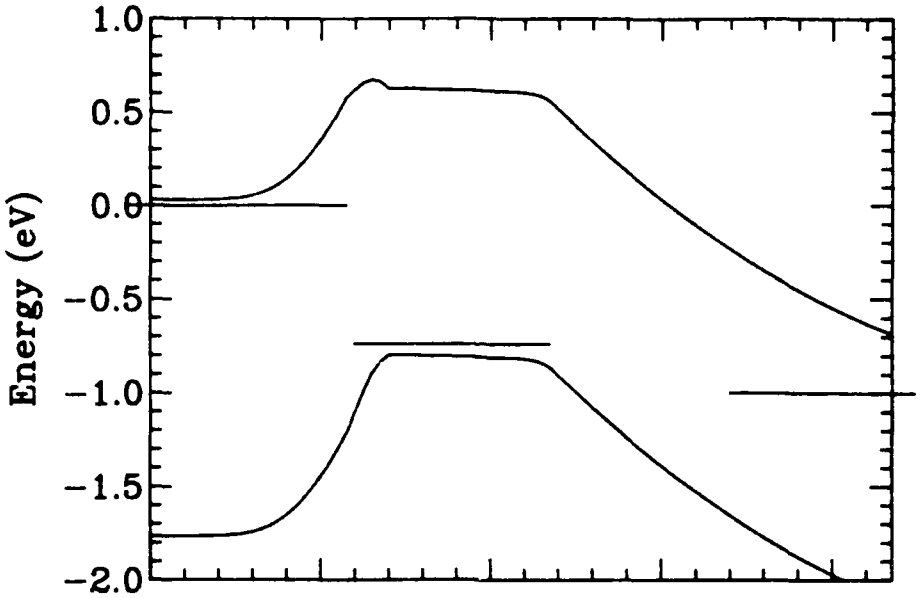


Figure 3. The Band-Profile Window

A recalculation of the self-consistent potential is triggered by adjusting one of the Fermi levels. To do this, move the pointer into the band-profile window and position it over the red Fermi-level line within the region whose Fermi level you want to change. Depress and hold the left mouse button. The cursor will change to a grasping hand symbol and the Fermi level will now follow the motion of the pointer. As the Fermi level is changed by moving the pointer up and down, the digital display in the display control panel changes to reflect the current value of the voltage (and this may be used to more precisely set the voltage). When the Fermi level has been set to the desired voltage, release the mouse button and the self-consistent potential will be recalculated. This is an iterative calculation, and the intermediate states are displayed so that the progress of the calculation can be monitored. When convergence is achieved, all of the intermediate results are erased and the graph is redrawn with the converged solution for the band profile. A log of the iterative calculation is also printed in the log window, under a heading `Fermi Screening Iteration Summary`. This includes the iteration number, a quantity `Max f` which is just the maximum deviation from Poisson's equation in eV, an a quantity `t` which is the Bank-Rose damping coefficient.

The format of the band profile display can be modified by control functions located in the display control panel, which is shown in Figure 4. On the top line is a cyclic choice item labeled `Display:` which has the values `Both bands`, `C band only`, and `V band only`. This controls which bands are displayed, so that one can view both the conduction and valence bands when modeling an HBT, but only the conduction band when modeling a MODFET, for example. To cycle through the choices for this item, position the pointer over the cycling arrows symbol and press the left mouse button. The energy range displayed can also be adjusted using the `+Emin`, `-Emin`, `+Emax`, and `-Emax` buttons, which increment or decrement the corresponding energy limit in steps of 1.0 V.

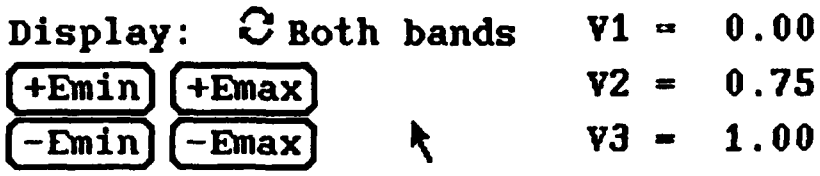


Figure 4. Display Control Panel

E. The Density-Profile Window

The density-profile window, illustrated in Figure 5, displays a plot of composition, doping and carrier density versus position. Doping and carrier density are plotted on the semi-log scale shown to the left. The electron density is plotted in yellow, the donor density in red, the acceptor density in green, and the hole density in cyan. The composition is plotted on the linear scale shown to the right. Al mole fraction is plotted in magenta and In mole fraction is plotted in blue. The composition and doping densities are displayed when the structure is interpreted after the `Model` button is pressed, and the carrier densities are updated whenever a new band profile is calculated.

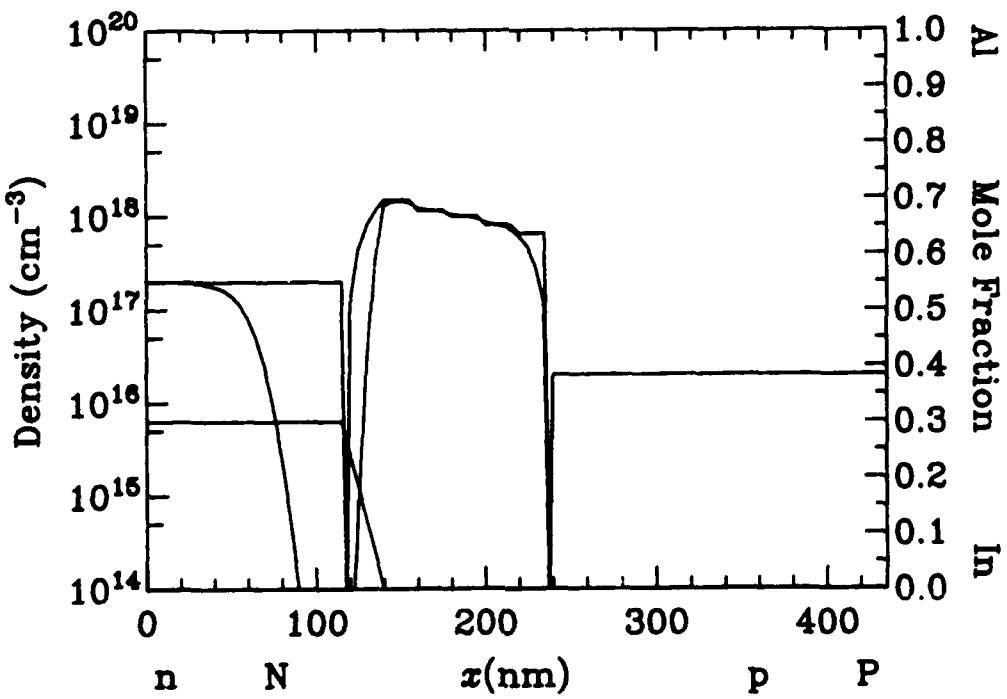


Figure 5. The Density-Profile Window

One can set an integration range over which the total electron, hole, or ionized impurity density will be summed, to obtain an areal density. The limits of integration are set by moving the pointer over the density-profile window. Pressing the left mouse button causes a vertical orange line to appear, which marks the lower (left-hand) integration limit. Move the pointer to the desired position and then release the button. The upper (right-hand) integration limit is similarly set with the middle mouse button. To select which quantities will be integrated, position the pointer within the density-profile window and press the right mouse button. A pop-up menu will appear with the choices `Electron density sum`, `Hole density sum`, `Ionized impurity sum`, and `Turn off range`.

To select an item from this menu, position the pointer over the item while holding down the right mouse button. An item tentatively selected in this fashion will appear in inverse video. The item is actually selected by releasing the mouse button while it is thus displayed. Once electron density summing, for example, has been selected, its menu item changes to `Electron density off`, so that summing can be discontinued as desired. When summing is turned on, it is performed after a new potential is calculated, and the result is displayed in the log window.

## IV. Special Topics

### A. The "V0" Option

It is possible, and sometimes necessary, to specify that a layer have no Fermi level associated with it and in `hband` this is done by specifying `v0`. This is most often required in the vicinity of deep depletion layers, and it is the price that must be paid for using a model which rigorously applies only in equilibrium (zero bias) to far-from-equilibrium situations. To understand the motivation for this feature, run `hband` on the following simple p-n junction:

```
v1  bulk
v1  50.0   1.0E18  0.0
v2  50.0  -5.0E17  0.0
v2  bulk
```

Notice that the electron and hole densities are depleted in the vicinity of the junction, as we would expect. Now apply a reverse bias of at least 0.6 V by either moving the left-hand Fermi energy down or the right-hand level up. You will observe that the conduction band passes very close to the right-hand Fermi level and thus a very unphysical layer of electrons appears on the right-hand (p-type) side of the junction. The way to solve this problem is to turn off the Fermi level in a part of the p-type layer by splitting the layer into two parts and specifying `v0` in the part next to the junction:

```
v1  bulk
v1  50.0   1.0E18   0.0
v0  20.0  -5.0E17   0.0
v2  30.0  -5.0E17   0.0
v2  bulk
```

The `v0` layer on the lower-doped side of the p-n junction avoids the unphysical electron layer for reverse biases up to about 2 V in this case. The use of the `v0` option should be guided by one's physical intuition.

### B. Graded Layers

It is possible to specify graded layers as well. The syntax is illustrated in the following design file:

```
v1  bulk
v1  30.0   1.0E18   0.3 Al
v1  40.0 graded
v2  30.0  -5.0E17   0.2 In
v2  bulk
```

The graded layer is assumed to be linearly graded in both composition and doping between the values of those layers which bound the graded layer.

### C. Stopping the Iteration

If it becomes desirable to interrupt the iterative calculation (typically because too small a mesh spacing was chosen so that the computations take excessively long), press the "Stop" key at the upper left corner of the keyboard. The iteration will be stopped upon completion of the current step.

## V. User Feedback

Please forward any comments, observations of bugs, or requests for added functionality to Bill Frensley, x4436, MS 154, VAX RESBLD:FRENSLEY.

## VI. Acknowledgment

The development of hband was supported by the Defense Advanced Research Projects Agency under contract N00014-87-C-0363 (monitored by the Office of Naval Research) and by the U. S. Air Force Wright Research and Development Center under contract F33615-89-C-1074.

# APPENDIX C

# QUANTUM KINETIC THEORY OF NANOELECTRONIC DEVICES

# QUANTUM KINETIC THEORY OF NANOELECTRONIC DEVICES[1]

*William R. Frensley*

Texas Instruments Incorporated
Dallas, Texas 75265

## 1. INTRODUCTION

One of the principal features of nanometer-scale structures is the appearance of quantum-mechanical effects in such phenomena as electron transport. Many of these effects, including the quantum Hall effect [1], the Aharonov-Bohm effect [2], and universal conductance fluctuations [3], are observed in systems which are kept very near to thermal equilibrium (that is, in the linear response regime). Such effects are observed only at cryogenic temperatures and only with sophisticated signal-detection schemes (such as a lock-in amplifier). In marked contrast to such phenomena are the quantum-interference effects seen in some semiconductor nanostructures, such as the quantum-well resonant-tunneling diode (RTD) [4,5]. These effects are observed when the system is driven far from equilibrium by an external bias voltage and they persist to well above room temperature. They could, if one so desired, be observed using only a low-precision voltmeter and a milliammeter. There is thus a persuasive reason for studying the physics of nanostructures driven far from equilibrium. We shall see that under such circumstances pure-state quantum mechanics is not an adequate description and must be replaced with a quantum kinetic theory.

The RTD is made of very thin heteroepitaxial layers designed such that the conduction-band profile includes a double-barrier structure. Multiple reflections of the electron wavefunction from these barriers gives rise to resonances in the transmission probability in the same way that such resonances occur in an optical Fabry-Perot interferometer. The structure and behavior of the RTD is summarized in Fig. 1. The $I(V)$ curve of a good experimental

[1]Supported in part by the Office of Naval Research and the Defense Advanced Research Projects Agency.



Copyright © 1989 by Academic Press, Inc.
All rights of reproduction in any form reserved.
ISBN 0-12-585000-X

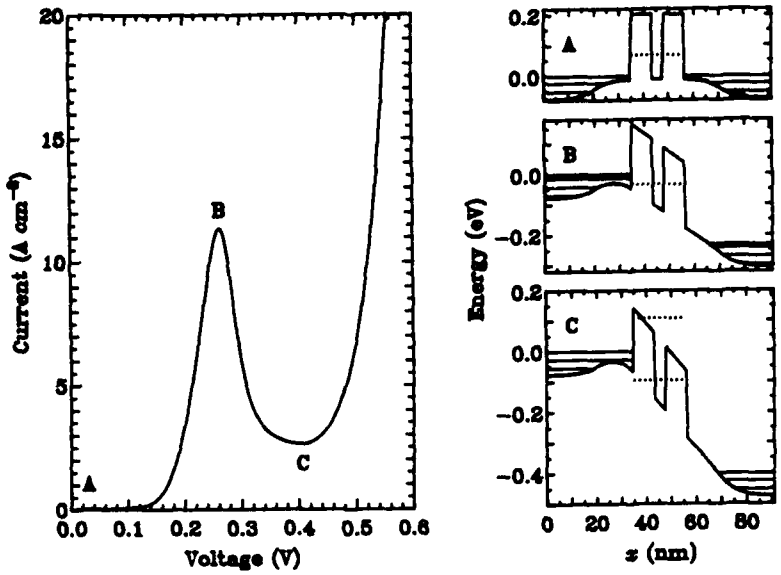


Fig. 1. Structure and behavior of the resonant-tunneling diode.

device measured at 77K is shown to the left and the conduction-band profiles at voltages corresponding to the labeled points are shown to the right. (Occupied electron states are indicated by horizontal hatching and the resonant levels by dotted lines.) In equilibrium, **A**, the chemical potentials are equal and no current flows. At such a voltage that the resonant level lines up in energy with the occupied states in the cathode, **B**, the resonant-tunneling current reaches a peak. At higher voltages the resonant level is pulled below the lowest occupied state in the cathode, **C**, the resonant-tunneling current ceases, leading to a negative differential resistance between **B** and **C**.

Why are quantum interference effects so much more prominent in the resonant-tunneling diode than those that occur in metallic nanostructures? The different topologies of the electron trajectories is a part of the reason. Aharonov-Bohm and similar devices are analogous to the Michelson interferometer, which is considerably less robust than the Fabry-Perot configuration. However, a much more fundamental reason is that the quantum effects in the RTD are observed far from thermodynamic equilibrium (*i.e.*, with a large chemical potential difference across the diode), where a much wider variety of phenomena are possible than in the linear response regime. The present work will be concerned with semiconductor nanostructures driven far from equilibrium. We shall assume that the electrons in such a structure interact only via their mean field (the Hartree potential), and that the Hartree potential and thus the spatial electron density is a physical observable. One might

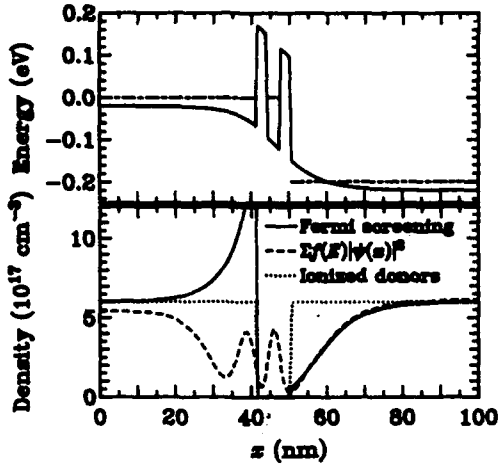


Fig. 2. Fermi-screened potential and resulting charge densities.

expect that under these circumstances elementary quantum mechanics would provide an adequate theory. In fact it is not adequate and we will see how the inadequacies appear in an attempt to evaluate the self-consistent potential. The problem can be traced to the *a priori* assumption that the single-particle density matrix is diagonal in the eigenbasis of the Hamiltonian. Removing this assumption leads one to a quantum kinetic theory.

## 2. SCHROEDINGER EQUATION AND SELF-CONSISTENCY

In the absence of any contrary results we would expect that the self-consistent potential for a resonant-tunneling diode under bias would resemble that obtained from the Thomas-Fermi screening theory, such as that shown in Fig. 2. Generalizing the Thomas-Fermi theory to the finite temperature case, we obtain the Fermi-screened potential $V(x)$ by solving

$$-\epsilon\nabla^2 V = q\left\{2(m^*/2\pi\hbar^2\beta)^{3/2}\mathcal{F}_{1/2}[\beta(\mu - qV)] - N_d\right\}, \qquad (1)$$

where $\mathcal{F}_{1/2}$ is the Fermi-Dirac integral, $\mu$ is the chemical potential, and $N_d$ is the density of ionized donors. The potential of Fig. 2 was obtained by solving (1) with the appropriate chemical potential in each of the thick contact layers and neglecting any charge density in the barriers or well. As one would expect the potential drop is accomodated by an accumulation layer on the left-hand side of the structure and a depletion layer on the right-hand side. The electron density implied by the Fermi-screening approximation is shown by the solid line. In this and all subsequent computations the temperature was taken to be 300 K.

Now, let us take the Fermi-screened potential and insert it into Schroedinger's equation. We find the eigenstates $\psi_l(E,x)$ incident from the left with unit amplitude and $\psi_r(E,x)$ incident from the right. Using these solutions we find the total electron density, which we will express as the diagonal elements of the density matrix:

$$\begin{aligned}\rho(x,x') &= \int_{V_l}^{\infty} \frac{dE}{2\pi\hbar v_l(E)} f(E-\mu_l)\psi_l(E,x)\psi_l^*(E,x') \\ &+ \int_{V_r}^{\infty} \frac{dE}{2\pi\hbar v_r(E)} f(E-\mu_r)\psi_r(E,x)\psi_r^*(E,x'), \qquad (2)\end{aligned}$$

where $V_{l,r}$ are the asymptotic potentials to the left and right, $v_{l,r}(E)$ is the velocity of an electron of energy $E$ at the respective boundary. Here $f$ is the Fermi-Dirac distribution function integrated over the transverse momenta: $f(E) = (m^*/\pi\hbar^2\beta)\ln(1+e^{-\beta E})$. The density resulting from this calculation is shown by the dashed line in Fig. 2, and it displays several interesting features. One is the small peak centered in the quantum well. This is the charge build-up due to resonant tunneling. Another interesting feature is the asymptotic values of the electron density, lower than the donor density on the left and slightly higher than the donor density on the right. This is due to the resonant transmission of a part of the electron distribution incident from the left. For most energies the electrons are reflected and thus for each incident $k$ there will be an equal density of electrons in the left-hand contact with $-k$. However these electrons will be absent for states in the transmission resonance. We can estimate the deficit as $j/qv_l(E_0)$ where $j$ is the tunneling current density and $E_0$ is the resonant energy. Numerical calculations verify that this value is equal to the electron deficit in the left-hand electrode. Similarly, the resonant-tunneling electrons contribute an excess density to the right-hand electrode which is well approximated by $j/qv_r(E_0)$. These effects are really artifacts of the assumption of purely ballistic transport inherent in Schroedinger's equation and will not persist if inelastic scattering processes are present.

The most important feature of the electron density inferred from Schroedinger's equation is the reduction in the electron density in the region where screening theory predicts an accumulation layer ($20\,\text{nm} \le x \le 40\,\text{nm}$). This decreased density is readily explained: The current density $\langle\psi|j|\psi\rangle$ from each scattering eigenstate is independent of $x$. As such a state propagates into a region of decreasing potential, its speed of propagation must increase and thus, to maintain the current constant, its amplitude must decrease.

Where, then, does the increased electron density in the screening theory come from? It comes from electron occupation of a greater number of states, rather than from increased amplitude in any given state. The potential "notch" permits states with nonnegligible amplitude on the left-hand side of the barrier and with energies below $V_l$. These states are connected via

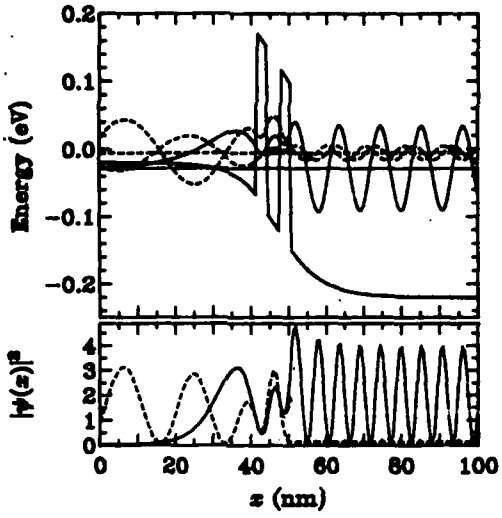


Fig. 3. Fermi-screened potential and resulting wavefunctions.

tunneling to the propagating states incident from the right. The discrepancy between screening and scattering theory is thus explained: Screening theory assumes that the notch states are in thermal equilibrium with the left-hand side of the structure while scattering theory assumes that they are in equilibrium with the right-hand side. Actually, the situation will be governed by the rates of two competing processes: (i) inelastic scattering of electrons from propagating states into the notch states and (ii) tunneling out of the notch states into the right-hand electrode [6]. Again, inelastic processes are the key to obtaining a physically reasonable distribution of electrons.

To evaluate the effects of inelastic processes one naturally turns first to the Fermi golden rule. Actually, the more complete expression underlying this picture is the Pauli master equation, which assumes that the density matrix is diagonal in the eigenbasis of the Hamiltonian [7]. In the RTD this means that the form (2) is assumed, with the distribution functions $f$ replaced by probabilities $P_i$ to be determined. The master equation is then

$$dP_i/dt = \sum_j [W_{ij} P_j(t) - W_{ji} P_i(t)], \tag{3}$$

where the $W_{ij}$ are the golden-rule transition rates. When applied to the RTD problem, this picture leads to a violation of the continuity equation. To observe this, let us look at the eigenstates derived from the Fermi-screened potential. Fig. 3 shows two typical states, one with $E_1 > V_l$ (dashed line, both real and imaginary parts shown) and the other in the "notch" with

$E_2 < V_l$ (solid line). The spatial distributions of these states are shown in the lower part of the figure. Now, the Pauli master equation (3) implies that a transition process like phonon scattering will transfer electron density at some rate from the state at $E_1$ to the state at $E_2$. Because of the very different spatial distributions of the these states, this must involve a current flow with nonzero divergence. However each of the states has a uniform current density and thus the diagonal density matrix describes a state with no current divergence. Using such a model, which violates continuity, in a self-consistent calculation is a very dangerous procedure. To satisfy the continuity equation, we must allow off-diagonal elements of the density matrix. This leads us to a quantum kinetic theory.

## 3. QUANTUM KINETIC THEORY

A quantum kinetic theory is expressed in terms of the single-particle density matrix $\rho(x, x')$, or a mathematically equivalent object such as the Wigner distribution function. The time evolution of $\rho$ is described by a kinetic equation, which should include the quantum-interference effects described by Schroedinger's equation, and may include the effects of inelastic processes such as those described by the Pauli master equation. The density matrix is directly obtained by solving this kinetic equation; thus the natural basis states (the eigenvectors of $\rho$) are obtained from the kinetic theory as a result, rather than inserted as an *a priori* assumption.

A quantum kinetic theory appropriate for nanostructure devices such as the RTD has been developed over the past few years [8,9]. Due to the openness of any device with respect to electron flow, the theory is most naturally expressed in terms of the Wigner distribution function $f(x, k)$. The kinetic equation has the form

$$\partial f/\partial t = \mathcal{L} f/i\hbar + \mathcal{C} f, \tag{4}$$

where $\mathcal{L}$ is the Liouville superoperator describing the ballistic motion and $\mathcal{C}$ is a collision superoperator including dissipative interactions. The effects of the electrical connections to the device are described by open-system boundary conditions which are time-irreversible and modify $\mathcal{L}$ so as to render it non-hermitian [8,10]. The kinetic equation without the collision term has been successfully used to calculate the dc, large-signal transient, and small-signal ac response of the RTD [8,11].

The form of the kinetic equation (4) is Markovian, which means that the time evolution depends only upon the state of the system at present, and not upon its prior history. Non-Markovian behavior can result when information about the state of the system is stored in degrees of freedom which are not explictily included in the kinetic model. These could include the occupation numbers and phases of phonon modes, electron correlations in the contacts, or two-or-more-electron correlation effects. Thus the Markovian kinetic equation

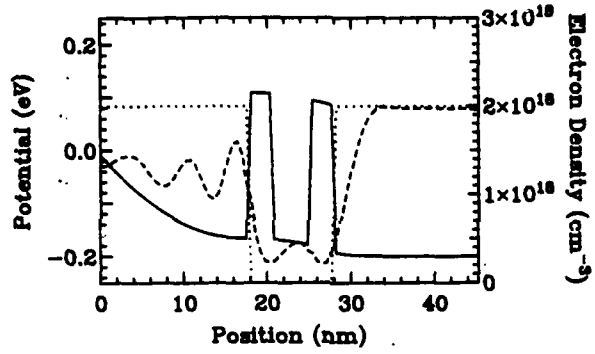


Fig. 4. Potential and density from self-consistent Wigner function with no scattering.

is only a first approximation, but we will see that at least it does not display the unphysical features that we observed in the scattering theory.

The form of the collision superoperator $\mathcal{C}$ is constrained by the requirement of continuity. An instantaneous scattering process cannot move an electron from one position to another, so $\mathcal{C}$ must contain a factor of $\delta(x - x')$. That is, $\mathcal{C}$ must be local in its effect upon the electron distribution, but it can be nonlocal in the sense that $\mathcal{C}(x, k; x, k')$ can depend upon the impurity distribution or phonon modes at other values of $x$. We would expect on physical grounds that $\mathcal{C}$ should be of the form of a master operator, such as appears in the Pauli equation (3). Thus $\mathcal{C}$ should have the form:

$$\mathcal{C}(x, k; x', k') = \delta(x - x') \left[ W_{kk'} - \delta(k - k') \int dk'' \, W_{k''k} \right], \tag{5}$$

where $W_{kk'}$ is the transition rate from $k'$ to $k$. Published analyses imply that, at least at some level of approximation, the $W_{kk'}$ are equal to the golden rule transition rates between plane wave states [12,13]. Note that the kinetic approach avoids making assumptions about which states are participating in a transition by considering all possible transitions between complete sets of states.

The influence of inelastic processes on the self-consistent potential and electron density of the RTD using the kinetic theory are illustrated in Figs. 4–6. The kinetic equation (4) for steady state was solved self-consistently with Poisson's equation for the Hartree potential, using a multidimensional Newton technique. A device with a somewhat larger doping level in the contacts than that of Figs. 2–3 was assumed, to reduce the screening length and thus the size of this rather time-consuming computation.

If no collision term is included, the self-consistent solution is that shown

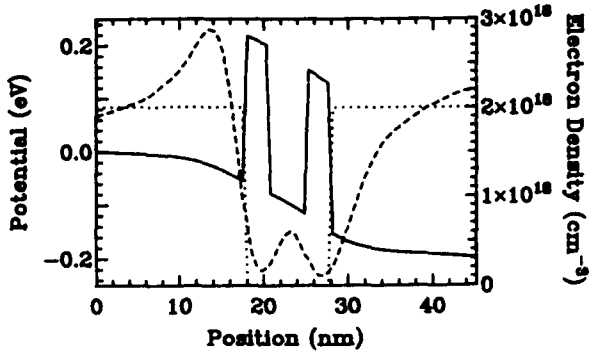


Fig. 5. Potential and density from self-consistent Wigner function with simple relaxation, $\tau = 100\,\mathrm{fs}$.

in Fig. 4. The solid line represents the potential, the dashed line is the resulting electron density, and the dotted line shows the ionized donor distribution. The problem we first observed in the Schroedinger model is also apparent here: No accumulation layer has formed on the left side of the barriers and the electron density is in fact depleted. This leads to an upward curving of the potential on the left side, which is certainly unphysical. Because the boundary in this case is artificial, occuring in contacting layers which are much thicker in the experimental devices, its position should have a negligible effect on the form of the solution. This can only happen if the electric field approaches a small value at the boundary.

The electric field is much better behaved if inelastic processes are included in the calculation. Fig. 5 shows the self-consistent solution with a simple relaxation-time collision operator ($W_{kk'} = f_0(k)/\tau$, where $f_0(k)$ is a normalized Maxwellian distribution) with $\tau = 100\,\mathrm{fs}$. In this case, the shape of the potential and charge distribution is much closer to that obtained from screening theory (Fig. 2). However, this relaxation rate is really too large for GaAs devices.

A more realistic model of the scattering processes is used in the calculation of Fig. 6. In this case $C$ was constructed using golden-rule transition rates for longitudinal optical (LO) and acoustic phonons in GaAs. It is apparent that the phonon scattering is trying to form an accumulation layer on the left-hand side, but the scattering rate is not large enough to enforce the screening-theory picture. Such a situation may well occur in structures with thin barriers and thus whose tunneling rate exceeds the inelastic scattering rate. However, the present calculation is not yet entirely satisfactory. If the electric field extended deep into the contact layers, it would certainly affect the shape of the distribution function which those layers supply to the device

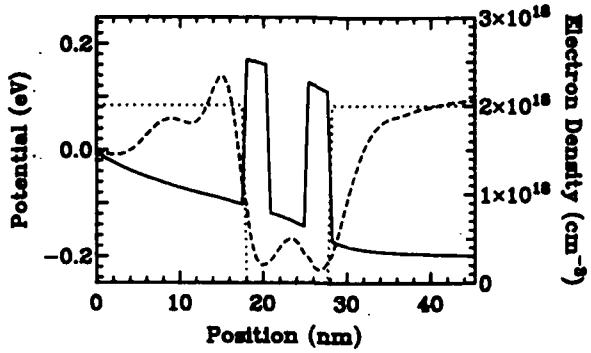


Fig. 6. Potential and density from self-consistent Wigner function with LO and acoustic phonon scattering.

(by displacing the peak of a Maxwellian distribution, for example). Such effects would tend to increase the density on the left and decrease it on the right, which would result in a potential closer to the screening theory result. Simulations which include a simple model of this effect do indeed show a marked reduction of the electric field at the boundaries [14].

## 4. SUMMARY

The quantum effects observed in nanostructures that are close to thermal equilibrium are quantitatively weak effects, but they can be adequately modeled by elementary quantum theory because the form of the density matrix in equilibrium, $\rho \propto e^{-\beta H}$, assures us that the electrons actually occupy the eigenstates of the Hamiltonian. The quantum effects can be much larger in nanostructures that are driven far from equilibrium, but then we have no assurance that $\rho$ is diagonal in the eigenbasis. The inadequacies of pure-state quantum mechanics become particularly apparent when one tries to include self-consistency in an analysis of the resonant-tunneling diode. Such an analysis requires a satisfactory treatment of inelastic processes, which cannot be obtained in terms of pure quantum states.

A satisfactory treatment of inelastic processes can be formulated at a kinetic level. When both self-consistency and inelastic scattering are included in such a model, we find that the shape of the self-consistent potential is qualitatively changed by modifications to the rate of inelastic scattering.

## REFERENCES


[1] D. R. Yennie, Rev. Mod. Phys. **59**, 781 (1987).

[2] A. G. Aronov and Yu. V. Sharvin, Rev. Mod. Phys. **59**, 755 (1987).

[3] P. A. Lee and T. V. Ramarkishnan, Rev. Mod. Phys. **57**, 287 (1985).

[4] L. L. Chang, L. Esaki, and R. Tsu, Appl. Phys. Lett. **24**, 593 (1974).

[5] T. C. L. G. Sollner, W. D. Goodhue, P. E. Tannenwald, C. D. Parker, and D. D. Peck, Appl. Phys. Lett. **43**, 588 (1983).

[6] N. S. Wingreen and J. W. Wilkins, Bull. Am. Phys. Soc. Ser. II **32**, 833 (1987).

[7] H. J. Kreuzer, *Nonequilibrium Thermodynamics and its Statistical Foundations*, (Oxford Univ. Press, New York, 1981), ch. 10.

[8] W. R. Frensley, Phys. Rev. B **36**, 1570 (1987).

[9] U. Ravaioli, M. A. Osman, W. Pötz, N. Kluksdahl, and D. K. Ferry, Physica **134B**, 36 (1985).

[10] W. R. Frensley, "Boundary Conditions for Open Quantum Systems Driven Far from Equilibrium," (unpublished).

[11] W. R. Frensley, Superlattices and Microstructures **4**, 497 (1988).

[12] I. B. Levinson, Zh. Eksp. Teor. Fiz. **57**, 660 (1969) [Sov. Phys —JETP **30**, 362 (1970)].

[13] J. Lin and L. C. Chu, J. Appl. Phys. **57**, 1373 (1985).

[14] R. K. Mains and G. I. Haddad, "Numerical Considerations in the Wigner Function Modeling of Resonant-Tunneling Diodes," (unpublished).

# APPENDIX D

# EFFECT OF INELASTIC PROCESSES ON THE SELF-CONSISTENT POTENTIAL IN THE RESONANT-TUNNELING DIODE

Solid-State Electronics Vol. 32, No. 12, pp. 1235–1239, 1989
Printed in Great Britain. All rights reserved

0038-1101/89 $3.00 + 0.00
Copyright © 1989 Pergamon Press plc

# EFFECT OF INELASTIC PROCESSES ON THE SELF-CONSISTENT POTENTIAL IN THE RESONANT-TUNNELING DIODE

William R. Frensley

Texas Instruments Incorporated
Dallas, Texas 75265

## ABSTRACT

The self-consistent electrostatic potential of a biased resonant-tunneling diode is examined using a quantum kinetic theory of open systems. The potential obtained is sensitively dependent upon the assumed magnitude of inelastic processes within the device and its contacts. If inelastic processes are neglected one finds a solution with an unphysically large electric field at one boundary, which is also obtained from an analysis using Schroedinger's equation. Including inelastic processes within the device permits screening of the electric field, leading to a much more credible potential. Furthermore, if the mean velocity of the electron distributions on the boundaries is allowed to shift in response to the boundary electric field, the resulting potential profiles closely resemble those obtained from simple screening theory.

## KEYWORDS

Resonant tunneling; Wigner distribution; kinetic theory; self-consistent potential; phonon scattering.

## INTRODUCTION

An understanding of the shape of the energy-band profile is essential to understanding the behavior of any semiconductor device. There are generally two significant contributions to the band profile. One is the the inherent band-edge energy due to the local chemical composition (in the case of heterostructure devices) which will be represented by $E_c(x)$, for the conduction-band energy as a function of position $x$. This is the quantity which gives rise to band discontinuities in the case of abrupt heterojunctions. The other significant contribution to the band profile is the self-consistent electrostatic potential due to the macroscopic distributions of mobile charges and ionized impurities. This contribution will be denoted by $qV(x)$, and is the central focus of the present work.

The evaluation of the self-consistent potential requires an algorithm for determining the distribution of mobile carriers given the potential. When the carriers are well described by classical models such as the simple drift-diffusion equation, the self-consistent calculation is a straightforward application of established semiconductor modeling techniques. However, when classical transport models are not appropriate, new approaches must be developed. The resonant-tunneling diode (RTD) (Chang, 1974; Sollner, 1983) is a prominent example of the latter case. We shall see that the simple models of this device lead to unsatisfactory results for the self-consistent potential.

## ELEMENTARY MODELS

One naturally begins an inquiry into the shape of the self-consistent potential by examining simple models of the phenomenon. For the present purposes these consist of the Thomas-Fermi screening and Hartree self-consistent models. We shall see that these models produce very different estimates of the electron distribution and thus of the self-consistent potential. These models make implicit assumptions about the role of inelastic processes which are very different, and this is the source of this discrepancy.

### Thomas-Fermi Screening Theory

The fundamental approximation made by the Thomas-Fermi theory is that the density of electrons is a local function of the difference between the band-edge potential and the chemical potential. Strictly speaking the Thomas-Fermi theory also assumes zero temperature, but the generalization to finite temperatures is well-known in the context of semiconductor device analysis. In this case the equation describing the potential $V(x)$

becomes

$$-\epsilon\nabla^2 V = q\left(N_c\mathcal{F}_{1/2}\{\beta[\mu-(qV+E_c)]\}-N_d\right), \tag{1}$$

where $N_c = 2(m^*/2\pi\hbar^2\beta)^{3/2}$ is the effective density of states, $\mathcal{F}_{1/2}$ is the Fermi-Dirac integral, $\mu$ is the chemical potential, and $N_d$ is the density of ionized donors. This is strictly an equilibrium model, but it is typically applied to nonequilibrium situations in which one can partition the device into regions which are locally in equilibrium separated by energy barriers in which the electron density is negligible. (Such a model is appropriate so long as the current density is low.) In the typical diode configuration, one will have two such regions characterized by chemical potentials $\mu_l$ and $\mu_r$. The boundary conditions on (1) are derived from the charge neutrality condition and are $qV_{l,r} = (\mu_{l,r} - E_c) - \mathcal{F}_{1/2}^{-1}(N_d/N_c)$, with it understood that appropriate values of $E_c$, $N_d$, and $N_c$ be used.

The result of such a screening calculation for a resonant-tunneling diode structure is shown in Fig. 1, neglecting any electron density in the barriers or the quantum well. As one would expect the potential drop is accomodated by an accumulation layer on the left-hand side of the structure and a depletion layer on the right-hand side. The electron density implied by the Thomas-Fermi approximation is shown by the solid line. It displays an unphysical cusp at the edge of the barrier, which is an artifact of the assumption that the density only depends upon the local potential. In this and all subsequent computations the temperature was taken to be 300 K.

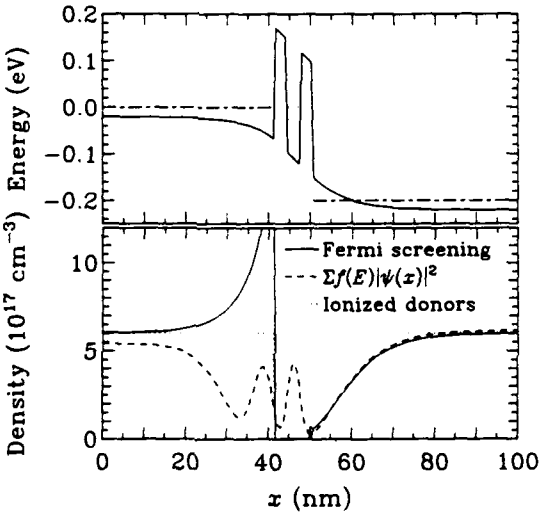


Fig. 1. Potential and Electron Density from the Thomas-Fermi Model. Also shown is the electron density obtained by using this poential in Schroedinger's equation, which does not show an accumulation layer.

## Hartree Self-Consistency Using Schroedinger's Equation

Another obvious approach to determining the self-sonsistent potential is to invoke the Hartree method, in which Schroedinger's equation is solved for each occupied state to obtain the electron distribution, and then $V$ is obtained by solving Poisson's equation. This approach has of course been quite successful (with appropriate elaborations) in evaluating the properties of systems in their ground state, or more generally in thermal equilibrium. It fails when applied to far-from-equilibrium systems, as in the present example of the RTD under bias.

To observe the origins of this failure, let us carry through the first step of an iteration to self-consistency. We will take the Thomas-Fermi potential evaluated above and use it in Schroedinger's equation to find the electron distribution. Because the RTD is an open system, we will make the standard assumption that the system is unbounded and the electrons are to be found in scattering eigenstates. These are the eigenstates $\psi_l(E,x)$ incident from the left with unit amplitude and $\psi_r(E,x)$ incident from the right. In the present work they are obtained by direct solution of a finite-difference approximation to Schroedinger's equation. Using these eigenstates we find the total electron density by constructing a density matrix in which the states incident from the left and right are assumed to be Fermi distributed with their respective chemical potentials:

$$\rho(x,x') = \int_{E_l}^{\infty}\frac{dE}{2\pi\hbar v_l(E)}f(E-\mu_l)\psi_l(E,x)\psi_l^*(E,x') + \int_{E_r}^{\infty}\frac{dE}{2\pi\hbar v_r(E)}f(E-\mu_r)\psi_r(E,x)\psi_r^*(E,x'), \tag{2}$$

where $E_{l,r} = qV_{l,r} + E_c(l,r)$ are the asymptotic band edge energies to the left and right, $v_{l,r}(E)$ is the velocity of an electron of energy $E$ at the respective boundary. Here $f$ is the Fermi-Dirac distribution function integrated over the transverse momenta:

$$f(E) = \sqrt{\frac{2\pi\hbar^2\beta}{m^*}} N_c \mathcal{F}_0(\beta E) = \frac{m^*}{\pi\hbar^2\beta} \ln(1 + e^{-\beta E}). \tag{3}$$

The density $\rho(x,x)$ resulting from this calculation is shown by the dashed line in Fig. 1, and it displays several interesting features. One is the small peak centered in the quantum well. This is the charge build-up due to resonant tunneling. Another feature is the asymptotic values of the electron density, lower than the donor density on the left and slightly higher than the donor density on the right. This is due to the resonant transmission of a part of the electron distribution incident from the left, which leaves a deficit in the distribution of reflected electrons on the left, and an excess on the right. These are only artifacts of the assumption of purely ballistic transport inherent in Schroedinger's equation and will not persist if inelastic scattering processes are present.

The most important feature of the electron density inferred from Schroedinger's equation is the reduction in the electron density in the region where Thomas-Fermi theory predicts an accumulation layer ($20\,\text{nm} \leq x \leq 40\,\text{nm}$). This decreased density is readily explained: The current density $\langle\psi|j|\psi\rangle$ from each scattering eigenstate is independent of $x$. As such a state propagates into a region of decreasing potential, its speed of propagation must increase and thus, to maintain the current constant, its amplitude must decrease.

Where, then, does the increased electron density in the Thomas-Fermi theory come from? It comes from electron occupation of a greater number of states, rather than from increased amplitude in any given state. The potential "notch" permits states with nonnegligible amplitude on the left-hand side of the barrier and with energies below $E_l$. These states are connected via tunneling to the propagating states incident from the right. The discrepancy between the simple models is thus explained: The Thomas-Fermi model assumes that the notch states are in thermal equilibrium with the left-hand side of the structure while scattering theory assumes that they are in equilibrium with the right-hand side. In reality the situation will be governed by the rates of two competing processes: (i) inelastic scattering of electrons from propagating states into the notch states and (ii) tunneling out of the notch states into the right-hand electrode (Wingreen and Wilkins, 1987). Again, inelastic processes are the key to obtaining a physically reasonable distribution of electrons.

## QUANTUM KINETIC THEORY

A proper description of dissipation cannot be obtained within the framework of elementary quantum mechanics, in which only pure states are comtemplated. The characteristic feature of dissipative processes is that one cannot determine into *which* state an electron will scatter, only the probabilies of scattering into a group of states. Thus, even if the electron is initially in a pure state, it will evolve into a mixed state, and must be described as such. On the other hand, quantum kinetic theory is expressed in terms of the single-particle density matrix $\rho(x,x')$, or a mathematically equivalent object such as the Wigner distribution function $f(q,p)$. The time evolution of $\rho$ or $f$ is described by a kinetic equation, which should include the quantum-interference effects described by Schroedinger's equation, and may include the effects of inelastic processes such as phonon scattering. The density matrix is directly obtained by solving this kinetic equation; thus the natural basis states (the eigenvectors of $\rho$) are obtained from the kinetic theory as a result, rather than inserted as an *a priori* assumption.

A quantum kinetic theory appropriate for quantum devices such as the RTD has been developed over the past few years (Frensley, 1987; Mains and Haddad, 1988; Kluksdahl *et al.*, 1989). Due to the openness of any device with respect to electron flow, the theory is most naturally expressed in terms of the Wigner distribution function $f(q,p)$. The kinetic equation has the form

$$\partial f/\partial t = \mathcal{L}f/i\hbar + \mathcal{C}f, \tag{4}$$

where $\mathcal{L}$ is the Liouville superoperator describing the ballistic motion and $\mathcal{C}$ is a collision superoperator including dissipative interactions. The effects of the electrical connections to the device are described by open-system boundary conditions which are time-irreversible and modify $\mathcal{L}$ so as to render it nonhermitian (Frensley, 1987, 1989). These boundary conditions fix the value of $f$ on the *inflowing* boundaries to be the equilibrium value given by (3). The kinetic equation without the collision term has been successfully used to calculate the dc, large-signal transient, and small-signal ac response of the RTD and has also been used to investigate the effects of phonon scattering in this device (Frensley, 1988).

The collision superoperator $C$ is potentially a very complex object, but at some level of approximation it must reduce to the semiclassical form:

$$C(q,p;q',p') = \delta(q-q')\left[W_{pp'} - \delta(p-p')\int dp''\, W_{p''p}\right], \tag{5}$$

where $W_{pp'}$ is the golden-rule transition rate between plane-wave states $p'$ and $p$. For the purposes of the present calculations the three-dimensional dependence of $C$ is projected down into one momentum dimension by assuming that $f$ factors into a function of the longitudinal momentum multiplied by a Maxwellian distribution of the transverse momenta, and integrating over the resulting transverse momenta (Frensley, 1988).

The influence of inelastic processes on the self-consistent potential and electron density of the RTD using the kinetic theory are illustrated in Figs. 2–4. The kinetic equation (4) for steady state was solved self-consistently with Poisson's equation for the Hartree potential $V$, using a multidimensional Newton technique. If no collision term is included, the self-consistent solution is that shown in Fig. 2. The solid line represents the potential, the dashed line is the resulting electron density, and the dotted line shows the ionized donor distribution. The problem we first observed in the Schroedinger model is also apparent here: No accumulation layer has formed on the left side of the barriers and the electron density is in fact depleted. This leads to an upward curving of the potential on the left side and thus a large electric field at the left-hand boundary. Similar solutions have been obtained by Kluksdahl, *et al.* (1989), and solutions of this sort are certainly unphysical. Because the boundary in this case is artificial, occuring in contacting layers which are much thicker in the experimental devices, its position should have a negligible effect on the form of the solution. This can only happen if the electric field approaches a small value at the boundary.

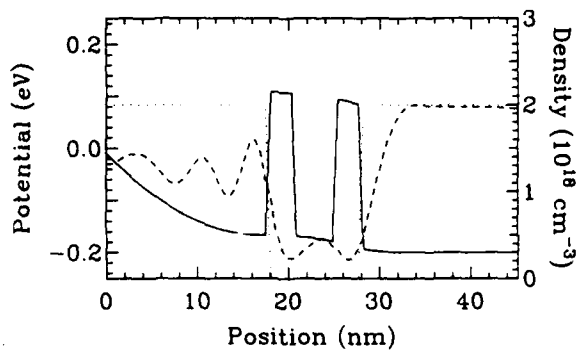


Fig. 2. Potential and Electron Density from a Self-Consistent Wigner-Function Calculation with No Dissipation. The unphysically large electric field at the left-hand boundary would also be obtained from solving Schroedinger's equation self-consistently.

A more plausible potential is obtained if inelastic processes are included in the calculation. Fig. 3 shows the self-consistent solution using a collision operator constructed from the golden-rule transition rates for longitudinal optical (LO) and acoustic phonons in GaAs. It is apparent that the phonon scattering is trying to form an accumulation layer on the left-hand side, but the scattering rate is not large enough to enforce complete screening. Such a situation may well occur in structures with sufficiently thin barriers so that the tunneling rate exceeds the inelastic scattering rate.

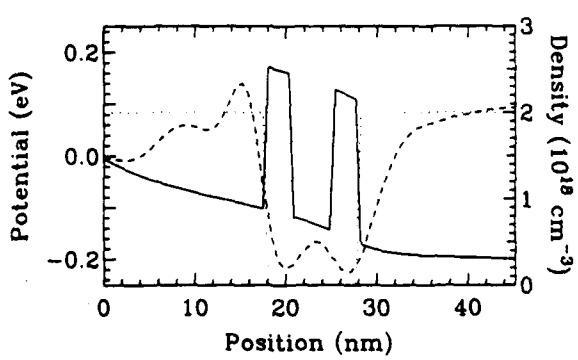


Fig. 3. Self-Consistent Wigner-Function Calculation Including Scattering by LO and Acoustic Phonons.

In steady state current must also be transported through the semiconductor contact layers, and this will modify the distribution of electrons which impinge upon the active region of the RTD. The simplest approximation is a drifted Fermi distribution, obtained by inserting $E = (p - p_0)^2/2m^*$ into (3) (Pötz, 1989), with $p_0 = -\mu_e m^* \nabla V$ where $\mu_e$ is the electron mobility. This models the effect of the resistivity of the contacting layers. Such a drifted distribution function was incorporated in the boundary conditions of the self-consistent calculations. The effect of such boundary conditions have also been investigated by Mains and Haddad (1988). The potential and electron density obtained from the present calculations are shown in Fig. 4. The field at the boundary was taken to extend indefinitely into the contact layers, and the mobility in these layers was taken to be 5000 $cm^2V^{-1}s^{-1}$. The resulting potential profile is quite similar to that expected from the Thomas-Fermi theory, with the electric field approaching a small value at each boundary. If only the contact resistivity is included in the calculation (phonon scattering in the device is neglected) the potential profile qualitatively resembles that of Fig. 3.

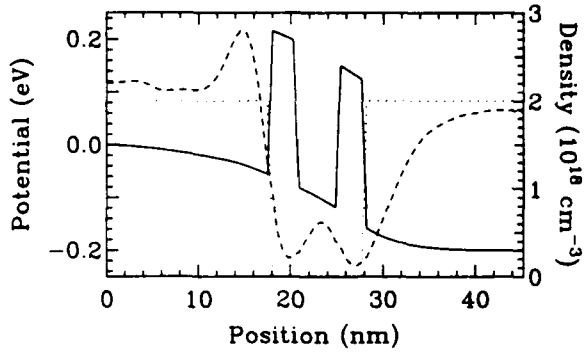


Fig. 4. Self-Consistent Wigner-Function Calculation Including Phonon Scattering and Contact Resistivity. The distribution function at the boundary was taken to be a drifted Fermi distribution with drift velocity determined self-consistently with the electric field at the boundary.

## SUMMARY

The self-consistent potential the RTD is determined by complex interactions between the various processes which affect the transport of electrons through the device. The models provided by elementary quantum mechanics do not provide an accurate description of the potential. This must be obtained from some form of quantum kinetic theory which incorporates realistic models of both the internal dissipation and the contact resistivity.

## ACKNOWLEDGMENT

This work was supported by the U. S. Office of Naval Research.

## REFERENCES

Chang, L. L., L. Esaki, and R. Tsu (1974). *Appl. Phys. Lett.* **24**, 593.

Frensley, W. R. (1987). *Phys. Rev.* **B36**, 1570.

Frensley, W. R. (1988). *Solid-State Electronics* **31**, 739.

Frensley, W. R. (1989). "Boundary Conditions for Open Quantum Systems Driven Far from Equilibrium," (unpublished).

Kluksdahl, N. C., A. M. Kriman, D. K. Ferry, and C. Ringhofer. *Phys. Rev.* **B39**, 7720.

Mains, R. K. and G. I. Haddad (1988). "Numerical Considerations in the Wigner Function Modeling of Resonant-Tunneling Diodes," (unpublished).

Pötz, W. (1989). *Superlattices and Microstructures* **6**, 189.

Sollner, T. C. L. G., W. D. Goodhue, P. E. Tannenwald, C. D. Parker, and D. D. Peck (1983). *Appl. Phys. Lett.* **43**, 588.

Wingreen, N. S., and J. W. Wilkins (1987). *Bull. Am. Phys. Soc.* Ser. II **32**, 833.

# APPENDIX E

# IMPROVED $Al_xGa_{1-x}As/Ga_{1-y}In_yAs/GaAs$ STRAINED-LAYER DOUBLE BARRIER RESONANT TUNNELING STRUCTURE

# IMPROVED $Al_xGa_{1-x}As/Ga_{1-y}In_yAs/GaAs$ STRAINED-LAYER DOUBLE BARRIER RESONANT TUNNELLING STRUCTURE

*Indexing terms: Semiconductor devices and materials, Tunnel diodes, Tunnelling, Gallium compounds*

We report the observation of differential negative resistance in a resonant tunnelling diode which consists of $Al_{0.35}Ga_{0.65}As$ barriers and a $Ga_{0.80}In_{0.20}As$ quantum well, grown on GaAs substrate by molecular beam epitaxy (MBE) at a constant substrate temperature of 550°C, for the entire structure. The current peak/valley ratio at resonance is 6 to 1 at 77 K. Our result demonstrates the feasibility of preparing device-quality MBE $Al_xGa_{1-x}As$ layers at low substrate temperature and fabricating quantum devices involving heterojunctions with severe strain.

Since the first demonstration of negative differential resistance (NDR) in double barrier (DB) resonant tunnelling (RT) diodes on a $GaAs/Al_xGa_{1-x}As$ heterojunction material,[1] considerable progress has been made in understanding the resonant tunnelling phenomenon in this material system.[2-8] Recently, several important applications of the RT phenomenon in a $GaAs/Al_xGa_{1-x}As$ DB structure have been investigated theoretically and/or experimentally, including far infra-red detection up to 2·5THz,[9] oscillations at millimetre-wave frequencies,[10] integration of RT diodes for digital and analogue applications,[11] and quantum-coupled devices.[12,13] Most recently, because of the advantages in employing a quantum-well material with bandgap smaller than that of GaAs emitters, several researchers have reported DBRT diodes with $Al_xGa_{1-x}As$ barriers and a pseudomorphic $Ga_{1-y}In_yAs$ layer as quantum well.[14-17] These advantages include flexibility in controlling the tunnelling probability and reduction of peak-current voltage, which in turn causes decrease in heat dissipation. Although $Ga_{1-y}In_yAs$ has a smaller bandgap than GaAs, the two materials are not lattice-matched. Both the bandgap difference and the lattice mismatch between these two materials are proportional to the InAs mole fraction. The pseudomorphic aspect of $Ga_{1-y}In_yAs/GaAs$ introduces a constraint called critical layer thickness (of $Ga_{1-y}In_yAs$)[18] in the design of DBRT structures. A $Ga_{1-y}In_yAs$ quantum well thinner than the critical layer thickness can have all the mismatch accommodated by elastic strain and therefore show better electrical and optical properties than the thicker layers. It is well established that at $y = 0{\cdot}20$ the critical layer thickness for $Ga_{1-y}In_yAs$ is about 150 Å.[18]

A common figure of merit in characterising the RT diodes is the current peak/valley ratio at the resonance. In the $Al_xGa_{1-x}As/Ga_{1-y}In_yAs/GaAs$ material system, the best result to date showed a peak/valley ratio of 13 at 77 K for $y = 0{\cdot}10$ and a ratio of 2·6 at 1 K for $y = 0{\cdot}20$.[14] We report in this letter our observation of NDR with improved peak/valley ratio of 6 for an $Al_{0.35}Ga_{0.65}As/Ga_{0.80}In_{0.20}As$ strained-layer RT diode at 77 K. The In concentration is extrapolated from photoluminescence and Rutherford backscattering measurements.

Epitaxial growth was carried out in a commercial Perkin-Elmer 425B MBE system equipped with conventional liquid-metal gallium, aluminium and indium sources. To reduce frequency recharges of solid arsenic, and thereby contamination of the liquid-metal sources, three arsenic cells were loaded into the growth chamber. With this measure we found we were able to make well over 200 growth runs (about 1·5 μm per run) without having to break the growth chamber vacuum to recharge the arsenic cells. Samples for this work were prepared after the growth chamber had been used for about 200 growth runs. One significant finding of this work is that while it is generally not possible to grow good-quality $Al_xGa_{1-x}As$ layers by MBE at substrate temperatures much below 600°C,[19] we found good-quality $Al_xGa_{1-x}As$ layers could be grown at 550°C or lower if the layers were 'doped' by a trace amount of indium (less than 0·1%). The indium doping can be accomplished by an indium flux from a source or by utilising residual indium left in the growth chamber (the so-called 'memory effect') due to previous growth runs involving indium. A detailed account will be published elsewhere.* Similar indium doping effects have also been observed in growth of $Al_xGa_{1-x}As$ by organometallic vapour phase epitaxy (OMVPE),[20] and MBE growth of high-quality $Al_xGa_{1-x}As$ layers and HEMTs by antimony doping has been reported.[21]

* SHIH, H. D., ANTHONY, J. M., DUNCAN, W. M., and YANG, C. H.: to be published

The sample structure consists of a 5000 Å $n^+$ (Si, doped to $\simeq 2 \times 10^{18}\,cm^{-3}$) GaAs buffer layer grown on an Si-doped $n^+$ GaAs substrate, followed by a 100 Å undoped GaAs spacer, 30 Å undoped $Al_{0.35}Ga_{0.65}As$, 50 Å undoped $Ga_{0.80}In_{0.20}As$ quantum well, 30 Å undoped $Al_{0.35}Ga_{0.65}As$ barrier and a 1000 Å undoped GaAs cap layer. The entire structure was grown at 550°C.

The GaAs emitter windows are first patterned by using photolithography. After depositing Au/Ni/Ge/Ag/Au films onto the surface, a lift-off process is used to define the emitters. The sample is then alloyed by rapid thermal annealing to form shallow ohmic contacts (less than 1000 Å, the thickness of the undoped cap layer). The collector ohmic contact is also made to the $n^+$ substrate. The device structure is shown in Fig. 1.

Fig. 2 shows the I/V characteristics of a RT diode measured at room temperature and 77 K. Positive polarity refers to the emitter (at the surface of the sample) being positively biased with respect to the collector contact (the $n^+$ substrate). The room temperature characteristics indicate the position of resonant tunnelling at 1·25 V. The large background current is probably contributed from thermo-ionic injection. At 77 K, NDR is clearly observed at the same voltage and the current peak/valley ratio increases to 6 : 1, which is the first reported observation of NDR with an InAs mole fraction as high as 20% in the $Ga_{1-y}In_yAs$ quantum well. The peak-current voltage position is the same for both room temperature and 77 K, indicating that the series resistance is not temperature-dependent. The $n^+$ emitter is defined by alloying, which leaves an undoped GaAs spacer near the first $Al_{0.35}Ga_{0.65}As$ barrier. Although the lowest quantum level in the quantum well lies close or below the conduction band minimum of GaAs regions near the $Al_{0.35}Ga_{0.65}As$ barriers, the conductance near zero bias is nearly zero.

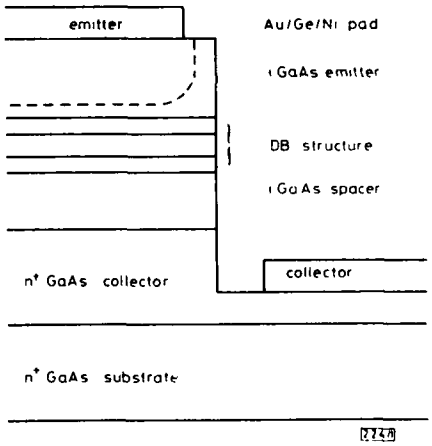


**Fig. 1** *Schematic cross-section of a typical strained-layer double barrier resonant tunneling structure*

The observation of NDR, with a large peak/valley ratio, in the severely strained $Ga_{0.80}In_{0.20}As/Al_{0.35}Ga_{0.65}As/GaAs$ material system promises another degree of freedom in designing quantum devices,[22,23] such as RT transistors. A higher electron transverse mobility will benefit the transverse conduction in three-terminal devices, and a smaller bandgap in the $Ga_{1-y}In_yAs$ quantum well can further hide the ground state.

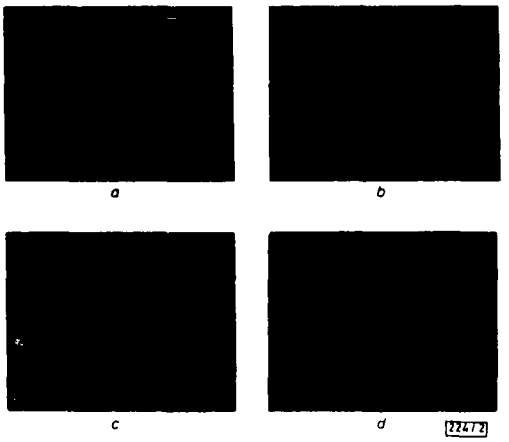


**Fig. 2** *Current-voltage characteristics of the DBRT structure measured with a curve tracer*

*a* Room temperature
*b, c, d* at 77 K
The zero-bias position for *c* is shifted to the lower-left corner

*Acknowledgments:* We would like to thank R. T. Bate for encouragement, D. L. Plumton for many helpful discussions, and A. L. Buehler and F. A. Ferreira for excellent technical assistance. One of us (HDS) would like to thank L. R. Dawson of Sandia National Laboratories for many useful discussions on strained layer epitaxy. This work was supported in part by the Office of Naval Research and the Defense Advanced Research Projects Agency under Contract Number N00014-87-C-0363.

C. H. YANG
H. D. SHIH

*Texas Instruments Incorporated*
*Central Research Laboratories*
*P.O. Box 655936, MS 154*
*Dallas, TX 75265, USA*

*15th March 1988*

## References

1 CHANG, L. L., ESAKI, L., and TSU, R.: 'Resonant tunneling in semiconductor double barriers', *Appl. Phys. Lett.*, 1974, **24**, pp. 593–595
2 RICCO, B., and AZBEL, M. YA.: 'Physics of resonant tunneling: the one-dimensional double-barrier case', *Phys. Rev. B*, 1984, **29**, pp. 1970–1982
3 LURYI, S.: 'Frequency limit of double-barrier resonant-tunneling oscillators', *Appl. Phys. Lett.*, 1985, **47**, pp. 490–492
4 FRENSLEY, W. R.: 'Wigner-function model of a resonant-tunneling semiconductor device', *Phys. Rev. B*, 1987, **36**, pp. 1570–1580
5 MENDEZ, E. E., WANG, W. I., RICCO, B., and ESAKI, L.: 'Resonant tunneling of holes in AlAs–GaAs–AlAs heterostructures', *Appl. Phys. Lett.*, 1985, **47**, pp. 415–417
6 OHMISHI, H., INATA, T., MUTO, S., YOKOYAMA, N., and SHIBATOMI, A.: 'Self-consistent analysis of resonant tunneling current', *Appl. Phys. Lett.*, 1986, **49**, pp. 1248–1250
7 GOLDMAN, V. J., and TSUI, D. C.: 'Resonant tunneling in magnetic fields: evidence for space-charge buildup', *Phys. Rev. B*, 1987, **35**, pp. 9387–9390
8 GOLDMAN, V. J., and TSUI, D. C.: 'Observation of intrinsic bistability in resonant-tunneling structures', *Phys. Rev. Lett.*, 1987, **58**, pp. 1256–1259
9 SOLLNER, T. C. L. G., GOODHUE, W. D., TANNENWALD, P. E., PARKER, C. D., and PECK, D. D.: 'Resonant tunneling through quantum wells at frequencies up to 2·5 THz', *Appl. Phys. Lett.*, 1983, **43**, pp. 588–560
10 SOLLNER, T. C. L. G., BROWN, E. R., GOODHUE, W. D., and LE, H. Q.: 'Observation of millimeter-wave oscillations from resonant tunneling diodes and some theoretical considerations of ultimate frequency limits', *Appl. Phys. Lett.*, 1987, **50**, pp. 332–334
11 SEN, S., CAPASSO, F., and CHO, A. Y.: 'Integration of GaAs/AlAs resonant tunneling diodes for digital and analog applications with reduced circuit complexity'. Proc. GaAs IC Symposium, 1987, pp. 61–64
12 HEILMEIER, G. H.: 'Microelectronics: End of the beginning or beginning of the end?', *in* 'International Electron Devices Meeting (IEDM) Technical Digest', pp. 2–5 (1984)
13 BATE, R. T., FRAZIER, G. A., FRENSLEY, W. R., LEE, J. W., and REED, M. A.: 'Prospects for quantum integrated circuits', *Proc. SPIE*, 1987, **792**, pp. 26–35
14 TOYOSHIMA, H., ANDO, Y., OKAMOTO, A., and ITOH, T.: 'New resonant tunneling diode with a deep quantum well', *Jpn. J. Appl. Phys.*, 1986, **25**, pp. L786–L788
15 LEE, G. S., HSIEH, K. Y., and KOLBAS, R. M.: 'Room-temperature negative differential resistance in strained-layer GaAs–AlGaAs–InGaAs quantum well heterostructures', *Appl. Phys. Lett.*, 1986, **49**, pp. 1528–1530
16 REED, M. A., and LEE, J. W.: 'Resonant tunneling in a GaAs/AlGaAs barrier/InGaAs quantum well heterostructure', *Appl. Phys. Lett.*, 1987, **50**, pp. 845–847
17 SODERSTROM, J., ANDERSSON, T. G., and WESTIN, J.: 'Resonant tunneling in double barrier structures with GaAs and (InGa)As quantum wells', *Superlattices and Microstructures*, 1987, **3**, pp. 283–285
18 FRITZ, I. J., GOURLEY, P. L., and DAWSON, L. R.: 'Critical layer thickness in $In_{0.20}Ga_{0.80}As$/GaAs single strained quantum well structures', *Appl. Phys. Lett.*, 1987, **51**, pp. 1004–1006
19 SHIRAKI, Y., MISHIMA, T., and MORIOKA, M.: 'Low temperature MBE growth of high quality AlGaAs', *J. Cryst. Growth*, 1987, **81**, pp. 164–168
20 SILLMON, R. S., GASKILL, D. K., OVADIA, S., and BOTTKA, N.: 'Isoelectronic indium doping of GaAs and AlGaAs grown by OM-VPE'. Paper N-1 at Electronic Materials Conference, University of California at Santa Barbara, June 24–26, 1987
21 WOOD, C. E. C., KERR, T. M., MCLEAN, T. D., WESTWOOD, D. I., MEDLAND, J. D, BLIGHT, S., and DAVIES, R.: 'State-of-the-art AlGaAs alloys by antimony doping', *J. Appl. Phys.*, 1986, **60**, pp. 1300–1305
22 WOODWARD, T. K., and MCGILL, T. C.: 'Integration of a resonant-tunneling structure with a metal-semiconductor field-effect transistor', *Appl. Phys. Lett.*, 1987, **51**, pp. 1542–1544
23 CAPASSO, F., and KIEHL, R. A.: 'Resonant tunneling transistor with quantum well base and high-energy injection: A new negative differential resistance device', *J. Appl. Phys.*, 1985, **58**, pp. 1366–1368

# APPENDIX F

## OBSERVATION OF NEGATIVE DIFFERENTIAL RESISTANCE IN $Al_{0.2}Ga_{0.6}As/Al_{0.4}Ga_{0.6}As/GaAs$ DOUBLE BARRIER RESONANT TUNNELING STRUCTURE

# OBSERVATION OF NEGATIVE DIFFERENTIAL RESISTANCE IN $Al_{0.2}Ga_{0.8}As/Al_{0.4}Ga_{0.6}As/GaAs$ DOUBLE BARRIER RESONANT TUNNELLING STRUCTURE

*Indexing terms: Semiconductor devices and materials, Tunnelling, Diodes*

Negative differential resistance has been observed in the current/voltage characteristics of a double barrier resonant tunnelling structure with $Al_{0.2}Ga_{0.8}As$ emitters, $Al_{0.4}Ga_{0.6}As$ barriers and GaAs quantum well for the first time. The NDR becomes clear at low temperatures below 77 K, and the current/voltage characteristic is asymmetric. Our results demonstrate that high-quality *abrupt* GaAs–$Al_xGa_{1-x}As$–$Al_yGa_{1-y}As$ heterojunctions can be of use in resonant tunnelling structures.

Resonant tunnelling (RT) in heterojunctions has been under investigation since the first report[1] on the observation of negative differential resistance (NDR) in a double barrier (DB) structure. Various two-terminal RT diodes of different materials systems, grown by molecular beam epitaxy (MBE), have been demonstrated. Recently, three-terminal operation of the so-called resonant tunnelling transistor has been proposed,[2] in which the tunnelling probability of hot electrons can be modulated by biasing the quantum well base. High speed switching capability of this unipolar transistor is expected due to the ultrashort intrinsic tunnelling time. To confine electrons in the quantum well (as the base of the tunnelling transistor) under biasing conditions the bandgap of the quantum well should be less than that of the collector.* For $GaAs/Al_xGa_{1-x}As$ heterostructures, which is the most mature MBE-grown material system, one way to lower the resonant level in the quantum well is to employ $Ga_{1-x}In_xAs$. For example, $Ga_{0.74}In_{0.26}As$ has a bandgap of ~1 eV, less than that of GaAs. However, the difficulty of using $Ga_{1-x}In_xAs$ is in the sample growth technique.[3] The increasing lattice-mismatch between $Ga_{1-x}In_xAs$ and GaAs with increasing In concentration results in dislocations and surface roughness, which destroy the resonant tunnelling phenomenon. Our approach is to increase the conduction band energy $E_c$ of the collector and emitter, to be greater than the lowest resonance level under bias conditions. In this paper, we report the first observation of NDR in a double barrier RT diode with such raised emitter structure, which has a GaAs quantum well, $Al_xGa_{1-x}As$ barriers ($x = 0.4$) and $Al_yGa_{1-y}As$ collector and emitter ($y = 0.2$).

The sample is grown on Si doped $n^+$-GaAs substrate by MBE in a Perkin-Elmer 425B system equipped with conventional effusion cells. The sample structure is shown in Table 1. It consists of 5000 Å $n^+$ GaAs buffer layer, a GaAs-$Al_{0.2}Ga_{0.8}As$ $n^+$ graded junction, 200 Å $n^+$ $Al_{0.2}Ga_{0.8}As$, 50 Å undoped $Al_{0.4}Ga_{0.6}As$ barrier, 100 Å undoped GaAs quantum well, 50 Å undoped $Al_{0.4}Ga_{0.6}As$ barrier, 200 Å $n^+$ $Al_{0.2}Ga_{0.8}As$, a $Al_{0.2}Ga_{0.8}As$ GaAs $n^+$ graded junction, and 5000 Å $n^+$ GaAs capping layer. Two Ga cells are employed for the growth of the *abrupt* $Al_xGa_{1-x}As/Al_yGa_{1-y}As$ heterojunctions with two different Al concentrations. Two terminal devices are defined by standard photolithography and mesa etching. Ohmic contacts are formed by NiGe/Au evaporation and alloying. The positive bias referred to as a positive voltage is applied to the top contact. The $I/V$ characteristic of a diode with an area of $4\,\mu m \times 4\,\mu m$ is shown in Fig. 1. At room temperature, see Fig. 1*a*, the nonlinear conduction below 200 mV indicates a non-ohmic transport. When the temperature is lowered to 77 K, as shown in Fig. 1*b*, the resonant tunnelling appears as a shoulder in the $I/V$ characteristics. However, at liquid helium temperature, see Fig. 1*c*, NDR is clearly observed. The peak current levels are $36\,\mu A$ and $10\,\mu A$ for both positive and negative biases, respectively, and the voltage positions are approximately the same, at 600 mV. Owing to the unknown contact resistance and self-consistent band bending effect, the voltage positions cannot be directly converted to resonant energy levels.

**Table 1** SCHEMATIC DEVICE STRUCTURE OF DBRT DIODE, WHERE $x = 0.4$ AND $y = 0.2$

| Å | | |
|---|---|---|
| 5000 | $n^+$ | GaAs cap |
| Graded | $n^+$ | $Al_yGa_{1-y}As$ to GaAs |
| 200 | $n^+$ | $Al_yGa_{1-y}As$ |
| 50 | $i$ | $Al_yGa_{1-y}As$ spacer |
| 50 | $i$ | $Al_xGa_{1-x}As$ barrier |
| 100 | $i$ | GaAs well |
| 50 | $i$ | $Al_xGa_{1-x}As$ barrier |
| 50 | $i$ | $Al_yGa_{1-y}As$ spacer |
| 200 | $n^+$ | $Al_yGa_{1-y}As$ |
| Graded | $n^+$ | GaAs to $Al_yGa_{1-y}As$ |
| 5000 | $n^+$ | GaAs buffer |
| Substrate | $n^+$ | GaAs |

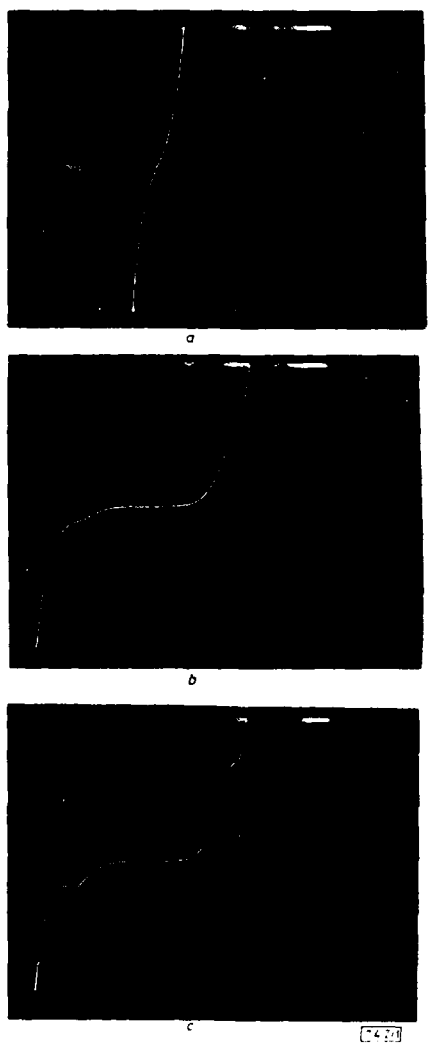

**Fig. 1** *I/V characteristics of DBRT structure*
*a* Room temperature *b* 77 K *c* 4.2 K

* SCHULMAN, J. N., and WALDNER, M.: 'Analysis of second level resonant tunneling diodes and transistors', preprint obtained from J.N. Schulman

Assuming a bandgap offset of 60/40, the resonant energy levels for the above DBRT structure can be calculated by the global transmission method[4] to be ~35 meV, ~138 meV, and ~292 meV above $E_c$ of the GaAs quantum well. The $E_c$ of the $Al_{0.2}Ga_{0.8}As$ emitter is approximately 115 meV above the lowest resonant level. The observed NDR is therefore attributed to a resonant tunnelling through either the second or the third resonance state. Notice that the third resonance level is slightly above the $E_c$ of the $Al_{0.4}Ga_{0.6}As$ barriers, therefore, modulation to the tunnelling current due to the third resonance will be rather weak.

In conclusion, our observation of NDR in the lattice-matched GaAs/AlGaAs material system demonstrates that the energy positions of the emitter, collector and the resonant levels can be tuned in a wide range of energies by using $Al_xGa_{1-x}As/Al_yGa_{1-y}As$ abrupt heterojunctions. The calculated energy positions of the resonance states at zero bias indicates that the electrons injected from the $Al_{0.2}Ga_{0.8}As$ can only resonantly tunnel into the excited states.

We would like to thank R. T. Bate for continuous encouragement. We are also grateful to M. J. Yang for reading the manuscript and for important suggestions. Excellent technical assistance from M. McCain, A. Buehler and F. Ferreira is greatly appreciated. This work is supported in part by the US Office of Naval Research and the Defense Advanced Research Projects Agency under contract N00014-87-C-0363.

C. H. YANG
H. D. SHIH

*Central Research Laboratories*
*Texas Instruments Incorporated*
*PO Box 655936, MS 154, Dallas, TX 75265, USA*

*2nd November 1988*

**References**

1 CHANG, L. L., ESAKI, L., and TSU, R.: 'Resonant tunneling in semiconductor double barriers', *Appl. Phys. Lett.*, 1974, **24**, pp. 593–595

2 JOGAI, B., and WANG, K. L.: 'Dependence of tunneling current on structural variations of superlattice devices', *ibid.*, 1985, **46**, pp. 167–169

3 YANG, C. H., and SHIH, H. D.: 'Improved $Al_xGa_{1-x}As/In_yGa_{1-y}As/GaAs$ strained-layer double barrier resonant tunnelling structure', *Electron. Lett.*, 1988, **24**, pp. 553–555

4 TSU, R., and ESAKI, L.: 'Tunneling in a finite superlattice', *Appl. Phys. Lett.*, 1973, **22**, pp. 562–564

# APPENDIX G

# DEPENDENCE OF PEAK CURRENT DENSITY ON IMPURITY DOPING IN DOUBLE BARRIER RESONANT TUNNELING STRUCTURES

*Inst. Phys. Conf. Ser. No 96: Chapter 9*
*Paper presented at Int. Symp. GaAs and Related Compounds, Atlanta, Georgia, 1988*


# Dependence of peak current density on impurity doping in double barrier resonant tunneling structures

C.H. Yang and R.J. Matyi

Texas Instruments Incorporated, Central Research Laboratories
P.O. Box 655936, MS 154, Dallas, TX 75265, U.S.A.

**ABSTRACT:** We report the design of high peak current density ($\simeq 10^5 A/cm^2$) double barrier resonant tunneling structures. The effects of ionic impurity to the peak current and voltage position at resonance are also studied. The observation of negative differential resistance for structures with heavily doped barriers ($1.0 \times 10^{18}/cm^3$) indicates that the resonant tunneling is not totally destroyed by ionic scattering, although the peak/valley ratio degrades. We discuss the data by self-consistent Poisson equation and a sequential resonant tunneling model, where the originally coherent transmission is broadened and damped due to the impurity scattering.

## 1. Introduction

Resonant tunneling (RT) structures have been extensively studied since the first observation of the negative differential resistance (NDR) in the current-voltage (I-V) characteristics of a double barrier (DB) structure (Chang et al. 1974). Recent high-frequency measurements (Sollner et al. 1983, and Whitaker et al. 1988) show that the resonant tunneling has potential applications in high-speed devices. On the other hand, theoretical investigations are focused on the mechanism responsible for the NDR, and on modeling the device characteristics. Although NDR is initially interpreted (Chang et al. 1974) as a result of phase coherent resonant tunneling, the I-V characteristics usually do not agree with those predicted by such a simple model. For example, at resonance, the calculated peak current and peak/valley current ratio are larger than those measured. In addition, in a typical DBRT structure, the energy width of either the impurity scattering ($\Gamma_{imp}$) or the inelastic scattering ($\Gamma_{in}$) is usually larger than that of the coherent transmission ($\Gamma_{coh}$). This implies that the resonant tunneling, originated from the interference between electronic wavefunctions, will tend to be sequential due to scattering.

In this paper, we demonstrate that the current density of DBRT structures can be comparable to that of bipolar transistors. We also present our experimental data showing the dependence of the peak current/voltage positions on the doping density of impurities in the barriers. Although the NDR is not totally destroyed, it degrades as doping level increases. The peak current also decreases with higher doping. Our

© 1989 IOP Publishing Ltd

observation is consistent with a sequential tunneling model (see, e.g., Büttiker 1988, and Jonson et al. 1987), in which the coherent tunneling is partially destroyed by the phase-breaking scattering, and, as a result, the total tunneling current decreases.

**2. High peak current density**

The samples showing high peak current density are grown on $n^+$-doped substrates by molecule beam epitaxy. The typical sample structure consists of a Si-doped 5000 Å GaAs ($2.0 \times 10^{18}/cm^3$) buffer layer, 200 Å undoped GaAs at both sides of the DBRT structure, 30 Å undoped $Al_{0.4}Ga_{0.6}As$ barriers, and a 70 Å undoped GaAs quantum well. A 5000 Å Si-doped GaAs ($1.0 \times 10^{17}/cm^3$) is grown at the top. The diodes are defined by standard photolithography and lift-off processes, with a device area of $50\mu m \times 50\mu m$. Ohmic contacts to the substrate and the top n-GaAs are formed by AuGe/Ag/Au alloying technique. A typical I-V characteristics at 77K is shown in Figure 1, measured by a curve tracer. The peak current at the second NDR in the forward bias condition (with the top electrode positively biased) is $\sim 330mA$ near 1.6V, which corresponds to a current density of $1.32 \times 10^5 A/cm^2$, comparable to that of a bipolar transistor. The peak to valley current ratio is close to 2:1. In the reverse bias condition, as shown in Figure 1(b), the second resonance appears at 5V with a peak current of 130 mA. The asymmetrical I-V characteristics comes from the asymmetrical doping level in the emitter and collector regions. When electrons are injected from the heavily doped ($1 \times 10^{18}/cm^3$) region, the DBRT structure suffers less distortion at resonance compared to the zero bias condition, which implies a higher peak transmission coefficient at resonance. The coherent transmission coefficient has a $\Gamma_{coh}$ of $\sim$ 20meV at the second resonance, relatively larger than that of the lowest resonance, 1.8meV. Both the heavy doping in the emitter region, and the large resonance width, resulting from thin barriers, contribute to the larger current density. Series resistance shifts the resonance voltage, but has little effect to the peak current.

**3. Doped barriers: coherent vs. incoherent**

Another set of DBRT samples are grown with selective Si-doping in the barriers. The baseline structure consists of a 5000Å $n^+$ GaAs ($1 \times 10^{18}$)buffer layer, 100Å undoped GaAs spacers, 80Å $Al_{0.4}Ga_{0.6}As$ barriers and 80Å GaAs quantum well, and a 5000Å $n^+$ GaAs cap layer. Three samples, labeled 1, 2, and 3 are identical except that the Si-doping density of the barriers varies from 0, $1 \times 10^{17}/cm^3$, and $1 \times 10^{18}/cm^3$, respectively. Diodes are fabricated by the same method as mentioned above. The area of the devices is 44 $\mu m \times 44\mu m$. The apparent current levels at peaks and valleys and the corresponding voltages, measured by a curve tracer at 77K, are plotted in Figure 2. The front contacts are biased positively. Near the first resonance, the valley current and voltage positions can be clearly taken, while for the second resonance, the large hysteresis makes the measurement of a true valley current difficult. The resonance voltage shifts to a smaller value as the doping density increases. Both the peak and valley currents decrease with a higher doping level, and the peak to valley ratio degrades from 2.5 to 1.4 for the first resonance.

The voltage shift can be explained by the band bending effect. The DBRT structure will always find itself a self-consistent solution under any bias conditions (Ohnishi

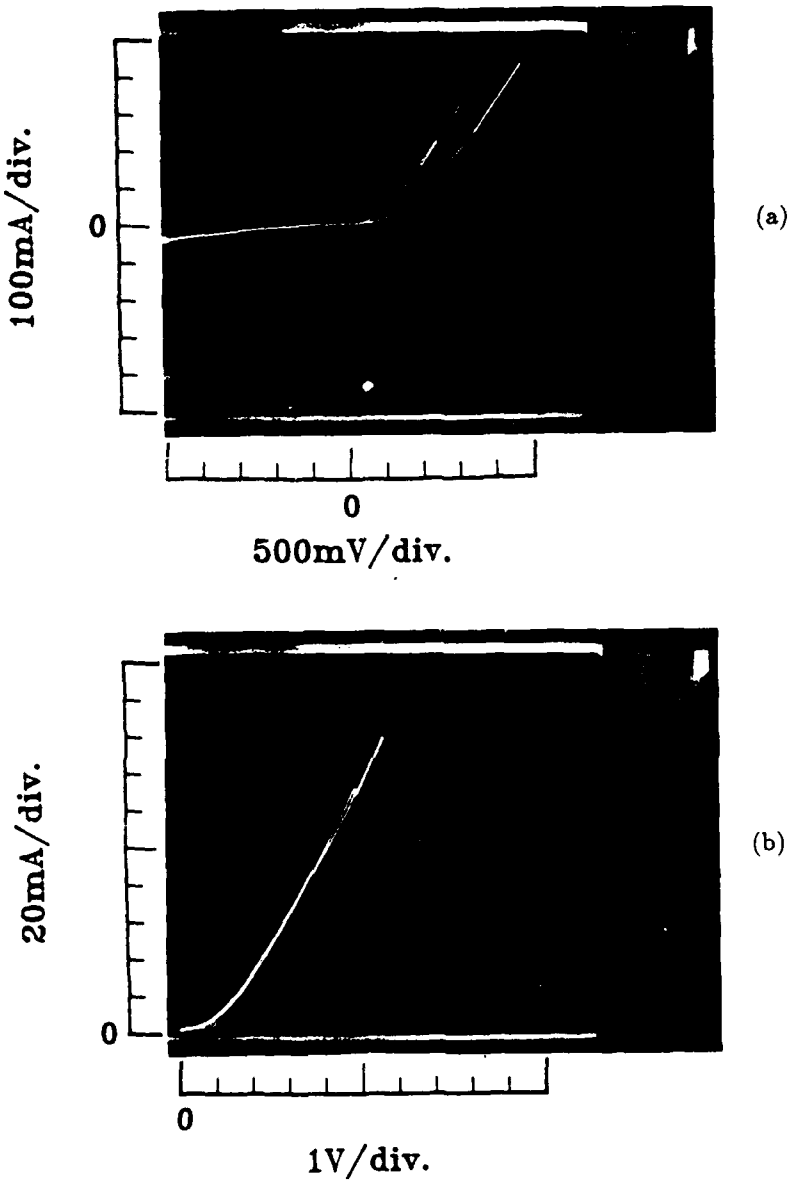


Fig. 1 The I-V characteristics of a thin (30 Å) barrier DBRT structure with the front contact (a) positively biased, and (b) negatively biased, at 77K.

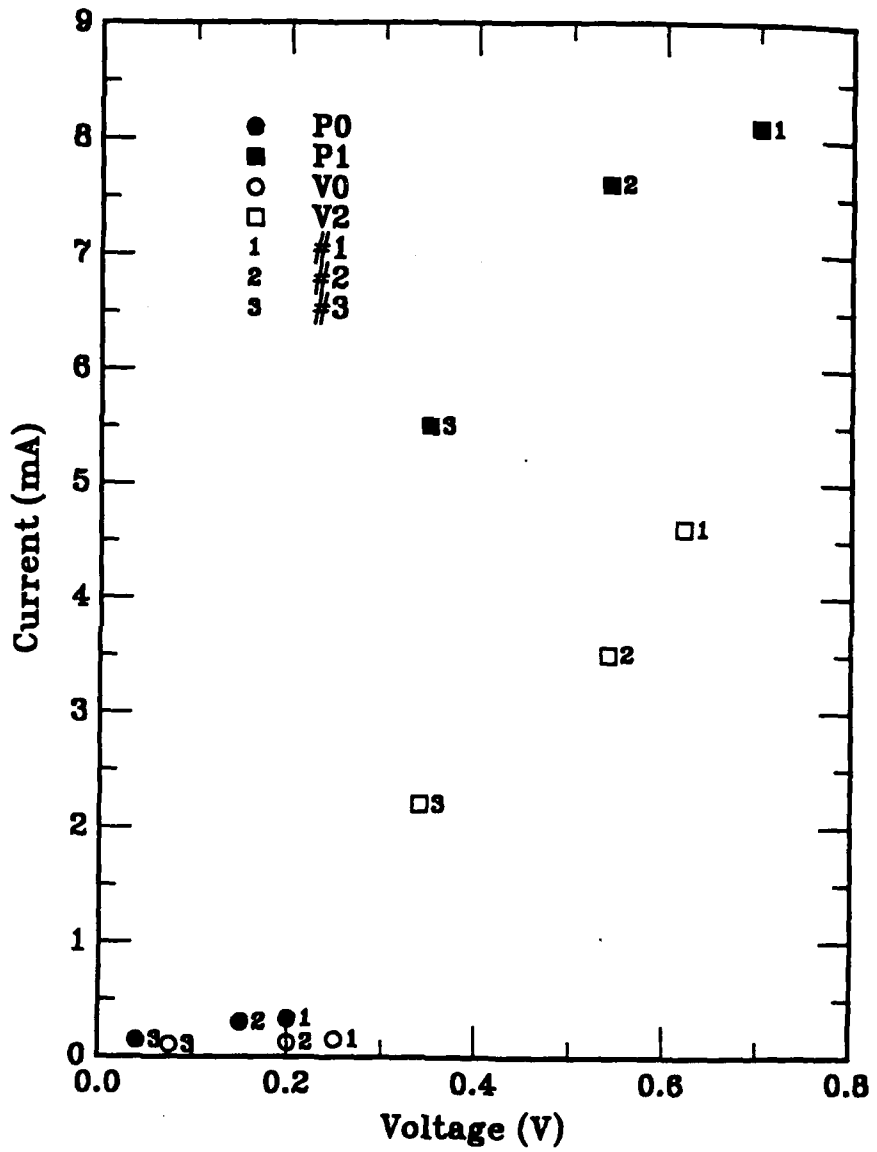


Fig. 2 The current-voltage positions for devices 1, 2, and 3, where P0, P1, V0, and V1 are the peaks (P) and valleys (V) of the lowest (0) resonances and the first excited (1) resonances.

et al. 1986). The ionized donors in the barriers lower the energy difference between the emitter Fermi level and the resonant states. Since the DBRT structure is less distorted at resonance, the peak current should increase (Schulman 1986, and Wolak et al. 1988) if we ignore the scattering and calculate the tunneling current by the coherent transmission only. However, our observation is in the opposite direction.

We interpret the doping dependence by the Breit-Wigner scattering formalism (Breit et al. 1936). In the case of DBRT, both inelastic and elastic scattering could destroy the phase coherence, and make the tunneling sequential. Although impurity scattering is elastic, the transverse momentum can not be conserved. Therefore, a heavier doping level in the barriers introduces more elastic scattering centers, and $\Gamma_{imp}$ increases. The originally sharp (small $\Gamma_{coh}$) transmission spectrum becomes broadened due to the scattering, but the total area under each resonance peak is maintained constant, i.e., the peak transmission decreases while the off-resonance transmission increases (Stone et al. 1985). This is consistent with our experimental observation, where both the total current density and the peak/valley current ratio decrease with increasing doping level. The absolute amplitudes of different time scales determine whether the conduction is dominated by coherent, sequential, or incoherent tunneling mechanism. The impurity scattering time in bulk n-type GaAs can be estimated by $\tau = m^*\mu/e$, from which $\Gamma_{imp}$ can be obtained by the relation $\Gamma_{imp} = \hbar/\tau$. For a bulk doping level of $1\times10^{17}/cm^3$ and $1\times10^{18}/cm^3$ at 77K (Ploog 1981), the corresponding $\Gamma_{imp}$'s are 3.5meV and 8.7meV, greater than $\Gamma_{coh}$'s of the first and second resonance, which are much less than 1meV. However, the attempt frequency, $\nu = v/2W$, is still greater than $\Gamma_{incoh}/\hbar$, which indicates that the phase coherency is not completely destroyed before an electron tunnels out of the second barrier, where $v$ is the velocity of electrons in the resonance state, and $W$ is the width of the quantum well. The $\Gamma_{in}$ depends mainly on the electron density and electron temperature, and can be as large as $\sim$ 6.6meV when a 0.1ps electron-electron or electron-phonon scattering time is assumed (Yang et al. 1985). In the extremely incoherent limit, where the attempt frequency is less than $\Gamma_{incoh}/\hbar$, no observation of NDR is expected. This completely incoherent case is a result of an infinitely broad resonance enhancement, and the DBRT structure can be considered as resistors put in series. The ratio between the coherent and incoherent currents is just $\Gamma_{coh}/\Gamma_{incoh}$, where the incoherent energy width, $\Gamma_{incoh}$, includes both the elastic and the inelastic scattering processes. The origin of the valley current is still not well understood, a measurement of valley current in the NDR region is further complicated by the hysteresis. Our observation of the doping dependence suggests that the formation of resonance states comes from the interference of electron wavefunctions in the DBRT region, since the transmission is sensitive to the impurity scattering. The location of the impurity is not critical for this observation due to the long range nature of the impurity scattering, but we obtain better control over the number of ionic impurities by doping in the barriers only.

## 4. Conclusion

In conclusion, we have demonstrated that DBRT structures can have a current density as high as that of bipolar transistors. We also investigated the dependence on the

increasing impurity scattering of the I-V characteristics of a series of DBRT structures. Our observation supports the Breit-Wigner resonant tunneling formalism, which has been used to help understand the tunneling characteristics. The NDR of DBRT structures comes from resonant enhancement of the transmission coefficient, even the enhancement can be broadened and damped by scattering. The attempt frequency is larger than the incoherent scattering rate in our system, which makes the observation of NDR still possible. The broadening is large enough such that the peak current and the peak/valley ratio decrease with increasing impurity scattering, which is experimentally tuned by changing the doping in the barriers of DBRT structures.

## 5. Acknowledgements

We would like to thank R.T. Bate for encouragement. Special thanks are due to K.K. Choi and M.J. Yang for their valuable suggestions. This work was supported in part by the Office of Naval Research and the Defense Advanced Research Projects Agency.

## 6. References

Breit G and Wigner E 1936 Phys. Rev. **49** 519

Büttiker M 1988 IBM J. Res. Develop. **32** 63, and references therein.

Chang L L, Esaki L and Tsu R 1974 Appl. Phys. Lett. **22** 562

Jonson M and Grincwajg A 1987 Appl. Phys. Lett. **51** 1729

Ohnishi H, Inata T, Muto S, Yokoyama N, and Shibatomi A 1986 Appl. Phys. Lett. **49** 1248

Ploog K 1981 Ann. Rev. Mater. Sci. **11** 171

Schulman J N 1986 J. Appl. Phys. **60** 3954

Sollner T C L G, Goodhue W D, Tannenwald P E, Parker C D, and Peck D D 1983 Appl. Phys. Lett. **43** 588

Stone A D and Lee P A 1985 Phys. Rev. Lett. **54** 1196

Whitaker J F and Mourou G A 1988 Appl. Phys. Lett. **53** 385

Wolak E, Lear K L, Pitner P M, Hellman E S, Park B G, Weil T, and Harris Jr. J S 1988 Appl. Phys. Lett. **54** 1196

Yang C H, Carlson-Swindle J M, Lyon S A, and Worlock J M 1985 Phys. Rev. Lett. **55** 2359

# APPENDIX H

# QUANTITATIVE RESONANT TUNNELING SPECTROSCOPY: CURRENT-VOLTAGE CHARACTERISTICS OF PRECISELY CHARACTERIZED RESONANT TUNNELING DIODES

# Quantitative resonant tunneling spectroscopy: Current-voltage characteristics of precisely characterized resonant tunneling diodes

M. A. Reed, W. R. Frensley, W. M. Duncan, R. J. Matyi,[a] A. C. Seabaugh, and H.-L. Tsai
*Central Research Laboratories, Texas Instruments Incorporated, Dallas, Texas 75265*

(Received 25 October 1988; accepted for publication 26 January 1989)

A systematic comparison of precisely characterized resonant tunneling structures is presented. A self-consistent band bending calculation is used to model the experimentally observed resonant peak positions. It is found that the peak positions can be accurately modeled if the nominal characterization parameters are allowed to vary within the measurement accuracy of the characterization. As a result, it is found that the asymmetries in the current-voltage characteristics are solely explainable by tunnel barrier thickness fluctuations.

The origin of negative differential resistance in double barrier/single quantum well resonant tunneling structures is qualitatively well understood.[1] However, a full accounting of the current-voltage characteristics requires precise physical and electrical measurement of the device material properties. We present here a systematic comparison of measurements on precisely characterized resonant tunneling structures with models of the current-voltage dependence.

A set of four specimens has been grown by molecular beam epitaxy (MBE) to provide devices which vary over seven orders of magnitude in resonant peak current density for the AlGaAs/GaAs/AlGaAs system. This is achieved by growing nominally identical structures which differ solely in barrier thickness. Photoluminescence test structures were grown to provide for measurement of the AlGaAs band gap, transmission electron microscopy was used to independently verify the layer thicknesses, and capacitance-voltage profiling provided an independent determination of the doping density. The current-voltage characteristics of these structures have been measured. A systematic shift of the resonant peak and a variation of the resonant peak voltage asymmetry with current density is observed and compared with modeling results. It is found that a self-consistent band bending model can accurately predict the voltage peak positions, although the structural parameters used are not necessarily the "nominal" values, yet values within the error of the characterization measurement.

The samples used in this study were grown on Si-doped $n^+$-GaAs conductive substrates using a Riber 2300 MBE system. The structures consist of a 0.5 $\mu$m Si-doped GaAs buffer and bottom contact layer, a (nominally) 150 Å undoped GaAs spacer layer, an undoped AlGaAs tunnel barrier, an undoped GaAs quantum well, a second undoped AlGaAs tunnel barrier of nominally identical thickness, another 150 Å undoped GaAs spacer layer, a 0.5 $\mu$m Si-doped GaAs top contact, a 0.5 $\mu$m undoped AlGaAs layer, an undoped GaAs 50 Å quantum well, a 0.1 $\mu$m undoped AlGaAs layer, and a 100 Å GaAs cap layer. The entire structure was grown at constant temperature at 600 °C (to minimize Si diffusion) as measured by a short wavelength pyrometer. The four specimens were grown sequentially to ensure a constant unintentional impurity background.

The active resonant tunneling structure is buried underneath a series of diagnostic photoluminescence structures. Conventional photoluminescence was performed at 4.2 and 300 K. The top quantum well photoluminescence exhibited typical full width at half maximum values of 10 meV. Photoluminescence of the thick AlGaAs layers was used for determination of the Al content. The band-gap relation of Casey and Panish[2] was assumed. The doping density of the $n^+$-GaAs layers was determined by standard capacitance-voltage profiling measurements, and the thicknesses of the tunnel barriers and quantum wells were determined by cross-sectional transmission electron microscopy (TEM). A summary of these structural parameters for the four samples studied is shown in Table I.

Prior to device fabrication, the top diagnostic layers were removed by a chemical etch so that contact could be made to the upper $n^+$-GaAs layer. Mesa devices ranging from $1.6\times10^{-7}$ cm$^{-2}$ to $4.1\times10^{-5}$ cm$^{-2}$ were fabricated by standard photolithography and chemical etching. Bonding pads contacted the upper top AuGeNi alloyed metal ohmic contact and a similar bottom contact through a $Si_3N_4$/polyimide passivation layer. Static current-voltage characteristics (four-point where necessary) were measured at 77 K.

Figure 1 shows a realistic conduction energy band profile of the 85 Å barrier thickness structure under (a) zero and (b) resonant bias. The model from which this figure was obtained finds the self-consistent solution of Poisson's equations for the electrostatic potential. The electrons in the con-

TABLE I. Summary of the structural parameters for the four resonant tunneling diode samples and the characterization techniques used.

| Barrier thickness (TEM) | RTD QW thickness (TEM) | Al content (PL, 300 K) | PL QW energy (PL, 4.2 K) | Contact doping density, cm$^{-3}$ ($CV$) |
|---|---|---|---|---|
| 118(±5) Å | 48(±5) Å | 27.7(±0.6) | 1.620 eV | 1.7(±0.2)$10^{18}$ |
| 85(±5) Å | 44(±5) Å | 26.4(±0.6) | 1.623 eV | 1.7(±0.2)$10^{18}$ |
| 65(±5) Å | 44(±5) Å | 27.7(±0.6) | 1.613 eV | 1.4(±0.4)$10^{18}$ |
| 32(±5) Å | 38(±5) Å | 25.0(±0.6) | 1.616 eV | 2.6(±0.1)$10^{18}$ |

[a] Present address: Department of Metallurgical and Mineral Engineering, University of Wisconsin at Madison, WI.

 0003-6951/89/131256-03$01.00 © 1989 American Institute of Physics 

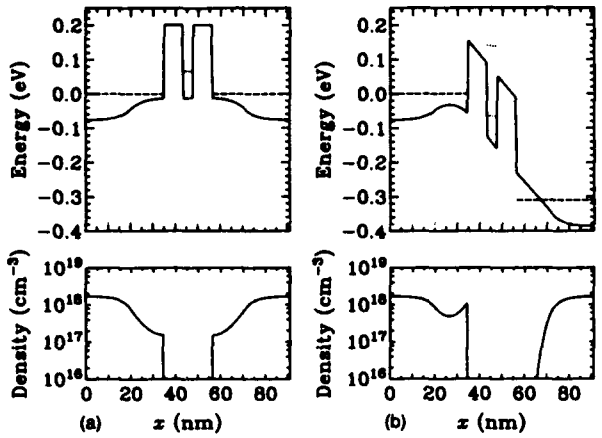


FIG. 1. Self-consistent band diagram using Poisson's equations for the electrostatic potential. The electrons in the contacts are treated in a finite temperature Thomas–Fermi approximation. The simulation does not include current flow. The structure is an 85 Å $Al_xGa_{1-x}As$ ($x = 0.264$) barrier/44 Å GaAs QW/85 Å $Al_xGa_{1-x}As$ ($x = 0.264$) barrier structure at $T = 77$ K for (a) no applied bias and (b) resonant bias. The energies of the bound states are denoted by a dotted line and the Fermi level by dashed lines.

tacts are treated in a finite-temperature Thomas–Fermi approximation (i.e., these electrons are assumed to be in local equilibrium with the Fermi levels established by their respective electrodes). One result of this calculation, illustrated in Fig. 1(a), is that the band profile near the quantum well is significantly perturbed by the contact potential of the $n^+$-undoped junction. This shifts the resonant state upward (with respect to the $n^+$-GaAs Fermi level) from that expected from a naive flatband picture. This contact potential thus shifts the resonant peak position [Fig. 1(b)] considerably; the model predicts a resonant voltage at 310 meV, much higher than that predicted by a flatband picture.

Figure 2 shows the experimental current-voltage characteristics of a typical $(4\,\mu m)^2$ mesa device of this structure at 77 K. Care must be exercised in the spectroscopy of the structures. Current-voltage characteristics of successively increasing mesa size (same epitaxial structure) progressively exhibit the well known plateau structure due to self-biasing.[3] This self-biasing perturbs and is observed to lower the apparent resonant peak position. For accurate spectroscopy, this effect must be avoided.

The experimental resonant peaks are not in very good agreement with the model calculation; the experimental peaks appear at 263 and 227 meV for positive and negative bias polarity, respectively, whereas the model predicts a value of 310 meV. (The convention here is that positive bias polarity implies electron injection from the top epitaxial contact.) What is also obvious is the asymmetry of the resonant peaks holds for both voltage and current. It is found that this asymmetry is not consistent for a large sampling of similar devices; the asymmetry ranges from zero to as much as 60 meV in voltage and a factor of 3.3 in current. However, the degree of asymmetry is correlated; a larger voltage asymmetry implies a larger current asymmetry.

To ascertain the degree of asymmetry and variation, characteristics of a large number of devices from the various epitaxial structures were measured. The resonant voltage peak positions as a function of resonant current density are shown in Fig. 3 (due to the above-mentioned complication of stabilizing oscillations, measurements from the 30 Å barrier were unreliable and are not presented here). The 118 Å barrier structure data exhibit a clear exponential behavior over two orders of magnitude, with the positive bias peaks occurring at lower voltages and current densities than the negative bias peaks. The 85 Å barrier structure data are not as clear, exhibiting considerable scatter. The origin of this scatter is not known. Additionally, the data exhibit the inverse of the 118 Å data; the positive bias peaks occur at higher voltages and current densities than the negative bias peaks. Finally, the 65 Å barrier structure deviates significantly from exponential behavior.

Examination of the 118 Å barrier structure data reveals the major cause of the asymmetry, both in current and voltage position. Consider a fluctuation in the thickness of one of the tunnel barriers of a nominal thickness barrier sample. This implies a change in the voltage position at which resonance occurs, and concurrently a change in the tunneling current. Figure 4 illustrates the 85 Å barrier structure with parameters varied *within* the error bars quoted in Table I; specifically, with the top barrier thickness equal to 80 Å, the bottom barrier thickness equal to 90 Å, and the quantum well equal to 48 Å. Figure 4(a) shows the modified structure under positive bias (the right-hand side of the figures corresponds to the top ohmic contact), and exhibits a resonant

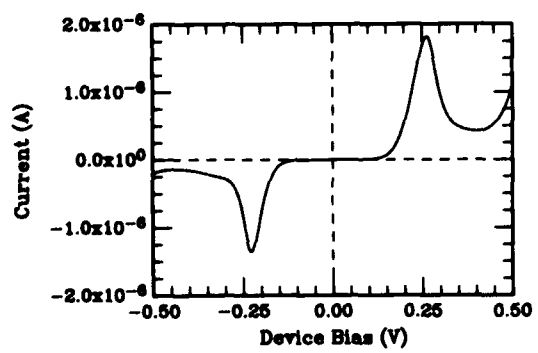


FIG. 2. Current-voltage characteristics of the 85 Å sample for square mesa areas of $1.6\times10^{-7}$ cm$^2$. Positive voltage corresponds to electron injection from the top contact. $T = 77$ K.

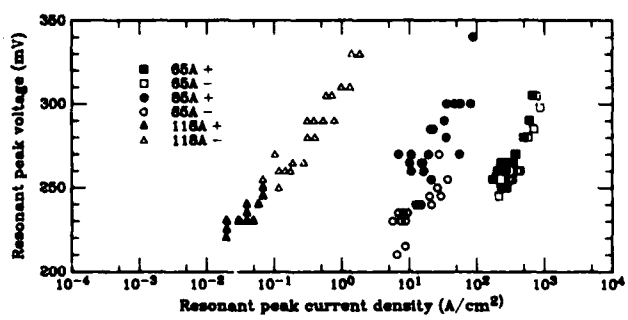


FIG. 3. Resonant peak voltage position vs resonant peak current density for a large sampling of three different barrier thickness structures. Both positive ( + ) and negative ( − ) voltage polarities are shown for the three structures of nominal barrier thickness 65, 85, and 118 Å. $T = 77$ K.

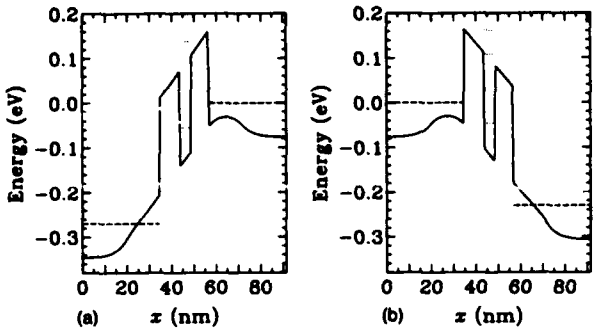


FIG. 4. Self-consistent band diagrams of a 90 Å bottm barrier/48 Å quantum well/80 Å top barrier structure at resonance. $T = 77$ K. (a) Positive bias and (b) negative bias polarities are the same as Fig. 2.

voltage at 270 meV. In the reverse bias direction [Fig. 4(b)], resonance occurs at 230 meV. These are in excellent agreement with experimentally observed values. Note that larger current densities correspond to electron injection first through the thinner (top) barrier.

Figure 3 shows that the inherently thinner top barriers of the 85 Å sample are a sample-dependent phenomenon; the 118 Å data reveal that the top barrier is thicker than the bottom barrier in the 118 Å sample. Likewise, the 65 Å sample appears to have approximately equal barrier thicknesses. These results imply that Si dopant redistribution, at least in these samples, is not a complication. Finally, the scatter in the 85 Å data with respect to the 118 and 65 Å data may imply that this sample has larger quantum well thickness fluctuations although this cannot be verified without further data on Al content and doping fluctuations.

The quantitative spectroscopy of these structures is relatively straightforward if one stays in the regime where the structure impedance is dominated by the tunnel barriers. Outside of this regime (e.g., for the 65 Å data) the device may be affected by an internal series resistance. The resonant voltage position for the 65 Å data is found to be linear with current density, and gives a contact resistance of $8.8 \times 10^{-5}$ $\Omega\ \mathrm{cm}^2$, equal for both positive and negative bias peak positions. This resistance can be fully accounted for by the AuGeNi ohmic metallization used here.

We have shown a self-consistent band bending model that can accurately predict experimentally observed resonant peak positions, and have compared it with precisely characterized resonant tunneling structures. It is found that, to accurately model the resonant voltage peak positions, the characterization values must be varied within the error bars of the measurement. Indeed, this technique can be used as an accurate diagnostic of the structure. Asymmetries in the electrical characteristics have been shown to be due to fluctuations in the tunnel barrier thicknesses.

We are thankful to R. K. Aldert, R. T. Bate, J. N. Randall, P. F. Stickney, F. H. Stovall, J. R. Thomason, and C. H. Yang for discussions and technical assistance. This work has been supported by the Office of Naval Research.

[1] L. L. Chang, L. Esaki, and R. Tsu, Appl. Phys. Lett. **24**, 593 (1974).
[2] H. C. Casey and M. B. Panish, *Heterostructure Lasers* (Academic, New York, 1978), pp. 187–194.
[3] J. F. Young, B. M. Wood, H. C. Liu, M. Buchanan, D. Landheer, A. J. SpringThorpe, and P. Mandeville, Appl. Phys. Lett. **52**, 1398 (1988).

# APPENDIX I

# PSEUDOMORPHIC BIPOLAR QUANTUM RESONANT-TUNNELING TRANSISTOR

T-ED/36/10//30064

# Pseudomorphic Bipolar Quantum Resonant-Tunneling Transistor

Alan C. Seabaugh
William R. Frensley
John N. Randall
Mark A. Reed
Dewey L. Farrington
Richard J. Matyi

Reprinted from
IEEE TRANSACTIONS ON ELECTRON DEVICES
Vol. 36, No. 10, October 1989

# Pseudomorphic Bipolar Quantum Resonant-Tunneling Transistor

ALAN C. SEABAUGH, MEMBER, IEEE, WILLIAM R. FRENSLEY, SENIOR MEMBER, IEEE, JOHN N. RANDALL, MEMBER, IEEE, MARK A. REED, SENIOR MEMBER, IEEE, DEWEY L. FARRINGTON, AND RICHARD J. MATYI

***Abstract*—A bipolar tunneling transistor has been fabricated in which ohmic contact is made to the strained $p^+$ InGaAs quantum well of a double-barrier resonant-tunneling structure. The heterojunction transistor consists of an n-GaAs emitter and collector, undoped AlAs tunnel barriers, and a pseudomorphic $p^+$ InGaAs quantum-well base. By making ohmic contact to the p-type quantum well, the hole density in the quantum-well base is used to modulate the base potential relative to the emitter and collector terminals. With control of the quantum-well potential, the tunneling current can be modulated by application of a base-to-emitter potential. This paper details the physical and electrical characteristics of the device. It is found that the base-emitter voltages required to bias the transistor into resonance are well predicted by a self-consistent calculation of the electrostatic potential.**

## I. Introduction

THERE are physical limits to the minimum size at which conventional transistors can operate [1], [2]. If still smaller and faster electron devices are to be found, then new transistor approaches are needed that are not subject to the same physical size restrictions. Recently the Bipolar Quantum Resonant-Tunneling Transistor (BiQuaRTT) has been reported [3], [4]. In this three-terminal resonant-tunneling device, tunneling transport is controlled by varying the potential of the p-type quantum well in a resonant-tunneling double-barrier (RTD) structure. The BiQuaRTT does not circumvent the scaling limitations of conventional transistor technology, but it is a precursor to other controlled-tunneling devices that could function in a smaller physical space. In this paper, we report the transport properties of an AlAs/InGaAs/AlAs pseudomorphic BiQuARTT grown on GaAs.

Capasso *et al.* [5]–[7] have conceived of and demonstrated a resonant-tunneling bipolar transistor (RTBT) that has an undoped RTD embedded in the base of an otherwise conventional heterojunction bipolar transistor. In the RTBT the neutral p-type base layer supplies free holes to the undoped quantum well forming a two-dimensional (2-D) hole gas; thus, the Fermi level in the RTD and the neutral p-base are aligned. The tunneling current through the device is controlled by application of base current steps, but is also affected by changing the voltage between collector and emitter since independent control of the resonant-tunneling condition is not provided.

In the BiQuaRTT, the p-doping is confined to the quantum well; 2-D holes therein are used to control the potential between the base and the emitter. In this way the electrostatic potential between the quantum well and the emitter electron reservoir is used to set the tunneling condition through the first tunnel barrier. This is a fundamental difference between the BiQuaRTT and RTBT concept. In the BiQuaRTT, the resonance condition is controlled by $V_{be}$ *independently* of the collector-to-emitter voltage $V_{ce}$. The large 2-D holes gas density serves to screen the electric field from the quantum well and thereby decreases the modulation of the quantum-well eigenstates by the collector–base field (Stark effect). In the BiQuaRTT, negative differential resistance (NDR) is not desired in the common-emitter transistor characteristics while in the RTBT the NDR is introduced by design. The double-barrier structure in the BiQuaRTT is utilized to produce a negative transconductance in the common-emitter transistor characteristics without negative output conductance. In fact, the collector conductance is relatively small, providing dc isolation between the base and collector, which NDR devices conspicuously lack. This is preferred for most compressed-function logic circuit applications.

Another RTBT device variation has been to place the resonant-tunneling double barrier in the emitter of a bipolar transistor. Both one [8], [9] and two [10]–[12] double-barrier structures have been integrated into the device. In this configuration, the transistor characteristics are essentially described by the combination of an RTD connected in series with the emitter of a bipolar transistor.

## II. Material and Device Structure

The epitaxial material was grown by molecular-beam epitaxy in a Riber MBE-2300 system. The layer design, shown in Fig. 1, utilizes three different bandgaps across the structure: the widest bandgap layer is used for the tunnel barriers while the higher bandgap of the emitter and

Manuscript received April 12, 1989; revised May 30, 1989. This work was supported by the Defense Advanced Research Projects Agency under ARPA Contract 9770400.1304 and was monitored by the Office of Naval Research.

A. C. Seabaugh, W. R. Frensley, J. N. Randall, M. A. Reed, and D. L. Farrington are with the Central Research Laboratories, Texas Instruments Incorporated, Dallas, TX 75265.

R. J. Matyi was with the Central Research Laboratories, Texas Instruments Incorporated, Dallas, TX 75265. He is now with the Department of Materials Science and Engineering, University of Wisconsin, Madison, WI 53706.

IEEE Log Number 8930064.

0018-9383/89/1000-2328$01.00 © 1989 IEEE

| | | |
|---|---|---|
| 300nm | n+GaAs | $2\times10^{18}$ cm$^{-3}$ |
| 200 | n-GaAs | $5\times10^{17}$ |
| 25 | GaAs | UNDOPED |
| 5 | AlAs | UNDOPED |
| 5 | InGaAs(x=0.23) | UNDOPED |
| 5 | p+InGaAs(x=0.23) | $1\times10^{19}$ |
| 5 | InGaAs(x=0.23) | UNDOPED |
| 5 | AlAs | UNDOPED |
| 25 | GaAs | UNDOPED |
| 500 | n-GaAs | $2\times10^{16}$ |
| 500 | n+GaAs | $2\times10^{18}$ |

n+GaAs SUBSTRATE

Fig. 1. Pseudomorphic BiQuaRTT material structure.

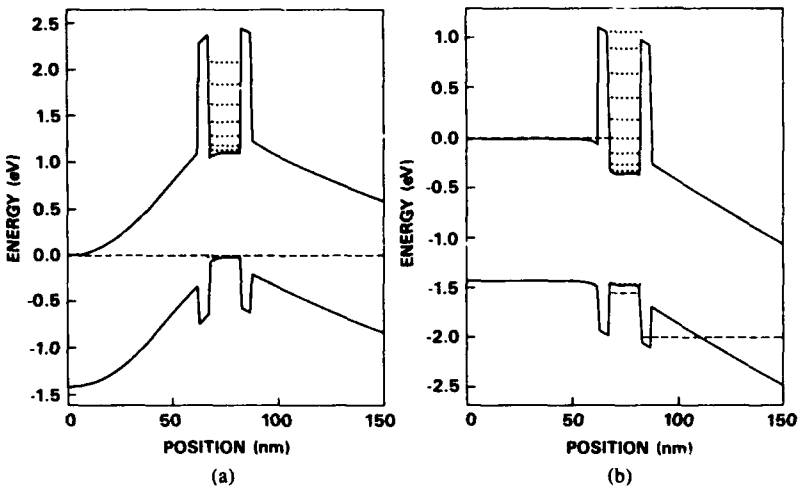


Fig. 2. Pseudomorphic BiQuaRTT energy band profile derived from a self-consistent simulation. The structure is shown in (a) equilibrium and (b) under bias to bring the emitter electron energy into resonance with the fourth allowed quantum well base state, $V_{be}$ = 1.5 V, $V_{ce}$ = 2.5 V, 300 K. The dashed lines designate the Fermi level position; the dotted lines designate the electron and hole states in the quantum well.

collector layer relative to the quantum well base serves to confine the holes in the base at the high base–emitter voltages necessary to bring the device into resonance. Moderate emitter doping provides a relatively narrow emitter electron energy distribution and a low valley current through the tunneling structure. A lightly doped collector layer is used to obtain a low base–collector conductance.

Starting from the substrate, the structure consists of a 500-nm $n^+$ GaAs buffer layer below a 500-nm n-GaAs collector. The RTD base is symmetric about a 5-nm InGaAs Be-doped layer in the center of the quantum well. InGaAs spacer layers of 5 nm on either side of the 5-nm Be-doped layer bring the quantum well width to 15 nm. This $In_{0.23}Ga_{0.77}As$ layer at a total thickness of 15 nm is less than the critical layer thickness for dislocation formation [13] and was chosen this large to ease the doping and contacting requirements. AlAs tunnel barriers of 5-nm thickness and 25-nm undoped GaAs spacer layers bound the quantum well on either side. The thick undoped layers are used in order to provide a neutral base with free holes. (Thinner AlAs tunnel barriers should improve the resonant tunneling characteristics of the device.) A 20-nm GaAs emitter region, doped to $5 \times 10^{17}$ cm$^{-3}$, is utilized on top of the quantum-well base, followed by a 300-nm $n^+$ contact layer.

Room-temperature energy band diagrams for the device are shown in Fig. 2: (a) in equilibrium and (b) under bias into resonance with $V_{be}$ = 1.55 V and $V_{ce}$ = 2.0 V. The n-type GaAs emitter is at left, with the p-type InGaAs quantum well base in the center, and the n-GaAs collector at the right. Γ-point AlAs tunnel barriers are assumed. The dashed lines indicate the Fermi level position, while the dotted lines indicate the eigenstates for electrons or holes within the well. These profiles are obtained from a self-consistent (zero current) solution of Poisson's equation for the electrostatic potential. The free-electron densities in the emitter and collector are calculated from the Fermi distribution for semiclassical electrons. The allowed carrier energies in the base are obtained from a solution of Schroedinger's equation. The hole density in the base is determined by integrating the product of the quantum-well-base 2-D density of states and the Fermi distribution in the base over energy.

From the energy band profiles it can be seen that the

quantum-well contact can be used to reduce the potential energy of the quantum-well electron states to the point where they are equal with the electron energies in the emitter. At this value of $V_{be}$, resonant tunneling across the base can occur. Further increase in $V_{be}$ lowers the resonant energy below the emitter electron energies, and the tunneling current is suppressed. Thus with increasing $V_{be}$, a decreased collector current is expected and therefore a negative transconductance [3].

A non-self-aligned process utilizing conventional photolithography and lift-off metallizations is used to form the transistor. Contact to the quantum well is achieved by implantation of Be. The triple Be implant of $1 \times 10^{15}$ $cm^{-2}$ at energies of 30, 80, and 160 keV is sufficient to convert the $2 \times 10^{18}$ $cm^{-3}$ n-type surface layer conductivity to p-type. The implantation is activated by rapid thermal annealing (RTA) at 750°C for 10 s. The implanted base region is isolated from the emitter by wet chemical etching to prevent the turn-on of the lateral base–emitter p-n junction.

## III. Characterization

Anomalous redistribution of Be in MBE-grown GaAs has been previously reported [14], [15]. In the BiQuaRTT, diffusion of Be beyond the quantum well must be suppressed to ensure independent control of the quantum-well potential. Secondary ion mass spectroscopy (SIMS) was used to profile the physical concentration of Be and Al in the BiQuaRTT material structure. The intensity of the Al and Be signals as measured by SIMS is shown in Fig. 3 and plotted as a function of sputtering time into the structure. The Be signal appears within the two Al peaks indicating that the Be has not diffused beyond the AlAs tunnel barriers. Further SIMS measurements reveal that the Be remains confined to the quantum well after RTA and that the implantation of Be extends to the quantum well.

Hall-effect measurements were made on a bridge test structure formed on a companion BiQuaRTT wafer with a 25-nm quantum-well base to verify the existence of free holes in the quantum-well base. An eight-contact bridge specimen was formed by mesa etching through the $n^+$ top layer and the quantum-well base. As with the transistor fabrication, ohmic contact to the quantum well was provided by implantation and RTA. Hall-effect measurements (4 K) revealed a positive Hall voltage, indicating p-type material and thus giving independent confirmation of free holes in the base. A mobility of 780 $cm^2/Vs$ and a hole density of $4 \times 10^{18}$ $cm^{-3}$ were inferred with simple geometry and single-carrier assumptions.

## IV. Transport Characteristics

Common-emitter transistor characteristics for the pseudomorphic BiQuaRTT of (Fig. 1) are shown in Fig. 4. The device shows a gain of approximately 13 at room temperature with a maximum current density of $2.1 \times 10^5$ $A/cm^2$. When the device cools to 77 K, the current density and gain are maintained although at higher base voltages. At 77 K, the emitter resistance is decreased (mobility enhancement) and the transition to the saturation regions is more abrupt. At larger collector currents, a negative output conductance region is apparent. As will become apparent, the negative conductance is not due to the RTD structure, since it occurs at larger base–emitter voltages than are required for resonant tunneling. (Our examination of this negative conductance indicates that it arises from interband scattering in the GaAs or AlAs con-

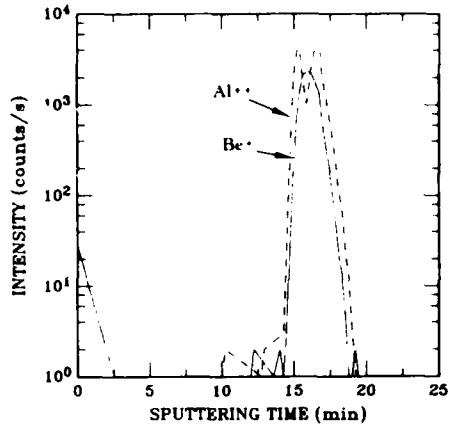


Fig. 3. SIMS profile of the pseudomorphic BiQuaRTT showing concentration profiles of singly ionized Be and doubly ionized Al.

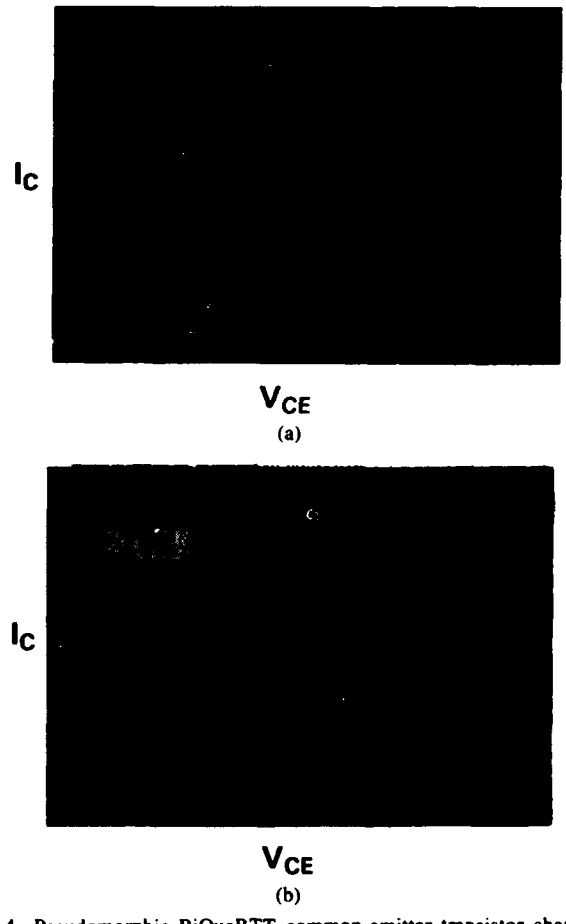


Fig. 4. Pseudomorphic BiQuaRTT common-emitter transistor characteristics at (a) room temperature and (b) 77 K. Emitter area is 9 $\mu m^2$; base-to-emitter contact spacing is 7 $\mu m$.

duction band.) A large collector–emitter offset voltage is also apparent in Fig. 4 and occurs because of the large series base resistance of the non-self-aligned process. For low collector–emitter voltage ($V_{ce} \sim < 1.5$ V) and for the base currents shown (Fig. 4), the base–collector junction turns on before the base–emitter junction giving rise to a negative collector current not visible in this quadrant of the current–voltage characteristics.

Under base voltage bias, negative transconductance is not observed; however, this can be understood in terms of the material structure. Referring back to the energy band diagram of Fig. 2(b), the first resonance can be predicted to occur through the $n = 4$ quantum well state at $V_{be} = 1.55$ V. Additional resonances can be anticipated at 1.73 and 2.13 V through the $n = 5$ and $n = 6$ eigenstates and beyond. The device was therefore operated with base voltage steps about this bias point. The resonances are most readily distinguished by measuring the collector current as $V_{be}$ is monotonically increased with constant $V_{ce} = 2.5$ V; see Fig. 5. With increasing $V_{be}$, the potential energy of the allowed states in the quantum well is lowered with respect to the electrons in the emitter. In the measurement at room temperature (dashed line), no evidence of tunneling current modulation is observed. However, with the device cooled to 77 K, clear inflections in the collector current are observed. By taking the derivative of the collector current with respect to the base–emitter voltage (right-hand axis of Fig. 5), we determine the measured base–emitter voltages at resonance to be approximately 1.6, 1.9, and 2.4 V. This is in remarkable agreement with the resonances expected from the electrostatic profile, 1.55, 1.73, and 2.13 V. Series resistance pushes the measured inflections out to higher base–emitter voltages, which is consistent with these measurements. The fact that negative transconductance is not observed implies that inelastic transport processes in this device are comparable to the resonant-tunneling current. This is due to the low resonant-tunneling current density resulting from the thick AlAs barriers.

To understand more fully the transport characteristics of this device, we measured the dependence of the base and collector currents on $V_{be}$ with the collector–base junction shorted together; see Fig. 6. Note first that transistor gain is not obtained until the transistor $V_{be}$ exceeds 2.4 V. Neglecting dynamic transport effects, this is sufficient voltage to allow transport across the device by thermionic emission over the AlAs tunnel barriers. The thick 5-nm AlAs barriers appear to inhibit current gain for lesser voltages.

The measured base current $i_b$ is described by the ideal diode relation, $i_b = i_o \exp(qV_{bei}/\eta kT)$, where $i_o$ is the junction saturation current, $\eta$ is the ideality factor, and $V_{bei}$ is the internal base-to-emitter voltage. The measured $V_{be}$ is given by $V_{be} = V_{bei} + i_b[R_b + (\beta + 1)R_e]$ where $R_b$ is the base series resistance, $R_e$ is the emitter resistance, and $\beta$ is the transistor gain. Using these relations, the base current characteristics were fit to the equation

$$V_{be} = (\eta kT/q) \ln (i_b/i_o) + i_b(R_b + R_e)$$

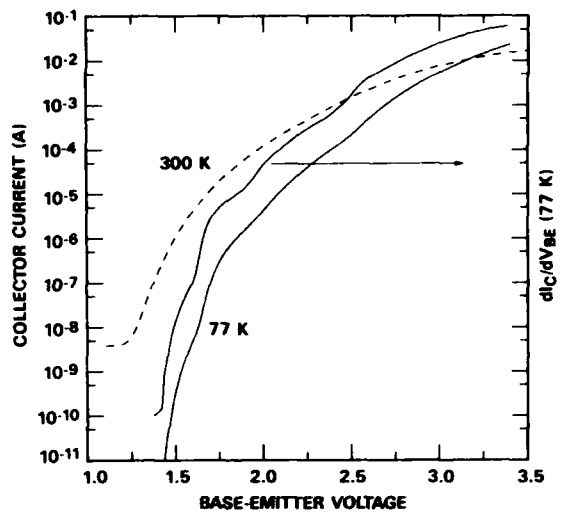


Fig. 5. Dependence of collector current on base-to-emitter voltage at $V_{ce} = 2.5$ V. The dashed line shows the collector current dependence at room temperature, while the solid lines show the 77 K result. The derivative of the collector current with respect to the base–emitter voltage is shown to emphasize the collector current inflections.

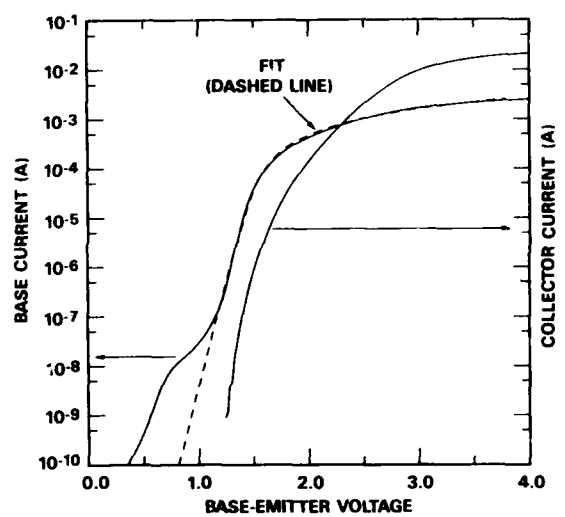


Fig. 6. Gummel plot for the BiQuaRTT at room temperature. Emitter area is 9 $\mu m^2$; base-to-emitter contact spacing is 5 $\mu$m. (Same transistor as Fig. 5 measurement.)

where, in the region of the fit, $\beta << 1$. With an ideality factor of $\eta = 2$, the fitted data are shown by the dashed line in Fig. 6 where the free parameters become $i_o = 1.55 \times 10^{-17}$ A and $R_b = 830\ \Omega$. From an independent measurement [16] on this same device, the room-temperature emitter resistance is found to be 440 Ω. We therefore obtain a base resistance of 390 Ω. This measurement of the base resistance is consistent with the expected geometrical resistance of the quantum well between the emitter and base contacts. For this non-self-aligned process, the base-to-emitter spacing is 5 $\mu$m and accounts for the high base resistance.

The fit in Fig. 6 is remarkably close for currents exceeding 0.1 $\mu$A. The excess current, occurring below 0.1 $\mu$A, is insensitive to surface treatment and shows a strong temperature dependence (see Fig. 7), characteristic of

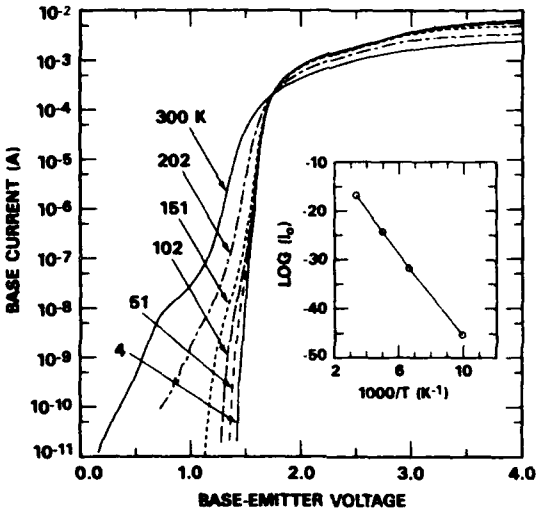


Fig. 7. Temperature dependence of the base current with $V_{cb} = 0$ V. The inset shows the temperature dependence of the base–emitter junction saturation current with $\eta = 2$. (Same transistor as Fig. 5 measurement.)

generation through deep centers in the base–emitter transition region.

The temperature dependence of the base current is shown in Fig. 7 (after [17]). The base resistance of the device drops by several hundred ohms as the temperature is decreased, presumably due to increasing mobility. If each of the curves are fit as was done in Fig. 6, it is possible to obtain the base saturation current $i_o$ as a function of temperature. A plot of the temperature dependence of $i_o$ appears in the inset, from which an activation energy of 0.86 eV is obtained. This energy is below the 1.12-eV energy gap of bulk $In_{0.23}Ga_{0.77}As$. The InGaAs layer is under biaxial compression, which should increase the bandgap by 50 to 100 meV [18]. The measured activation energy of 0.86 eV then suggests that the saturation current is determined by generation through mid-gap deep levels. Twice 0.86 eV or 1.72 eV is equal to the total energy required to move an electron from the InGaAs valence band to the indirect $X$ conduction band minimum of the AlAs barriers. By fitting the data in this way, we do not arrive at the energy for the tunneling transitions; however, these transitions are again apparent in the measured data as inflections in the current–voltage characteristics.

## V. Discussion

One can compare the superlattice BiQuaRTT of [3] with the pseudomorphic BiQuARTT described here, as both utilize a 15-nm quantum well, 5-nm tunnel barriers, and have identical geometrical device structures. The outstanding difference between these devices is that in the superlattice BiQuaRTT, room-temperature negative transconductance is observed, while in the pseudomorphic BiQuaRTT, the tunneling transport is considerably weaker. This can be understood in terms of the structural differences between the devices; however, a complete understanding of this class of quantum-well transistor will require further experimental and theoretical effort.

The superlattice BiQuaRTT utilized 5-nm $Al_{0.4}Ga_{0.6}As$ tunnel barriers compared with the 5-nm AlAs barriers described in the present device. The AlAs barriers result in a reduced resonant-tunneling current density since the larger AlAs barrier height reduces the transmission energy width of the RTD.

In the superlattice BiQuaRTT, the emitter and collector layers of the device are GaAs/$Al_{0.4}Ga_{0.6}As$ superlattices. These superlattices act to compress the energy distribution of electrons in the emitter and collector by the formation of minibands. The width of the first miniband is estimated to be approximately 9 meV. This can be expected to increase the peak-to-valley ratio of the RTD over that of bulk emitter and collector layer of the same average composition. It may be possible to obtain negative transconductance in this structure by tunneling the resonant tunneling between the two superlattices.

Considerable lattitude for improvement of the pseudomorphic BiQuaRTT exists. The 5-nm AlAs tunnel barriers can be thinned to provide more ideal Γ-point tunnel barriers with larger resonant-tunneling current density. The 15-nm quantum-well thickness, which was intentionally made large to ease the contacting requirements, gives rise to many quantum-well energy levels. This is undesirable for a large negative transconductance device. The number of quantum-well states is readily reduced by thinning the quantum well. The thinner base will require higher quantum-well doping and a self-aligned transistor geometry to minimize the base resistance.

## VI. Conclusions

We have demonstrated a pseudomorphic BiQuaRTT in which contact is made to a Be-doped quantum well. The transport characteristics show evidence of tunneling-current control by modification of the quantum-well potential. The voltages at which the transistor is biased into resonance are well predicted by a self-consistent numerical simulation of the electrostatic potential. Measurements of the temperature dependence of the device transport characteristics indicate that improved device performance can be expected with reduced base resistance and thinner AlAs tunnel barriers.

*Note added:* The idea of contacting the p-doped quantum well of an RTD to control the tunneling current has been previously and independently conceived [19].

## Acknowledgment

The authors would like to acknowledge the technical assistance of B. Garmon, R. Thomason, F. Goodman, and T. Brandon, and the editing assistance of J. Fuller. Thanks are also expressed to R. T. Bate for his direction and encouragement during this work and to J. H. Luscombe, C.-H. Yang, and F. Morris for their stimulating questions and helpful discussions.

## References

[1] J. R. Barker, "A look into the future," in *GaAs FET Principles and Technology*, J. V. DiLorenzo and D. D. Khandelwal, Eds. Dedham, MA: Artech, 1982.

[2] R. T. Bate, "The future of microstructure technology—The industry view," *Superlattices and Microstructures*, vol. 2, no. 1, pp. 9-11, 1986.

[3] M. A. Reed, W. R. Frensley, R. J. Matyi, J. N. Randall, and A. C. Seabaugh, "Realization of a three-terminal resonant tunneling device: the bipolar quantum resonant tunneling transistor," *Appl. Phys. Lett.*, vol. 54, no. 11, pp. 1034-1036, 1989.

[4] A. C. Seabaugh, M. A. Reed, W. R. Frensley, J. N. Randall, and R. J. Matyi, "Realization of pseudomorphic and superlattice resonant tunneling transistors," in *IEDM Tech. Dig.*, 1988, pp. 900-902.

[5] F. Capasso and R. A. Kiehl, "Resonant tunneling transistor with quantum well and high-energy injection: A new negative differential resistance device," *J. Appl. Phys.*, vol. 58, no. 3, pp. 1366-1368, 1985.

[6] F. Capasso, S. S. Sen, A. C. Gossard, A. L. Hutchinson, and J. H. English, "Quantum-well resonant tunneling bipolar transistor operating at room temperature," *IEEE Electron Device Lett.*, vol. EDL-7, no. 10, pp. 573-576, 1986.

[7] F. Capasso, "Resonant tunneling transistors and superlattice devices by band-gap engineering," in *Proc. Int. Symp. GaAs and Related Compounds, Inst. Phys. Conf. Ser.*, no. 83 (Las Vegas, NV), 1986, pp. 17-25.

[8] T. Futatsugi *et al.*, "A resonant-tunneling bipolar transistor (RBT): A proposal and demonstration for new functional devices with high current gains," in *IEDM Tech. Dig.*, 1986, pp. 286-289.

[9] T. Futatsugi, Y. Yamaguchi, S. Muto, N. Yokoyama, and A. Shibatomi, "InAlAs/InGaAs resonant tunneling bipolar transistors (RBTs) operating at room temperature with high current gains," in *IEDM Tech. Dig.*, 1987, pp. 877-888.

[10] F. Capasso, S. Sen, A. Y. Cho, and D. L. Sivco, "Multiple negative transconductance and differential conductance in a bipolar transistor by sequential quenching of resonant tunneling," *Appl. Phys. Lett.*, vol. 53, no. 12, pp. 1056-1058, 1988.

[11] S. Sen, F. Capasso, A. Y. Cho, and D. L. Sivco, "Multiple-state resonant-tunneling bipolar transistor operating at room temperature and its application as a frequency multiplier," *IEEE Electron Device Lett.*, vol. 9, no. 10, pp. 533-535, 1988.

[12] ——, "New resonant tunneling bipolar transistor (RTBT) with multiple negative differential resistance characteristics operating at room temperature with large current gain," in *IEDM Tech. Dig.*, 1988, pp. 877-888.

[13] P. J. Orders and B. F. Usher, "Determination of critical layer thicknesses in $In_xGa_{1-x}As/GaAs$ heterostructures by x-ray diffraction," *Appl. Phys. Lett.*, vol. 50, no. 15, pp. 980-982, 1987.

[14] D. L. Miller and P. M. Asbeck, "Be redistribution during growth of GaAs and AlGaAs by molecular beam epitaxy," *J. Appl. Phys.*, vol. 57, no. 6, pp. 1816-1822, 1985.

[15] P. Enquist, G. W. Wicks, L. F. Eastman, and C. Hitzman, "Anomalous redistribution of beryllium in GaAs grown by molecular beam epitaxy," *J. Appl. Phys.*, vol. 58, no. 11, pp. 4130-4134, 1985.

[16] I. Getreu, *Modeling the Bipolar Transistor.* Beaverton, OR: Tektronix, 1976, pp. 140-142

[17] S. Tiwari, S. L. Wright, and A. W. Kleinsasser, "Transport and related properties of (Ga,Al)As/GaAs double heterostructure bipolar junction transistors," *IEEE Trans. Electron Devices*, vol. ED-34, no. 2, pp. 185-198, 1987.

[18] N. G. Anderson, W. D. Laidig, R. M. Kolbas, and Y. C. Lo, "Optical characterization of pseudomorphic $In_xGa_{1-x}As$-GaAs single-quantum-well heterostructures," *J. Appl. Phys.*, vol. 60, no. 7, pp. 2361-2367, 1986.

[19] B. Riccò and P. M. Solomon, "Tunable resonant tunneling semiconductor emitter structure," *IBM Tech. Disclosure Bull.*, vol. 27, no. 5, pp. 3053-3056, 1984.

*

**Alan C. Seabaugh** (S'78-M'85) received the B.S., M.S., and Ph.D. degrees in electrical engineering from the University of Virginia. His doctoral dissertation concerned the measurement and interpretation of photocurrent transients in semi-insulating GaAs using a novel ac impedance bridge technique.

From 1979 to 1986, he was employed by the National Bureau of Standards where he developed a variety of electronic and photoelectronic measurement techniques for characterizing compound semiconductors. He joined the Central Research Laboratories of Texas Instruments Incorporated in 1986, where he worked on microwave MODFET's, selective reactive-ion etching, and heterojunction *C-V* profiling. In early 1988, he changed tasks to develop resonant tunneling transistors. His current interests are in the transport properties of hot-electron and resonant-tunneling devices. On a part time basis, he lectures at the University of Texas at Dallas.

Dr. Seabaugh is a member of the APS.

*

**William R. Frensley** (M'78-SM'84) received the B.S. degree in physics from the California Institute of Technology, Pasadena, in 1973 and the Ph.D. degree in physics from the University of Colorado, Boulder, in 1976. His dissertation research concerned the theory of the electronic structure of semiconductor heterojunctions. He continued this work in a post-doctoral position at the University of California at Santa Barbara.

In 1977, he joined the Central Research Laboratories of Texas Instruments Incorporated, where at first he did experimental and theoretical work on GaAs MESFET's. He has also been involved in the development of GaAs bipolar transistor IC's and more novel, vertically structured GaAs FET's. His research interests are presently directed toward the theory of electron transport in quantum-scale semiconductor devices.

Dr. Frensley is a member of the American Physical Society. He was an Associate Editor of IEEE TRANSATIONS ON ELECTRON DEVICES from 1983 to 1986.

*

**John N. Randall** (S'80-M'81) received the B.S., M.S., and Ph.D. degrees in electrical engineering from the University of Houston in 1975, 1977, and 1981, respectively. His work at the University of Houston involved the microfabrication of subtenth-micrometer structures with e-beam and X-ray lithography to be used in an e-beam memory system.

After receiving the Ph.D., he joined M.I.T.'s Lincoln Laboratory where he worked for three and a half years. At the Lincoln Laboratory, he was involved primarily with masked ion-beam lithography, but was also involved with reactive-ion etching, X-ray lithography, low-pressure chemical vapor deposition, and other microfabrication techniques. He joined Texas Instruments Incorporated in 1985 and is a member of the technical staff in the Central Research Laboratories. He is presently responsible for microfabrication of quantum effect devices. Other work at Texas Instruments has concerned the investigation of masked ion-beam lithography, which included development and modeling of ion beam masks. He has published in numerous technical journals.

Dr. Randall is a member of the AVS and SPIE.

*

**Mark A. Reed** (M'84-SM'87) received the B.S. degree (Honors) in physics in 1977, the M.S. degree in physics in 1979, and the Ph.D. degree in solid-state physics in 1983 from Syracuse University.

He then joined Texas Instruments Incorporated as a Member of the Technical Staff in the Central Research Laboratories. His research activities at TI have included the investigation of mesoscopic systems, tunneling phenomena in heterojunction systems, artificially structured materials and devices, localization phenomena, and high magnetic field effects in semiconductors. In 1986 he became an Adjunct Professor of Physics at Texas A&M University. In 1988 he was elected to Senior Member of the Technical Staff at TI. He is the author of more than 40 professional publications in numerous journals. He is co-editor of the book *Nanostructure Physics and Fabrication* and is the author of several book chapters. He holds six U.S. patents.

Dr. Reed is a member of the APS, Sigma Xi, and the OSA.

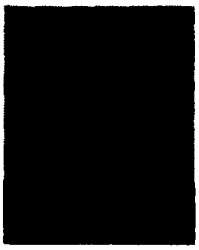

**Dewey L. Farrington** received the A.S. degree in electronic technology from Oklahoma State University in 1978 and the B.S. degree in physics from the University of Texas, Dallas, in 1987.

He joined Texas Instruments in 1978. He spent two years in the Missile Division before joining the Radar Division as a Field Representative in Europe for the Tornado (MRCA) project at customer locations (one year in England and two years in Italy). Upon returning to Dallas, he moved to the Central Research Laboratories as a Research Assistant in the SIMS Laboratory. He is presently a Member of the Technical Staff at TI and is primarily responsible for the SIMS Laboratory.

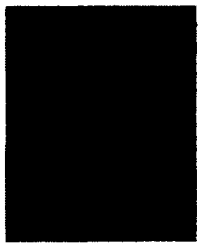

**Richard J. Matyi** received the Ph.D. degree in materials science from Northwestern University in 1982.

He joined Texas Instruments Incorporated in 1982. His work included X-ray diffraction analysis of semiconductor materials, the growth of compound semiconductor structures for microwave and ultrasmall electronics applications using molecular-beam epitaxy, and the cointegration of GaAs and silicon device structures. He is now an Assistant Professor in the Department of Materials Science and Engineering at the University of Wisconsin, Madison.

# APPENDIX J

# QUANTUM-WELL RESONANT-TUNNELING TRANSISTORS

Presented at the Twelfth Biennial Conference on Advanced Concepts in High Speed Semiconductor Devices and Circuits, August 7,8,9, 1989, Cornell University.

# Quantum-Well Resonant-Tunneling Transistors[1]
(invited)

A. C. Seabaugh, W. R. Frensley, Y.-C. Kao,
J. N. Randall, and M. A. Reed
Central Research Laboratories
Texas Instruments Incorporated
Dallas, TX 75265

*"At any rate, it seems that the laws of physics present no barrier to reducing the size of computers until bits are the size of atoms, and quantum behavior holds dominant sway".*

*Richard P. Feynmann, 1985 [1]*

## INTRODUCTION

Recently, resonant-tunneling transistors (RTTs) have been formed by making an ohmic contact to the quantum well of a resonant-tunneling diode [2-4]. These transistors are of interest because they offer the possibility of greater circuit density, higher speed, and increased logical function per device over conventional transistor technology. In addition, they provide a stepping stone to proposed quantum-coupled devices and circuits [5,6].

Prior investigations of resonant-tunneling transistors have focused on incorporating the resonant-tunneling diode into the terminals of bipolar [7-11], field-effect [12,13], or hot electron [14-18] transistors. Figure 1 compares previous resonant-tunneling bipolar transistor (RTBT) designs with the bipolar quantum resonant-tunneling transistor (BiQuaRTT) of Reed, et al. [2,3] (center). Each of the energy band diagrams was recalculated (by solution of Poisson's equation) from published material descriptions to allow a direct comparison of the device structures. The *npn* transistor structure and resonant-tunneling double-barrier can be seen in each of the energy diagrams. The initial approaches of Capasso, et al. [7] and Futatsugi, et al. [8] are shown at the top of the figure. Futatsugi, et al. placed the RTD at the emitter/base junction (Fig. 1 upper left) while Capasso, et al. (upper right) put the undoped RTD just inside the *p*-type base. The effect in both devices is approximately the same. Since the initial publications, the RTBT

[1]This work was supported by the Defense Advanced Research Projects Agency (DoD) under ARPA No. 9770400.1304 and monitored by the Office of Naval Research.

has been fabricated in the InAlAs/InGaAs system lattice-matched to InP. These devices are shown in the lower half of the figure. Both a single RTD ( lower left) and two RTDs in series (lower right) have been moved into the emitter of the transistor structure.

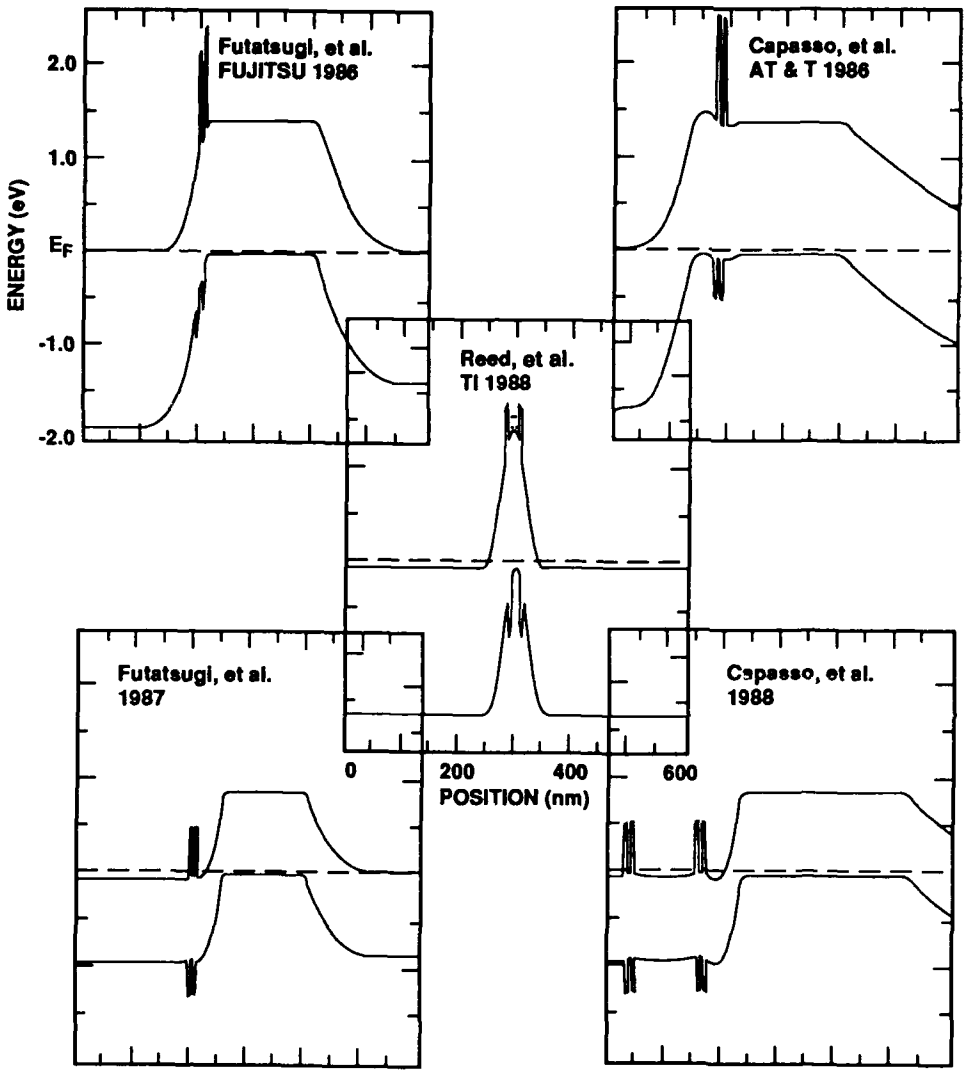


Fig. 1. Energy band profile comparison of bipolar resonant-tunneling transistors. The literature references are, in counterclockwise order starting in the upper right, Capasso, et al. [7], Futatsugi, et al. [8], Futatsugi, et al. [10], and Capasso, et al. [11], and in the center, Reed, et al. [2,3]. The top two and center structures are GaAs/AlGaAs materials, while the lower structures are InGaAs/InAlAs materials.

The BiQuaRTT (center of Fig. 1) differs from previous RTBTs in that the *p*-dopants are located within the quantum well. In addition, the resonant-tunneling double-barrier quantizes the allowed energies at which the electron can transverse the two-dimensional base. To increase the emitter injection efficiency, the quantum well base consists of a lower bandgap semiconductor than the emitter. An ohmic contact to the quan-

tum well is used to control the potential of the quantum well and therefore the tunneling current across the base. With base widths of 15 nm or less, the BiQuaRTT could also exhibit nonequilibrium (ballistic) electron transport [19] not expected in the wide-base GaAs RTBTs [20].

## BiQuaRTT CHARACTERISTICS

Room temperature energy band diagrams for one implementation of a pseudomorphic-base BiQuaRTT [4] are shown in Fig. 2.

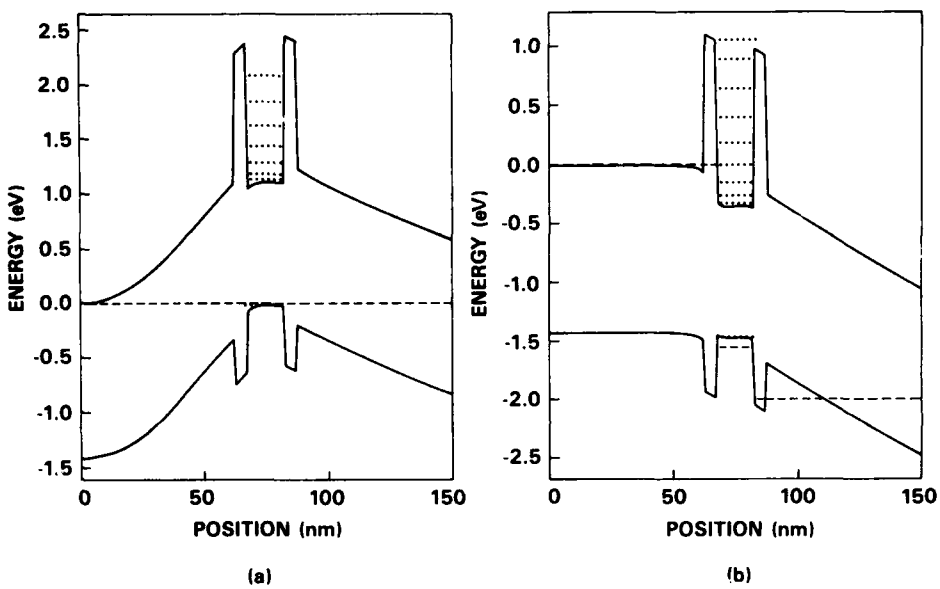


Fig. 2. Pseudomorphic BiQuaRTT energy band profile. The structure is shown in (a) equilibrium and (b) under bias to bring the emitter electron energy into resonance with the fourth allowed quantum well base state, $V_{be}$=1.5V, $V_{ce}$=2.5V, 300 K. The dashed lines designate the Fermi-level position; the dotted lines designate the electron and hole states in the quantum well.

The *n*-type GaAs emitter is at left, with the *p*-type InGaAs quantum well base in the center, and the *n*- GaAs collector at the right. Gamma-point AlAs tunnel barriers are assumed. These profiles are obtained from a self-consistent (zero current) solution of Poisson's equation for the electrostatic potential. The free-electron densities in the emitter and collector are calculated from the Fermi distribution for semiclassical electrons. The allowed carrier energies in the base are obtained from a solution of Schroedinger's equation. The hole density in the base is determined by integrating the product of the quantum-well-base 2-d density-of-states and the Fermi distribution in the base over energy.

Growth of the structure begins with a 500 nm $n^+$ GaAs buffer layer followed by a 500 nm $n$- GaAs collector. The RTD base is symmetric about a 5 nm InGaAs Be-doped layer in the center of the quantum well. InGaAs spacer layers of 5 nm on either side of the 5 nm Be-doped layer bring the quantum well width to 15 nm. AlAs tunnel barriers of 5 nm thickness and 25 nm undoped GaAs spacer layers bound the quantum well on either side. A 200 nm GaAs emitter region, doped to $5 \times 10^{17}$ $cm^{-3}$, is grown above the quantum-well base, followed by a 300 nm $n^+$ contact layer.

From the energy band profiles (Fig. 2), it can be seen that the quantum well contact can be used to reduce the potential energy of the quantum well electron states. The transmission probability for electron transport across the base will then depend on the alignment of the emitter electron distribution and the allow quantum well base states. Thus with monotonically increasing $V_{be}$, collector current increases, then decreases (negative transconductance), then increases again, and so on through the higher order states.

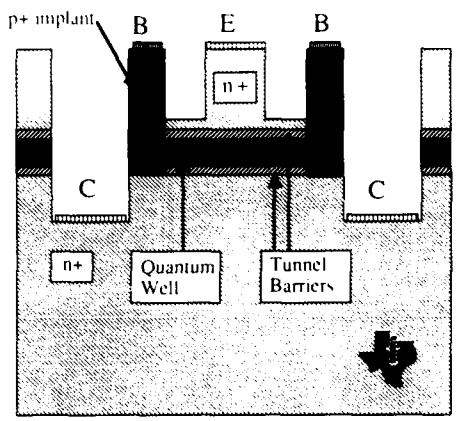


Fig. 3. Transistor cross section.

A non-self-aligned fabrication process utilizing conventional photolithography and lift-off metallizations is used to form the transistor, Fig. 3. Contact to the quantum well is achieved by implantation of Be. The triple Be-implant of $1 \times 10^{15}$ $cm^{-2}$ at energies of 30, 80, and 160keV is sufficient to convert the $2 \times 10^{18}$ $cm^{-3}$ $n$-type surface layer conductivity to $p$-type. The implantation is activated by rapid thermal annealing (RTA) at 750°C for 10 seconds. The implanted base region is isolated from the emitter by wet chemical etching to prevent the turn-on of the lateral base-emitter $p$-$n$ junction.

Common-emitter transistor characteristics for the pseudomorphic BiQuaRTT[4] show a room temperature gain of approximately 13. Evidence for resonant-tunneling is observed in the measured dependence of collector current on $V_{be}$ (Fig. 4).

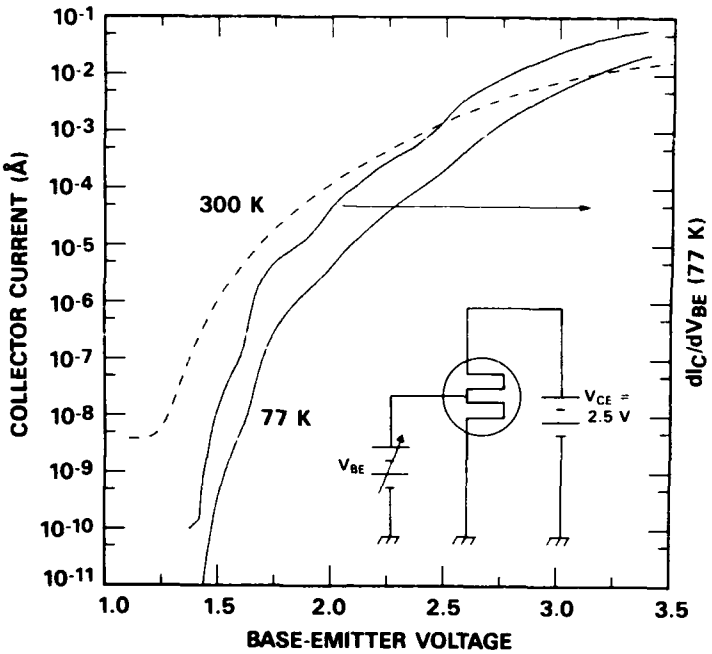


Fig. 4. Dependence of collector current on base-to-emitter voltage at $V_{ce}$=2.5 V. The dashed line shows the collector current dependence at room temperature, while the solid lines show the 77 K result. The derivative of the collector current with respect to the base-emitter voltage is shown to emphasize the collector current inflections.

The right hand axis shows the derivative of the collector current with respect to $V_{be}$ from which we observe clear inflections in the collector current for $V_{be}$ = 1.6, 1.9, and 2.4 V. This is in agreement with the resonance voltage predicted from the electrostatic band profiles of 1.55, 1.73, and 2.13 V. When the base series resistance is accounted for, the agreement is still better. Negative transconductance is typically observed in resonant-tunneling transistors. The fact that negative transconductance is not observed in this device implies that inelastic transport processes in this device are comparable to the resonant-tunneling current. This is probably due to the low resonant-tunneling current-density which occurs through the thick AlAs barriers.

Another embodiment of the BiQuaRTT [3] utilizes a superlattice emitter and collector to provide an effectively wider bandgap emitter than the GaAs quantum well. The energy band diagram for this device is shown in Fig. 5(a). The structure consists of a 1 μm undoped GaAs buffer, Si-doped GaAs contact layers of 2 x $10^{18}$ $cm^{-3}$ (1.5 μm bottom contact, 0.5 μm top contact), a superlattice emitter and collector consisting of 50 periods of 8 nm AlGaAs + 2 nm $Al_{0.4}Ga_{0.6}As$ Si doped to 2 x $10^{18}$ $cm^{-3}$ except for three periods adjacent to the tunnel barriers, 5 nm undoped $Al_{0.4}Ga_{0.6}As$ tunnel barriers,and a 15 nm *p*-type quantum well. The center 5 nm of the quantum well was doped *p*-type with Be to

$1 \times 10^{19}$ $cm^{-3}$.The room-temperature common-emitter transistor characteristics for this device show typical current gain of 50. Under base voltage bias the device exhibits room temperature negative transconductance as shown in Fig. 5(b).

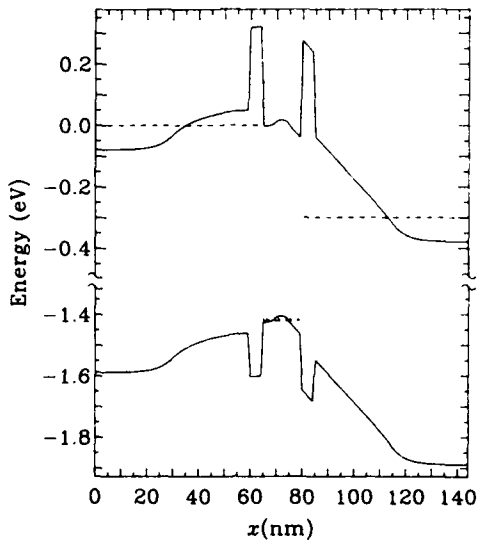


Fig. 5. (a) Room temperature energy band profile for the superlattice BiQuaRTT with $V_{be}$=1.42 and $V_{ce}$= 0.3 V. The superlattice potential is not computed, rather an average uniform Al mole fraction (x=0.07) in the emitter and collector is used as an approximation.

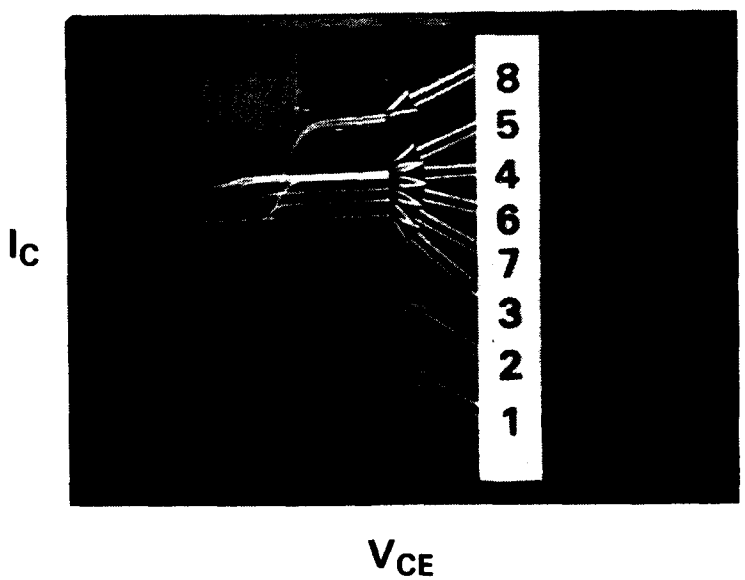


Fig 5. (b) Room-temperature common-emitter characteristics with base voltage steps. Numbers point to the collector current and show the increase, then decrease, then increase in collector current with a monotonically increasing base voltage.

In addition to increasing the effective bandgap of the emitter and collector layers over that of GaAs, the superlattices also act to compress the energy distribution of electrons in the emitter and collector by the formation of minibands. The width of the first miniband is estimated to be approximately 9 meV. The effects of these superlattice injectors and collectors are currently under investigation.

## The QuESTT

A unipolar resonant-tunneling transistor has been independently conceived by Frensley and Reed [21], Schulman and Waldner [22], and Haddad et al. [23]. In our laboratory, this resonant-tunneling hot electron transistor (RHET) is known as the QuESTT or Quantum Excited-State Tunneling Transistor. A representative energy band profile for the device is shown in Fig. 6.

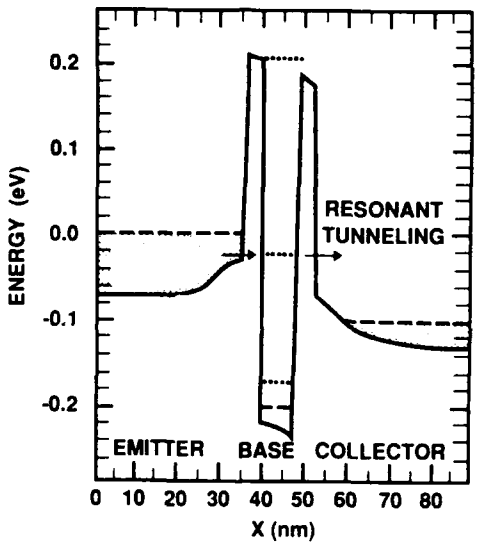


Fig. 6. Energy band profile for the QuESTT utilizing GaAs emitter and collector layers, AlGaAs tunnel barriers, and an InGaAs quantum well.

Without base doping it is possible to bandgap engineer a structure such that the quantum well ground state is occupied and confined. Electrical contact is then made to this ground state. Transport across the device occurs through the first excited state while the charge in the ground state is used to control the resonant-tunneling condition. Evidence that this device concept will be realized in the near future has been provided by Heiblum, et al. [24] who observe transport through the excited states in their THETA devices for base quantum well widths in the range 29-72 nm.

This device is of interest because it does not contain the large *p-n* junction depletion layers which introduce an additional delay in the transit time of electrons across the device. The depletion layers also limit the ultimate scalability of the transistor in the vertical direction. In addition the device provides an important test vehicle for investigating charge

transport through quantum well states and means for controlling the transfer of charge into and out of quantum wells.

## APPLICATIONS

The use of resonant-tunneling for compressing the function of many transistors into a single transistor stage is well established [15, 17, 25, 26]. This reduces the number of interconnects between devices and the wiring delay, thereby increasing speed. Demonstrated circuits include an exclusive-NOR [15], a flip flop [25], and a four bit parity generator [26]. If the resonant-tunneling transistor stage can be realized in a compact structure offering ballistic transport, computational speed is gained by both reducing the number of logical elements and by increasing the device speed.

Resonant-tunneling transistors have recently been fabricated with reduced parasitics for microwave characterization. Imamura, et al. [27] have reported an $f_T$ = 63 GHz and $f_{max}$ =44 GHz in an InGaAs/InAlAs RHET device characterized at 77K. Lunardi, et al. [28] report room temperature results from an InGaAs/InAlAs RTBT finding an $f_T$ in the tunneling mode of between 12 and 18 GHz. Analog multipliers using these devices have also been demonstrated [15, 26, 28, 29]. High frequency performances will undoubtedly increase in the coming years with improvements in device fabrication and layout.

## CONCLUDING REMARKS

We have demonstrated bipolar resonant-tunneling transistors and proposed unipolar transistors which are formed by making direct contact to the quantum well of a resonant-tunneling diode structure. Experimental and theoretical efforts are now underway to understand the performance limits of these devices. Base resistance is a potentially significant limitation in these devices, however techniques for heavy doping continue to advance [30,31]. Both digital and microwave applications for these devices have been enumerated. In addition to the more conventional uses of the RTT, it is important to explore other means for interconnecting these devices to produce useful circuit functions.

## ACKNOWLEDGEMENTS

The authors would like to acknowledge the technical assistance of T. Brandon, B. Garmon, P. Stickney, F. Stovall, R. Thomason, and F. Goodman, the materials and characterization work of R. Matyi and D. Farrington, and the direction of R. Bate.

## REFERENCES


[1] R. P. Feynmann, *Optics News*, 11 (February 1989).

[2] A. C. Seabaugh, M. A. Reed, W. R. Frensley, J. N. Randall, and R. J. Matyi, *IEDM Tech. Digest 1988*, 900.

[3] M. A. Reed, W. R. Frensley, R. J. Matyi, J. N. Randall, and A. C. Seabaugh, *Appl. Phys. Lett.*, **54**, 1034 1989.

[4] A. C. Seabaugh, W. R. Frensley, J. N. Randall, M. A. Reed, D. L. Farrington, and R. J. Matyi, *IEEE Trans. Electron Dev.*, to be published October 1989.

[5] R. T. Bate, *VLSI Handbook*, ed. by N. G. Einspruch, 615 (Academic Press 1985) and *Superlattices and Microstructures*, **2**, 9 (1986).

[6] G. Frazier, *Concurrent Computations*, ed. by S. K. Tewsburg, B. W.Dickinson, and S. C. Schwartz, 1 (Plenum Publishing, 1988).

[7] F. Capasso, S. S. Sen, A. C. Gossard, A. L. Hutchinson, and J.H. English, *IEEE Electron Device Lett.*, **EDL-7**, 573 (1986) and *IEDM Tech. Digest 1986*, 282.

[8] T. Futatsugi, Y. Yamaguchi, K. Ishii, K. Imamura, S. Muto, N.Yokoyama, and A. Shibatomi, *IEDM Tech. Digest* 1986, 286 and *Jpn. J. Appl. Phys.*, L132 (1987).

[9] F. Capasso, *Inst. Phys. Conf. Ser.* No. **83**, 17 (1986) and *Springer Ser. Electron. Photonics*, **22**, 50 (1986).

[10] T. Futatsugi, Y. Yamaguchi, S. Muto, N. Yokoyama, and A. Shibatomi, *IEDM Tech. Digest* 1987, 877.

[11] F. Capasso, S. Sen, A. Y. Cho, and D. L. Sivco, *Appl. Phys. Lett.* **53**, 1056 (1988).

[12] T. K. Woodward, T. C. McGill, and R. D. Burnham, *Appl. Phys. Lett.*, 451 (1986)

[13] F. Capasso, S. Sen, and A. Y. Cho, *Appl. Phys. Lett.*, **51**, 526 (1987).

[14] N. Yokoyama, K. Imamura, S. Muto, S. Hiyamizu, and H. Nishi, *Jpn. J. Appl. Phys.*, **24**, L853 (1985).

[15] T. Mori, H. Ohnishi, K. Imamura, S. Muto, and N. Yokoyama, *Appl. Phys. Lett.*, **49**, 1779 (1986).

[16] K. Imamura, S. Muto, H. Ohnishi, T. Fujii, and N. Yokoyama, *Electron. Lett.*, **23** 870 (1987) and K. Imamura, S. Muto, and N. Yokoyama, *Fujitsu Sci. & Tech. J.*, 24 (1988).

[17] N. Yokoyama, K. Imamura, H. Ohnishi, T. Mori, S. Muto, and A. Shibatomi, *Solid State Electron.*, **31**, 577 (1988).

[18] K. Imamura, T. Mori, H. Ohnishi, S. Muto, and N. Yokoyama, *Electron. Lett.*, **25** 34 (1989).

[19] K. Berthold, A. F. J. Le·:, J. Walker, and R. J. Malik, *Appl. Phys. Lett.*, **52**, 2247 (1988).

[20] F. Capasso. S. Sen, A. Y. Cho, and A. L. Hutchinson, *Appl. Phys. Lett.*, **50**, 930 (1987).

[21] W. R. Frensley and M. A. Reed, U. S. Patent Appl. Ser. No. 768542 (1985).

[22] J. N. Schulman and M. Waldner, *J. Appl. Phys.*, **63**, 2859 (1988).

[23] G. I. Haddad, R. K. Mains, U. K. Reddy, and J. R. East, *Superlattices and Microstructures*, **5**, 437 (1989).

[24] M. Heiblum, M. V. Fischetti, W. P. Dumke, D. J. Frank, I. M. Anderson, C. M. Knoedler, and L. Osterling, *Phys. Rev. Lett.*, **58**, 816 (1987).

[25] N. Yokoyama and K. Imamura, *Electron. Lett.*, **22** 1228 (1986).

[26] S. Sen, F. Capasso, A. Cho, and D. Sivco, *Electron. Lett.*, **24**,1507 (1988), and *IEDM Tech. Digest* 1988, 834.

[27] K. Imamura, T. Mori, H. Ohnishi, S. Muto, and N. Yokoyama, *Electronics Lett.*, **25**, 34 (1989).

[28] L. M. Lunardi, S. Sen, F. Capasso, P. R. Smith, D. L. Sivco, and A. Y. Cho, *IEEE Electron Device Lett.*, **10**, 219 (1989).

[29] S. Sen, F. Capasso, A. Cho, and D. Sivco, *IEEE Electron Device Lett.*, **EDL-9**, 533 (1988).

[30] R. J. Malik, R. N. Nottenberg, E. F. Schubert, J. F. Walker, and R. W. Ryan, *Appl. Phys. Lett.*, **53**, 2661 (1988).

[31] R. A. Hamm, M. B. Panish, R. N. Nottenburg, Y. K. Chen, and D. A. Humphrey, *Appl. Phys. Lett.*, **54**, 2587 (1989).

# APPENDIX K

# IMPLANT AND ANNEALED OHMIC CONTACT TO A THIN QUANTUM WELL

# Implant and annealed ohmic contact to a thin quantum well

C. H. Yang,[a] D. L. Plumton, R. Lodenkamper, and H. D. Shih
*Texas Instruments Inc., Central Research Laboratories, P. O. Box 655936, MS 154, Dallas, Texas 75265*

(Received 30 May 1989; accepted for publication 4 August 1989)

We demonstrate for the first time that ion implantation and implant activation annealing, combined with a heavily doped InGaAs surface layer, can be used to make nonalloying shallow ohmic contact to an $n$-type InGaAs (or GaAs) quantum well. Quantum Hall effect and Shubnikov–de Haas oscillations are clearly observed, which indicates that electrons in the quantum well remain two dimensional despite the post-implantation high-temperature annealing. This technique can be applied to devices that would need to make shallow ohmic contact to a thin ($\sim 100$ Å or less) quantum well, where existing selective etching approaches fail to work.

Recent development of semiconductor crystal growth technologies, such as molecular beam epitaxy[1] (MBE), makes possible the growth of artificial heterostructures where materials can be altered within a few monolayers. Such sample preparation technologies have important device applications. For example, a quantum well high electron mobility transistor (HEMT) with a pseudomorphic material system has shown to have the highest current-gain cutoff frequency.[2] In addition, using a quantum well base is of crucial importance to the implementation of a family of unipolar tunneling transistors,[3–8] where a dc current gain greater than 1 has been demonstrated in both GaAs/AlGaAs and InGaAs/InAlAs/InP material systems.[9] However, there is difficulty in making shallow electrical contact to a thin quantum well. Although a self-limiting etching process can stop at the quantum-well interface, materials within the first 100 Å or so would be consumed.[10] Furthermore, subsequent alloying forms spikes[11] that could penetrate through the quantum well and electrically short the surface electrode to the substrate. Thus, the thickness of the quantum well in such vertical tunneling devices cannot be narrower than 250–300 Å.[12] This range of thickness is greater than that needed to show a significant change in the device transport characteristics.[13] In the case of GaAs or InGaAs quantum wells, to make the separation between the lowest subbands comparable to or greater than the energy spread of incoming electrons or thermal spread at 300 K, the base width should be at least on the order of 100 Å.

Our approach to solve this problem is to use low-energy ion implantation and nonalloying $n^{++}$-InGaAs contacts. Low-energy Si implantation can selectively dope the semiconductor and reach the quantum well with controlled penetration depth from the surface, which eliminates the necessity of etching down to the quantum well. The nonalloying contact[14] at the surface allows electrical connection without forming sharp metallurgical spikes. In this letter, we present magnetoresistance data and demonstrate for the first time that electrons in a quantum well are still two dimensional after post-implantation high-temperature annealing. The fact that the ohmic behavior persists from 300 K to liquid-helium temperature also indicates that this approach can be an alternative to make ohmic contacts to a quantum well.

A typical sample structure is shown in Fig. 1(b). It is grown on a (100) semi-insulating GaAs substrate by MBE. The structure consists of a 1 $\mu$m undoped GaAs buffer, a 50 Å $n^+$ ($1.0\times10^{18}/\mathrm{cm}^3$) GaAs, a 100 Å $n^+$ ($\sim 4.0\times10^{18}/\mathrm{cm}^3$) $In_{0.15}Ga_{0.85}As$, a 50 Å $n^+$ ($1.0\times10^{18}/\mathrm{cm}^3$) GaAs, a 1000 Å undoped GaAs, and a 500 Å graded junction to $In_{0.45}Ga_{0.55}As$ (heavily doped, more than $1.0\times10^{19}/\mathrm{cm}^3$) as the surface nonalloying contact layer. The specific contact resistance before implantation derived from a plot of the measured resistance versus the spacings of contact pads (transmission line method[15]) is $\sim 1.0\times10^{-6}\ \Omega\,\mathrm{cm}^2$. For low-temperature magnetoresistance measurements, the samples are fabricated into Hall bars [see Fig. 1(a)]. First, the contact regions are implanted ($Si^{29}$, dose $1.0\times10^{14}/\mathrm{cm}^2$). Before implantation, a thin layer of $Si_3N_4$ is used to protect the semiconductor and avoid channeling of Si atoms. During post-implantation high-temperature (850 °C) annealing, a new layer of $Si_3N_4$ is then deposited as an annealing cap. Metal contact layers are deposited by evaporation for external contacts, e.g., 100 Å Ti, 500 Å Pt, followed by 3000 Å Au. Hall bar geometry is finally defined by using standard photolithography and wet chemical etching techniques.

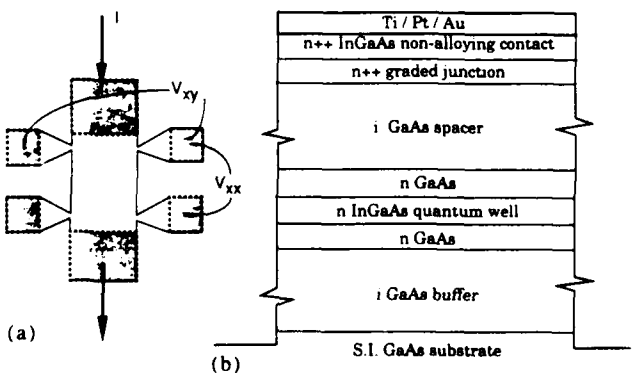


FIG. 1. (a) Schematic of top view of the Hall bar geometry, defined by wet mesa etching. The dashed region is first implanted, annealed, and then deposited with Ti/Pt/Au. For magnetoresistance measurements, test current (1 $\mu$A) is passed through the end contacts, while the transverse and longitudinal voltages are measured at the other pins as shown. (b) The schematic of the sample structure where InGaAs quantum well is sandwiched by doped GaAs layers.

[a] Present address: University of Maryland, Electrical Engineering Department, College Park, MD 20742.

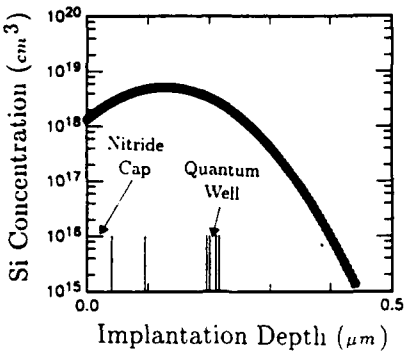


FIG. 2. Calculated implantation profile using the approximation discussed in Ref. 16. The short vertical segments indicate the positions of heterointerfaces [see Fig. 1(b)]. The surface of the samples during implantation is covered by a thin layer (400 Å) of silicon nitride.

The implantation energy (100 keV) and dose ($1.0\times10^{14}/cm^3$) are chosen such that the donor density at the quantum well is $\sim1.0\times10^{17}/cm^3$. The implantation profile calculated by using the results of Anholt *et al.*[16] is shown in Fig. 2. Rapid thermal annealing with a two-step heating procedure (700 °C for 2 min followed by 850 °C for 10 s) is used.[17] Although the annealing procedure may not be optimized to maximize the activation percentage and minimize the interdiffusion of As and In, it serves the purpose of demonstrating our new approach.

In the following, we present current-voltage ($I$-$V$) characteristics to show that the $In_{0.15}Ga_{0.85}As$ quantum well electrons are still two dimensional after high-temperature annealing. (Similar features discussed below are also observed in a set of samples with an $In_{0.15}Ga_{0.85}As$ quantum well sandwiched by doped $Al_{0.4}Ga_{0.6}As$ layers.) Figure 3 shows the $I$-$V$ characteristic between two arbitrary pins of a Hall bar at 4.2 K. The linearity of the result indicates that the electrical contact is ohmic even at 4.2 K. The ohmic conduction is in fact observed between any pair of contacts on the Hall bar.

To test that the conduction is from (two-dimensional) electrons in the $In_{0.15}Ga_{0.85}As$ quantum well, a series of three samples with a decreasing surface doping level, $1.0\times10^{19}/cm^3$, $1.0\times10^{18}/cm^3$, and $1.0\times10^{17}/cm^3$, is fabricated. Without implantation and annealing procedures, only the one with heavily doped surface layer ($1.0\times10^{19}/cm^3$) shows nonalloying ohmic conduction between metal pads of the Hall bar at various temperatures, while the others are nonohmic at room temperature and become nonconducting near zero voltage at low temperatures. The results indicate that nonalloying ohmic behavior comes from heavy doping of the surface $In_{0.45}Ga_{0.55}As$, and the surface Fermi level is still pinned below the conduction-band minimum.[18]

To demonstrate that the electrons are two dimensional after high-temperature annealing, we performed magnetoresistance measurements.[19] The magnetoresistance versus magnetic field $B$ from 0 to 9 T at 4.2 K is plotted in Fig. 4, where the field direction is perpendicular to the quantum well plane. There is no dependence when the magnetic field is parallel to the surface, indicating that the electrons are two dimensional. The $\rho_{xx}$ shows Shubnikov–de Haas (SdH) oscillations, while the $\rho_{xy}$ displays the quantum Hall effect at a strong field and is linearly proportional to the magnetic field at low fields. The slope of the Hall measurement at low fields corresponds to an electron density of $1.76\times10^{12}/cm^2$. From the oscillation period in $1/B$ of $\rho_{xx}$, we determine a two-dimensional electron density of $1.45\times10^{12}/cm^2$. The discrepancy is a result of a parallel conduction from the surface $n^{++}$-$In_{0.15}Ga_{0.85}As$. Also shown in Fig. 4 (dashed line) is the expected classical Hall resistance when a density of $1.45\times10^{12}/cm^2$ is assumed. The quantum Hall plateaus therefore occur with their Hall resistances less than $h/\nu e^2$. The two-dimensional electron mobility is estimated as 1300 $cm^2/V$ s from $\rho_{xx}$ at zero magnetic field, shown in Fig. 4.

In conclusion, we have demonstrated that electrons in a 100 Å quantum well retain their two-dimensional density of states characteristics after high-temperature annealing procedures. This finding, together with the $n^{++}$-InGaAs nonalloying surface layer on top of GaAs, is shown to be a new approach in making shallow ohmic contact to a quantum well. Our results thus have important device applications, in particular, to those with the need to electrically contact a

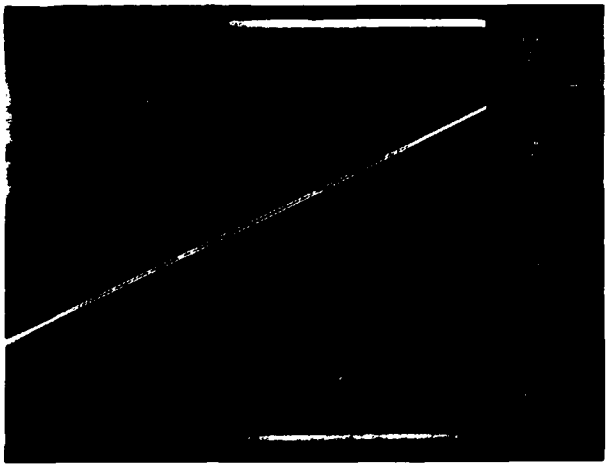

FIG. 3. $I$-$V$ characteristics of two contacts on a Hall bar fabricated by using

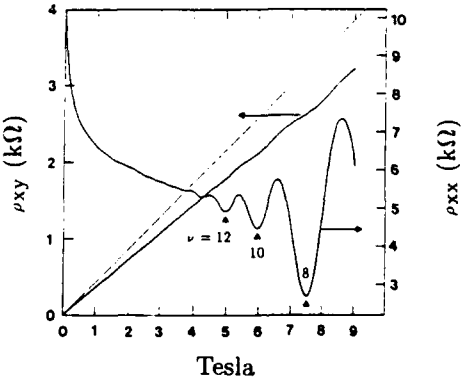


FIG. 4. Magnetoresistance of a Hall bar at 4.2 K. Both $\rho_{xx}$ and $\rho_{xy}$ are measured with the magnetic field parallel to the sample growth direction. The dashed line is the calculated classical Hall resistance for a single layer of two-dimensional electron gas, assuming that the carrier density is the same as that inferred from SdH oscillations. Filling factors $\nu$ of 12, 10, and 8 are

quantum well but without penetrating to a deeper layer.

We thank R. T. Bate for encouragement and M. J. Yang for helpful discussions. Excellent technical assistance from M. McCain, A. L. Buehler, and F. A. Ferreira is greatly appreciated. This work was partially supported by the Office of Naval Research and the Defense Advanced Research Projects Agency under contract No. N-00014-87-C-0363.

[1]The subject is reviewed, e.g., by L. L. Chang and K. Ploog, eds., *Molecular Beam Epitaxy and Heterostructures* (Martinus Nijhoff, Dordrecht, The Netherlands, 1985).

[2]U. K. Mishra, A. S. Brown, and S. E. Rosenbaum, *Technical Digest of the International Electron Devices Meetings* (IEEE, New York, 1988), p. 180.

[3]A. F. J. Levi, J. R. Hayes, P. M. Platzman, and W. Wiegmann, Phys. Rev. Lett. **55**, 2071 (1985).

[4]M. Heiblum, Solid-State Electron. **24**, 343 (1981); Phys. Rev. Lett. **55**, 2200 (1985).

[5]K. Imamura, S. Muto, and N. Yokoyama, Fujitsu Sci. Tech. J. **24**, 54 (1988).

[6]S. Luryi, Appl. Phys. Lett. **52**, 501 (1988).

[7]A. Kastalsky and M. Milshtein, Appl. Phys. Lett. **52**, 398 (1988).

[8]F. Beltram, F. Capasso, S. Luryi, S. G. Chu, A. Y. Cho, and D. L. Sivco, Appl. Phys. Lett. **53**, 219 (1988).

[9]K. Imamura, S. Muto, T. Fujii, N. Yokoyama, S. Hiyamizu, and A. Shibatomi, Electron. Lett. **22**, 1148 (1986).

[10]Paul Saunier (private communications).

[11]T. S. Kuan, J. Appl. Phys. **54**, 6952 (1980).

[12]M. Heiblum, D. Galbi, and M. Weckwerth, Phys. Rev. Lett. **62**, 1057 (1989).

[13]M. Heiblum, M. V. Fischetti, W. P. Dumke, D. J. Frank, I. M. Anderson, C. M. Knoedler, and L. Osterling, Phys. Rev. Lett. **58**, 816 (1987).

[14]T. Nittono, H. Ito, O. Nakajima, and T. Ishibashi, Jpn. J. Appl. Phys. **25**, 865 (1986).

[15]See, e.g., R. E. Williams, *GaAs Processing Techniques* (Artech House, Dedham, MA, 1984).

[16]R. Anholt, P. Balasingam, S. Y. Chou, and T. W. Sigmon, J. Appl. Phys. **64**, 3429 (1988).

[17]D. L. Plumton, W. M. Duncan, and L. T. Tran, Mater. Res. Soc. Symp. Proc. **92**, 475 (1987).

[18]H. Tamura, A. Yoshida, and S. Muto, Jpn. J. Appl. Phys. **26**, L7 (1987).

[19]See, e.g., T. Ando, A. B. Fowler, and F. Stern, Rev. Mod. Phys. **54**, 437 (1982).

# APPENDIX L

# A NEW FIELD-EFFECT RESONANT TUNNELING TRANSISTOR: OBSERVATION OF OSCILLATORY TRANSCONDUCTANCE

# New field-effect resonant tunneling transistor: Observation of oscillatory transconductance

C. H. Yang,[a], Y. C. Kao, and H. D. Shih
*Texas Instruments Inc., Central Research Laboratories, P.O. Box 655936, MS 154 Dallas, Texas 75243*

(Received 3 July 1989; accepted for publication 23 October 1989)

We present device characteristics of a field-effect, unipolar, resonant tunneling transistor. An oscillatory tunneling current in the transfer characteristics is observed for the first time. Our observation confirms a recent hypothesis that a mere three-to-two dimensional resonant tunneling can occur when the scattering rate is less than the attempt frequency of tunneling electrons in the quantum well.

Resonant tunneling (RT) phenomena in heterostructures grown by molecular beam epitaxy (MBE) have attracted much interest recently.[1] This in part is because the system provides a vehicle for studying microscopic tunneling mechanisms. In addition, RT can be useful in high-speed device applications. For example, a GaAs/AlGaAs-based double-barrier (DB) diode oscillator has been shown to operate up to 400 GHz.[2] For applications in circuits, a three-terminal device is often preferred. Among the few tunneling transistors studied,[3] the Stark-effect transistor[4] (SET) is of particular interest. The idea is that the tunneling probability of electrons from bulk to a two-dimensional quantum well (QW) could be resonantly enhanced due to energy and momentum conservation. As a result, the tunneling conductance of a SET would show peaks in the transfer characteristics. Recently, Beltram *et al.* reported[5] the observation of negative differential resistance (NDR) and negative transconductance in a structure similar to SET with a single tunneling barrier. Their interpretation was based on the assumption that electrons, after they tunnel through the barrier, can flow along the 120 Å undoped QW to the drain. However, the surface Fermi level pinning of GaAs would completely deplete the exposed GaAs QW in dark at 7 K, and the large testing voltage suggests an alternative explanation.[6]

In this letter, we report the fabrication and device characteristics of a field-effect resonant tunneling transistor. The structure is similar to that of a SET, but now the tunneling barrier consists of a DB RT structure. The DB RT structure serves as an energy filter, where the electron energy spread is on the order of meV. As will be shown below, the tunneling current between source (bulk) and drain (2D QW) oscillates in the transfer characteristics, due to resonance effects.

We implement this three-terminal device concept by a four-terminal structure: the terminals are source, drain, front gate, and back gate. Figure 1(a) shows the device structure and the energy-band diagram. Since the qualitative characteristics of interest are not sensitive to the exact structure, we will only present data taken from the structure shown in Fig. 1(a). The structure, grown on an $n^+$ substrate by molecular beam epitaxy, consists of a 2 $\mu$m undoped GaAs buffer, a 8000 Å undoped $Al_{0.37}Ga_{0.63}As$, a 200 Å $n^+$ ($1\times10^{18}/cm^3$) GaAs QW, a 30 Å undoped $Al_{0.37}Ga_{0.63}As$ barrier, a 70 Å undoped GaAs, a 30 Å undoped $Al_{0.37}Ga_{0.63}As$ barrier, a 1500 Å $n^+$ GaAs ($1\times10^{18}/cm^3$), and a 500 Å graded nonalloying $n^+$-$In_{0.45}Ga_{0.55}As$ capping layer. The devices are defined by standard photolithography. Silicon implantation is used to make shallow ohmic contacts to define the drain region. Previously, we have shown[7] that after high-temperature (850 °C) annealing, the electrons in the 240 Å QW are still two dimensional, and the $n^+$-$In_{0.45}Ga_{0.55}As$ nonalloying contact remains ohmic at

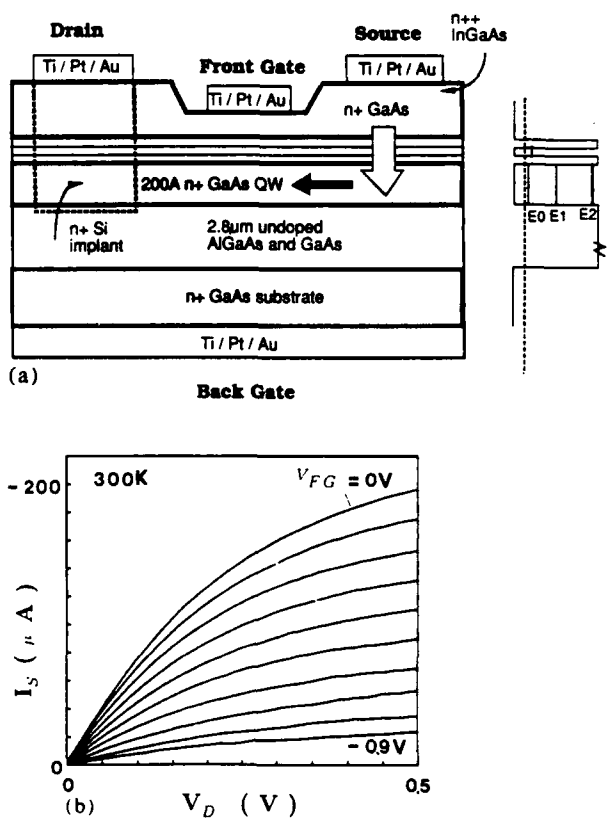


FIG. 1. (a) Schematic cross section of a resonant tunneling transistor structure (not to scale). The area enclosed by a dashed line is Si implanted. The 3D–2D tunneling (see context) process is indicated by the hollow arrow, while the solid arrow represents the current path in the GaAs QW. (b) $I$-$V$ characteristics of source, drain, and front gate. $V_{BG}$ is kept at 10 V (source

[a] Present address: Electrical Engineering Department, University of Mary-

low temperatures. After source and drain are defined (Ti/Pt/Au evaporation and lift-off), the surface $In_{0.45}Ga_{0.55}As$ and part of the $n^+$-GaAs are removed by etching. A Schottky gate (Ti/Pt/Au evaporation) is finally defined as the front gate, while the heavily doped substrate performs as the back gate. The device characteristics of source, drain, and front gate therefore behave as a typical metal-semiconductor field-effect transistor (MESFET), as shown in Fig. 1(b). The front Schottky gate can deplete the region underneath, and hence the conduction between source and drain. The thickness of $n^+$-GaAs under front gate is therefore estimated to be close to the $n^+$-GaAs depletion length, which is about 400 Å.

The operating principle is explained in Fig. 2, where the schematic energy-band diagrams are plotted under various bias conditions. We limit the bias at drain $V_D$ (source is common) to a small positive value, in order to (1) make electrons flow from source to drain, (2) minimize the electric field in the direction parallel to the QW, and (3) avoid hot-electron energy relaxation problems. Figures 2(b) and 2(d) are the cases where RT might occur, and 2(a) and 2(c) are for conditions that tunneling is tuned off-resonance. The smooth rising background is partially due to the increasing conductivity of the QW as in the case of FETs, and multiple peaks in transconductance are expected if multiple RT states in the QW are engaged.

The aforementioned oscillatory features in transfer characteristics have been observed in our field-effect tunneling transistor at 77 and 4.2 K. As shown in Fig. 3(a), the source current $I_S$ (and drain current $I_D$), measured at a

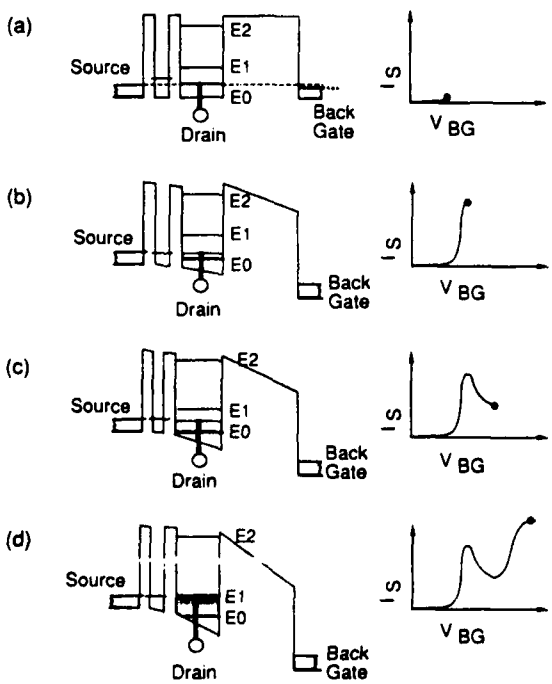


FIG. 2. Proposed transfer characteristics $I_S$ vs $V_{BG}$ are plotted when $V_D$ (source is common) is fixed at a small bias, and $V_{BG}$: (a) is slightly above zero; (b) aligns incoming energy approximately to $E_0$; (c) aligns incoming energy in between $E_0$ and $E_1$; (d) aligns incoming energy approximately to $E_1$.

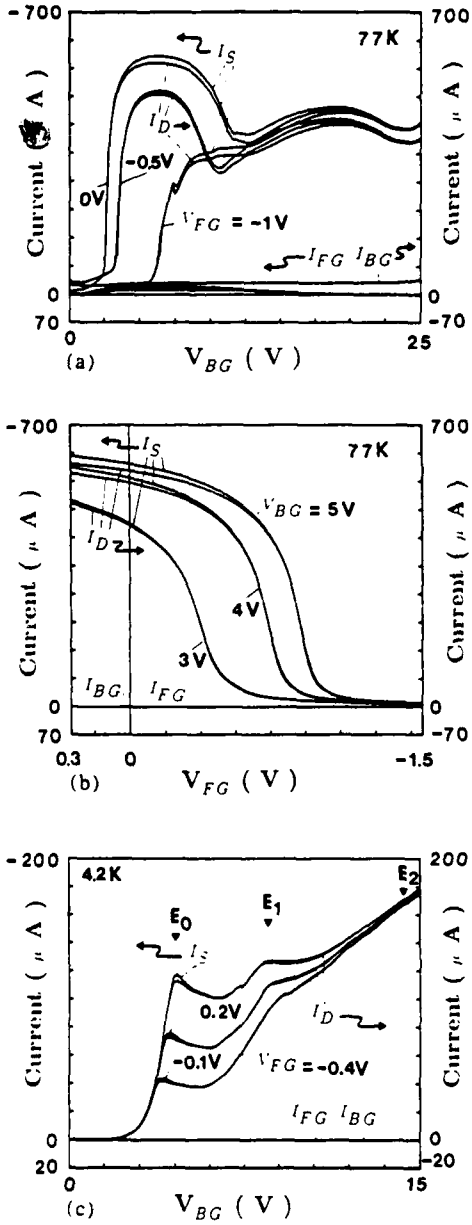


FIG. 3. (a) $I_S$, $I_D$, $I_{FG}$, $I_{BG}$ of the tunneling transistor as a function of $V_{BG}$, while $V_{FG}$ is 0, $-0.5$, and $-1$ V, and $V_D$ is 0.1 V. (b) $I_S$, $I_D$, $I_{FG}$, $I_{BG}$ of the tunneling transistor as a function of $V_{FG}$, and $V_D$ is 0.1 V. (c) $I_S$, $I_D$, $I_{FG}$, $I_{BG}$ of the tunneling transistor as a function of $V_{BG}$, while $V_D$ is 0.2 V and $V_{FG}$ is swept from 0.2 to $-0.4$ V at steps of 0.3 V.

fixed $V_D$ of 0.1 V, oscillates when $V_{BG}$ varies from 0 to 15 V. This observation of oscillatory tunneling current is different from that of any other three-terminal devices showing negative transconductance[8] in that our device displays multiple current peaks and such negative transconductance characteristic is observable in a wide range of source-drain bias. In particular, the characteristics remain the same near zero $V_D$. On the other hand, when $V_{FG}$ is employed, in contrast to the case of using the back gate, $I_S$ (and $|I_D|$) is gradually reduced when $V_{FG}$ is more negative, as shown in Fig. 3(b). The feature, that when $V_{FG}$ is in control the transconductance shows only a single peak and remains positive, is in

agreement with the characteristics of a typical MESFET. There is a small amount of leakage current through the front gate and through the back gate under bias at 77 K, but both are much less than $I_S$ or $I_D$. That $I_S$ and $I_D$ are almost identical in amplitude and differ only by sign, indicates that the signal comes from the current path between source and drain.

The oscillatory features shown in Fig. 3(a) become sharper at lower temperatures. Figure 3(c) plots the transfer characteristics, using back gate at 4.2 K. As many as three current peaks are observed. The transfer characteristics using front gate is qualitatively unchanged, and the leakage currents through front gate and through the back gate are simply further reduced. Notice that $V_D$ is kept small (0.2 V) compared to $V_{BG}$ (few volts), and the distance between source and drain (10 $\mu$m) is longer than that between source and back gate (2.8 $\mu$m). The electric field underneath the source pad is therefore approximately perpendicular to the barrier, and the complications in analysis due to large $V_D$ such as hot-electron relaxation and nonuniform tunneling probability are therefore avoided. The observation of current oscillations shown in Figs. 3(a) and 3(c) provides conclusive evidence that a mere 3D to 2D tunneling can produce resonance effects.

The width of the peaks in Fig. 3(c) can be used to estimate the scattering time at 4.2 K. Taking the known QW width we have calculated the lowest three resonance levels to be at 7.5 meV ($E_0$), 29.6 meV ($E_1$), and 66.2 meV ($E_2$) from the bottom of the QW. Using 22.1 meV ($E_1 - E_0$) to calibrate the separation between the lowest two resonant states, we obtain full widths of $\sim 8$ meV and $\sim 13$ meV for the two peaks labeled $E_0$ and $E_1$ in Fig. 3(c), respectively. The corresponding scattering times, by uncertainty principle, are $\sim 82$ fs for $E_0$ and $\sim 50$ fs for $E_1$, with the assumption that the intrinsic resonance width is negligible. Scattering would broaden the energy dependence of RT coefficient, and makes the resonant states in the quantum well less well defined. In the limit where scattering time goes to zero, the resonance would be extremely broad as if there is no resonance at all.[9,10] Furthermore, in our device structure, electrons must be scattered after tunneling due to energy relaxation, before they can contribute to the signal. We therefore conclude, based on our observation of distinct peaks in tunneling current, that for this particular device the scattering rate is less than the attempt frequency.[9,10]

Our finding has important implications in understanding the negative differential resistance characteristics of DB RT. While the original Esaki's coherent tunneling picture[11] is challenged by discrepancies when comparing predictions of $I$-$V$ curves with experimental results, the phenomenological Breit–Wigner formalism[9,10] offers a qualitative interpretation but fail to explain the microscopic details. Our finding suggests a partially coherent, partially incoherent tunneling process. Electrons, while bouncing back and forth in the QW, can tunnel through the second barrier[12,13] before the Fabry–Perot étalon type of interference is completely set up. However, resonance effects can still be observed as long as the scattering rate is less than the attempt frequency.

We thank R. T. Bate for encouragement, and excellent technical support from M. McCain, J. R. Thomason, and F. H. Stovall. We owe special thanks to R. Hudgens, B. Kim, D. L. Plumton, J. N. Randall, P. Saunier, J.-Y Yang, and M.-J. Yang for their suggestions at various stages. This work is supported in part by the Office of Naval Research and the Defense Advanced Research Projects Agency under contract number N00014-87-C-0363.

[1] S. Luryi, in *Heterojunction Band Discontinuities: Physics and device applications*, edited by F. Capasso and G. Margaritondo (North-Holland, Amsterdam, 1987), Chap. 12.
[2] E. R. Brown, Bull. Am. Phys. Soc. **34**, 533 (1989).
[3] M. Heiblum, M. I. Nathan, D. C. Thomas, and C. M. Knoedler, Phys. Rev. Lett. **55**, 2200 (1985), and references therein.
[4] A. R. Bonnefoi, D. H. Chow, and T. C. McGill, Appl. Phys. Lett. **47**, 888 (1985).
[5] F. Beltram, F. Capasso, S. Luryi, S.-N. G. Chu, A. Y. Cho, and D. L. Sivco, Appl. Phys. Lett. **53**, 219 (1988); *Proceedings of the 15th International Symposium on GaAs and Related Compounds*, edited by J. S. Harris (IOP, Bristol, 1989), p. 599.
[6] C. H. Yang and H. D. Shih, in *Proceedings of the 15th International Symposium on GaAs and Related Compounds*, edited by J. S. Harris (IOP, Bristol, 1989), p. 611.
[7] C. H. Yang, D. L. Plumton, R. Lodenkamper, and H. D. Shih, Appl. Phys. Lett. **55**, 1650 (1989).
[8] For a review, see, e.g., F. Capasso, in *Semiconductors and Semimetals*, edited by R. K. Willardson and A. C. Beer (Academic, New York, 1987), Vol. 24, Chap. 6.
[9] M. Johnson and A. Grincwajg, Appl. Phys. Lett. **51**, 1729 (1987).
[10] See, e.g., M. Buttiker, IBM J. Res. Develop. **32**, 63 (1988).
[11] R. Tsu and L. Esaki, Appl. Phys. Lett. **22**, 562 (1973).
[12] S. Luryi, Superlatt. Microstruct. **5**, 375 (1989).
[13] C. H. Yang, M. J. Yang, and Y. C. Kao, Phys. Rev. B **40**, 6272 (1989).

# APPENDIX M

# IMPROVED MBE GROWTH STRUCTURES FOR HIGH-PERFORMANCE DEVICE APPLICATIONS

# Texas Instruments

**Improved MBE Growth of InGaAs-InAlAs Heterostructures for High-Performance Device Applications**

**Y.C. Kao, A.C. Seabaugh, H.Y.Liu, T.S. Kim, M.A.Reed, P. Saunier, B. Bayraktaroglu, and W.M. Duncan**

Presented at the First International Conference on InP and Related materials for Advanced Electronics and Optical Devices
Norman, OK March,20-22, 1989

**TR-088940** **08/01/89**

## DISTRIBUTION

J.M. Anthony 147
R.T. Bate 154
E. Beam 147
K.E. Bean 147
B. Bayraktaroglu 134
K. Bradshaw 134
G.E. Brehm 245
C.T. Chang 4947
C.C. Cho 147
L.T. Claiborne 145
D.R. Collins 134
L. Colombo 147
T.V. Cordner 404
M.W. Cowens 147
F.H. Doerbeck 404
W.M. Duncan 147
S. Evans 404
L.A. Files 147
W.R. Frensley 154
B.E.Gnade 147
G.H. Heilmeier 400
T.S. Henderson 134
C. Hoel 219
R.D. Hudgens 134
Y.C. Kao 147
J.A. Keenan 147
M.A. Khatibzadeh 134
T.S. Kim 147
M.A.Kinch 150
R.J. Koestner 147
P.K. Liao 147
H.Y. Liu 147
H.M. Macksey 404
D.N. McQuiddy 245
T.M. Moore 147
F. Morris 134
P.A. Penz 154
D.L. Plumton 134
A.J. Purdes 147
M.A. Reed 154
C.G. Roberts 150
J.B. Sampsell 134
P. Saunier 134
H.F. Schaake 147
A. Seabaugh 134
T.J. Shaffner 147
H. Shichijo 134
D.W. Shaw 147
R. Stratton 136
H.L. Tsai 147
H.Q. Tserng 134
M.A. Vernon 404
M.S. Wdowik 404
R.E. Williams 404
W.R. Wisseman 134
L.C. Witkowski 134
H.T. Yuan 134
TRS(2) 8433

# Improved MBE growth of InGaAs-InAlAs heterostructures for high-performance device applications

Y.C. Kao, A.C. Seabaugh, H.Y. Liu, T.S. Kim, M.A. Reed
P. Saunier, B. Bayraktaroglu, and W.M. Duncan

Texas Instruments Incorporated, Central Research Laboratories
P.O. Box 655936, MS147, Dallas, Texas 75265

## ABSTRACT

In this paper, we report the improvements in structural quality of the InGaAs-InAlAs heterostructures grown on InP by molecular beam epitaxy (MBE). The effect of heteroepitaxial growth parameters on modulation-doped n-InAlAs/InGaAs-InP structures is examined by Hall measurement. Practical growth conditions have been developed for device fabrication. Low-temperature (4.2 K) magnetotransport measurement and resonant tunneling spectroscopy are used to characterize the modulation-doped structures and resonant tunneling barrier structures, respectively. Both measurements indicate the high quality of the heterostructures. Barrier height effect on resonant tunneling diode structures is discussed. InAlAs-InGaAs heterojunction bipolar transistors (HBTs) and high-electron-mobility transistors (HEMTs) have been successfully fabricated on InP in this work.

## 1. INTRODUCTION

InGaAs-InAlAs pseudomorphic and lattice-matched heterojunctions on InP substrates are of particular interest for use in high-performance transistor structures such as heterojunction bipolar transistors (HBTs), high electron mobility transistors (HEMTs), and resonant tunneling transistors (RTTs) because of the superior electron transport properties of InGaAs and the large conduction band offset (0.52 eV obtained for the InGaAs/InAlAs heterojunction).[1] This paper reports improvements in structural quality of InGaAs-InAlAs heterostructures grown by molecular beam epitaxy (MBE).

We employed x-ray diffraction, photoluminescence (PL), and Hall measurements to characterize the grown films. Measurements on modulation-doped HEMT structures and resonant tunneling diodes (RTDs) by low-temperature magnetotransport and resonant tunneling spectroscopy, respectively, provided complementary information on electrical transport along and across the heterojunction. Electronic properties of the InGaAs-InAlAs device structures, including HBT, HEMT, and RTD structures, are also discussed.

## 2. GROWTH IMPROVEMENTS

Many reports discuss growth improvements in the quality of InAlAs and InGaAs films on InP, mainly by optimizing growth temperature and the V/III ratio.[2,3] However, the growth conditions for both compounds are usually not compatible because of a large congruent temperature difference. In this study, InAlAs and InGaAs growth conditions suitable for fabrication of various heterojunction devices were first established. A Riber-2300 MBE system with conventional thermal group III sources and an $As_4$ source was used for InAlAs/InGaAs growth on InP:Fe(100) substrates. Indium-free mounting of 2-inch wafers, which is important for ease of device fabrication, was developed and used in this work. Before growth, native oxides on InP substrates were

thermally removed by heating over 500 °C for 5 minutes under an $As_4$ beam. Typical growth rate was 0.9 $\mu$m/hour. Reproducible beam fluxes of all group III elements were measured daily at the growth position using an ion gauge. Accurate In-to-Ga (or In-to-Al) flux ratio, corresponding to either lattice-matched or pseudomorphic condition, was consistently achieved in order to yield structures with proper In composition within 2%. Unintentionally doped InGaAs layers were n-type with a net donor concentration of $3.3 \times 10^{15}$ $cm^{-3}$, while undoped InAlAs layers were semi-insulating.

Figure 1 shows the dependence of the PL linewidth on growth temperature for three different V/III ratios. Each curve shows a minimum linewidth at different temperatures. A broadening linewidth at both higher and lower temperatures can be observed, while the temperature of minimum linewidth increases with greater V/III flux ratio. Minimum linewidths of 18, 16, and 13 were obtained at 500, 525, and 550 °C for V/III ratios of 3, 7, and 15, respectively. Two mechanisms, competing with each other, can account for the PL linewidth broadening. At low temperatures, the surface mobility of Al atoms is too low for Al to diffuse effectively onto the lattice sites as in the case of AlGaAs growth. Increasing growth temperature improves the crystalline quality and the PL linewidth decreases. Figure 1 also shows that, the greater the V/III ratio, the higher the temperature needed for comparable crystalline quality. On the other hand, the broadening linewidth with high temperature is related to incorporation of As vacancies, probably resulting from increasing As desorption from the surface. In this case, growth under a low V/III ratio would have a higher desorption rate and, therefore, results in a poorer film. Although the best linewidth of 12.8 meV was achieved under a high growth temperature of 550 °C and a high V/III ratio of 15, the drawbacks of rapid As-source consumption and incompatibility with lower InGaAs growth temperature are apparent. On the other hand, films grown at 525 °C with medium As pressure have satisfactorily high quality for device fabrication.

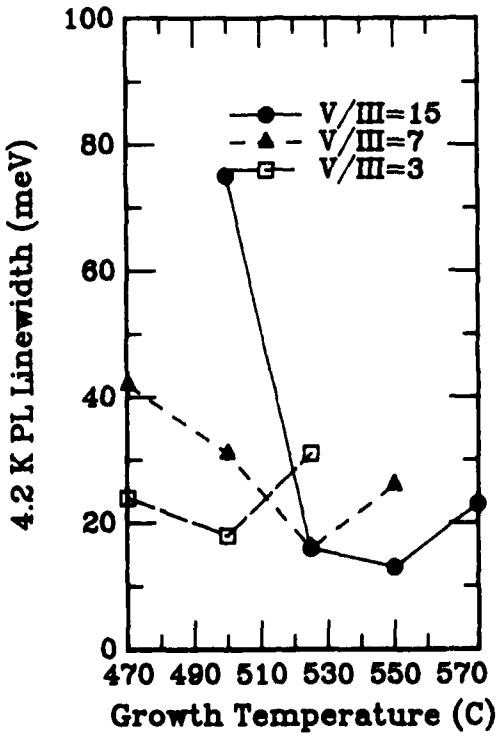


Fig.1 4.2 K PL linewidth of InAlAs versus growth temperature under three V/III ratios.

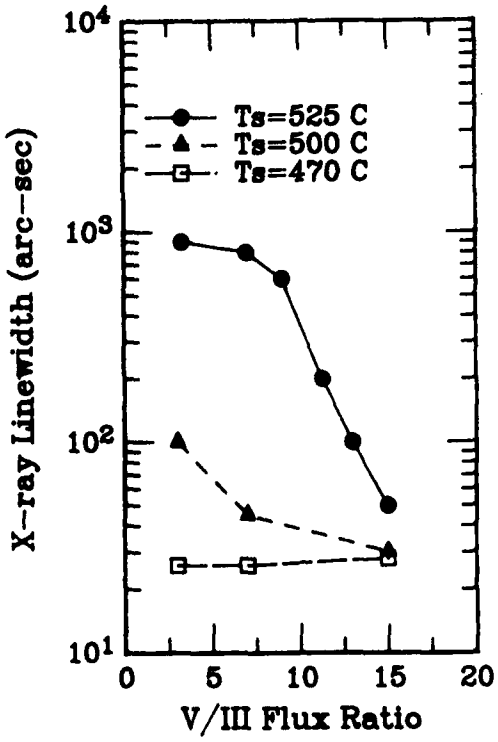


Fig.2 X-ray linewidth of InGaAs versus V/III ratio under three different growth temperatures.

As broader PL linewidths are usually obtained on InAlAs films, typical InGaAs layers have PL linewidths of 4 to 6 meV when grown under conditions similar to InAlAs growth except at lower growth temperatures. X-ray linewidth is sensitive to InGaAs quality but is not as sensitive to doping level as PL. To facilitate x-ray linewidth measurements, some samples were grown with lattice slightly mismatched to InP. There is little difference in film quality for growth under similar conditions with lattice mismatch up to 0.4%. Figure 2 shows the x-ray full width at half maximum (FWHM) of the InGaAs films as a function of V/III ratio under different growth temperatures. For a high growth temperature around 525°C and low As overpressure, poor InGaAs films with high FWHM values resulted, possibly because of As-vacancy incorporation. The film quality improved dramatically as the V/III ratio was increased above 10, and the FWHM values reached a minimum value of about 50 arc-seconds as the V/III ratio approached 15. For films grown at a certain temperature, a higher flux ratio always results in better growth, although the film quality becomes less and less sensitive to flux ratio as the growth temperature is decreased. The best films were grown at 470 °C with little flux ratio dependence. However, the films grown with a flux ratio of 7 were found to have higher PL intensity and slightly better electron mobility.

## 3. MATERIAL QUALITY

Two concerns surface when determining the growth conditions for device fabrication. First, high As overpressure is favorable in growing the best InGaAs and InAlAs; however, it is not practical to prepare these ternary layers with very high $As_4$ flux since high flux leads to frequent recharge of the solid arsenic cell. A V/III flux ratio of 15 to 1 is about 5 to 10 times higher than a normal GaAs/AlGaAs run. Second, because of growth temperature incompatibility between InAlAs and InGaAs, growth interruption is sometimes necessary, causing a potential impurity incorporation problem if interruption is too long. Using 2-inch InP with non-Indium soldering mounting can ease the problem since a 75 °C temperature change can be exercised in less than one minute. With these concerns in mind, several InAlAs/InGaAs heterostructures were prepared to evaluate the growth conditions and to characterize the heterojunction. Hall effect and low-temperature magnetotransport measurements on HEMT structures were used to evaluate the transport characteristics along the length of the heterointerface, while RTD assessed the transport across the interface.

### 3.1 Hall Effect and Magnetotransport Characterization

Four modulation-doped n-InAlAs/InGaAs heterostructures designed for microwave HEMT device applications were prepared to evaluate the growth conditions for device fabrication.[4] The undoped InGaAs channel thickness was 50 nm, sitting on top of a 500-nm-thick InAlAs buffer. Both medium (7) and high (15) V/III flux ratios were used. The InAlAs growth temperature was fixed at 525 °C ; while 470 and 525 °C were chosen for InGaAs growth. The growth parameters are listed in Table 1(a). The spacer layer thickness, supplied charge density, measured Hall mobilities, and sheet concentrations at 300 K and 77 K are also listed.

All four samples show fairly high and consistent values of sheet charge at both 300 and 77 K. The mobilities are higher with the InGaAs layer grown at 470 °C with a medium flux ratio or with the InGaAs grown at 525 °C with a high flux ratio. High InGaAs growth temperature under a medium flux ratio, or low InGaAs growth temperature under a high ratio, yields film with low mobilities, indicating less perfect heterointerfaces. The growth conditions were then selected either with InAlAs and InGaAs grown at 525 and 470 °C , respectively, under a medium flux ratio; or with both layers grown at 525 °C under a high flux ratio. The former condition was used to prepare all the heteroepitaxial device structures in this study, and the latter was used when superlattice layers were needed.

Low-temperature magnetotransport of the InGaAs/InAlAs HEMT structures was performed

in dark conditions,[5] immersed in the cryogen for thermal stability. Standard Hall bridges were defined by chemical etching with AuGe/Ni/Au ohmic contacts applied by evaporation and alloying. DC measurement techniques were used, with a typical constant-current source of 10 $\mu$A. The absence of electron heating was verified by varying the excitation current. For magnetotransport measurements, the magnetic field perpendicular to the plane of the 2-dimensional electron gas (2DEG) was swept from 0 to 9.0 Teslas.

Figure 3 shows the best mobility results. The standard HEMT structural parameters are listed in Table 1(b). At 4.2 K, the structure exhibits an electron mobility of $1.05 \times 10^5$ cm$^2$/V-s at a carrier density of $1.4 \times 10^{12}$ cm$^{-2}$ measured by Shubnikov-de Haas oscillations. Well defined quantum Hall plateaus are evident, and are quantized to the resistance values given by

$$\rho_{xy} = \frac{h}{e^2 i} = 25,813/i \text{ ohms}, \tag{1}$$

where $i$ is the number of filled Landau levels. The values agree to within the experimental resolution. Quantized Hall plateaus down to filling factors of $i = 4$ are evident.

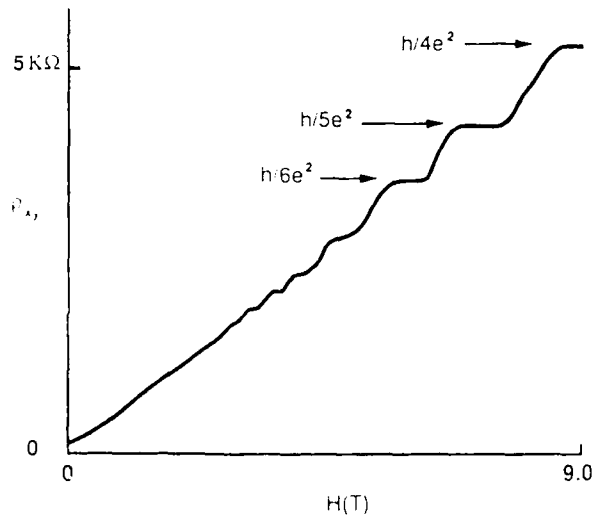


Fig.3 4.2 K Hall resistance of a standard n-InAlAs/InGaAs modulation-doped structure.

Table 1. Structural parameters of n-InAlAs/InGaAs HEMT structures for (a) Hall, and (b) low temperature magnetotransport measurements.

| | $T_{InAlAs}$ (°C) | $T_{InGaAs}$ (°C) | V/III Ratio | Total Charge (cm$^{-2}$) | Spacer (nm) | 300 K $\mu$ (cm$^2$/Vs) | 300 K $n_s$ (cm$^{-2}$) | 77 K $\mu$ (cm$^2$/Vs) | 77 K $n_s$ (cm$^{-2}$) |
|---|---|---|---|---|---|---|---|---|---|
| (a) | 525 | 470 | 7 | $5 \times 10^{12}$ | 5 | 9,800 | $2.1 \times 10^{12}$ | 53,000 | $1.7 \times 10^{12}$ |
| | 525 | 525 | 7 | $5 \times 10^{12}$ | 5 | 6,400 | $2.2 \times 10^{12}$ | 33,000 | $1.8 \times 10^{12}$ |
| | 525 | 470 | 15 | $5 \times 10^{12}$ | 5 | 6,000 | $2.1 \times 10^{12}$ | 31,000 | $1.7 \times 10^{12}$ |
| | 525 | 525 | 15 | $5 \times 10^{12}$ | 5 | 8,200 | $2.2 \times 10^{12}$ | 45,000 | $1.8 \times 10^{12}$ |
| (b) | Standard HEMT Structure | | | $5 \times 10^{12}$ | 2 | 9,800 | $2.1 \times 10^{12}$ | 47,000 | $1.9 \times 10^{12}$ |
| | Double-Heterojunction Pseudo-HEMT Structure | | | $8 \times 10^{12}$<br>$2 \times 10^{12}$ | 5<br>5 | 8,600 | $5.6 \times 10^{12}$ | 21,000 | $4.8 \times 10^{12}$ |

A double-heterojunction/single-quantum-well HEMT structure was also investigated. The sample consists of a 20-nm pseudomorphic $In_{0.6}Ga_{0.4}As$ quantum well clad by InAlAs barriers. There are 5-nm spacers between the quantum well with Si doping of $5x10^{18}$ $cm^{-3}$ (in 18 nm) and $2x10^{18}$ $cm^{-3}$ (in 10 nm) on the top and bottom, respectively, of the well. This structure is distinct from normal HEMT structures in that dopants are incorporated on both sides of the quantum well. The Shubnikov-de Haas oscillations exhibit two distinct Fourier components, yielding two 2DEG density values of $n(1) = 2.1x10^{12}$ $cm^{-2}$ and $n(2) = 6.2x10^{11}$ $cm^{-2}$ (Figure 4). The accompanying quantum Hall plateaus do not fall on the quantized values because of the parallel conduction paths in the quantum well. Parallel conduction through the InAlAs is not present, as demonstrated by the flatness of the plateaus. These results imply two parallel 2DEGs that are held by the ionized donors on both inverted and normal interfaces of the quantum well, indicating high quality of the heterointerface.

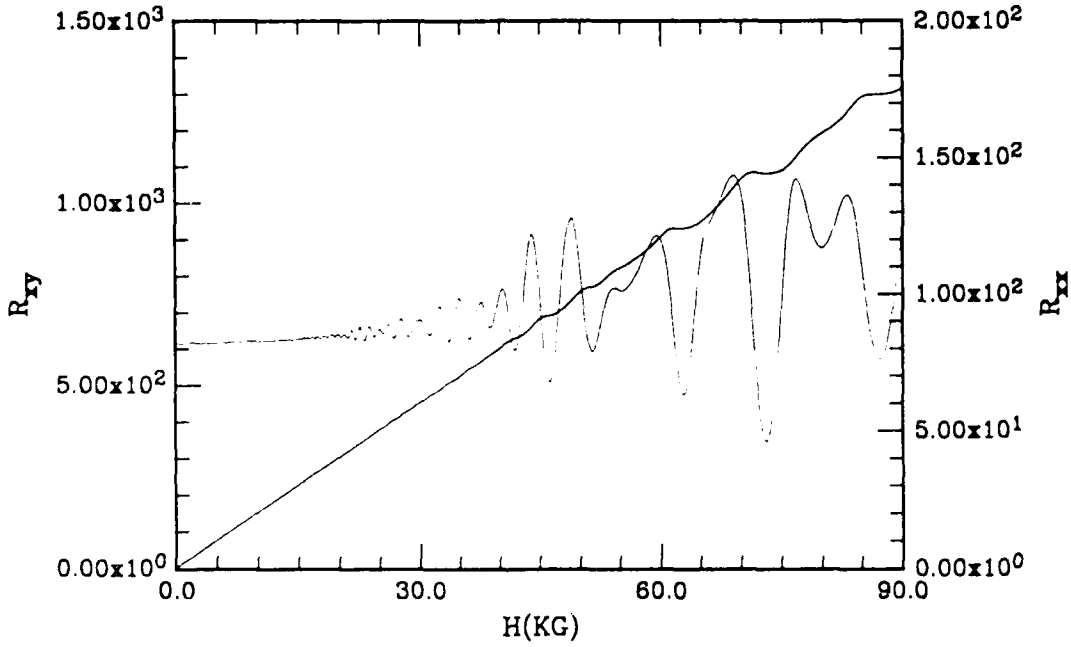


Fig.4 Low-temperature (1.0 K) magnetotransport measurements of a double-hetero single-quantum-well modulation-doped structure. Hall resistance is on the left scale and magnetoresistance is on the right scale.

## 3.2 Resonant Tunneling Diode Characterization

We have characterized the effect of $In_xAl_{1-x}As$ barrier composition on the RTD characteristics of the pseudomorphic $In_{0.53}Ga_{0.47}As$ /$In_xAl_{1-x}As$ RTD structure as x is varied from 0.35 to 0.69. From the lattice-matched condition at x = 0.52, this range in mole fraction spans a range of barrier strain from tensile to compressive. X-ray rocking curves were used to established the material composition.

The RTD structure, grown on semi-insulating InP substrates, consisted of an 800-nm InGaAs contact layer doped to $2x10^{18}$ $cm^{-3}$, 200 nm of InGaAs at $2x10^{17}$ $cm^{-3}$, a 20-nm InGaAs undoped spacer layer, a 3-nm InAlAs tunnel barrier, and a 4.5-nm InGaAs quantum well. The structure is symmetric in layers grown above the well except for the top $2x10^{18}$ $cm^{-3}$ contact layer, which is 200-nm thick rather than 800-nm thick. The InGaAs layers were lattice-matched, while the InAlAs tunnel barriers were varied in composition. Mesa devices with areas ranging from 9 to 900 $\mu m^2$ were formed by conventional lithographic steps, lift-off metallization, and wet chemical etching. Rapid thermal annealing, 350 °C for 5 seconds, lowered the contact resistivity from its

nonalloyed value in the $10^{-6}$ ohm-cm$^2$ range into the mid to low $10^{-7}$ ohm-cm$^2$ range.

The I-V characteristics of the lattice-matched InAlAs tunnel barrier RTD are shown in Figure 5. This structure, with InGaAs grown at nominally 470 °C and InAlAs tunnel barriers grown at 525 °C , gives a peak-to-valley current ratio of 5.1 at a current density of $2.1 \times 10^4$ A/cm$^2$. This material structure, with slightly different layer dopings and thicknesses, has been previously reported by Muto *et al.* [6,7]. At a growth temperature of 470 °C they obtained a peak-to-valley current ratio of 5.5 at a current density of $4.8 \times 10^4$ A/cm$^2$. The difference in peak current density can be attributed to the higher doping densities in Muto's devices. When the device is cooled to liquid nitrogen temperature, the peak-to-valley current ratio increases to 15.2 with current density increasing to $2.4 \times 10^4$ A/cm$^2$. This is slightly greater than the Muto result (peak-to-valley ratio of 12) but at half the current density.

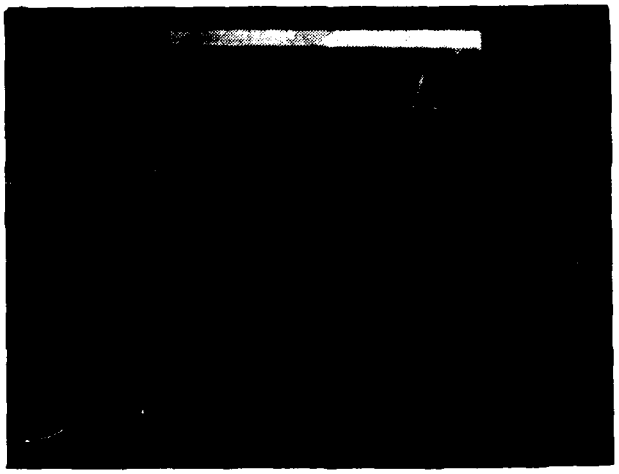

Fig.5 Room-temperature I-V characteristics for a lattice-matched InGaAs/InAlAs RTD.

The dependence of RTD peak current density and peak-to-valley current ratio on the atomic fraction x of In in the $In_xAl_{1-x}As$ tunnel barriers is shown in Figure 6. The In fraction x was found to be 0.35, 0.45, 0.52 (lattice-matched), 0.59, and 0.69. Room-temperature measurements were made of both forward and reverse diode polarities. Some general trends emerge with change in the InAlAs barrier composition. As the In fraction increases starting from 0.35, the conduction band discontinuity between InGaAs and the InAlAs layers decreases. This results in a wider transmission resonance and, therefore, an increasing peak current density as the In fraction increases. Valley current density increases at a greater rate than peak current density and a modest decrease in peak-to-valley ratio with increasing In fraction is observed. These same trends have been previously described by Inata et al.[8]

We can also gather information about the structure from observing the dependence of peak current density on bias polarity. When one of the tunnel barriers is thinner than the other, the resulting peak current density will be greatest for the bias polarity in which the electron traverses the thinnest barrier first.[9] With the exception of the $In_{0.69}Al_{0.31}As$ barrier, the thinnest tunnel barrier was always indicated nearest the surface. (For the x=0.69 diodes, two devices showed thinner barriers on top, while two devices showed thinner barriers on the bottom). For the x=0.35 devices, the peak current density is virtually the same for both directions of bias polarity, indicating that the barrier thicknesses are also the same. For x=0.35, it is also interesting to examine the peak-to-valley ratios which differ considerably for the two bias polarities. When electrons are directed up, the peak-to-valley ratio is considerably degraded over the case when the electrons are directed down. The valley current is increased when electrons pass through the lower barrier first. This might be caused by a rougher surface on the lower barrier giving rise to greater scattering and higher valley current.

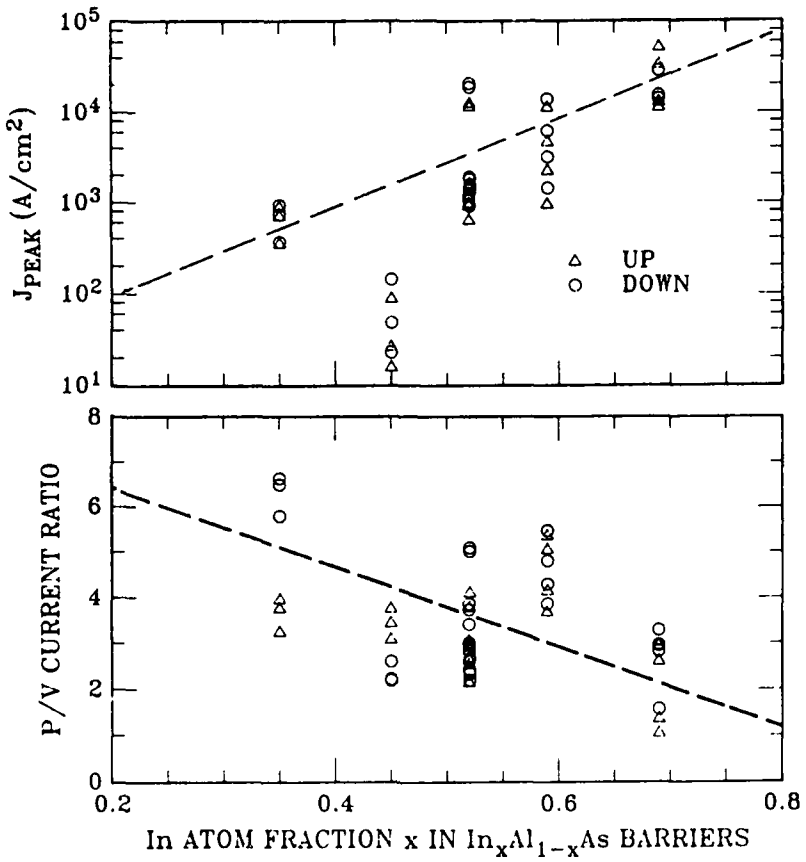


Fig.6 Dependence of peak current density and peak-to-valley current ratio on the tunnel barrier InAs mole fraction. The triangles (△) indicate electrons traversing from substrate to surface, while open circles (o) refer to the opposite electron direction.

## 4. DEVICE RESULTS

Various devices with InGaAs and InAlAs active regions have been successfully grown on InP by MBE using the optimized growth conditions. Growth interruption improved the abruptness of the interface and facilitated the growth temperature difference.

InP based HBTs are being developed by several research groups for high-speed and linear microwave applications. The high electron mobility of InGaAs reduces the base transit time in these devices, which, together with the reduced contact resistances, yields higher current gain cut-off frequencies, ($f_T$). Such devices are preferred for digital applications to improve the circuit speed and for their low emitter-base turn on voltages to reduce power consumption. We have fabricated InAlAs/InGaAs HBTs on InP substrates in this work. The wide-bandgap emitter in this structure was InAlAs, whereas the base and the collectors were made of InGaAs. A graded layer between the base and the emitter smoothed the bandgap discontinuity at the heterointerface. Another graded layer was used as a transition from the emitter layer to the smaller bandgap emitter contact layer. All layers were grown lattice-matched to InP. The dc common emitter characteristics of the HBT are shown in Figure 7. A typical current gain $\beta$ of 500 was obtained over a large range of collector current densities. The device breakdown voltage was about 3 V; lower than standard AlGaAs/GaAs HBTs due to the smaller bandgap of the InGaAs collector. The Gummel plots shown in Figure 8 indicate that the current gain remains almost constant over about 6 decades of current ranges. Such uniform beta values are indicative of low surface and interface recombination centers. Uniform beta values also indicate that the device dimensions

can be scaled down without compromising the current gain. The measured emitter-base turn-on voltage was 0.65 V compared with 1.45 V for standard AlGaAs/GaAs HBTs.

Fig.7 DC common emitter I-V characteristics of an InAlAs/InGaAs-on-InP HBT. The CE current gain of 500 is obtained.

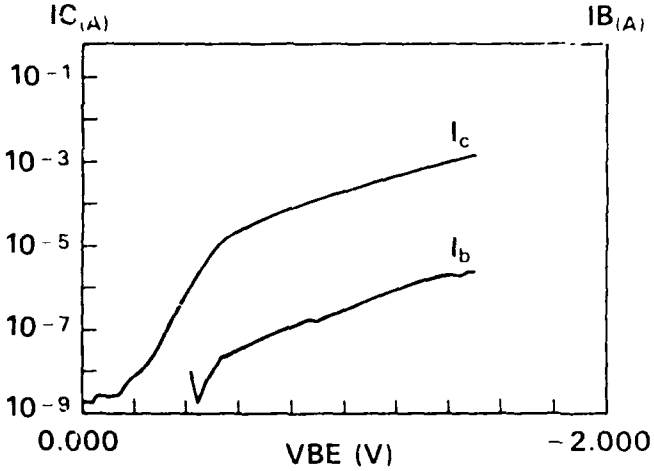


Fig.8 Gummel plots for InAlAs/InGaAs-on-InP HBT. The current gain remains constant over 6 decades of current ranges.

Modulation-doped n-InAlAs/InGaAs microwave HEMT devices were fabricated in this study. Devices with gate widths of 75 and 50 $\mu$m were fabricated on this material. The process is conventional: a mesa is first etched using a sulfuric acid, hydrogen peroxide, and water solution. AuGe/Ni/Au source drain ohmic contacts are deposited and alloyed at 375 °C for 3 minutes. The measured contact resistance is in the low $10^{-7}$ ohm-cm$^2$. The source-drain spacing is 1.5 $\mu$m. The 0.3-$\mu$m gates are defined using e-beam exposure and recessed to the desired value. Ti/Pt/Au with a total thickness of 600 nm is evaporated and lifted. After 100 nm of silicon nitride is deposited, fabrication of the bonding pads and air bridges complete the front-side processing. The wafer is then lapped to 4 mils and metallization of the backside is performed before the individual chips are scribed apart.

The I-V characteristics of a 25 $\mu$m x 0.3 $\mu$m test device are shown on Figure 9. The maximum transconductance is 600 mS/mm. S-parameter measurements indicate that the extrinsic $f_T$ is 65 GHz. The extrapolated $f_{max}$ is 150 GHz.

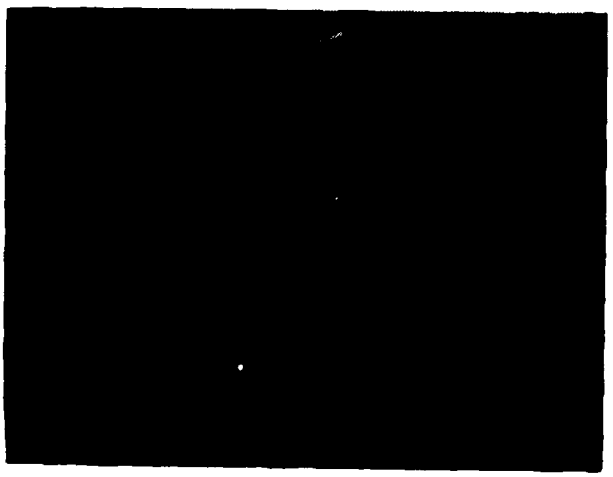

Fig.9 I-V characteristics of a 25 $\mu$m x 0.3 $\mu$m InAlAs/InGaAs HEMT. The vertical and horizontal scale is 1 mA/div and 200 mV/div, respectively. the step is 200 mV with $V_G$=0.2V.

## 5. SUMMARY

Lattice-matched InAlAs-InGaAs on InP heterostructures were successfully grown by MBE. The improved growth conditions were obtained with InAlAs and InGaAs grown at 525 °C and 470 °C, respectively, under a medium flux ratio of 7. The conditions were confirmed by Hall measurements on HEMT structures. Well defined quantum Hall plateaus on the HEMT structures were measured by 4.2 K magnetotransport. Two parallel 2DEGs on a double heterojunction HEMT structure were also obtained. InAlAs/InGaAs RTDs show very high quality negative differential resistance (NDR) characteristics ($J_p/J_v = 15.2$ with $J_p = 2.4\text{x}10^4$ A/cm$^2$ at 77 K). We also studied the effect of barrier composition on the NDR characteristics of InGaAs/$In_xAl_{1-x}As$ RTDs with x varying from 0.35 to 0.69. The higher barrier can improve the peak-to-valley current ratio by significantly reducing valley current. HBTs with constant $\beta$ of 500 over 6 decades of current range were achieved. HEMTs with 0.3-$\mu$m gate lengths exhibit a maximum transconductance of 600 mS/mm. S-parameter measurements indicate that the extrinsic $f_T$ is 65 GHz. The extrapolated $f_{max}$ is 150 GHz without optimized device processing. Processing improvements should further enhance device performance based on this InAlAs/InGaAs-on-InP material system.

## 6. ACKNOWLEDGEMENT

The authors would like to thank J.R. Thomason, B. Garmon, and P. Stickney for their technical assistance. This work was in part supported by an ONR/DARPA contract: N00014-84-C-0700.

## 7. REFERENCES

1. S. Hiyamizu, T. Fujii, S. Muto, T. Inata, Y. Nakata, Y. Sugiyama, and S. Sasa, *J. Crystal Growth* **81**, 349 (1987).
2. D.F. Welch, G.W. Wicks, L.F. Eastman, P. Parayanthal, and F.H. Pollak, *Appl. Phys. Lett.* **46**, 169 (1985).
3. C.E.C. Wood, *III-V Alloy Growth by Molecular-beam Epitaxy*, in *GaInAsP Alloy Semiconductors*, T.P. Pearsall ed., John Wiley & Sons, New York, 87-106 (1982).
4. A.S. Brown, U.K. Mishra, J.A. Henige, and M.J. Delaney, *J. Vac. Sci. Technol. B* **6(2)**, 678 (1988).
5. D.C. Tsui and A.C. Gossard, *Appl. Phys. Lett* **38**, 550 (1981).
6. S. Muto, T. Inata, Y. Sugiyama, Y. Nakata, T. Fujii, H. Ohnishi, and S. Hiyamizu, *Jpn. J. Appl. Phys.* **26**, L220 (1987).
7. Y. Sugiyama, T. Inata, S. Muto, Y. Nakata, and S. Hiyamizu, *Appl. Phys. Lett.* **52**, 314 (1988).
8. T. Inata, S. Muto, S. Sasa, T. Fujii, and S. Hiyamizu, *Extended Abstracts of the 19th Conf. on Solid State Devices and Materials, Tokyo*, 359 (1987).
9. M.A. Reed, W.R. Frensley, W.M. Duncan, R.J. Matyi, A.C. Seabaugh, and H.L. Tsai, *Appl. Phys. Lett.* **54**, 1256 (1989).

# APPENDIX N

# REALIZATION OF A THREE-TERMINAL RESONANT TUNNELING DEVICE: THE BIPOLAR QUANTUM RESONANT TUNNELING TRANSISTOR

# Realization of a three-terminal resonant tunneling device: The bipolar quantum resonant tunneling transistor

M. A. Reed, W. R. Frensley, R. J. Matyi,[a] J. N. Randall, and A. C. Seabaugh
*Central Research Laboratories, Texas Instruments, Incorporated, Dallas, Texas 75265*

(Received 30 August 1988; accepted for publication 22 December 1988)

A new three-terminal resonant tunneling structure in which current transport is controlled by directly modulating the potential of the quantum well is proposed and demonstrated. Typical current gains of 50 at room temperature are observed.

Resonant tunneling[1,2] provides a controllable current transport mechanism in semiconductor heterostructures. Recent attention has been focused upon exploiting this transport mechanism in three-terminal device configurations.[3–6] Many of these proposed and fabricated devices show behavior which could equally well be obtained from the series connection of a conventional semiconductor device and a resonant tunneling diode.[7] This letter presents a new bipolar quantum resonant tunneling transistor (BiQuaRTT) in which the tunneling current is directly controlled by modulating the potential *inside* a quantum well.[8]

The BiQuaRTT consists of a resonant tunneling diode structure in which the quantum well is doped $p$ type and separately contacted. It operates in a manner similar to a conventional bipolar transistor in that the potential in the base (i.e., the quantum well) is controlled by the density of holes as established by the Fermi level of the base contact. Operation via electron tunneling, however, imposes new constraints on the structure of the device. Because the resonant quantum state necessarily lies above the local conduction band, the conduction band in the emitter must be biased to an energy higher than that in the base, to obtain sufficient tunneling current. If a bipolar device were to be built in a conventional resonant tunneling diode structure where the band gaps of the quantum well and the two contacting layers are equal, such a bias condition would produce catastrophic leakage currents in the parasitic $pn$ junctions at the base contact. These leakage currents are suppressed by employing wider band-gap material in the emitter and collector layers of the BiQuaRTT.

A number of options exist for the creation of wider band-gap regions in the emitter and collector (with respect to the quantum well). One option is to utilize a $Al_xGa_{1-x}As$ emitter/$Al_yGa_{1-y}As$ tunnel barrier/$Al_zGa_{1-z}As$ quantum well structure ($y > x > z \geq 0$). Another is to utilize multimaterial systems, such as a GaAs emitter/$Al_xGa_{1-x}As$ tunnel barrier/$In_yGa_{1-y}As$ quantum well structure.[9] A third option, implemented here, is to create a wider band-gap material in the emitter/collector by using superlattices, i.e., a ($GaAs/Al_xGa_{1-x}As$) superlattice emitter/$Al_yGa_{1-y}As$ tunnel barrier/GaAs quantum well structure. The bottom of the first conduction-band miniband serves to emulate a homogeneous alloy raised injector region. In the present structure, a single Al source was used ($x = y$), although clearly more complex engineering can be obtained with multiple sources.

Figure 1 shows a schematic band diagram of the epitaxial structure. The structure was grown on a semi-insulating (Cr-doped) GaAs substrate using a Riber 2300 MBE system. The structure consisted of a 1.0 $\mu$m undoped GaAs buffer, GaAs contacts Si doped to $2\times10^{18}$ cm$^{-3}$ (1.5 $\mu$m bottom contact, 0.5 $\mu$m top contact), a superlattice emitter and collector consisting of 50 periods 80 Å GaAs + 20 Å $Al_{0.4}Ga_{0.6}As$ Si doped to $2\times10^{18}$ cm$^{-3}$ except for three undoped periods adjacent to the tunneling barriers, 50 Å undoped $Al_{0.4}Ga_{0.6}As$ tunnel barriers, and a 150 Å GaAs quantum well. The center 50 Å of the quantum well was doped $p$ type with Be to $1\times10^{19}$ cm$^{-3}$. The superlattices, AlGaAs barriers, and the quantum well were all grown at 640 °C as measured by a short wavelength pyrometer, while the GaAs contacts were grown at 600 °C. A cross-section transmission electron micrograph of the structure verified the dimensions.

The energy-band profile of the present BiQuaRTT design under a typical bias is shown in Fig. 2. The model from which this figure was obtained finds the self-consistent solution of Poisson's equation for the electrostatic potential. The electrons in the contacts are treated in a finite-temperature Thomas–Fermi approximation (i.e., these electrons are assumed to be in local equilibrium with the Fermi levels established by their respective electrodes.) The superlattice layers are represented as homogeneous alloys, the effective composition (of 0.07) determined by solving an envelope wave function approximation for the superlattice minibands. The

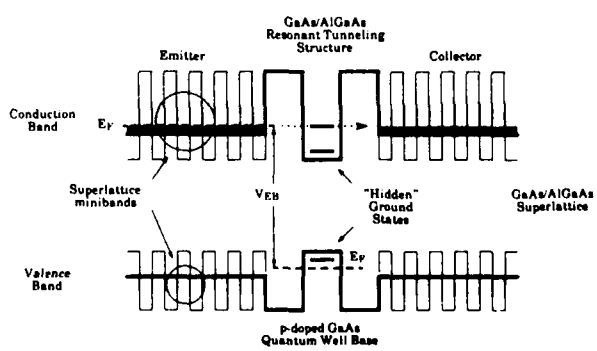


FIG. 1. Schematic band structure diagram of the BiQuaRTT. The emitter and collector are superlattices that clad the double-barrier resonant tunneling structure, and the base is a $p$-doped quantum well with a "hidden" ground state.

[a] Present address: Department of Metallurgical and Mineral Engineering, University of Wisconson, Madison, WI 53706.

 © 1989 American Institute of Physics 

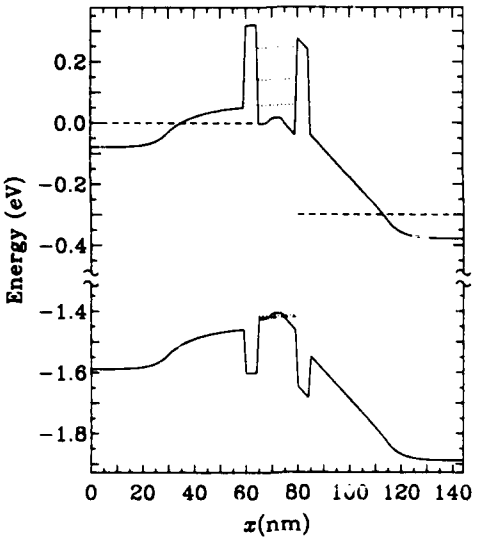


FIG. 2. Energy-band profile obtained from a numerical simulation of the present BiQuaRTT structure at 300 K with $V_B = 1.42$ V and $V_C = 0.30$ V. The energies of the resonant electron states and the first confined heavy hole state are shown by dotted lines, and the Fermi levels of the respective electrodes are shown by dashed lines. The presence of a resonant level within a few kT of the emitter Fermi level and the confinement of the hole state are apparent. This simulation neglects current flow, self-consistently solving for the carrier distribution and potental under an assumption of local quasiequilibrium.

confined holes in the base are treated quantum mechanically by solving Schroedinger's equation for the ground state and multiplying the resulting probability density by the Fermi distribution. In the present simulation the base is biased to $+1.42$ V to pull the quantum well potential down to the vicinity of that of the emitter.

Devices were fabricated using contact lithography, lift-off metallization processes, and implantation. To form a low-resistance contact to the quantum well, a triple Be implant was used consisting of consecutive doses of $1\times10^{15}$ $cm^{-2}$ at 30, 80, and 160 keV. A rapid thermal anneal at 750 °C for 10 s was sufficient to activate the anneal. Ohmic contact to the base was achieved with Ti/Pt/Au, while a Ni/Ge/Au composite formed the collector and emitter contacts. A shallow etch was performed between the emitter and base (implanted contact) to improve isolation between these two contacts. A $Si_3N_4$ passivation layer was deposited over the entire structure.

Figure 3 shows the common emitter characteristics (current bias) $I_C$ vs $V_{CE}$ of a typical BiQuaRTT structure at room temperature. It should be noted that negative differential resistance should not be observable in this structure if indeed the contact to the quantum well is obtained and the well is not depleted. Typical current gains of 50 are observed, although a singular device exhibited a current gain of 450.

The distinguishing characteristic of this structure is that transport is determined by tunneling through the quantum well states that are biased into resonance by the base potential. Because the quantum well potential is controlled by the base voltage, the familiar signature of a negative differential resistance for a resonant tunneling diode appears as a negative transconductance in this structure. Figure 4 shows the

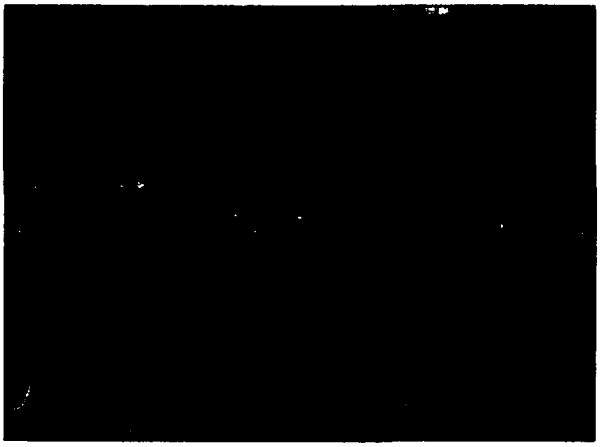

FIG. 3. Common emitter characteristics (current bias) $I_C$ vs $V_{CE}$ of a typical BiQuaRTT structure. Emitter area = $(5\,\mu m)^2$, $T = 300$ K.

common emitter characteristics, voltage bias, of the same device shown in Fig. 3. The inset to the figure shows the transconductance, which becomes negative at $V_B = 1.1$ V. The negative transconductance values shown here are typical; values as high as $-4.0$ mS (for similar 5 $\mu$m square mesas) have been observed. It should be noted that the maximum current density of $5.6\times10^3$ A/cm$^2$ (i.e., before the transconductance becomes negative) is approximately the same as the current density of this resonant tunneling peak observed in a control structure identical except for the *p*-type quantum well doping.

An important characteristic shown in Fig. 4 is that the transconductance asymptotically becomes *positive* (for $V_B > 1.25$ V). This is due to initiation of resonant tunneling through the next excited state of the quantum well. Parasitic base leakage current of the implanted *pn* junction, for which Fig. 5 has been corrected, prevented observation of further

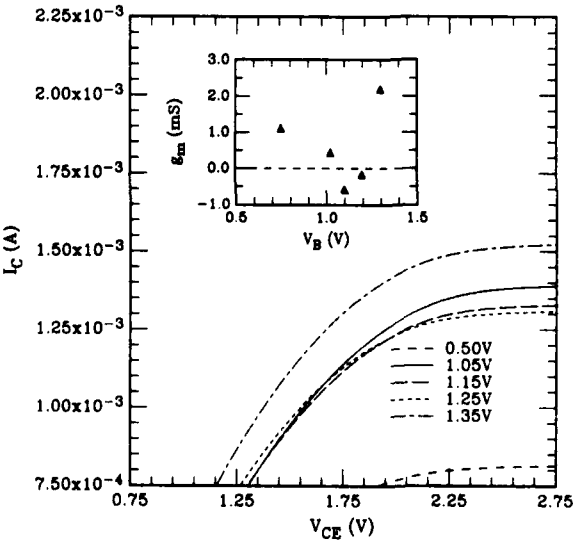


FIG. 4. Common emitter characteristics (voltage bias) $I_C$ vs $V_{CE}$ of the BiQuaRTT structure shown in Fig. 3. Emitter area = $(5\,\mu m)^2$, $T = 300$ K. The inset shows the transconductance $g_m$ as a function of base potential $V_B$. For $1.05\text{ V} < V < 1.25$ V, the transconductance is negative.

transconductance peaks due to tunneling through higher excited states. Properly designed structures, such as those utilizing InGaAs quantum wells (for larger dynamic range), should allow structures with multiple transconductance peaks.

In summary, a new three-terminal resonant tunneling structure in which current transport is controlled by directly modulating the potential of the quantum well has been demonstrated. Typical current gains of 50 at room temperature and transconductance indicative of resonant tunneling through quantum well states are observed.

This work was supported by the Air Force Wright Aeronautical Laboratories. We are indebted to R. T. Bate for constant support and encouragement, to H.-L. Tsai for TEMs, to B. Bayraktaroglu, B. Kim, F. Morris, D. L. Plumpton, and C.-H. Yang for discussions, and to P. F. Stickney, F. H. Stovall, and J. R. Thomason for technical assistance.

[1] L. L. Chang, L. Esaki, and R. Tsu, Appl. Phys. Lett. **24**, 593 (1974).
[2] T. C. L. G. Sollner, W. D. Goodhue, P. E. Tannenwald, C. D. Parker, and D. D. Peck, Appl. Phys. Lett. **43**, 588 (1983).
[3] F. Capasso and R. A. Kiehl, J. Appl. Phys. **58**, 1366 (1986).
[4] A. R. Bonnefoi, T.C. McGill, and R.D. Burnham, IEEE Electron Dev. Lett. **EDL-6**, 636 (1985).
[5] N. Yokoyama, K. Imamura, S. Muto, S. Hiyamizu, and H. Nishi, Jpn. J. Appl. Phys. **24**, L853 (1985).
[6] F. Capasso, S. Sen, A. C. Gossard, A. L. Hutchinson, and J. H. English, IEEE Electron Device Lett. **EDL-7**, 573 (1986).
[7] T. K. Woodward, T.C. McGill, and R.D. Burnham, Appl. Phys. Lett. **50**, 451 (1987).
[8] W. R. Frensley and M.A. Reed, U. S. patent application serial No. 825 720, filed Jan. 31, 1986. The unipolar embodiment of this device concept (W. R. Frensley and M. A. Reed, U. S. patent application serial No. 768 542, filed Aug. 23, 1985) has been independently invented: J. N. Schulman and M. Waldner, J. Appl. Phys. **63**, 2859 (1988); and G. I. Haddad, R. K. Mains, U. K. Reddy, and J. R. East, presented at the *Fourth International Conference on Superlattices, Microstructures, and Microdevices*, Trieste, Italy, August 1988 (to be published).
[9] M. A. Reed and J. W. Lee, Appl. Phys. Lett. **50**, 845 (1987).